

2023

## Development of Novel Anticancer Agents Targeting Glioblastoma

Kate Byrne

*Technological University Dublin, [kate.byrne@tudublin.ie](mailto:kate.byrne@tudublin.ie)*

Follow this and additional works at: <https://arrow.tudublin.ie/sfehthes>

 Part of the [Medicine and Health Sciences Commons](#)

---

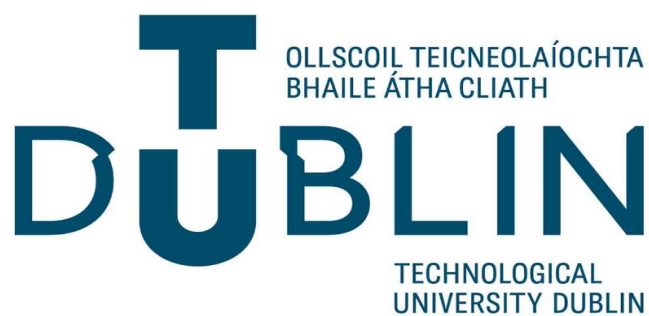
### Recommended Citation

Byrne, Kate, "Development of Novel Anticancer Agents Targeting Glioblastoma" (2023). *Theses*. 17.  
<https://arrow.tudublin.ie/sfehthes/17>

This Doctoral Thesis is brought to you for free and open access by the School of Food Science and Environmental Health at ARROW@TU Dublin. It has been accepted for inclusion in Theses by an authorized administrator of ARROW@TU Dublin. For more information, please contact [arrow.admin@tudublin.ie](mailto:arrow.admin@tudublin.ie), [aisling.coyne@tudublin.ie](mailto:aisling.coyne@tudublin.ie), [vera.kilshaw@tudublin.ie](mailto:vera.kilshaw@tudublin.ie).



This work is licensed under a [Creative Commons Attribution-Share Alike 4.0 International License](#).



# **Development of Novel Anticancer Agents Targeting Glioblastoma**

Submitted by

Kate Byrne, BSc (Hons.)

**Doctor of Philosophy**

Food Science and Environmental Health, Environmental  
Sustainability and Health Institute, Technological University Dublin

**Supervisors:**

Dr Gemma K. Kinsella,

Professor James F. Curtin,

Professor John C. Stephens

2023



## ABSTRACT

Glioblastoma (GBM) is the most common and aggressive malignant grade IV brain tumour. It remains an incurable disease whereby the median survival rate is 15 months and 5.5 % of all patients survive five years post diagnosis. The current therapeutic strategies include the use of maximal safe surgical resection, radiotherapy, and the use of the gold standard chemotherapeutic, Temozolomide (TMZ), which is referred to as the “Stupp Protocol”. Earlier research identified two compounds, which are structurally different but exhibit a similar biological effect to Metformin, the first in-line treatment for type II diabetes. Combining drugs which target cell metabolism such as Metformin with chemotherapeutic agents and or radiotherapy has become an attractive treatment for cancer. It was hypothesized that these compounds may have anti-cancer properties due to their ability to impede cell metabolism.

In this work, a structure activity relationship (SAR) study was carried out to discover more effective compounds which are also more selective for the cancerous U251-MG cell line. To probe the SAR, a series of twenty substituted pyrazolo[1,5- $\alpha$ ]pyrimidinones were screened using an MTT cell proliferation assay against the U-251MG cell line and HEK293 cell line. Four compounds from this screen were shown to be statistically significant in terms of their low  $\mu\text{M}$   $\text{IC}_{50}$  values for the U251-MG cell line and were deemed to be hit compounds. To further explore the SAR, additional analogues of the hit compounds were synthesised, purified, and characterised. The synthesis method used for each compound was a one-pot method for the microwave assisted synthesis of substituted pyrazolo[1,5- $\alpha$ ]pyrimidinones which was established by the Stephens research group in

Maynooth University. The analogue compounds were biologically screened and a further two hit compounds were determined.

An in-depth look into the six hit compounds and their ability to induce cell death in the cancerous U251-MG cell line was carried out. The compounds were screened in conjunction with TMZ to determine whether a synergistic effect would be observed however this was not the case and the compounds were found to be not suitable to be used as part of a co-treatment study.

Flow cytometry and inhibitor studies were carried out to elicit a potential mechanism of cell death by the hit compounds. Flow cytometry confirmed the MTT cell viability assay whereby observed cell death was confirmed in the hit compounds using both the propidium iodide and JC-1 dye. Inhibitor studies were then carried out to further narrow down a mode of cell death where three inhibitors were used as part of the study: the E-64 inhibitor, SP600125 and the zVAD-fmk inhibitor. The main inhibitor of interest was the zVAD-fmk inhibitor, a pan caspase inhibitor which can inhibit the induction of apoptosis. Statistical significance for this inhibitor was observed in four hit compounds. One hit compound was inhibited by the E-64 cysteine protease inhibitor one hit compound was inhibited by the SP600125 JNK inhibitor.

3D cell culture was carried out to determine if any of the hit compounds have the potential to elicit cell death *in vivo*. There was only one hit compound which obtained an  $IC_{50}$  below the current marketed drugs  $IC_{50}$  threshold ( $< 50 \mu M$ ) with an  $IC_{50}$  value of  $33.55 \mu M$ . A second hit compound obtained an  $IC_{50}$  value which was slightly above the threshold at  $51.72 \mu M$ . With additional studies these two novel compounds could potentially be used as therapeutics in the treatment of GBM.

## **DECLARATION**

I certify that this thesis which I now submit for examination for the award of PhD, is entirely my own work and has not been taken from the work of others, save and to the extent that such work has been cited and acknowledged within the text of my work. This thesis was prepared according to the regulations for graduate study by research of the Technological University Dublin and has not been submitted in whole or in part for another award in any other third level institution. The work reported in this thesis conforms to the principles and requirements of TU Dublin's guidelines for ethics in research. TU Dublin has permission to keep, lend or copy this thesis in whole or in part, on condition that any such use of the material of the thesis be duly acknowledged.



Signature

Date \_\_31-March-2023\_\_

Candidate

## **ACKNOWLEDGEMENTS**

This is not necessarily the most important section of the thesis although one can argue that it is certainly the most read. I'm not one for words and so will do my best to do this section justice. I would like to thank the following people who encouraged me to carry out this work and those who aided and abetted in my procrastination.

First and foremost, I would like to express my sincere gratitude to my three supervisors Dr. Gemma Kinsella, Professor James Curtin, and Professor John Stephens. Dr. Gemma Kinsella, thank you for your unwavering patience and ability to manage me over this prolonged period. You have the patience of a saint and deserve a medal. Professor James Curtin, your knowledge and expertise has been invaluable throughout this project and for that I am eternally grateful. Professor John Stephens, thank you for making my entire experience in Maynooth so enjoyable, it was the highlight of my entire PhD. You went above and beyond in guiding and helping me with the chemistry, and I really appreciate it.

To my parents Gareth and Grace-Ann, thank you for your constant support and encouragement over the course of my academic career and for always having a glass of wine on standby for one of my many meltdowns. Without a shadow of a doubt, I have been blessed with the best parents who would do anything for me. To my sister Zoe, you were always on hand to listen, offer advice and help when I needed it. It is much appreciated. Also, you're next!!

Thomas J. Butler, TJ. I will never forget one of our first interactions when I started this journey, you said that you'd be gone soon, and that I probably wouldn't see you again. Well, jokes on you – it's been five years and I'm not going anywhere! Thank you for providing me with a space to write for the last seven months as I am physically incapable of writing alone without getting distracted. You're my best pal and I look forward to wrecking your head for the foreseeable future.

To the ESHI gang Megan, Jamie, Rory, Brian, Tadhg, Aaron and Siobhán, you're the reason chieftain is banned in barbers and the reason I now know when it is National Martin Day in the Czech Republic, I'll say less. Thank you for all the memories and for making this whole experience so enjoyable. I have made friends for life.

To my best friend in the whole world Hannah, we've come a long way from drinking €4 warm wine and Arcade Fire concerts. Even though we're living miles apart I know that when I do see you next it will be like no time has passed. To my compadré Niamh, thank you for always supporting me and listening to my ramblings. I look forward to many more Oktoberfest's together and some "techno party" when I do eventually come to Rotterdam. To Sebnem, you're a friend for life and I'm just sad I never met you sooner.

To my boyfriend, human and partner in crime Johannes, thank you for always putting up with me. I'm looking forward to spending our next chapter together.

Thank you everyone.



## **ABBREVIATIONS**

**ABC** Adenosine Triphosphate Binding Cassette

**ACKRs** Atypical Chemokine Receptors

**ADC** Apparent Diffusion Coefficient

**ADME** Absorption Distribution Metabolism Excretion

**AMP** Adenosine Monophosphate

**AMPK** Adenosine Monophosphate-Activated Protein Kinase

**ANOVA** Analysis of Variance

**APC** Adenomatous Polyposis Coli

**ATCC** American Type Culture Collection

**ATP** Adenosine Triphosphate

**BBB** Blood Brain Barrier

**BCNU** Carmustine (*bis*-chloroethylnitrosourea)

**BCRP** Breast Cancer Resistance Protein

**BCSFB** Blood-Cerebrospinal Fluid Barrier

**BOLD** Blood Oxygen Level Dependant

**BVZ** Bevacizumab

**CB** Cannabinoid receptor type

**CBD** Cannabidiol

**CCNU** Lomustine (1- (2-chloro-ethyl)-3-cyclohexyl-1-nitrosourea)

**CI** Confidence Interval

**CL** Classical Subtype

**CNS** Central Nervous System

**CT** Computerised Tomography

**CW** Carmustine Wafer

**DMEM** Dulbecco's Modified Eagles Medium

**DMSO** Dimethyl sulfoxide

**DNA** Deoxyribonucleic acid

**DR** Death Receptor

**DWI** Diffusion Weighted Imaging

**ECM** Extracellular Matrix

**ECS** Endocannabinoid system

**EDTA** Ethylenediaminetetraacetic acid

**EGF** Epidermal Growth Factor

**EGFR** Epidermal Growth Factor Receptor

**EOR** Extent of Resection

**EORTC-NCIC** European Organisation for Research and Treatment of Cancer-National  
Cancer Institute of Canada

**ETC1** Electron Transfer Chain 1

**FACS** Fluorescence Assisted Cell Sorting

**FBS** Foetal Bovine Serum

**FDA** Food and Drug Administration

**FITC** Fluorescein isothiocyanate

**FTIR** Fourier Transform Infrared Spectroscopy

**FSC** Forward Scatter

**GABRA1** Gamma-Aminobutyric Acid Type A Receptor Alpha1 Subunit

**GBM** Glioblastoma

**GC** Gas Chromatography

**G-CIMP** Glioma-CpG Island Methylator Phenotype

**GDP** Guanosine Diphosphate

**GIT** Gastrointestinal Tract

**GPCR** G-Protein Coupled Receptor

**GSC** Glioblastoma Stem Cell

**GTP** Guanosine Triphosphate

**Gy** Gray

**HBOC** Hereditary Breast and Ovarian Cancer

**HER1** Human Epidermal Growth Factor 1

**HEK** Human Embryonic Kidney

**HIV** Human Immunodeficiency Virus

**HPV** Human Papillomavirus

**ICB** Immune Checkpoint Blockade

**ICP** Intracranial Pressure

**IDDM** Insulin Dependent Diabetes Mellitus

**IDH** Isocitrate Dehydrogenase

**IG** Infiltrating Glioma

**IM** Intramuscular

**IV** Intravenous

**JC-1** 5,5,6,6'-tetrachloro-1,1',3,3'-tetraethylbenzimidazolylcarbocyanine iodide

**LC-MS** Liquid Chromatography – Mass Spectrometry

**LL** Lower Left Quadrant

**LR** Lower Right Quadrant

**LKB1** Liver Kinase B1

**mAbs** Monoclonal Antibodies

**MAPK** Mitogen Activated Protein Kinase

**MES** Mesenchymal

**MET** Mesenchymal-Epithelial Transition

**MiRNA** micro-Ribonucleic Acid

**MMR** Mismatch Repair

**MR** Magnetic Resonance

**MRI** Magnetic Resonance Imaging

**MRP** Multidrug Resistance-Associated Protein

**MTIC** [(methyl-triazine-1-yl)-imidazole-4-carboxamide]

**MTOR** Mammalian Target of Rapamycin

**MTT** 3-(4,5-Dimethylthiazol-2-yl)-2,5-diphenyltetrazolium bromide

**MTX** Methotrexate

**MW** Microwave

**MYB** Myeloblastosis

**MYBL<sub>1</sub>** Myeloblastosis Ligand 1

**NEFL** Neurofilament Light

**NES** Neuroectodermal Stem Cell Marker

**NF** Neurofibromin

**NIDDM** Non-Insulin Dependent Diabetes Mellitus

**NSAIDs** Non-Steroidal Anti-Inflammatory Drugs

**PBS** Phosphate Buffered Saline

**PCV** Procarbazine Lomustine Vincristine Sulfate

**PCR** Polymerase Chain Reaction

**PD-1** Programmed cell death receptor-1

**PDGF** Platelet Derived Growth Factor

**PDGFR** Platelet Derived Growth Factor Receptor

**PDGFRA** Platelet Derived Growth Factor Receptor A

**PE-Cy5** R-phycoerythrin

**P-Gp** P-Glycoprotein

**PI** Propidium Iodide

**PLNTY** Polymorphous Low-grade Neuroepithelial Tumour of the Young

**PN** Proneural

**Poly-HEMA** poly-2-hydroxyethyl methacrylate

**PTEN** Phosphatase and Tensin Homolog

**PWI** Perfusion-Weighted Imaging

**QSAR** Quantitative Structure-Activity Relationship

**RAS** Rat Sarcoma virus protein

**RCBV** Relative Cerebral Blood Volume

**RNA** Ribonucleic acid

**S1P** Sphingosine 1-Phosphate

**SAR** Structure Activity Relationship

**SARS-CoV-2** Severe Acute Respiratory Syndrome Coronavirus-2

**SC** Subcutaneous

**SSC** Side Scatter

**TEM** Transmission Electron Microscopy

**TERT** Human Telomerase Reverse Transcriptase

**THC** Tetrahydrocannabinol

**TJ** Tight Junction

**TMZ** Temozolomide

**TNF- $\alpha$**  Tumour Necrosis Factor  $\alpha$

**TNFRSF** Tumour Necrosis Factor Receptor Super Family

**TNM** Tumour Node Metastasis

**TP53** Tumour Protein 53 gene

**UICC** Union for International Cancer Control

**UL** Upper Left Quadrant

**UR** Upper Right Quadrant

**UV** Ultraviolet

**VEGF-A** Vascular Endothelial Growth Factor A

**WHO** World Health Organisation

## TABLE OF CONTENTS

Abstract .....	i
Declaration .....	iii
Acknowledgements .....	iv
Abbreviations .....	vi
Table of Contents .....	xiii
List of Figures .....	xxii
List of Tables .....	xxv
 <b>INTRODUCTION</b>	 <b>- 27 -</b>
1.1. Tumours of the Central Nervous System .....	- 28 -
1.1.1 Brain Tumour Grading.....	- 29 -
1.2. Glioblastoma, GBM .....	- 32 -
1.2.1 The Four Subtypes of GBM.....	- 33 -
1.3. Diagnosis and Treatment in Glioblastoma .....	- 34 -
1.3.1 Imaging Strategies in Brain Tumours .....	- 35 -
1.3.2 The Stupp Protocol .....	- 36 -
1.4. Chemotherapeutic Agents .....	- 37 -
1.4.1 Temozolomide, TMZ.....	- 38 -
1.4.2 TMZ Structure and Mechanism of Action.....	- 40 -
1.4.2.1 TMZ Treatment .....	- 42 -
1.4.3 Other Chemotherapeutic Agents for GBM.....	- 43 -
1.5. The Blood-Brain Barrier and GBM Treatment .....	- 44 -
1.5.1 Lipinski's Rule of Five .....	- 47 -
1.5.2 Drug Transport Across the Blood-Brain Barrier .....	- 49 -
1.6. Search for Novel Therapeutic Targets for GBM .....	- 50 -
1.6.1 Cancer Immunotherapy.....	- 50 -
1.6.2 Drug Repurposing .....	- 53 -
1.6.2.1 Metformin.....	- 54 -



1.6.2.2	Mode of Action of Metformin.....	- 55 -
1.6.2.3	Drug Repurposing of Metformin.....	- 57 -
1.6.2.4	Rationale.....	- 59 -
1.7.	Aims and Objectives.....	- 61 -
<b>2.</b>	<b>INITIAL <i>IN VITRO</i> STRUCTURE ACTIVITY RELATIONSHIP STUDY OF PYRAZOLO[1,5-A]PYRIMIDINONES FOR THE TREATMENT OF GBM</b>	<b>- 63 -</b>
2.1.	Cell Culture .....	- 64 -
2.1.1	U251-MG Cell Line.....	- 65 -
2.1.2	HEK293 Cell Line .....	- 65 -
2.1.3	Cell Viability Assays .....	- 66 -
2.1.3.1	MTT Assay.....	- 67 -
2.1.4	Pharmacological Analysis.....	- 68 -
2.1.4.1	Dose-Response Curves.....	- 69 -
2.1.5	The Pyrazolo[1,5- $\alpha$ ]pyrimidinone Family .....	- 70 -
2.2.	Materials and Methods .....	- 72 -
2.2.1	Pyrazolopyrimidinone Synthesis .....	- 72 -
2.2.2	General Cell Culture, Maintenance and Sub-Culture .....	- 72 -
2.2.2.1	Cell Culture .....	- 72 -
2.2.2.2	Cell Culture Subculture.....	- 73 -
2.2.2.3	Cell Freezing Method.....	- 73 -
2.2.2.4	Cell Defrosting .....	- 74 -
2.2.3	Cell Density for Cell Viability Assay .....	- 74 -
2.2.4	MTT Cell Viability Assay .....	- 74 -
2.2.5	Spectrophotometer Data Analysis .....	- 75 -
2.2.6	Statistical Analysis.....	- 75 -
2.2.7	Physicochemical Properties .....	- 76 -
2.3.	Results .....	- 77 -
2.3.1	Initial Compound Evaluation using U251-MG and HEK293 Cell Lines.-	- 77 -
2.3.1.1	Group 1 Compounds .....	- 77 -
2.3.1.2	Group 2A Pyrazolo[1,5- $\alpha$ ]pyrimidinones .....	- 83 -

2.3.1.3	Group 2B Pyrazolo[1,5- $\alpha$ ]pyrimidinones.....	89
2.3.1.4	Group 2C Pyrazolo[1,5- $\alpha$ ]pyrimidinones.....	93
2.3.1.5	Group 3 Pyrazolo[1,5- $\alpha$ ]pyrimidinones .....	97
2.3.1.6	Group 4 Pyrazolo[1,5- $\alpha$ ]pyrimidinones .....	100
2.3.2	Comparison of U251-MG and HEK293 Cell Line Results .....	105
2.3.2.1	Group 1 Pyrazolo[1,5- $\alpha$ ]pyrimidinones .....	108
2.3.2.2	Group 2A Pyrazolo[1,5- $\alpha$ ]pyrimidinones .....	109
2.3.2.3	Group 2B Compounds.....	112
2.3.2.4	Group 2C Compounds.....	112
2.3.2.5	Group 3 and 4 Compounds.....	112
2.3.3	Statistical Analysis.....	113
2.3.4	Physicochemical Properties of the Hit Compounds .....	116
2.4.	Discussion.....	120
<b>3.</b>	<b>SYNTHESIS OF PYRAZOLO[1,5-A]PYRIMIDINONE COMPOUNDS &amp; <i>IN VITRO</i> EVALUATION AGAINST GBM</b>	<b>125</b>
3.1.	Introduction .....	126
3.1.1	Pyrazolopyrimidinones .....	126
3.1.2	Pyrazolopyrimidinones and Microwave Chemistry .....	128
3.1.3	Improving Biological Activity.....	129
3.2.	Results and Discussion .....	134
3.2.1	5-Aminopyrazoles.....	134
3.2.2	3.3.1.1 Synthesis of 5-Aminopyrazole 1.....	136
3.2.3	Structural Characterisation of 5-Aminopyrazole 1 .....	137
3.2.4	Synthesis of Pyrazolo[1,5- $\alpha$ ]pyrimidinones .....	138
3.2.5	Structural Characterisation of Pyrazolo[1,5- $\alpha$ ]pyrimidinones.....	142
3.2.5.1	TUM-2A-001 .....	142
3.2.5.2	TUM-2A-004 .....	143
3.2.5.3	TUM-2A-005 .....	144
3.2.5.4	TUM-2A-007 .....	146

3.2.5.5	TUM-2A-008 .....	147
3.2.5.6	TUM-2A-013 .....	148
3.2.5.7	TUM-2A-014 .....	150
3.2.5.8	TUM-2A-015 .....	151
3.2.5.9	TUM-2A-016 .....	152
3.2.5.10	TUM-2A-017 .....	153
3.2.6	Conclusions on the Synthesis of Pyrazolo[1,5- $\alpha$ ]pyrimidinones.....	155
3.3.	Experimental.....	163
3.3.1	General Experimental .....	163
3.3.1.1	Purification of Reagents and Solvents for Synthetic Work.....	163
3.3.2	Purification of Products .....	163
3.3.2.1	Thin Layer Chromatography .....	163
3.3.2.2	Flash Column Chromatography .....	163
3.3.2.3	Rotary Evaporator .....	163
3.3.3	Analysis of Products .....	164
3.3.3.1	Liquid Chromatography-Mass Spectrometry (LC-MS) Analysis.....	164
3.3.3.2	Nuclear Magnetic Resonance Spectroscopy (NMR) Analysis .....	164
3.3.4	Materials and Methods for Biological Evaluation .....	165
	The method employed in the biological evaluation of the analogue compounds is the same of that outlined in Chapter 2. ....	165
3.4.	Synthesis of 5-Aminopyrazole Intermediates.....	165
3.5.	Synthesis of Substituted Pyrazolo[1,5- $\alpha$ ]pyrimidinones .....	167
3.5.1	5-(3,5-Bis(trifluoromethyl)phenyl)-2-phenylpyrazolo[1,5- $\alpha$ ]pyrimidin-7(4H)-one (TUM-2A-001).....	168
3.5.2	5-(3,5-Bis(trifluoromethyl)phenyl)-2-(4-bromophenyl)pyrazolo[1,5- $\alpha$ ]pyrimidin-7(4H)-one (TUM-2A-004).....	169
3.5.3	5-(3,5-Bis(trifluoromethyl)phenyl)-2-(4-chlorophenyl)pyrazolo[1,5- $\alpha$ ]pyrimidin-7(4H)-one (TUM-2A-005).....	170
3.5.4	5-(3,5-Bis(trifluoromethyl)phenyl)-2-(4-(trifluoromethyl)phenyl)pyrazolo[1,5- $\alpha$ ]pyrimidin-7(4H)-one (TUM-2A-007) .....	171

3.5.5	5-(3,5-Bis(trifluoromethyl)phenyl)-2-(4-nitrophenyl)pyrazolo[1,5-a]pyrimidin-7(4H)-one (TUM-2A-008).....	172
3.5.6	5-(3,5-Bis(trifluoromethyl)phenyl)-2-(3-(trifluoromethyl)phenyl)pyrazolo[1,5-a]pyrimidin-7(4H)-one (TUM-2A-013).....	173
3.5.7	5-(3,5-Bis(trifluoromethyl)phenyl)-2-(2-(trifluoromethyl)phenyl)pyrazolo[1,5-a]pyrimidin-7(4H)-one (TUM-2A-014).....	174
3.5.8	5-(3,5-Bis(trifluoromethyl)phenyl)-2-(3-bromophenyl)pyrazolo[1,5-a]pyrimidin-7(4H)-one (TUM-2A-015).....	175
3.5.9	5-(3,5-Bis(trifluoromethyl)phenyl)-2-(2-bromophenyl)pyrazolo[1,5-a]pyrimidin-7(4H)-one (TUM-2A-016).....	176
3.5.10	5-(3,5-Bis(trifluoromethyl)phenyl)-2-(3-nitrophenyl)pyrazolo[1,5-a]pyrimidin-7(4H)-one (TUM-2A-017).....	177
3.6.	Optimised HIT Compound Cell Viability Assays.....	178
3.7.	Results and Discussion of Biological Evaluation.....	179
3.7.1	U-251 MG Cell Line.....	179
3.7.2	HEK293 Cell Line .....	182
3.7.3	Comparison of U-251 MG Cell Line and HEK293 Cell Line.....	184
3.7.4	Statistical Analysis - ANOVA.....	186
3.8.	Biological Evaluation Discussion.....	187
<b>4.</b>	<b>EVALUATION OF HIT COMPOUNDS FOR SUITABILITY IN A CO-TREATMENT STUDY FOR GBM AND DETERMINATION OF POTENTIAL MECHANISM OF ACTION OF HIT COMPOUNDS</b>	<b>189</b>
4.1.	Introduction .....	190
4.1.1	Co-Treatment Studies .....	190
4.1.2	Drug Co-Treatment.....	191
4.1.3	Flow Cytometry .....	193
4.1.3.1	Cell Death and Flow Cytometry.....	193
4.1.3.2	Propidium Iodide.....	196
4.1.3.3	JC-1 Dye.....	196

4.1.4	Inhibitor Studies.....	197
4.1.5	3D Cell Culture.....	200
4.2.	Materials and Methods .....	204
4.2.1	Co-Treatment Studies .....	204
4.2.1.1	Preparation of Stock Solution for TMZ .....	204
4.2.1.2	TMZ Combination Therapy .....	204
4.2.2	Flow Cytometry .....	205
4.2.2.1	Propidium Iodide.....	205
4.2.2.2	Propidium Iodide Analysis.....	206
4.2.2.3	Propidium Iodide Flow Cytometry Analysis .....	209
4.2.2.4	JC-1 Dye.....	209
4.2.2.5	JC-1 Dye Analysis.....	210
4.2.2.6	JC-1 Dye Flow Cytometer Analysis.....	210
4.2.3	Inhibitor Studies.....	211
4.2.3.1	E-64 Inhibitor .....	211
4.2.3.2	SP600125 Inhibitor .....	211
4.2.3.3	zVAD-fmk Inhibitor.....	212
4.2.4	3D Cell Culture Low Attachment Plate Method .....	212
4.2.4.1	Spheroid Cell Viability Analysis.....	214
4.2.5	Spectrophotometer Data Analysis .....	214
4.2.6	Statistical Analysis.....	215
4.3.	Results .....	216
4.3.1	Co-Treatment Study.....	216
4.3.1.1	TMZ Analysis .....	217
4.3.1.2	TMZ Co-Treatment .....	219
4.3.2	Flow Cytometry .....	222
4.3.2.1	TUM-2A-001 PI Analysis.....	222
4.3.2.2	TUM-2A-004 PI Analysis.....	226
4.3.2.3	TUM-2A-007 PI Analysis.....	229
4.3.2.4	TUM-2A-008 PI Analysis.....	231

4.3.2.5	TUM-2A-015 PI Analysis .....	233
4.3.2.6	TUM-2A-016 PI Analysis .....	235
4.3.2.7	HIT Compound Propidium Iodide Analysis .....	237
4.3.2.8	TUM-2A-001 JC-1 Dye Analysis .....	242
4.3.2.9	TUM-2A-004 JC-1 Dye Analysis .....	247
4.3.2.10	TUM-2A-007 JC-1 Dye Analysis .....	249
4.3.2.11	TUM-2A-008 JC-1 Dye Analysis .....	251
4.3.2.12	TUM-2A-015 JC-1 Dye Analysis .....	253
4.3.2.13	TUM-2A-016 JC-1 Dye Analysis .....	255
4.3.2.14	HIT Compound JC-1 Dye Analysis .....	257
4.3.3	Inhibitor Studies.....	263
4.3.3.1	E-64 Inhibitor .....	263
4.3.3.2	SP600125 Inhibitor .....	266
4.3.3.3	zVAD-fmk Inhibitor.....	270
4.3.4	3D Cell Culture .....	273
4.5.2.1	Cell Viability Assay .....	273
4.4.	Discussion.....	285
<b>5.</b>	<b>GENERAL DISCUSSION</b>	<b>289</b>
<b>6.</b>	<b>FUTURE WORK</b>	<b>297</b>
<b>7.</b>	<b>REFERENCES</b>	<b>300</b>
<b>APPENDICES</b>		<b>I</b>
A1.	Chemistry .....	ii
1.1.1	TUM-2A-001 Intermediate.....	iii
1.1.1.1	<sup>1</sup> H NMR Spectrum .....	iii
1.1.1.2	LC-MS Spectrum .....	iv
1.1.1.3	FTIR Spectrum .....	v
1.1.2	TUM-2A-001 .....	vi
1.1.2.1	<sup>1</sup> H NMR Spectrum .....	vi

1.1.2.2	$^{13}\text{C}$ NMR Spectrum .....	vii
1.1.2.3	LC-MS Spectrum .....	viii
1.1.2.4	FTIR Spectrum .....	ix
1.1.3	TUM-2A-004 .....	x
1.1.3.1	$^1\text{H}$ NMR Spectrum .....	x
1.1.3.2	$^{13}\text{C}$ NMR Spectrum .....	xi
1.1.3.3	LC-MS Spectrum .....	xii
1.1.3.4	FTIR Spectrum .....	xiii
1.1.4	TUM-2A-005 .....	xiv
1.1.4.1	$^1\text{H}$ NMR Spectrum .....	xiv
1.1.4.2	LC-MS Spectrum .....	xv
1.1.4.3	FTIR Spectrum .....	xvi
1.1.5	TUM-2A-007 .....	xvii
1.1.5.1	$^1\text{H}$ NMR Spectrum .....	xvii
1.1.5.2	LC-MS Spectrum .....	xviii
1.1.5.3	FTIR Spectrum .....	xix
1.1.6	TUM-2A-008 .....	xx
1.1.6.1	$^1\text{H}$ NMR Spectrum .....	xx
1.1.6.2	$^{13}\text{C}$ NMR Spectrum .....	xxi
1.1.6.3	LC-MS Spectrum .....	xxii
1.1.6.4	FTIR Spectrum .....	xxiii
1.1.7	TUM-2A-013 .....	xxiv
1.1.7.1	$^1\text{H}$ NMR Spectrum .....	xxiv
1.1.7.2	LC-MS Spectrum .....	xxv
1.1.7.3	FTIR Spectrum .....	xxvi
1.1.8	TUM-2A-014 .....	xxvii
1.1.8.1	$^1\text{H}$ NMR Spectrum .....	xxvii
1.1.8.2	$^{13}\text{C}$ NMR Spectrum .....	xxviii
1.1.8.3	LC-MS Spectrum .....	xxix
1.1.8.4	FTIR Spectrum .....	xxx

1.1.9	TUM-2A-015 .....	xxx
1.1.9.1	<sup>1</sup> H NMR Spectrum .....	xxx
1.1.9.2	<sup>13</sup> C NMR Spectrum .....	xxxii
1.1.9.3	LC-MS Spectrum .....	xxxiii
1.1.9.4	FTIR Spectrum .....	xxxiv
1.1.10	TUM-2A-016 .....	xxxv
1.1.10.1	<sup>1</sup> H NMR Spectrum .....	xxxv
1.1.10.2	<sup>13</sup> C NMR Spectrum .....	xxxvi
1.1.10.3	LC-MS Spectrum .....	xxxvii
1.1.10.4	FTIR Spectrum .....	xxxviii
1.1.11	TUM-2A-017 .....	xxxix
1.1.11.1	<sup>1</sup> H NMR Spectrum .....	xxxix
1.1.11.2	<sup>13</sup> C NMR Spectrum .....	xl
1.1.11.3	LC-MS Spectrum .....	xli
1.1.11.4	FTIR Spectrum .....	xlii



## LIST OF FIGURES

Figure 1.1 Structures of chemotherapeutic agents used in the treatment of GBM.....	38 -
Figure 1.2 Mechanism of Action of TMZ in cells .....	40 -
Figure 1.3 The Blood Brain Barrier Architecture in a Normal and Tumour Brain ....	46 -
Figure 1.4 Structure of Metformin.....	55 -
Figure 1.5 Mechanisms of Action of Metformin.....	57 -
Figure 1.6 (i) Structure of TUM-2C-005. (ii) Dose response curve shown.....	59 -
Figure 1.7 General structure of the pyrazolo[1,5- $\alpha$ ]pyrimidinones.....	60 -
Figure 2.1 The MTT Assay.....	68 -
Figure 2.2 The four pyrazolo[1,5- $\alpha$ ]pyrimidinone groups.....	70 -
Figure 2.3 General structure of group 1 pyrazolo[1,5- $\alpha$ ]pyrimidinone compound ....	77 -
<b>Figure 2.4 Dose response curve for group 1 pyrazolo[1,5-<math>\alpha</math>]pyrimidinones .....</b>	<b>79 -</b>
Figure 2.5 Pooled data dose response curves for compounds in group 1 .....	82 -
Figure 2.6 General structure of group 2A analogue compounds .....	83 -
Figure 2.7 Dose response curves for compounds in group 2A.....	85
Figure 2.8 Dose response curves for compounds in group 2A.....	88
Figure 2.9 General structure of group 2B compounds.....	89
<b>Figure 2.10 Dose response curve for the compound in group 2B .....</b>	<b>91</b>
Figure 2.11 Dose response curve for the compound in group 2B .....	92
Figure 2.12 General structure of group 2C compound .....	93
Figure 2.13 Pooled data dose response curve for the compound in group 2C .....	94
Figure 2.14 Pooled data dose response curve for the compound in group 2C .....	96
Figure 2.15 General structure of group 3 compounds .....	97
Figure 2.16 Dose response curves for the compounds in group 3.....	98
Figure 2.17 Dose response curves for the compounds in group 3.....	100
Figure 2.18 General structure of group 4 compounds .....	100
Figure 2.19 Dose response curves for the compounds in group 4.....	102
Figure 2.20 Dose response curves for the compounds in group 4.....	104
Figure 2.21 Cell line comparison of TUM-1-005 .....	109
Figure 2.22 Structures of compounds .....	110
Figure 2.23 Cell line comparison using both the U251-MG and HEK293 cell line.....	111
Figure 2.24 Cell line comparison of TUM-2C-002 .....	112
Figure 3.1 General structure of a pyrazolopyrimidinone (Kelada et al., 2018).....	126
Figure 3.2 Bioactive pyrazolo[1,5- $\alpha$ ]pyrimidinones.....	127
Figure 3.3 General one-pot method for the formation of pyrazolo[1,5- $\alpha$ ]pyrimidinones (Kelada, 2018) .....	129
Figure 3.4 Hit compounds whereby the core scaffold and R1 substituent remain the same and the R2 substituent varies. ....	131
Figure 3.5 Proposed mechanism for the formation of 5-aminopyrazoles.....	135
Figure 3.6 Synthesis of 5-aminopyrazole 1. ....	136

Figure 3.7 Structure of 5-aminopyrazole 1 with protons numbered for structural characterisation. ....	137
Figure 3.8 Proposed mechanism for the formation of pyrazolopyrimidinones. ....	138
Figure 3.9 Synthetic route to pyrazolo[1,5- $\alpha$ ]pyrimidinone TUM-2A-001. ....	139
Figure 3.10 Structures of the synthesised pyrazolo[1,5- $\alpha$ ]pyrimidinones and their corresponding yields .....	141
Figure 3.11 Structure of TUM-2A-001 with labelled hydrogen atoms. ....	142
Figure 3.12 Structure of TUM-2A-004 with labelled hydrogen atoms. ....	143
Figure 3.13 Structure of TUM-2A-005 with labelled hydrogen atoms. ....	144
Figure 3.14 Structure of TUM-2A-007 with labelled hydrogen atoms. ....	146
Figure 3.15 Structure of TUM-2A-008 with labelled hydrogen atoms. ....	147
Figure 3.16 Structure of TUM-2A-013 with labelled hydrogen atoms. ....	148
Figure 3.17 Structure of TUM-2A-014 with labelled hydrogen atoms. ....	150
Figure 3.18 Structure of TUM-2A-015 with labelled hydrogen atoms. ....	151
Figure 3.19 Structure of TUM-2A-016 with labelled hydrogen atoms. ....	152
Figure 3.20 Structure of TUM-2A-017 with labelled hydrogen atoms. ....	153
Figure 3.21 Structure of group 2A analogue compounds .....	155
Figure 3.22 An overlay of the <sup>1</sup> H NMR spectra.....	158
Figure 3.23 5-aminopyrazole 1: 3-Phenyl-1H-pyrazol-5-amine .....	165
Figure 3.24 General Procedure A for the Synthesis of 5-Aminopyrazole Intermediates .....	166
Figure 3.25 General Procedure B for the Synthesis of Pyrazolo[1,5- $\alpha$ ]pyrimidinones .....	167
Figure 3.26 Structure of group 2A analogue compounds.....	178
Figure 3.27 Dose response curves for compounds in group 2A .....	181
Figure 3.28 Dose response curves for compounds in group 2A. Assay Conditions: HEK293 cell line and the MTT cell viability assay. Cells were analysed 5 days after treatment, N=3. Where the X axis denotes the logarithmic concentration of compound, and the Y axis denotes the % cell viability. ....	183
Figure 4.1 Inhibitor Structures .....	199
Figure 4.2 A visual representation of the 3D cell culture method using low adhesion plates (Wanigasekara et al., 2022). ....	213
Figure 4.3 TMZ screen .....	219
Figure 4.4 Dose response curves for a combined treatment of TMZ and the hit compounds .....	221
Figure 4.5 PI dye used on TUM-2A-001 hit compound using U251-MG cells. ....	223
Figure 4.6 Quadrant graphs of forward scatter (FSC-A) verses PE-A were plotted of TUM-2A-001 treated U251-MG cells .....	224
Figure 4.7 TUM-2A-001 and PI .....	225

Figure 4.8 (i) Graph showing total TUM-2A-004 cell population excluding cellular debris .....	227
Figure 4.9 TUM-2A-004 Quadrant graphs of forward scatter (FSC-A) verses PE-A were plotted of TUM-2A-004.....	228
Figure 4.10 (i) Graph showing total TUM-2A-007 cell population excluding cellular debris.....	229
Figure 4.11 TUM-2A-007 Quadrant graphs .....	230
Figure 4.12 (i) Graph showing total TUM-2A-008 cell population .....	231
Figure 4.13 TUM-2A-008 Quadrant graphs .....	232
Figure 4.14 (i) Graph showing total TUM-2A-015 .....	233
Figure 4.15 TUM-2A-015 Quadrant graphs .....	234
Figure 4.16 (i) Graph showing total TUM-2A-016 cell population .....	235
Figure 4.17 TUM-2A-016 Quadrant graphs .....	236
Figure 4.18 Hit Compounds, TUM-2A-004, TUM-2A-007, TUM-2A-008, TUM-2A-015 and TUM-2A-016 were treated with PI.....	238
Figure 4.19 TUM-2A-001 and JC-1 Dye Analysis.....	243
Figure 4.20 JC-1 and TUM-2A-001 .....	244
Figure 4.21 TUM-2A-001 and JC-1 .....	245
<b>Figure 4.22 Graph showing total cell population excluding cellular debris.....</b>	<b>247</b>
Figure 4.23 (i) 19.92 % apoptotic cell population observed in negative control for TUM-2A-004. ....	248
Figure 4.24 Graph showing total cell population excluding cellular debris.....	249
Figure 4.25 (i) 4.62 % apoptotic cell population observed in negative control for TUM-2A-007 .....	250
Figure 4.26 (i) Graph showing total cell population excluding cellular debris .....	251
Figure 4.27 (i) 9.67 % apoptotic cell population observed in negative control for TUM-2A-008 .....	252
Figure 4.28 (i) Graph showing total cell population excluding cellular debris .....	253
Figure 4.29 (i) 6.88 % apoptotic cell population observed in negative control for TUM-2A-015 .....	254
Figure 4.30 (i) Graph showing total cell population excluding cellular debris .....	255
Figure 4.31 (i) 10.47 % apoptotic cell population observed in negative control for TUM-2A-016 .....	256
Figure 4.32 Hit Compounds, TUM-2A-004, TUM-2A-007, TUM-2A-008, TUM-2A-015 and TUM-2A-016 were treated with JC-1 Dye .....	258
Figure 4.33 Bar chart highlighting the changes in % cell viability when controls and hit compounds are treated with E-64 inhibitor.....	264
Figure 4.34 Bar chart highlighting the changes in % cell viability when controls and hit compounds are treated with SP600125 inhibitor .....	268
Figure 4.35 Bar chart highlighting the changes in % cell viability when controls and hit compounds are treated with the zVAD-fmk inhibitor .....	271

Figure 4.36 Results of 3D cell line screen on hit compounds .....	275
Figure 4.37 Development of 3D tumoursphere U251-MG cells in 3D cell culture model .....	278
Figure 4.38 Development of 3D tumoursphere U251-MG cells in 3D cell culture model .....	279
Figure 5.1 Structure of the analogue compound whereby there is an R <sup>1</sup> substituent group on the pyrimidine ring and there is an R <sup>2</sup> substituent group on the pyrazole ring.....	291

## LIST OF TABLES

Table 2-1 Prism 8.0.0 statistical significance values, significance level and summary. ....	76 -
Table 2-2 Results for group 1 evaluation using U251-MG cell line .....	78 -
Table 2-3 Results for group 1 evaluation using HEK293 cell line and the MTT cell viability assay. Cells were analysed 5 days after treatment, N=3. X is denoted where an experimental value was not possible. ....	81 -
Table 2-4 Results of U251-MG cell screen on group 2A compounds.....	84 -
Table 2-5 Results of HEK293 cell line screen on group 2A compounds .....	87
Table 2-6 Results of U251-MG screen on Group 2B compounds.....	90
Table 2-7 Results of group 2B compound screen on HEK293 cell line.....	92
Table 2-8 Results of U251-MG cell line screen on the group 2C compound .....	94
Table 2-9 Results of HEK293 cell line screen on the group 2C compound.....	95
Table 2-10 Results of U251-MG cell line screen on group 3 compound .....	98
Table 2-11 Results of HEK293 cell line screen on group 3 compounds.....	99
Table 2-12 Results of U251-MG cell line screen on group 4 compounds .....	101
Table 2-13 Results of HEK293 cell line screen on 4 compounds .....	103
Table 2-14 Comparison of IC <sub>50</sub> data generated to determine statistical significance...	106
Table 2-15 Summary of results from two-way ANOVA statistical analysis .....	114
Table 2-16 Summary of Statistical Compounds of Interest including calculated molecular properties (Bioinformatics, 2022).....	118
Table 3-1 Analogue compounds to be synthesised.....	133
Table 3-2 The synthesised HIT compounds and their analogues .....	160
Table 3-3 Results of U-251 MG cell screen on group 2A compound .....	180
Table 3-4 Results of HEK293 cell line screen on group 2A compounds .....	182
Table 3-5 Comparison of IC <sub>50</sub> data generated to determine statistical significance.....	185
Table 3-6 Summary of results from two-way ANOVA statistical analysis .....	186

Table 3-7 A comparison of the changes in the IC <sub>50</sub> values for TUM-2A-004, TUM-2A-015 and TUM-2A-016 when the bromo substituent is moved to different positions in the phenyl ring. ....	188
Table 4-1 3D cell culture techniques .....	201
Table 4-2 Hit compounds used for flow cytometry analysis, .....	208
Table 4-3 Prism statistical significance values, significance level and summary. ....	215
Table 4-4 Chemotherapeutic agents currently used in the treatment of GBM .....	217
Table 4-5 Table outlining the hit Compounds and their corresponding IC <sub>50</sub> values ....	220
Table 4-8 Summary of results from one-way ANOVA statistical analysis for TUM-2A-001 .....	226
Table 4-9 Summary of results from one-way ANOVA statistical analysis for PI treated HIT Compounds .....	239
Table 4-10 PI flow cytometry analysis of results from one-way ANOVA statistical analysis.....	241
Table 4-11 JC-1 dye flow cytometry analysis of results from one-way ANOVA statistical analysis.....	246
Table 4-12 Summary of results from one-way ANOVA statistical analysis for JC-1 Dye .....	259
Table 4-13 Summary of results from one-way ANOVA statistical analysis for flow cytometry using the JC-1 dye .....	262
Table 4-14 Summary of results from one-way ANOVA statistical analysis for the hit compounds & E-64 inhibitor treated hit compounds.....	265
Table 4-15 Summary of results from one-way ANOVA statistical analysis for the hit compounds & SP600125 inhibitor treated hit compounds .....	269
Table 4-16 Summary of results from one-way ANOVA statistical analysis for the hit compounds & zVAD-fmk inhibitor treated hit compounds .....	272
Table 4-17 Results of 3D tumoursphere screen on hit compounds .....	276
Table 4-18 Summary table of results obtained from co-treatment studies .....	284

## **1. INTRODUCTION**

### **1.1. Tumours of the Central Nervous System**

Brain and spinal cord tumours are named based on the type of cell they formed in and where the tumour first formed in the CNS (Ludwig & Varacallo, 2019). An astrocytic tumour begins in star shaped brain cells called astrocytes which help keep nerve cells healthy. The total glial population is comprised of microglia, astrocytes, oligodendrocytes and their progenitors NG2-glia. Glial cells constitute a large fraction of the mammalian brain, anything between 33 and 66 % of the total brain mass depending on the species (Jäkel & Dimou, 2017). The best-known function of glia in an adult brain is the formation of the myelin sheaths around axons thus allowing fast conduction of signalling which is essential for nervous system function. Glial cells are also essential regulators of the formation, maintenance and function of synapses (Jessen, 2004). Glial cells can then form tumours which are referred to as gliomas (Holland, 2000).

In 2020, brain and nervous system cancer accounted for 2.5 % of all cancer related deaths globally, this translates to 251,329 patients in total (Sung et al., 2021). According to the central statistics office in Ireland, there were 91 males and 90 females who died in the years 2018 – 2019 from a brain and CNS related cancer (National Cancer Registry Ireland, 2020). The figures expressed above do not reflect the impact of Severe Acute Respiratory Syndrome Coronavirus-2 (SARS-CoV-2) as they are based on extrapolations of data collected prior to the pandemic. The full extent of the COVID-2 pandemic is still to be determined as this resulted in delays in cancer diagnosis and treatment, suspension of screening programs, health system closures and reduced availability of and access to care. The aforementioned factors will ultimately result in an increase in advanced stage diagnoses and increased cancer mortality (Ferlay et al., 2021)(Sung et al., 2021). In

Ireland, brain and CNS cancers account for 3.9 % of all male related cancers and 2.8 % of all female related cancers. It was determined that 1.1 % of all patients diagnosed with brain and CNS cancers survive in Ireland (National Cancer Registry Ireland, 2020).

### **1.1.1 Brain Tumour Grading**

Astrocytomas are tumours which are found in the CNS and are derived from astrocytes, star shaped cells which form in the brain. The term “astrocytoma” widely applies to tumours that exhibit astrocytic differentiation. (Komori, 2015) According to the 2016 WHO classification, isocitrate dehydrogenase 1-mutant (IDH1-mutant) diffuse astrocytic tumours were assigned to three different tumour types depending on histological parameters (Mesfin & Al-Dhahir, 2022). The first tumour type is referred to as a Diffuse Astrocytoma it is a grade II astrocytoma. It can be described as a slow-growing invasive tumour with a tendency to progress to a higher-grade tumour. The second tumour type is referred to as an Anaplastic Astrocytoma. This is a grade III astrocytoma with a higher pace of growth and is more invasive to the brain with a tendency to progress to a higher-grade tumour. The third tumour type is referred to as a Glioblastoma (GBM). This is a grade IV astrocytoma with the highest severity and cannot progress to a higher-grade tumour.

Isocitrate dehydrogenase 1 and 2 (IDH1 and IDH2) are key enzymes involved in cellular metabolism, epigenetic regulation, redox states and DNA repair (Sharma, 2018). Genes which encode for isocitrate dehydrogenase 1 and 2, IDH1 and IDH2 are frequently mutated in multiple types of cancer whereby approximately 90 % of mutations are IDH1 type (Omuro & DeAngelis, 2013)(Yang et al., 2012). According to the current 2021 WHO



classification, all IDH-mutant astrocytic tumours are considered as a single type but are then assigned the CNS WHO grade II, III or IV (Louis et al., 2021). For IDH-wildtype diffuse astrocytic tumours to be assigned the highest grade in adults they must show the presence of one or more of three genetic parameters.

The parameters are as follows: human telomerase reverse transcriptase (TERT) promoter mutation, epidermal growth factor receptor (EGFR) gene amplification, combined gain of entire chromosome 7 and loss of entire chromosome 10 (Louis et al., 2021). Telomerase is an enzyme in cells that helps to keep them alive by adding DNA to ends of chromosomes (telomeres). Every time a cell divides, the telomeres lose a small amount of DNA and become shorter. Over time, the chromosomes become more damaged, and the cells die. Telomerase prevents this from happening. It should be noted that cancer cells usually have more telomerase when compared to healthy cells (NCI, 2023). Human telomerase reverse transcriptase gene promotor mutations have been observed in multiple types of malignant tumours. It is believed that telomerase activity is induced by TERT overexpression as transcription factor binding motifs are generated because of the mutation. The maintenance of telomerase is one of the hallmarks of cancer as the TERT mutation is generally associated with disseminated disease (Y. Zhang et al., 2021). Epidermal growth factor receptor (EGFR) is also referred to as human epidermal growth factor 1 (HER1) and is a receptor tyrosine kinase that belongs to the ErbB family of proteins. Activation of EGFR leads to enhancement of cell proliferation and survival however functional activation of EGFR via amplification or mutation/overexpression has been identified in many tumour types and has been associated with proliferation, invasion and metastasis (Kato et al., 2019).

As of 2021, the WHO changed their classification of tumour grading to reflect the discovery of genetic alterations in many CNS tumours (Bale & Rosenblum, 2022). Prior to this change, the grading system assigned was based on certain pathological features such as vascular proliferation, mitotic activity, necrosis and proliferative potential and was graded from I to IV (Wesseling & Capper, 2018). The 2021 WHO classification system recognises the clinical and molecular distinction between diffuse gliomas which occur in adults and those that occur primarily in children, termed paediatric type (Louis et al., 2021). Low grade gliomas and glioneuronal tumours represent over 30 % of paediatric CNS tumours thus making them the most frequently encountered brain tumours in children (Bale & Rosenblum, 2022). Two new families of tumour types have been added to reflect the importance of separating paediatric type gliomas from other diffuse gliomas- paediatric type diffuse low grade glioma and paediatric type diffuse high grade glioma (Louis et al., 2021).

Gliomas, glioneuronal tumours and neuronal tumours are now divided into six different families (Louis et al., 2021). It should be noted that the term “paediatric type” glioma is used for the ages from birth to the age of 19 and then the term “adult type” is used (Hauser, 2021). The first family refers to adult type diffuse gliomas, this includes most primary brain tumours such as GBM. The second family refers to paediatric type diffuse low-grade gliomas; these are expected to have a good prognosis. The third family refers to paediatric type diffuse high-grade gliomas; these are expected to behave aggressively. The fourth family refers to circumscribed astrocytic gliomas; these have a more solid growth pattern than the diffuse gliomas. Circumscribed refers to where the mass of the tumour is clearly defined along 75 % of its surface. The fifth family refers to glioneuronal

(mixed glial and neuronal tumour) and neuronal tumours (tumours made from abnormal neurons): Tumours featuring neuronal differentiation. The sixth family refers to ependymomas, they have marked epithelial characteristics and molecular features.

## **1.2. Glioblastoma, GBM**

GBM is the most common and aggressive malignant brain tumour and accounts for 45.2 % of all malignant primary brain tumours and 54 % of all gliomas (Shah et al., 2021). GBM remains an incurable disease whereby the median survival rate is 15 months and 5.5 % of all patients survive five years post diagnosis (Shah et al., 2021).

Despite patients receiving treatment such as surgical resection and chemotherapy, the vast majority of tumours are recurring and have a dismal outcome due to recurrent GBM being resistant to therapy. Genome-wide transcriptome analysis has led to classify GBM into four further subtypes: mesenchymal (MES), classical (CL), proneural (PN) and neural which is based on bulk tumour transcription profile (Steponaitis & Tamasauskas, 2021). This classification does not allow for inter and intra heterogeneity of GBM (Katrina Kan et al., 2020). Inter-heterogeneity refers to the presence of one or more clone of cancer cell within a tumour mass and intra-heterogeneity refers to the presence of different genetic alterations in different metastatic tumours from a single patient (Yancovitz et al., 2012).

### **1.2.1 The Four Subtypes of GBM**

Each of the subtypes exhibit different clinical characteristics, genetic abnormalities, survival rates and responses to therapeutic treatment (Harder et al., 2018).

The proneural (PN) subtype is the most prevalent subtype – 32.73 % and is largely observed in grade II and III gliomas (Fedele et al., 2019). Patients with the PN subtype were found to be significantly younger and display the best prognosis (Fedele et al., 2019). The PN subtype shows amplification of the platelet-derived growth factor receptor A (PDGFRA) and deletion of the TP53 tumour suppressor gene. When PDGFRA is altered, it produces too much of its protein which leads to uncontrolled cell growth.

The classical (CL) subtype can be observed in 19.77 % of patients (Fedele et al., 2019). The CL subtype was shown to present amplification or mutation of the epidermal growth factor receptor (EGFR) and high expression of the neural precursor and stem cell marker (NES) (Fedele et al., 2019). EGFR is a protein that is found on the surface of certain cells, when it is bound by epidermal growth factor it sends signals to the cell to keep growing.

The Mesenchymal subtype is observed in 32.4 % of patients (Fedele et al., 2019). Along with the classical subtype, Mesenchymal displays the worst clinical outcome (Fedele et al., 2019). It contains mesenchymal markers such as Mesenchymal-Epithelial Transition (MET) and has been associated with mutations or deletions of the neurofibromin (NF1) gene. Neurofibromin protein stimulates RAS intrinsic phase guanosine triphosphate (GTPase) activity; this promotes the conversion of active RAS-GTP to inactive RAS-GDP (Simanshu et al., 2017). The loss of the NF1 gene results in intracellular levels of

RAS-GTP thus promoting oncogenesis (PA, 2017) (Verhaak R.G., 2011). It is also characterized by EGFR amplification and phosphatase and tensin homolog (PTEN) loss (Olar & Aldape, 2014).

The Neural subtype contains many of the same mutations in genes as seen in the other groups. It is observed in 15.09 % of patients and has an intermediate correlation with overall survival (Fedele et al., 2019). This subtype is characterized by the presence of neuron markers such as neurofilament light (NEFL) and gamma-aminobutyric acid type A receptor alpha1 subunit (GABRA1) (Bradley et al., 2008).

### **1.3. Diagnosis and Treatment in Glioblastoma**

Current therapeutics for GBM are limited and offer a modest prognosis, they are also associated with side effects and an array of limitations. To date, there are no approved targeted therapies for GBM and furthermore, patients that respond to first in line treatment rarely respond to subsequent secondary treatment (Katrina Kan et al., 2020). There is a need for improvement in both GBM diagnosis and treatment.

The symptoms of brain tumours can be physical such as experiencing fatigue or headaches or behavioural such as hallucinations, depression, anxiety, or memory problems. The most common recorded symptoms are fatigue, sleep disturbance, drowsiness and dry mouth (Comelli et al., 2017). GBM is primarily diagnosed in older patients where the median age is 64 years at diagnosis. The incidence increases with age where it peaks from 75 - 85 years and then the incidence rate drops after 85 years (Hanif et al., 2017). In order to diagnose a brain tumour, the patient must be referred for magnetic resonance imaging (MRI) (Penfold et al., 2017).

### **1.3.1 Imaging Strategies in Brain Tumours**

An MRI is considered the gold standard for defining brain tumour anatomy as it is a more sensitive technique than a computerised tomography (CT) scan and offers better visualisation of the brain tumour (Vagvala et al., 2022). However, over the last decade a variety of advanced imaging techniques have been developed which provide more information such as chemical composition and physiological data. The current advanced techniques are as follows: perfusion-weighted imaging (PWI), diffusion weighted imaging (DWI), magnetic resonance (MR) spectroscopy, blood oxygen level dependant (BOLD) imaging and molecular imaging. The first three techniques are the most commonly used (Al-Okaili et al., 2006).

PWI provides information on cerebral hemodynamic parameters such as relative cerebral blood volume (rCBV) and cerebral blood flow. (Jaafari et al., 2021) Perfusion is quantified in terms of flow rate (ml/min) normalised to the tissue mass (per 100 g brain tissue.) (Holdsworth & Bammer, 2008) Increased blood perfusion is a sign of hypervascularity and is shown in newly diagnosed and recurrent brain tumours. (Butowski, 2015)

DWI is an MRI technique that measures differences in apparent diffusion coefficient (ADC). This relies on the microscopic motion of water molecules within tissue. ADC decreases with increased viscosity and cellular density as well as reduction of extracellular space. Tumours with densely packed cells such as medulloblastomas show restricted diffusion compared to normal brain tissue (Butowski, 2015).

These techniques are routinely used as they can distinguish pseudo progression from true tumour progression and can accurately determine a patient's early stage response to therapies (Harder et al., 2018) (de Gooijer et al., 2018). Pseudo progression can be defined as an increase in the size of the primary tumour or the appearance of a new lesion which is then followed by tumour regression. This can lead to premature cessation of treatment (Ma et al., 2019).

### **1.3.2 The Stupp Protocol**

The Stupp Protocol refers to the current therapeutic strategies used to treat glioblastoma. These include the use of maximal safe surgical resection, radiotherapy and the use of chemotherapeutic agents (Parodi et al., 2019) (Wick et al., 2018). This protocol has not changed in fifteen years, it offers a modest prognosis and is associated with side effects and an array of limitations (Poon et al., 2021). Surgery is the initial therapeutic approach as part of the Stupp Protocol and remains a hallmark in the treatment of malignant brain tumours. Pre-operative issues such as the patient's medical condition, use of antiepileptic or corticosteroid drugs and signs of intracranial hypertension need to be accounted for so that surgical conditions can be improved (Fernandes et al., 2017). The goals of surgical treatment are maximal safe surgical resection, tissue specimen for pathological diagnosis and improved quality of life. The most important treatment predictor is the extent of resection (EOR) as a more extensive surgical resection is associated with longer life expectancy (Manrique-Guzman et al., 2017). Due to the invasive nature of glioblastoma, there are cells which remain after surgery that can contribute to tumour recurrence (Mannas et al., 2014). Surgical resection is then followed by combined radiotherapy and chemotherapy (Cai & Sughrue, 2018).

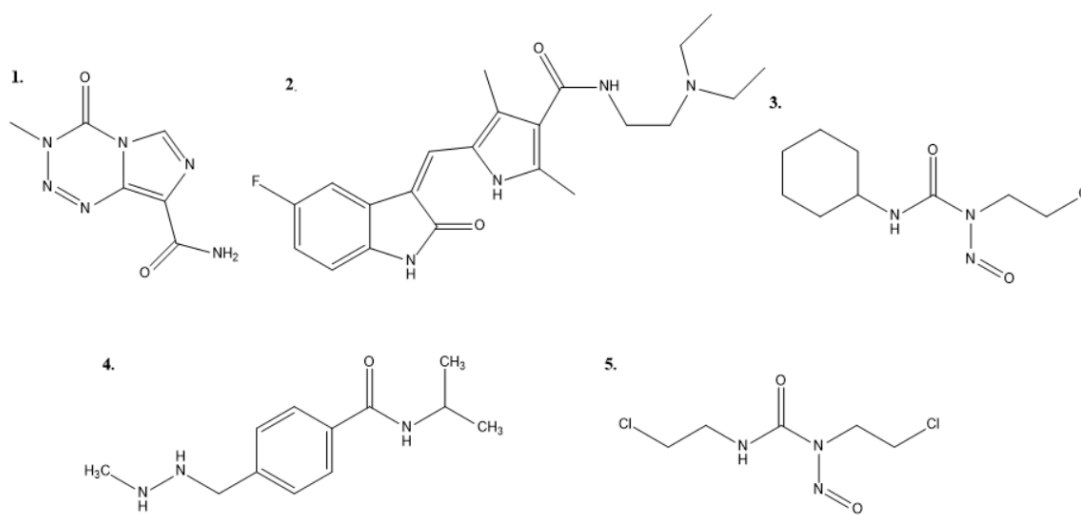
Radiation therapy is the second stage of the Stupp Protocol. It is a treatment that uses high doses of radiation to kill cancer cells and shrink tumours (Chaput & Regnier, 2021). Radiation therapy is a commonly prescribed treatment for GBM and can be used as a primary treatment if the surgeon believes removing the tumour would be too risky or it can be used after an operation to destroy any remaining cancer cells that were not visible or accessible to the surgeon (Seo et al., 2019). During radiation therapy, X-rays, gamma rays or photons are aimed at the brain tumour (or any tumour) to destroy the cancerous cells. As cancerous cells are destroyed and eliminated by the body's immune system, this helps alleviate pressure on the brain (Gonzalez et al., 2018). The third stage of the Stupp Protocol involves the delivery of a chemotherapeutic agent which is carried out after surgery and radiation therapy. The gold-standard chemotherapeutic agent used in the treatment of GBM is referred to as Temozolomide (TMZ) (Parodi et al., 2019).

#### **1.4. Chemotherapeutic Agents**

The term “Chemotherapy” was coined by the German chemist Paul Ehrlich in the 1900's. It was defined as “the use of chemicals to treat disease” (Colvin, 2003). Chemotherapeutic agents are anticancer drugs which travel to various parts of the body to attack cancer cells. The success of cancer chemotherapy depends on the development of drugs that selectively destroy tumour cells or limit their proliferation without causing severe side effects (Schirmacher, 2019). Drug treatment in neurological diseases such as brain tumours are particularly difficult due to the CNS protective barrier which consists of the blood-brain barrier (BBB) and the blood-cerebrospinal fluid barrier (BCSFB). Many approved anticancer drugs do not readily cross the BBB thus limiting the options for glioblastoma



treatment (Mannas et al., 2014). The most used chemotherapeutic agents for the treatment of GBM are Lomustine (CCNU), Carmustine (BCNU), Sunitinib, Procarbazine, and the gold standard Temozolomide (TMZ) (D. Wang et al., 2019) (Fernandes et al., 2017). An image depicting the structures of the most used chemotherapeutic agents for GBM is shown in Figure 1.1.



**Figure 1.1 Structures of chemotherapeutic agents used in the treatment of GBM. 1. Temozolomide 2. Sunitinib 3. Lomustine 4. Procarbazine 5. Carmustine**

#### **1.4.1 Temozolomide, TMZ**

TMZ is the most frequently used approved chemotherapeutic agent for GBM treatment (D. Wang et al., 2019). The standard treatment used for treating glioblastoma is that devised by the European Organisation for Research and Treatment of Cancer-National Cancer Institute of Canada (EORTC-NCIC) (Kumari et al., 2017). It states the first line treatment is surgery, radiation and six months of maintenance TMZ and is referred to as the “Stupp Protocol” (Fernandes et al., 2017) (Kumari et al., 2017). The use of TMZ has

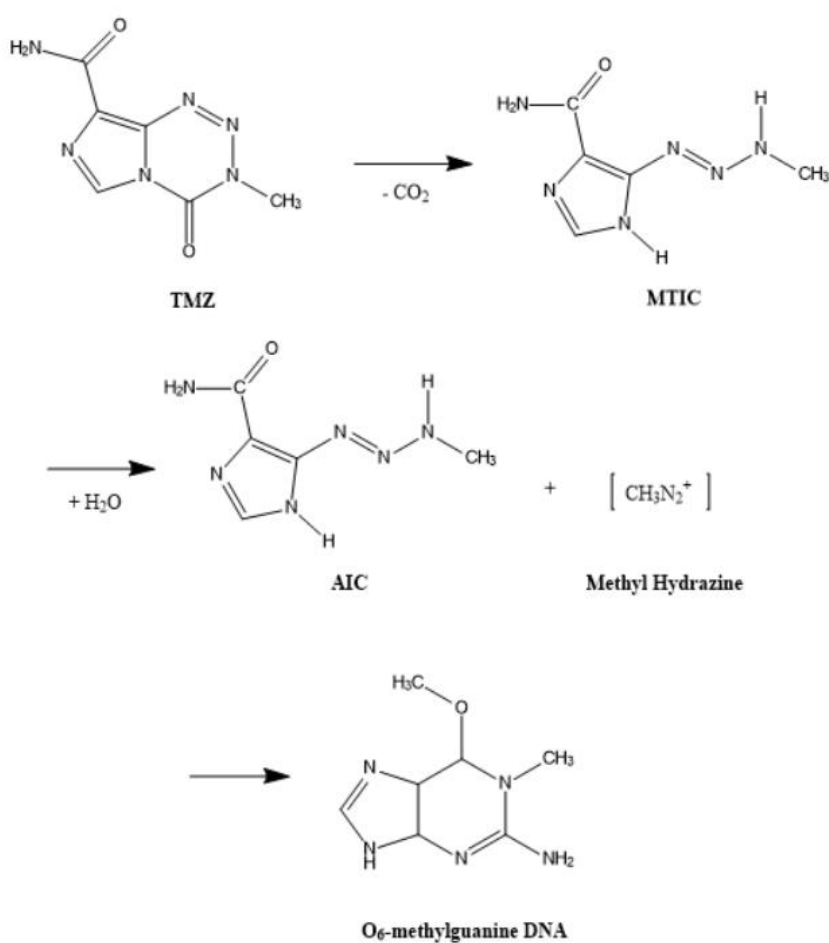
increased the patient median survival rate from 12.1 months to 14.6 months and the percentage of patients alive after 2 years has increased from 10.4 % to 26.5 % (Wang et al., 2019).

TMZ is part of a large class of DNA alkylating agents that were discovered to have anti-tumorigenic effects in the 1940's and quickly became one of the first type of drugs to be used as chemotherapeutics. TMZ itself was not synthesised till the late 1970's and was then approved for use in the EU and US in the 2000's. TMZ is sold under brand names such as 'Temodar' and 'Temodal'. It is a small lipophilic prodrug with a molecular weight of 194 Daltons and is stable at acidic pH. Factors such as these are what allow TMZ to be administered orally and also allow it to cross the BBB (J. Zhang et al., 2011) (Singh et al., 2021).

However, prolonged TMZ treatment leads to resistance and a poor response to subsequent treatments (Agarwala & Kirkwood, 2000). TMZ also requires continuous administration due to its low solubility in physiological media and shorter plasma half-life (1.8 hours). The dosage of TMZ delivered is 150 to 200 mg m<sup>-2</sup> for five days every 28 days for six cycles (Weller et al., 2013). Higher doses of TMZ allow for positive outcomes such as tumour death however there are negative effects associated such as cardiomyopathy, haematological toxicity and pneumonia that can result in the cessation of treatment (Ayob & Ramasamy, 2018). The limitations associated with TMZ therapy have resulted in using TMZ in conjunction with other therapeutics in a bid to improve its efficacy (Pushpakom et al., 2018).

### 1.4.2 TMZ Structure and Mechanism of Action

A DNA alkylating agent is a type of drug which can target existing nucleic acid molecules. When the alkylating agent forms an intra-strand link between two parts of the same nucleic acid chain in the DNA, this can distort the strand and inhibit transcription (Warwick, 1963). TMZ interferes with cancer cells by slowing their growth and spread throughout the body (Atlee, 2007). The mechanism of action for TMZ in cells is shown in Figure 1.2.



**Figure 1.2 Mechanism of Action of TMZ in cells**

TMZ is a prodrug and so it is not an active drug itself. TMZ gets absorbed in the small intestine after oral administration and crosses the BBB due to its small size (194 Da). TMZ gets hydrolysed at physiological pH ( $> 7$ ) and is converted to its active intermediate MTIC, [(methyl-triazine-1-yl)-imidazole-4-carboxamide]. TMZ undergoes hydrolytic ring opening at the electropositive C4 position of TMZ. The ring opens and generates MTIC with the loss of  $\text{CO}_2$  (Di Martino et al., 2017). MTIC undergoes hydrolysis and degrades to form 5-aminoimidazole-4-carboximide (AIC) and methyl hydrazine which is a DNA methylating species. Methyl hydrazine is the active compound that transfers the methyl group to DNA bases, most importantly the guanine base (Barciszewska AM, Gurda D, Glodowicz P, Nowak S, 2015).

The methyl hydrazine cation undergoes a methylation reaction at the O6 of guanine. It should be noted that TMZ only displays cytotoxicity once this methylation has occurred. During DNA replication, O6-methylguanine causes the addition of thymidine instead of cytosine in new DNA strands. The DNA repair mechanisms are unable to adjust to the newly methylated DNA which then results in apoptosis, the cell killing response (Moody CL, 2014) (Kim K-W, Roh JK, Wee H-J, 2016).

There is a narrow pH window close to physiological pH at which the process of TMZ prodrug activation to methyl group transfer can take place and accounts for 6 % of TMZ modification in cells. Brain tumours have a more alkaline pH when compared with the surrounding healthy tissue in the brain. Methylation can occur at the N7 site of guanine and accounts for 70 % of TMZ modification in cells and it can also occur at the N3-methyladenine site which occurs for 9 % of TMZ treatment cases. Both cases result in no

TMZ toxicity or extreme toxicity respectively whereby TMZ does not work. Where methylation occurs at the O6 part of guanine is the most favourable situation for prodrug activation (J. Zhang et al., 2011). The use of TMZ in GBM treatment has resulted in tumour resistance and recurrence. This is due to the widespread exposure to TMZ and the highly heterogenous and mutation prone nature of GBM. It is very common for tumours to become resistant to TMZ and there are over 50 % of patients who do not respond to TMZ therapy (Singh et al., 2021).

#### ***1.4.2.1 TMZ Treatment***

The dosage of TMZ delivered is 75 mg m<sup>-2</sup> per day for a period of 6 weeks and then TMZ 75 mg m<sup>-2</sup> per day with radiation therapy 150 – 200 mg m<sup>-2</sup> per day for five days every 28 days for six cycles (Singh et al., 2021). Higher doses of TMZ allow for positive outcomes such as tumour death however there are negative effects from the increased dose such as cardiomyopathy, haematological toxicity and pneumonia (Ayob & Ramasamy, 2018). These negative outcomes can result in the cessation of treatment (Ayob & Ramasamy, 2018). The limitations associated with TMZ therapy have resulted in the efficacy testing in the development of carriers for TMZ such as solid lipid nanoparticles and polymers (Bradshaw et al., 2016). TMZ has also been used in conjunction with repurposed drugs in a bid to improve its efficacy.

### 1.4.3 Other Chemotherapeutic Agents for GBM

Lomustine (CCNU) (Figure 1.1) is an orally administered alkylating agent which was approved for treatment in 1977. It is used in the treatment of Hodgkin disease, lymphoma and brain cancer (Das et al., 2020). The toxicity of Lomustine is similar to that of other alkylating agents whereby common side effects include nausea, vomiting, gastrointestinal upset and nephrotoxicity (Das et al., 2020). A phase three clinical trial was carried out and has suggested that Lomustine-Temozolomide therapy in conjunction with radiotherapy might be superior to stand alone Temozolomide therapy in newly diagnosed Glioblastoma (Herrlinger et al., 2019). The trial had no deaths however the size of the trial was limited to seventeen German hospitals which is why the findings suggest that the combination of Lomustine-Temozolomide only *might* be a superior treatment as the trial needs to be carried out on a larger scale to be considered statistically significant (Das et al., 2020). Procarbazine (Figure 1.1) is also another example of an orally administered alkylating agent that can be used as a stand-alone treatment for GBM or in conjunction with Temozolomide (Herrlinger et al., 2019).

Sunitinib (Figure 1.1) is an oral multi-targeted tyrosine kinase inhibitor, which is used in the treatment of metastatic renal cell carcinoma and has shown potential in the treatment of GBM (Hao & Sadek, 2016). To date, Sunitinib has been used as part of a phase II trial (trial number NCT03025893) in conjunction with Lomustine in patients with recurrent GBM (Taylor et al., 2019).

Carmustine Wafers (CW) (Figure 1.1) are a form of the medication Carmustine (BCNU) and are used in the treatment of recurrent GBM as an adjunct to surgery (Ene et al., 2016).

Carmustine is an alkylating agent commonly used in cancers related to the nervous system (McDermott et al., 2022). CW are recommended for patients for whom near total surgical resection is feasible or in whom craniotomy is indicated (Chowdhary et al., 2015). The success of CW has led to the development of TMZ delivery through a polymer wafer which can be used as an alternate or complimentary treatment (Shapira-Furman et al., 2019). Preclinical studies were carried out using CW, TMZ wafers and wafers that were co-loaded with both BCNU and TMZ by treating an intracranial 9 L gliosarcoma model in F344 rats. It was determined that the rats who received the TMZ wafer had a higher survival rate (18 days) over the rats who received the CW (15 days). The rats who received the BCNU-TMZ wafer had the highest overall survival rate (28 days) with 25 % of them surviving long term. Despite the success of the BCNU-TMZ combination in rats, they have not previously been delivered on a co-loaded wafer successfully in a clinical setting. The research carried out can be used to improve local drug delivery and increase therapeutic options for patients with GBM (Shapira-Furman et al., 2019).

### **1.5. The Blood-Brain Barrier and GBM Treatment**

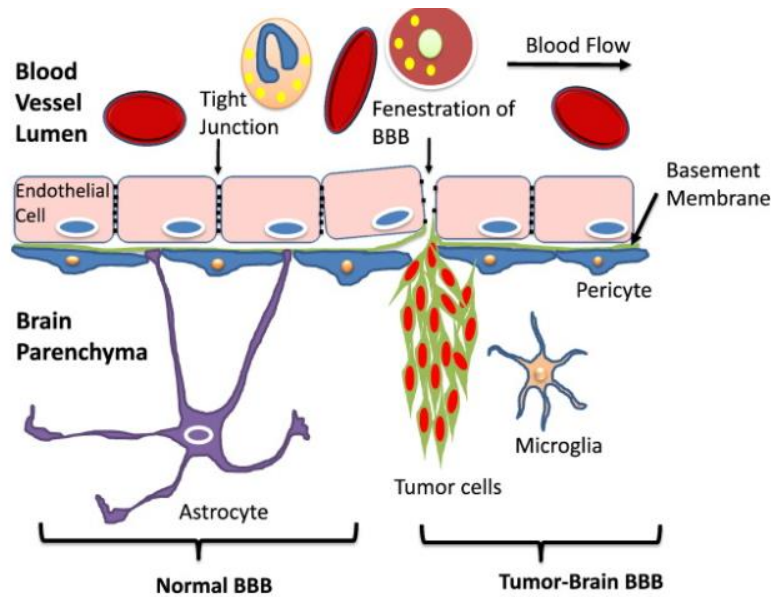
Drug treatment in neurological diseases such as brain tumours is particularly difficult due to the CNS protective barrier which consists of the blood-brain barrier (BBB) and the blood-cerebrospinal fluid barrier (BCSFB). These barriers play an important role in protecting the CNS from toxic and infectious agents. However, because of this, the BBB is a difficult obstacle for effective drug delivery (Lu et al., 2014).

The BBB plays a crucial role in maintaining an extracellular environment; it is a dynamic boundary which responds to stress such as hypoxia, pain and inflammation. The BBB only allows the free passage of water, ions and a small number of lipophilic molecules.

The penetration of the BBB using large molecules or hydrophilic drugs is very limited. It has been reported that 98 % of small molecules and 100 % of large molecules cannot penetrate the BBB (Nam et al., 2018).

The majority of approved anticancer drugs do not readily cross the BBB thus limiting the options for GBM treatment (Mannas et al., 2014). The BBB consists of endothelial cells that enclose the brain and spinal-cord capillaries and different types of perivascular cells such as pericytes, astrocytes, microglial cells and smooth muscle cells (Nam et al., 2018). Substances that wish to pass the BBB (fenestration) are restricted and must travel via the paracellular route between the microvascular endothelial cells or via the transcellular route through these cells (Lee, 2017). The primary components of the BBB are the endothelial cells which are joined together via tight junctions (TJ) which limit water-soluble substances or ions travelling via the paracellular route (Dumitru et al., 2018). Further limitations of substances passing into the BBB are seen in the transcellular route as a result of low endocytic activity of brain endothelial cells. An image depicting the blood brain architecture in a normal BBB verses a tumour BBB is shown in Figure 1.3.





**Figure 1.3 The Blood Brain Barrier Architecture in a Normal and Tumour Brain** (Ljubimova et al., 2017).

A leaky tight junction is present in human glioma, the presence of which can result in increased chances of cerebral oedema occurrence (Cook et al., 2020). Cerebral Oedema can be defined as fluid build-up around the brain which causes an increase in intracranial pressure (Cook et al., 2020). Brain oedema can be classified as vasogenic or cytotoxic where cytotoxic oedema is characterised by cell swelling caused by intracellular accumulation of fluid. In contrast, vasogenic oedema is defined as extracellular accumulation of fluid resulting from the disruption of the BBB (Michinaga & Koyama, 2015). The vasogenic type of oedema is the most common and is more important as it is associated with brain inflammation and brain tumours (Nehring et al., 2022). Two of the most common types of brain tumour: high-grade astrocytoma and metastatic adenocarcinoma are products of cerebral oedema. The micro vessels of these tumours

lose their BBB properties and leak fluid into the brain. It can be said that BBB stability in lower grade gliomas is better than in GBM (Davies, 2002).

The pharmacological approach to crossing the BBB is such that a molecule which is known to be active against a CNS target is modified so that it can cross the BBB (Gabathuler, 2009). The physiological approach is the delivery of neuroactive drugs via transporters. Drugs can be modified to take advantage of native BBB transporter systems, or the drug can be conjugated to a ligand that recognises receptors expressed at the BBB. This is referred to as receptor-mediated transcytosis and examples of said receptors include the insulin receptor, transferrin receptor and low-density lipoprotein receptor (Pulgar, 2019).

The BBB is also equipped with substances that limit brain penetration of anticancer drugs and chemotherapeutics for example efflux pumps which belong to the adenosine triphosphate (ATP)-Binding Cassette (ABC) protein family. Examples of efflux pumps belonging to this family are as follows: P-glycoproteins (P-gp), Multidrug Resistance-Associated Proteins (MRPs) and Breast Cancer Resistance Protein (BCRP) (Dumitru et al., 2018)(Lisa Iorio et al., 2016).

### **1.5.1 Lipinski's Rule of Five**

In 1997 Christopher Lipinski and colleagues looked at the physicochemical properties of approved drugs and proposed a "Rule of Five" where predictions could be made to determine the likelihood of a small molecule being orally active. This guideline prioritised compounds which have molecular masses of less than five hundred Daltons, calculated the log of the octanol-water partition coefficient (LogP) of less than five, five

or fewer hydrogen bond donors and ten or fewer hydrogen bond acceptors and the polar surface area should be less than seventy angstroms (Mullard, 2018) (Benet et al., 2016).

The Novartis Institutes for Biomedical Research published in the Journal of Medicinal Chemistry where the rule of five was re-assessed and argued that this rule does not stand the test of time. Work carried out for this paper included the assessment of the physicochemical properties of four hundred and nine small molecules that the FDA has approved since 2007 (Shultz, 2019). From this, it was found that the molecular mass had increased from the baseline where the majority of FDA approved drugs have a mass greater than six hundred Daltons. The threshold for hydrogen bond acceptors has also increased to a maximum of thirteen (Shultz, 2019).

There are limitations to Lipinski's rule of five whereby lipophilic substances with low molecular weight tend to be substrates for P-gp. P-gp or multidrug resistant protein (MRP1) is an adenosine triphosphate (ATP) binding cassette transporter (ABCB1) which has been extensively investigated as it is a major cause of failure in cancer treatment (Waghray & Zhang, 2018). P-gp prevents cellular uptake of most cancer therapeutics and causes multidrug resistance (Seelig, 2020). Almost 60 % of all marketed anti-tumour agents can be recognized by P-gp (D. Wang et al., 2019). Examples of anti-cancer drugs which are susceptible to P-gp mediated efflux include Paclitaxel which is used to treat ovarian cancer and Doxorubicin which is used in the treatment of breast cancer and leukaemia (Waghray & Zhang, 2018). P-gp works whereby the drugs are pumped out of the cells back to the blood flow which results in reduced therapeutic efficacy and poor brain accumulation of drugs (D. Wang et al., 2019). Overexpression of drug efflux transporters, especially P-gp is a common feature of GBM, thus restricting the entry of

chemotherapeutic agents in the brain (D. Wang et al., 2019). P-gp's have the ability to identify small molecule chemotherapeutic agents such as Temozolomide (TMZ), Methotrexate (MTX) and Paclitaxel as substrates. It can then pump the drugs out of the tumour region and BBB back to the brain capillary lumen which explains their poor response in GBM therapy (D. Wang et al., 2019).

BRCP is a type of ABC transporter protein which is found in different human tissues such as liver, kidney, testis, placenta and mammary gland. Its expression has been reported in tumours such as breast, colorectal and Glioblastoma cell lines. BRCP has been shown to reduce the ability of substances to penetrate the BBB (Lisa Iorio et al., 2016). As a result of this, the BBB as a therapeutic target has become increasingly more important.

### **1.5.2 Drug Transport Across the Blood-Brain Barrier**

The presence of the blood-brain barrier prevents the brain uptake of most pharmaceuticals which makes it difficult to develop new drugs for the treatment of brain diseases. This is due to the presence of epithelial-like tight junctions within the brain capillary endothelium (Pardridge, 2012). All the current products of biotechnology are large molecules which do not cross the BBB, furthermore 98 % of small molecules are not transported across the BBB (Pardridge, 2012). In order to bypass the BBB and deliver therapeutics into the brain, three different approaches are currently used: invasive, pharmacological and physiological (Gabathuler, 2009).

A physiological approach is a physical based technique that disrupts the BBB which includes the use of a polymer or microchip which directly releases therapeutics upon implantation to the CNS (Gabathuler, 2009). An example of such a therapeutic would be

Carmustine wafers, which are used in the treatment of high-grade glioma and recurrent glioblastoma as an adjunct to surgery and radiation (Chowdhary et al., 2015).

## **1.6. Search for Novel Therapeutic Targets for GBM**

Due to the difficulty of drugs passing across the BBB, there is need to discover new drug targets and therapeutics. The “Stupp Protocol” has not changed in 18 years (Stupp et al., 2005). No human clinical trials to date have demonstrated a superior effect with a novel therapeutic agent and so there is an urgent need for further drug discovery to be carried out (Poon et al., 2021). The use of therapies such as immunotherapy and drug repurposing for GBM has become a hot topic in recent years and will be discussed (Bausart et al., 2022)(Lyne & Yamini, 2021).

### **1.6.1 Cancer Immunotherapy**

Immune checkpoints can be defined as vital molecules and pathways of the immune system with defined roles for controlling immune responses from being destructive to healthy cells in the body. They include inhibitory receptors and ligands which check the recognition of most cancers by the immune system (Banday & Abdalla, 2022). Their role is to protect tissues from damage due to excessive immune response but also to protect against autoimmunity (Bausart et al., 2022). Cancer cells have been shown to take advantage of this system by escaping immune surveillance and upregulating inhibitory immune checkpoint expression and activating negative regulators on tumour specific immune cells. Cancer immunotherapy aims at harnessing the specificity and killing mechanisms of the immune system to target and eradicate malignant cells (Sahu & Suryawanshi, 2021). It has revolutionised the field of oncology whereby immunotherapy methods have already been used in the treatment of various different cancers including

brain cancer. Examples of current immunotherapy strategies that are being used to treat cancer are Immune Checkpoint Blockade (ICB) agents and monoclonal antibodies (mAbs) (Bausart et al., 2022).

The main checkpoints that have been successfully targeted in cancer treatments are programmed cell death receptor-1 (PD-1), its ligand PD-L1 and cytotoxic T-lymphocyte antigen 4 (CTLA-4) (Sahu & Suryawanshi, 2021). Inhibition of these T-cell negative regulators with monoclonal antibodies (mAbs) increases the immune response in many cancers such as melanoma and non-small-cell lung cancer. Ipilimumab is a monoclonal antibody that acts as a checkpoint inhibitor for CTLA-4 and was the first drug approved by the FDA in 2011 for the treatment of advanced melanoma. Nivolumab was the first mAb to target PD-1 and was approved in 2014 for the treatment of metastatic melanoma and has since been approved to treat non-small-lung cancer and squamous cancer of the head and neck (Bausart et al., 2022). The use of the CTLA-4 inhibitor, Ipilimumab is used in immunotherapy treatment for GBM. It is administered in four dosages of  $3 \text{ mg kg}^{-1}$  given over 90 minutes at three-week intervals. Side effects include gastrointestinal and skin responses, seizures and intracranial hypertension. Multiple clinical studies have shown that Ipilimumab monotherapy is ineffective and so it is used in conjunction with other immunomodulatory drugs. The use of Temozolomide and Ipilimumab is being investigated in a phase I trial (identifier NCT02311920) (Chowdhury et al., 2021).

The PD-1 / PD-L1 protein is expressed on the surface of GBM cells and so by blocking the PD-1 / PD-L1 pathway this suppresses T cells and ultimately leads to tumour cell regression. Nivolumab is a monoclonal antibody that targets the PD-1 receptor and was

shown to be receptive in GBM treatment and has been used in several phase III studies. One phase III study (identifier NCT02017717) utilised Nivolumab and an already approved drug for GBM, Bevacizumab. The trial failed to meet its targets as it failed to increase the patient's overall survival rate. A more recent phase III trial carried out by Bristol Myers Squibb (identifier NCT02667587) utilised the addition of immunotherapy whereby patients received TMZ, Nivolumab and radiation therapy. The trial was carried out on 693 patients with newly diagnosed GBM however this too failed to improve the patient's median overall survival rate. Despite the disappointing clinical trial results, the use of immunotherapy for GBM has not been abandoned. An anti-PD1 mAb, Pembrolizumab was given as a first step in a bid to shrink the tumour to patients with recurrent GBM and it significantly improved the overall progression-free survival rate (identifier NCT02054806). The primary reason for the disappointing results is due to the fact the ICB agents reduce immunosuppression exerted on T cells and then stimulate an immune response exerted on the tumour. Even when the ICB agents are combined with a standard treatment of care, the immune system is not enhanced due to the immunosuppressive characteristics of radiation therapy and chemotherapy. Promising results have now been shown when ICB agents are used as part of the first steps in treatment (neoadjuvant treatment) and not used alongside radiation therapy and chemotherapy (Bausart et al., 2022).

### 1.6.2 Drug Repurposing

Drug repurposing is also known as drug re-positioning or reprofiling. It is a strategy used to identify new uses for already approved drugs which are outside the scope of their original medical indication (Pushpakom et al., 2018). Drug repurposing is an advantage in terms of reducing cost and time as the drug is not subject to phase 1 clinical trials (Yadavalli et al., 2019).

Drug repurposing can be initially carried out computationally (*in silico*), this is referred to as virtual screening. It is one of the systematic methods used for drug repurposing as it requires significantly less time and money to be carried out (Jesús Naveja et al., 2016). Examples of drug repurposing for the treatment of GBM include the use of non-steroidal anti-inflammatory drugs (NSAIDs), disulfiram and metformin (Seliger & Hau, 2018).

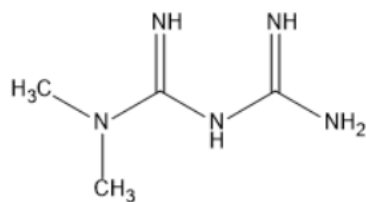
No significant results have been found for the use of NSAID's in the treatment of GBM, however, a meta-analysis found that there is a decreasing risk of glioma with increasing NSAID use such as aspirin (Seliger & Hau, 2018). Disulfiram is used to treat alcohol abuse and was also found to inhibit glioma initiating cells even when they were sensitive to Temozolomide. Disulfiram reversed hypoxia induced resistance to TMZ in mouse models at low nanomolar levels (Karen Tsui et al., 2018). There are currently six clinical trials being carried out (Seliger & Hau, 2018). Disulfiram has been identified as a promising drug to treat GBM when used as part of a co-treatment in conjunction with TMZ (Huang et al., 2019).



### ***1.6.2.1 Metformin***

The term “Diabetes Mellitus” is given to the disorder which describes abnormal glucose tolerance. It is characterized by chronic hyperglycaemia with a fasting glucose level of 7 mmol L<sup>-1</sup> or greater (Holt T, 2010). The WHO have classified the two different types of diabetes as type 1 and type 2. Type 1 diabetes is also referred to as Insulin-dependent diabetes mellitus (IDDM) and is an absolute insulin deficiency (Bilous, R; Donnelly, 2010). Type II diabetes is referred to as non-insulin dependent diabetes mellitus (NIDDM) and was formerly referred to as adult-onset diabetes (Rena G, Hardie DG, 2017). Insulin replacement is the drug therapy used to manage type 1 diabetes (Molitch, 1990). Drug therapy in conjunction with insulin therapy is used to manage hyperglycaemia in type II diabetes; the first line treatment given to patients is metformin (Bolen S, Tseng E, Huftless S, Segal JB, Suarez-Cuervo C, Berger Z, Wilson LM, Chu Y, Lyoha E, 2016).

Metformin was discovered through the synthesis of galegine compounds derived from the plant, *Galega Officinalis* – French lilac (Katzung B, Masters S, 2012). Galegine was initially used as a treatment to lower blood glucose levels in the 1920’s; however, it was found to be too toxic. In the 1950’s, two compounds that were synthesized previously from galegine derivatives, phenformin and metformin were tested for their hypoglycaemic effects. The older biguanide, phenformin was discontinued from the market due to its association with lactic acidosis and that there were no documented long-term benefits from its use (Katzung B, Masters S, 2012) (Rena G, Hardie DG, 2017) (Goodarzi MO, 2005) (Hardie, 2013). Metformin (1, 1-dimethyl-biguanide) is the only therapeutically available biguanide. Its structure can be seen in Figure 1.4.



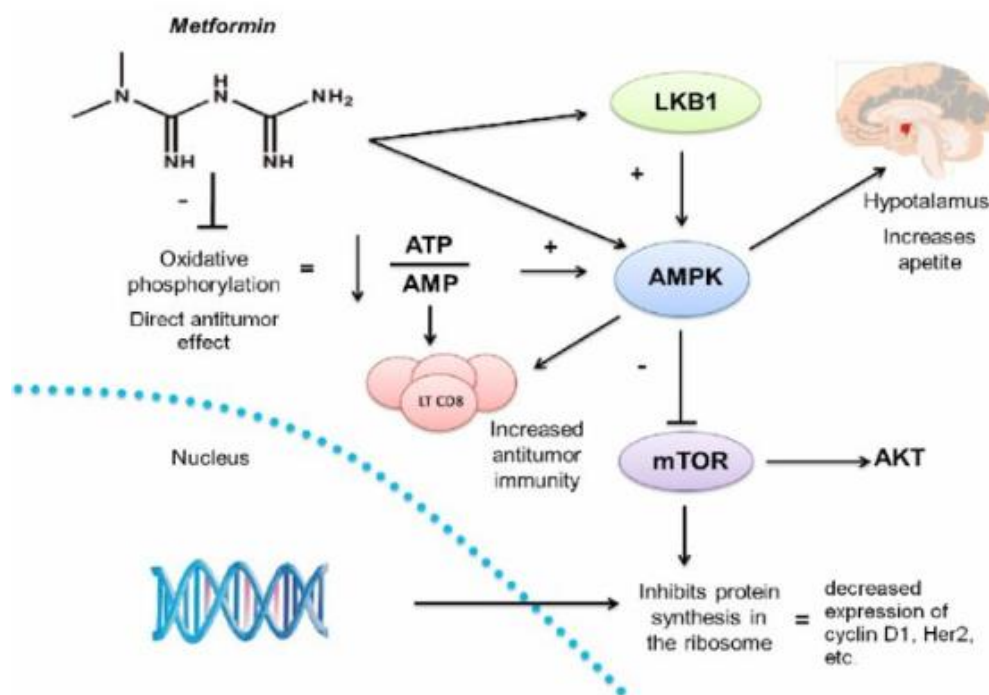
***Figure 1.4 Structure of Metformin***

#### ***1.6.2.2 Mode of Action of Metformin***

Despite Metformin being a first line therapeutic for the treatment of type II diabetes, it works by lowering glucose levels due to its actions primarily in the liver (Rena G, Hardie DG, 2017). One established effect of metformin is to decrease cellular energy levels. The AMP-activated protein kinase (AMPK) and mammalian target of rapamycin (mTOR) complex 1 (mTORC1) are key regulators of metabolism that are respectively activated and inhibited in response to cellular energy depletion (Howell et al., 2017). It has been shown that mTOR is upregulated in cancer and so mTOR inhibitors such as Metformin can play an important role in cancer prevention (Hua et al., 2019).

The mode of action of Metformin is to inhibit hepatic gluconeogenesis, antagonize glucagon action and activate AMPK. AMPK acts as an intracellular energy sensor in the liver and therefore has a role in the regulation of gluconeogenesis and metabolism. The mechanism of action of AMPK is such that; it is activated by stresses that increase the cellular concentration of AMP relative to ATP due to limited ATP production such as hypoxia or increased energy expenditure such as muscle contraction (Richter EA, 2010).

Metformin inhibits the mitochondrial electron transport chain complex 1 (ETCI). By inhibiting Complex 1; this prevents mitochondrial ATP production which activates AMPK (Rena G, Hardie DG, 2017) (Jang et al., 2011). Metformin exhibits Liver Kinase B1, LKB1 dependent and independent activation of AMPK. LKB1 activates AMPK through phosphorylation as it is a protein threonine kinase. LKB1 is a regulator of energy homeostasis, metabolism, and protein synthesis. It has been reported that deletion of LKB1 cells results in hyperglycaemia and eliminates the glucose-lowering effect of Metformin. This supports the theory that Metformin works by inhibiting complex 1, therefore stimulating AMPK and increasing glucose uptake in the muscle cells (Katzung B, Masters S, 2012) (Findlay et al., 2016). An image depicting the mechanism of action of Metformin is shown in Figure 1.5.



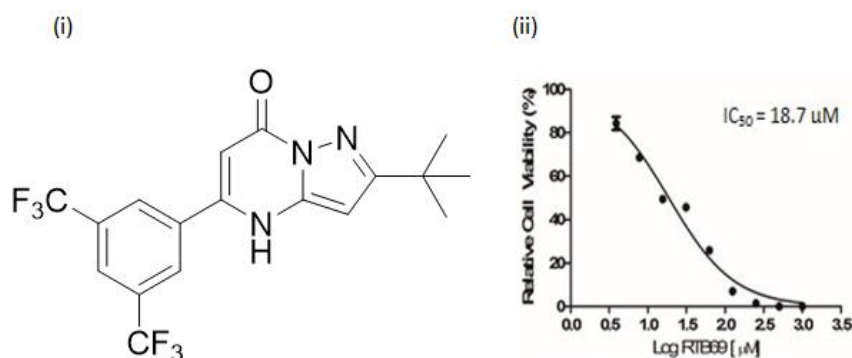
**Figure 1.5 Mechanisms of Action of Metformin.** There are two possible mechanisms in which Metformin can activate AMPK. It can be activated by the decrease in the ATP/AMP ratio and/or the activation of LKB1. The activation of AMPK also promotes the inhibition of mTOR (Yamada et al., 2010).

### 1.6.2.3 Drug Repurposing of Metformin

The anti-diabetic drug Metformin has been repurposed as it has demonstrated an ability to reduce cancer incidence and mortality, specifically in gliomas. It has been shown to inhibit proliferation of human glioma cells *in vitro* (U-251MG cell line) and has also affected tumour growth in mice models through the regulation of AMPK (Seliger et al., 2019) (Würth et al., 2013). Research involving the Kinsella and Stephens (Maynooth University) research group resulted in two novel compound families which are structurally different but exhibit a similar biological effect to Metformin: RTC1 and

TUM-1-005. The novel compounds have a proven impact on cell metabolism which shows the inhibition of the electron transport chain and Complex 1 (Devine, et al., 2020). A hypothesis was made that the novel compounds may have anti-cancer properties due to their ability to impede cell metabolism.

To explore the anticancer hypothesis, the novel compounds (RTC1 and TUM-1-005) and metformin underwent preliminary anticancer studies by carrying out a cell viability assay on the the HeLa cervical cancer cell line. In the cancer cell viability assay, active compounds were defined as those eliciting a greater than 50 % reduction of cell viability in three independent screens. Four analogues of TUM-1-005 were tested along with metformin and it was found that metformin was not effective for the HeLa cells (Conway, Curtin, & Howe, 2016). However, it was determined that the novel compounds elicited a greater potency than metformin which was determined by carrying out an alamarBlue™ cell proliferation assay on the HeLa cell line**Error! Reference source not found..** After the initial HeLa study, a second cell line was used which was the U251-MG GBM cell line. It was determined that the U-251MG GBM cell line was resistant to metformin but was sensitive to two novel based metformin compounds, one of which was TUM-2C-005 (Figure 1.6). TUM-2C-005 was shown to be an effective compound with an IC<sub>50</sub> value of 18.7 µM as shown in Figure 1.6 (Conway et al., 2016).



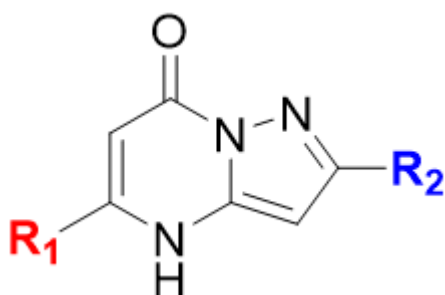
**Figure 1.6** (i) Structure of TUM-2C-005. (ii) Dose response curve shown where U-251MG cells were exposed to increasing concentrations of TUM-2C-005 (RTB69) (0-1000uM) and were analysed using the alamarBlue™ cell viability assay after 48 hours. N=3. Cells normalised to an untreated control. Analysis carried out using Prism software, version 5 (Conway et al., 2016).

#### 1.6.2.4 Rationale

The work carried out by (Conway et al., 2016) showed that the TUM-2C-005 compound had anti-cancer activity against the cancerous U251-MG cell line. The current state of the art carries on from this work whereby analogues of the TUM-2C-005 compound were biologically screened for anti-cancer activity, specifically anti-GBM activity. A family of 20 pyrazolo[1,5- $\alpha$ ]pyrimidinones were developed and evaluated for their anti-cancer effects using two cell lines, the cancerous U251-MG glioblastoma cell line and the immortalised human embryonic kidney (HEK293) cell line. The cancerous cell line was chosen as it was the cell line used by (Conway et al., 2016) and so would act as a useful comparison for the earlier work. The U251-MG cell line an epithelial and adherent cell

line as per the American Type Culture Collection (ATCC). The immortalised cell line was selected as it is also an epithelial and adherent cell line as per the ATCC. The non-cancerous cell line was used to determine whether the compounds had selectivity for the cancerous cells over the non-cancerous cells (ATCC, 2023).

The compounds screened are a family of 20 substituted pyrazolo[1,5- $\alpha$ ]pyrimidinones that have an  $R^1$  substituent on the pyrimidine ring and an  $R^2$  substituent on the pyrazole ring. The structure is shown on Figure 1.7 **Error! Reference source not found..** The pyrazolo[1,5- $\alpha$ ]pyrimidinones were organised into groups based on structural changes made at the  $R^1$  and  $R^2$  position, with the core scaffold remaining unchanged. This was done in order to carry out a structure activity relationship (SAR) study to determine their suitability to be used as a treatment for GBM. The aims and objectives of this study are outlined as per section 1.7.



**Figure 1.7** General structure of the pyrazolo[1,5- $\alpha$ ]pyrimidinones evaluated with an  $R^1$  substituent group on the pyrimidine ring and an  $R^2$  substituent group on the pyrazole ring.

## 1.7. Aims and Objectives

Treating GBM is challenging as most approved anti-cancer drugs do not readily cross the BBB and there is the issue of tumour recurrence, thus limiting the options for treatment. Given the aggressive and complex nature of GBM, the identification and validation of effective treatments that target the CNS are a serious unmet medical need. Based on the promising initial GBM results for TUM-2C-005, the following research question can now be posed:

*Can novel anti-GBM compound(s) be identified, optimized and validated in relevant in vitro cancer cell assays?*

From this, the aims and objectives of this PhD thesis were defined.

The aims and objectives of the first study outlined as per Chapter 2 are to evaluate the existing library of 20 TUM-2C-005 analogue compounds for GBM. A structure activity relationship (SAR) study will be carried out to enhance and improve the compounds structure and toxicity. Each of the analogue compounds will be split into different groups (1 – 4) based on changes being made to their substituent groups with the core scaffold of each compound remains unchanged. The selectivity of the compounds for the cancerous U251-MG cell line over the non-cancerous HEK293 cell line will also be evaluated to identify potential hit compounds by utilising *in vitro* cell viability assays.



The second study carried out is outlined as per Chapter 3. The aim of this chapter is to synthesise one intermediate 5-aminopyrazole compound used in the generation of the TUM-2A-001 pyrazolo[1,5- $\alpha$ ]pyrimidinone, and ten substituted pyrazolo[1,5- $\alpha$ ]pyrimidinones to expand the SAR study. Previously identified hit compounds as per Chapter 2 (TUM-2A-001, TUM-2A-004, TUM-2A-007 and TUM-2A-008) will be synthesised as well as analogues of these compounds. Each compound will be synthesised in good yield, purified, and characterised using analytical chemistry techniques such as  $^1\text{H}$  NMR spectroscopy,  $^{13}\text{C}$  NMR, LC-MS and FTIR.

The final study carried out is outlined as per Chapter 4. The first aim of this chapter is to determine whether the hit compounds are suitable to be used as part of a co-treatment study with the current gold standard chemotherapeutic treatment as per the “Stupp Protocol”. The second aim of this chapter is to determine whether the compounds are eliciting cell death, this was carried out using flow cytometry. The flow cytometry analysis will confirm the 2D cell viability assays that were carried out as per Chapter 2 and Chapter 3. The third aim of this chapter is to elicit a particular type of cell death that could be occurring by utilising inhibitor studies. Three inhibitors will be used: E-64, SP600125 and zVAD-fmk. Each inhibitor looks at different common pathways which induce apoptosis. The final aim of this chapter is to utilise 3D cell culture to ascertain whether the hit compounds have the potential to induce cell death *in vivo* and if a lead compound can be identified.

**2. INITIAL *IN VITRO* STRUCTURE ACTIVITY RELATIONSHIP STUDY OF  
PYRAZOLO[1,5- $\alpha$ ]PYRIMIDINONES FOR THE TREATMENT OF GBM**

## **2.1. Cell Culture**

Cell culture is a process in which cells are grown and maintained under carefully controlled conditions outside of a living animal, *in vitro* (Carter & Shieh, 2015). The ideal features of a cell culture system are those that can replicate the characteristics and responses of human tissue types (Stacey, 2012). In 1952, the HeLa cervical cancer cell line became the first human cancer cell line to become immortalised (Mittelman & Wilson, 2013). Immortalised cell lines can be defined as either tumorous cells that do not stop dividing or cells that have been artificially manipulated to proliferate indefinitely and can therefore be cultured over several generations. By passaging said cells, scientists can transfer a fraction of multiplying cells into new dishes thus providing space for further proliferation (Carter & Shieh, 2015). The discovery of cell culture has facilitated cancer research by allowing for the study of tumour transformation, gene expression and molecular pathways in cancer (Torsvik et al., 2014). Advancements in cell culture technology have allowed for the manufacture of vaccines, biopharmaceuticals, and the development of new therapeutic principles whereby cell culture can be used in drug screening and to assess the efficacy and toxicity of drugs (Yao & Asayama, 2017).

### **2.1.1 U251-MG Cell Line**

GBM cell lines have been established to be used as tools to unravel the mechanism of its disease. The first GBM cell line was established in 1981 at the Wallenberg laboratory in Uppsala, Sweden and was referred to as the “Uppsala” or the U-373 MG cell line (Jin et al., 2018)(Torsvik et al., 2014). The cell line was derived from a male patient with malignant astrocytoma, where grade IV astrocytoma’s are also called GBM (Torsvik et al., 2014). The American Type Culture Collection (ATCC) reported that their stock of U373-MG cells were showing different genetic properties to stock from the originators laboratory and shared similarities with another glioblastoma cell line, U-251. In light of this, the ATCC investigated the authenticity of its own cell line, and it was found that U373-MG was found to be identical to U251 through STR-PCR profiling. The U373-MG cell line was then renamed to U251-MG (ECACC Cell Lines: U251-MG (Formerly Known as U-373 MG), 2021.). The change in the naming convention is important as this project is a continuation of the work carried out by (Conway et al., 2016) where the cell line used was referred to as U373-MG and the name of the cell line given as part of this study is referred to as U251-MG.

### **2.1.2 HEK293 Cell Line**

The immortalised human embryonic kidney (HEK293) cell line was cultured in 1973 at the University of Leiden, Netherlands. The cell line is derived from the kidney of an aborted human embryo of unknown parenthood (Lin et al., 2014). This cell line occurred from the transformation and culturing of normal HEK cells and sheared adenovirus 5 DNA and is named HEK293 as it was the 293<sup>rd</sup> experiment. The addition of the adenovirus 5 to the HEK genome resulted in an immortalised cell line as it interfered with

cell cycle control and prevented apoptosis. The type of kidney cell in which HEK293 arose from is unknown and is difficult to characterise as the adenovirus 5 DNA could have disrupted cell morphology and expression.

Today, HEK293 cells are used in cell biology and biotechnology as they are an immortalised cell line, second in use only to HeLa cells (Lin et al., 2014). HEK293 cells grow easily in serum-free culture and produce high levels of protein which is why this cell line has been used widely for years. It should also be noted that the HEK293 cell line is an immortalised cell line (HEK293 Cell Line Origins, Cytogenetics, and Expression, 2021.).

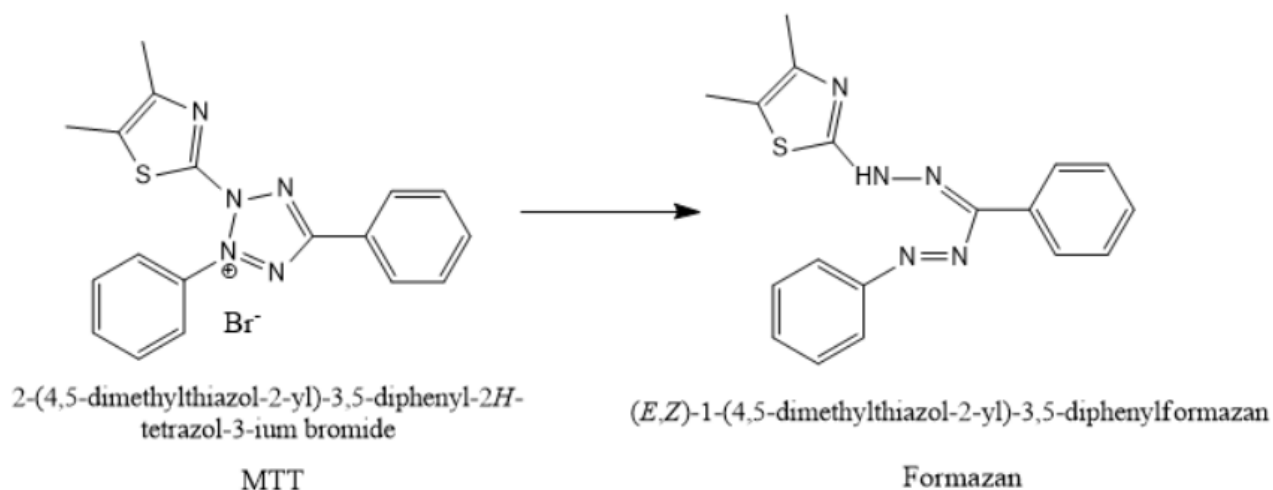
### **2.1.3 Cell Viability Assays**

Cell viability is defined as the quantification of the number of live healthy cells in a sample. Cell viability assays are carried out to determine the overall health of cells, optimise experimental conditions and to measure cell survival following treatment with compounds such as in a drug screen (Stoddart, 2011). The most common cell viability assay that is carried out is the manual cell count using a microscope and haemocytometer however this is a time-consuming and therefore low throughput method (Posimo et al., 2014). Assays which were initially developed to study cell viability are also used to study cell proliferation where cell proliferation refers to the number of actively dividing cells in a population. Dye-based assays have been developed which measure metabolic content and are used to determine cell viability and proliferation. The cell viability assay of interest for this study is the MTT (3-(4,5-dimethylthiazol-2-yl)-2,5-diphenyltetrazolium bromide) tetrazolium reduction assay (Ghasemi et al., 2021).

### **2.1.3.1 MTT Assay**

The colorimetric MTT (3-(4,5-dimethylthiazol-2-yl)-2,5-diphenyltetrazolium bromide) tetrazolium reduction assay was originally developed by Mossman in 1983 and was one of the first assays to be developed for the 96 well plate format which was intended for high throughput screening. The assay was then adapted by Cole in 1988 to be used to carry out chemosensitivity testing for human small cell lung cancer cell lines. It is now a gold-standard colorimetric assay used to carry out cell viability and proliferation studies (Ghasemi et al., 2021).

The MTT assay is used to measure cellular metabolic activity and acts as an indicator of cell viability, cell proliferation and cytotoxicity. The MTT assay is a colorimetric assay which is based on the reduction of the yellow tetrazolium salt to purple formazan crystals shown in Figure 2.1 (Protocol Guide: MTT Assay for Cell Viability and Proliferation | Sigma-Aldrich, 2021). Viable cells with active metabolism convert MTT to an insoluble purple formazan crystal where cell viability is directly proportional to the quantity of formazan crystals formed. The quantity of formazan is determined by recording the changes in absorbance at 570 nm using a plate reader spectrophotometer (Riss et al., 2004). The MTT assay is considered the gold standard for determination of cell viability and proliferation and was the first homogenous cell viability assay developed for a 96-well format that was suitable for high throughput screening (Kuethe et al., 2017)(Ghasemi et al., 2021).



**Figure 2.1 The MTT Assay:** the reduction of the yellow tetrazolium salt to the insoluble purple formazan crystal.

#### 2.1.4 Pharmacological Analysis

Determination of the half maximal (50 %) inhibitory concentration ( $IC_{50}$ ) is essential for understanding the pharmacological and biological characteristics of a chemotherapeutic agent. The MTT assay is currently the most extensively used method for  $IC_{50}$  measurements (Ghasemi et al., 2021). A MTT assay provides data from which a dose-response curve can be generated whereby the  $\log_{10}$  of the dose or concentration of the drug is on the x axis and the measured effect is on the y axis (GraphPad, 2020). The curves that were generated as part of this study are referred to as reverse sigmoidal curves which is termed the displacement or inhibition curve and is used to identify the  $IC_{50}$  of the compound (Patrick, 2017).

#### ***2.1.4.1 Dose-Response Curves***

The effect of a drug is the product of the concentration of the drug at its binding site, however specific responses to drug concentrations are non-linear as the drug effect is a function of dose (concentration) and time. Dose-response or concentration-response curves are generated using a logarithmic x-axis scale for drug dose (concentration) and a y-axis scale for effect at a specific time point (Currie, 2018). Dose-response curves such as the curve of the log (inhibitor) vs normalised response are generated during pharmacological screening (GraphPad Prism 7 Curve Fitting Guide - Equation: [Inhibitor] vs. Normalized Response -- Variable Slope, 2020). Normalising the data refers to forcing the curve to run between 0 % and 100 %. This allows the  $IC_{50}$  to be determined which is the concentration at which a substance exerts half its maximal inhibitory effect. The dose-response curve is also measured and analysed according to a standardised protocol which assumes the dose-response or concentration-response curve has a standard slope. This is based on a four-parameter logistic fit “4PL” which mathematically is equal to the Hill slope of -1.0 (Prinz, 2010).

The Hill slope is the slope expected when a ligand binds to a receptor following the law of mass action, which states that binding occurs when a ligand and receptor collide as they both have the correct orientation and enough energy. The law also assumes that binding is reversible (Bagshaw, 2013). Therefore, the dose-response curve formed reflects binding curves.

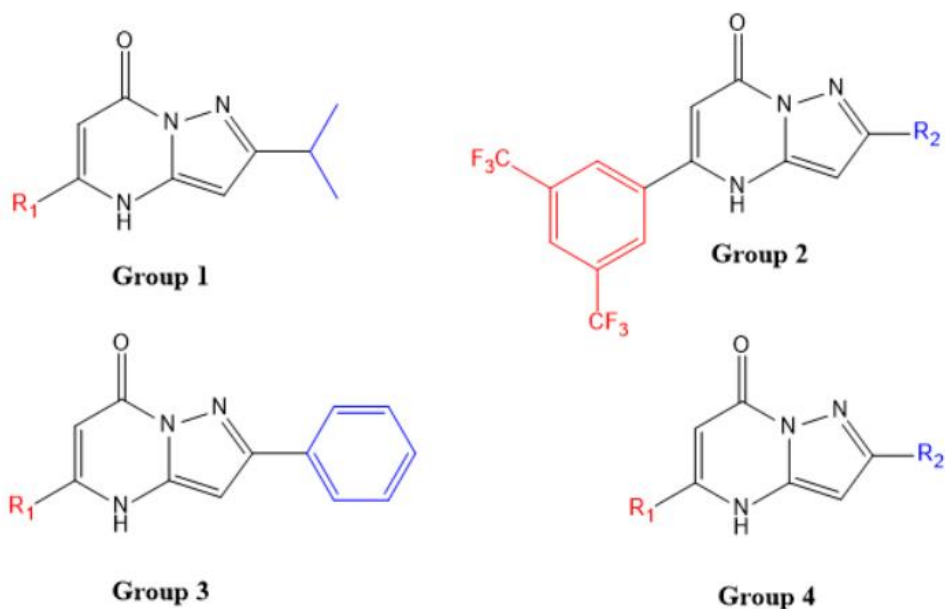
The Hill slope value refers to the steepness of the curve whereby the ideal mathematical value is -1.0 for an inhibition curve. A Hill slope with a more negative value represents a



steeper slope and a Hill slope with a more positive value represents a shallower curve, for example -2.0 would be steeper and -0.5 shallower (GraphPad Prism 7 Curve Fitting Guide - Equation: [Inhibitor] vs. Normalized Response -- Variable Slope, 2020).

### 2.1.5 The Pyrazolo[1,5-*a*]pyrimidinone Family

There was a total of 20 of pyrazolo[1,5-*a*]pyrimidinones that were screened as part of this initial study. The compounds were split into four groups whereby they were grouped based on structural changes to the compounds as shown in **Error! Reference source not found.**



**Figure 2.2** The four pyrazolo[1,5-*a*]pyrimidinone groups screened as part of the study whereby the core scaffold remains unchanged in each compound. The structural changes were made to the compounds at either the R<sup>1</sup> or R<sup>2</sup> position or both positions as denoted in red and blue respectively.

Group one (4 compounds) had a consistent isopropyl group at the R<sup>2</sup> position where R<sup>1</sup> was varied. Group two contained ten compounds and was split into three sub-groups: 2A, 2B and 2C. Each compound in group 2 contained a 1,3-bis(trifluoromethyl)phenyl group at the R<sup>1</sup> substituent and the R<sup>2</sup> substituent was varied. In the 2A subgroup the R<sup>2</sup> substituent had to be a substituted aryl ring, in the 2B subgroup the R<sup>2</sup> substituent had to be a heterocyclic ring and in the 2C subgroup the R<sup>2</sup> substituent was an alkyl chain. There were two compounds screened in group 3 where the R<sup>1</sup> substituent was varied and the R<sup>2</sup> substituent was a phenyl ring. There was a total of four compounds screened in group 4 where both the R<sup>1</sup> and R<sup>2</sup> substituents were varied for each compound.

It will then be determined whether any of the compounds show selectivity towards the cancerous GBM U251-MG cell line over the non-cancerous HEK293 cell line. Selectivity will be determined through the IC<sub>50</sub> values obtained from each of the compounds. A selective compound will be one that has a lower IC<sub>50</sub> value observed in the cancerous cell line as opposed to the non-cancerous cell line. The IC<sub>50</sub> values obtained will also need to be statistically significant to be deemed selective.

## **2.2. Materials and Methods**

### **2.2.1 Pyrazolopyrimidinone Synthesis**

The synthesis of the 5-aminopyrazoles and the substituted pyrazolo[1,5- $\alpha$ ]pyrimidinones were prepared using modified literature values taken from the one-pot approach developed by the Stephens research group (Kelada *et al.*, 2018). The compounds synthesised in this chapter were prepared by postgraduate chemists in Maynooth University. The method of synthesis is outlined in the following chapter.

### **2.2.2 General Cell Culture, Maintenance and Sub-Culture**

The cell lines used in this study were the human glioblastoma cell line, U251-MG, and the Human Embryonic Kidney cell line, HEK293. The U251-MG cell line was a gift from Michael Carty (Trinity College Dublin.) The HEK293 cell line was a gift from Darren Fayne (Trinity College Dublin). Both cell lines were initially purchased from the American Type Culture Collection, ATCC.

#### **2.2.2.1 Cell Culture**

U251-MG and HEK293 cells were cultured in Dulbecco's Modified Eagles Medium, DMEM (Merck) which was supplemented with 10 % Fetal Bovine Serum, FBS (Merck) and 1 % Penicillin-Streptomycin antibiotics (Merck) – this will be referred to as media throughout. Cells were maintained in an incubator containing 5 % CO<sub>2</sub> at 37 °C. Media was changed every 2 – 3 days until 70 – 80 % confluency was reached to ensure that the cells were in the logarithmic phase, cells were then subcultured.

#### ***2.2.2.2 Cell Culture Subculture***

Cells were routinely subcultured as follows:

The old media was aseptically pipetted out of a confluent T75 flask and disposed of in the appropriate waste container. Cells were then washed with sterile phosphate buffered saline (PBS) (10 mL) (Merck). This was done by aseptically pipetting the PBS in the flask and then removing the PBS from the flask. Cells were detached from the stock flask using Trypsin-EDTA (Merck) after a period of three minutes in an incubator. A 1:1 ratio of media was then added to the flask aseptically to stop the trypsin activation and prevent cell death. The cells were then counted using a haemocytometer. The split ratio used was 1:3 and the cell seeding density used was  $2 \times 10^3$  cells mL<sup>-1</sup> (Service, 2020) (ECACC Cell Lines: U-373 MG (Uppsala) -, 2021).

#### ***2.2.2.3 Cell Freezing Method***

Cell freezing media was prepared as follows: sterile 5 % DMSO was added to prepared cell culture media aseptically. After following the cell sub-culture method outlined in section 2.2.2.2, a 1:1 ratio of media and Trypsin-EDTA was transferred to a 15 mL centrifuge tube. The centrifuge tube was placed inside a balanced centrifuge (ThermoFisher Scientific) and then the cells were spun down at 1,200 rpm for 5 minutes. The media was discarded to waste, taking care not to disturb the cell pellet. Cell freezing media was added to the centrifuge tube and pipetted up and down to ensure a homogenous solution of freezing media and cells. 1 - 4 mL of cells in cell-freezing media solution was transferred to a labelled cryogenic vial and stored at -80 °C overnight before liquid nitrogen storage.

#### **2.2.2.4 Cell Defrosting**

The cryogenic vial was removed from liquid nitrogen and placed into a pre-heated water bath to defrost. Excess media was pipetted into a T75 flask, and the contents of the cryogenic vial were placed into a flask once contents defrosted. The cells were allowed to adhere for 24 hours and then passaged into new media.

#### **2.2.3 Cell Density for Cell Viability Assay**

Cells were counted using a haemocytometer and were then seeded at  $2 \times 10^3$  cells per well in a 96 well plate (Sarstedt) at 100  $\mu$ L per well in standard media. The plates were then incubated at 37 °C. Cell viability was determined by carrying out a MTT assay (see section 2.2.4) after removing the old media at the appropriate time point and adding MTT solution.

#### **2.2.4 MTT Cell Viability Assay**

The MTT assay was used to investigate cell viability when performing the cell proliferation studies in both cell lines. The MTT solution was prepared for one 96 well plate as follows: MTT compound (Merck) (5 mg per 96 well plate) in PBS (1 mL per 5 mg MTT) and media (9 mL per 5 mg MTT) were combined. When the appropriate incubation time was reached, the media was removed from the wells. 100  $\mu$ L of fresh MTT solution was pipetted into each of the wells. The plates were then left to incubate for 3 hours at 37 °C. After incubation, the MTT solution was removed from the wells. 100  $\mu$ L of DMSO was then pipetted into the wells and the plates were left to stand for 15 minutes. Absorbance at 570 nm was then read on a Perkin Elmer Multiskan Go Microplate Spectrophotometer. The data was then normalised to the assay control,

DMEM and cell growth was calculated as a change of viability over time. All experiments were carried out using a minimum of three independent times.

#### **2.2.5 Spectrophotometer Data Analysis**

The absorbance unit values were extracted for viability calculations using the statistical analyses software GraphPad Prism version 8.0.0 for Windows, GraphPad Software, San Diego, California USA, [www.graphpad.com](http://www.graphpad.com). (GraphPad, 2020) All experiments were performed a minimum of three independent times. Cell viability was calculated by removing any background absorbance from the MTT blank reading. The mean absorbance value was calculated from each test per plate.

#### **2.2.6 Statistical Analysis**

Statistical analysis was carried out using the GraphPad Prism version 8.0.0 for Windows, GraphPad Software, San Diego, California USA, [www.graphpad.com](http://www.graphpad.com) (GraphPad, 2020). The statistical analysis performed was such that the IC<sub>50</sub> values for the compounds were determined, curve fitting and analysis of variance (ANOVA) was carried out as well. One-way ANOVA was carried out whereby each treatment was compared to the negative control to determine statistical significance; this is referred to as Dunnett's T3 multiple comparisons test. The P value style used on prism was the GraphPad style which reports the P values as per Table 2-1 (GraphPad, 2020).

**Table 2-1 Prism 8.0.0 statistical significance values, significance level and summary.**

P Value	Wording	Summary
<b>&lt;0.0001</b>	Extremely Significant	****
<b>0.0001 to 0.001</b>	Extremely Significant	***
<b>0.001 to 0.01</b>	Very Significant	**
<b>0.01 to 0.05</b>	Significant	*
<b>≥ 0.05</b>	Not Significant	ns

### **2.2.7 Physicochemical Properties**

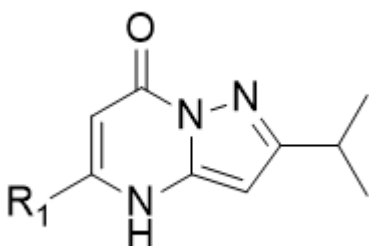
The predicted physicochemical properties of the hit compounds were determined using the SwissADME web tool (Bioinformatics, 2022). This was performed where a Simplified Molecular Input Line Entry System (SMILES) notation was generated for each hit compound and the webserver produces predicted physicochemical and ADME properties for the compound. Examples of such properties generated using this tool include lipophilicity, water solubility, pharmacokinetics, druglikeness and medicinal chemistry properties. For the purpose of this analysis only the data from the physicochemical property and lipophilicity section was used to predict whether the compounds can pass through the BBB.

## 2.3. Results

### 2.3.1 Initial Compound Evaluation using U251-MG and HEK293 Cell Lines

#### 2.3.1.1 Group 1 Compounds

The group 1 pyrazolo[1,5- $\alpha$ ]pyrimidinones are such that the  $R^1$  substituent is varied and the  $R^2$  substituent is retained as an isopropyl group. The general structure of the group 1 compounds can be seen in Figure 2.3.

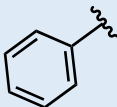
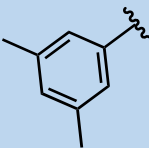
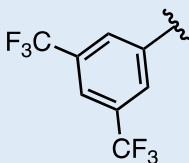


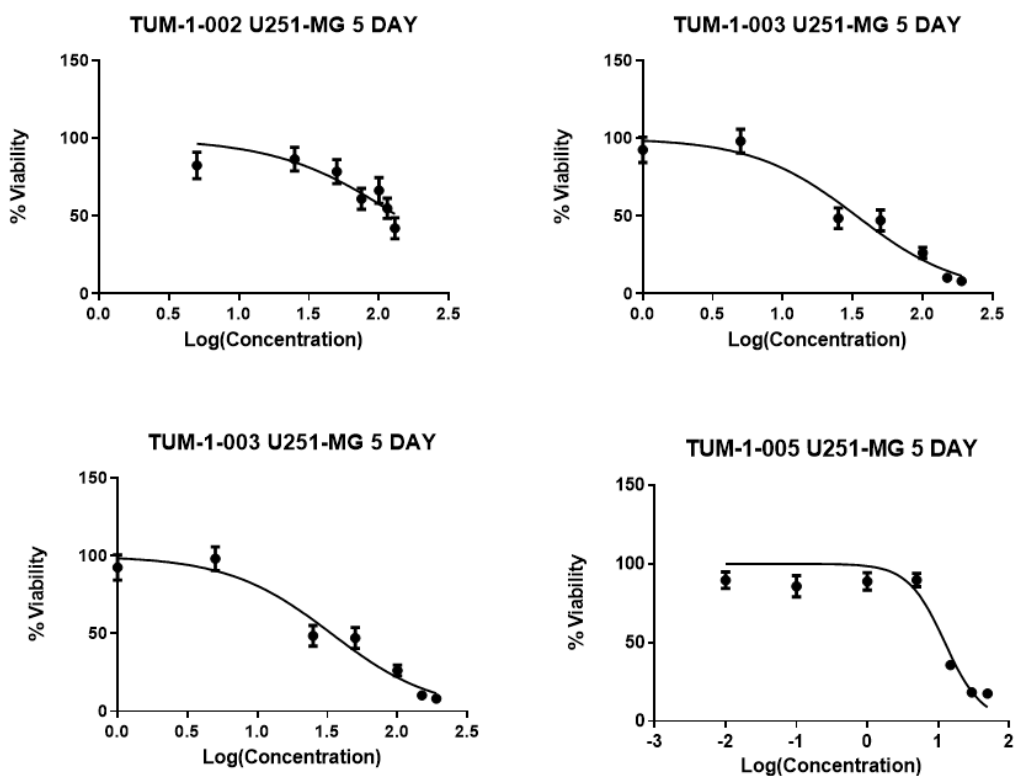
**Figure 2.3** General structure of group 1 pyrazolo[1,5- $\alpha$ ]pyrimidinone compound whereby the  $R^1$  substituent is varied and there is an isopropyl substituent at the  $R^2$  position.

Four group one compounds were evaluated using the U251-MG cell line and the results of the study are shown in Table 2-2 and Figure 2.4. The group one compounds was also evaluated using the non-cancerous HEK293 cell line and results are shown in Table 2-3 and Figure 2.5. The compounds that do not elicit a sufficient biological response are set as those which have an  $IC_{50}$  value greater than 50  $\mu M$  (Gao et al., 2019) and those with a large  $IC_{50}$  range and Hill slope range at a 95 % confidence interval.



**Table 2-2 Results for group 1 evaluation using U251-MG cell line. MTT cell viability assay carried out on the U251-MG cell line. Cells were analysed 5 days after treatment, N=3. X is denoted where an experimental value was not possible.**

Compound Name	R <sup>1</sup> Group	IC <sub>50</sub> Value (μM)	IC <sub>50</sub> 95% CI (μM)	Hill Slope Value	Hill Slope 95% CI
TUM-1-002	CH <sub>3</sub>	X	79.67 to 1538	-2.025	-8.789 to -0.2791
TUM-1-003		20.69	X to 50.40	-2.604	X to -0.6608
TUM-1-004		9.17	5.475 to 14.24	-1.024	-1.839 to -0.6263
TUM-1-005		14.90	11.16 to 19.69	-2.014	-4.297 to -1.212



**Figure 2.4 Dose response curve for group 1 pyrazolo[1,5-*a*]pyrimidinones. U251-MG cell line and the MTT cell viability assay. Cells were analysed 5 days after treatment, *N*=3. Where the X axis denotes the logarithmic concentration of compound, and the Y axis denote the % cell viability of the pooled data for the group 1 compounds.**

One compound in group 1, TUM-1-002 did not show any biological activity against the U251-MG cell line whereby an IC<sub>50</sub> value > 50  $\mu$ M was determined experimentally (see Table 2-2). A large IC<sub>50</sub> value range is observed, this is also observed in TUM-1-003. Ideally a narrow range is desired as it makes the values more accurate. Both TUM-1-002 and TUM-1-003 exhibited the largest Hill slope values as well as large Hill slope ranges.

It was not possible to attain a Hill slope range for TUM-1-003 as denoted by X in Table 2-2.

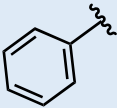
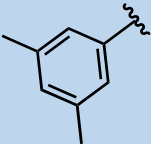
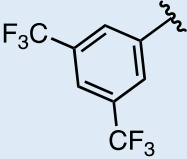
Lower IC<sub>50</sub> values (< 20 µM) were obtained for both TUM-1-004 and TUM-1-005 and both compounds have narrow IC<sub>50</sub> ranges. TUM-1-004 and TUM-1-005 both have low Hill slope values which can be observed by the symmetrical sigmoidal curve shown in Figure 2.4. Narrow Hill slope ranges were also observed for both compounds.

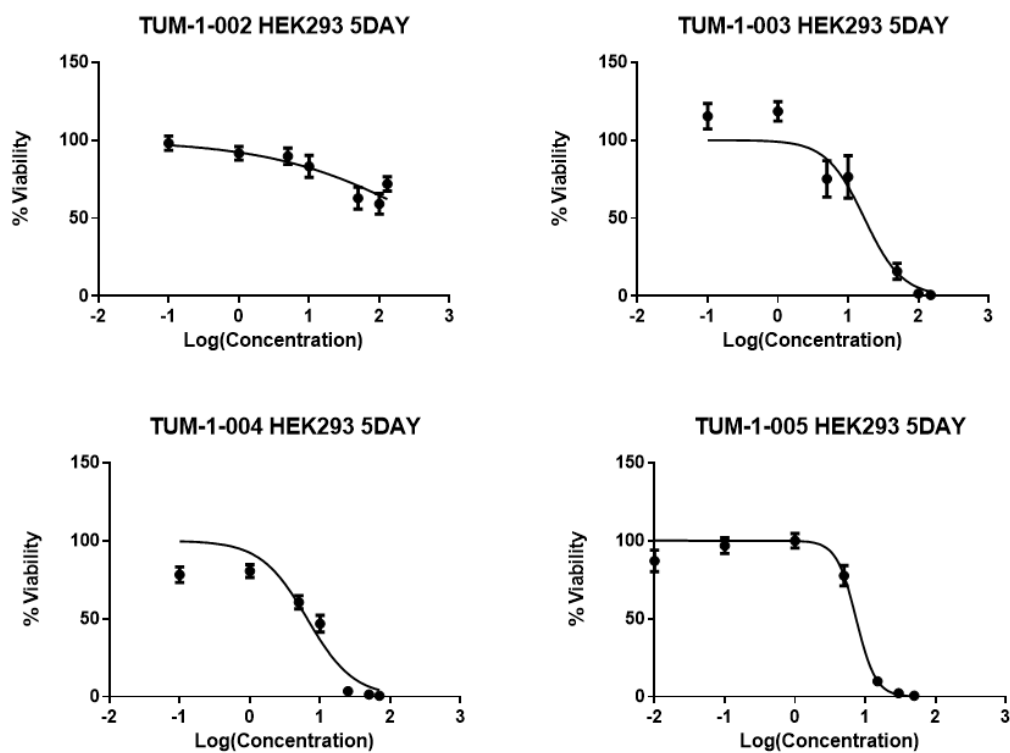
The results of the group 1 compound screen on the HEK293 cell line can be observed in Table 2-3. It can be said that the compounds which do elicit a biological response are those which have an IC<sub>50</sub> value of < 50 µM. (Gao et al., 2019) A concentration-response curve was generated and is shown in Figure 2.5.

As per the results outlined in Table 2-3, the only compound which does not elicit a biological response on the HEK293 cell line is TUM-1-002 due to its large experimental IC<sub>50</sub> value and IC<sub>50</sub> range. The remaining three compounds have low IC<sub>50</sub> values however it was not possible to generate an IC<sub>50</sub> range or Hill slope range for TUM-1-005 as denoted by X in Table 2-3.

Based on this analysis, TUM-1-002 will not be studied further as it exhibited no biological activity in either cell line. TUM-1-003 is not selective for the cancer cell line as the IC<sub>50</sub> value obtained in the HEK293 cell line (9.99 µM) was lower than that observed in the U251-MG cell line (20.69 µM). Detailed statistical analysis will be carried out for all compound sub-groups in both section 2.3.2 and 2.3.3.

**Table 2-3 Results for group 1 evaluation using HEK293 cell line and the MTT cell viability assay. Cells were analysed 5 days after treatment, N=3. X is denoted where an experimental value was not possible.**

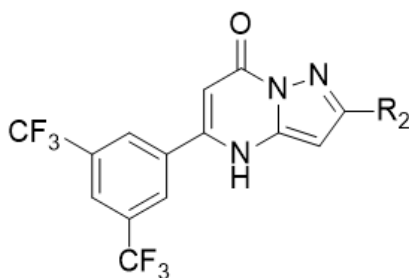
Compound Name	R <sup>1</sup> Group	IC <sub>50</sub> Value (μM)	IC <sub>50</sub> 95% CI (μM)	Hill Slope Value	Hill Slope 95% CI
TUM-1-002	CH <sub>3</sub>	X	111.9 to 418183	-0.4043	-0.9640 to -0.1250
TUM-1-003		9.99	5.733 to 18.88	-1.715	X to -0.8621
TUM-1-004		6.58	3.673 to 9.632	-1.314	-2.483 to -0.7443
TUM-1-005		7.45	X to 9.314	-3.104	X to -2.042



*Figure 2.5 Pooled data dose response curves for compounds in group 1. HEK293 cell line and the MTT cell viability assay. Cells were analysed 5 days after treatment, N=3. Where the X axis denotes the logarithmic concentration of compound, and the Y axis denotes the % cell viability.*

### 2.3.1.2 Group 2A Pyrazolo[1,5- $\alpha$ ]pyrimidinones

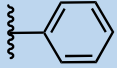
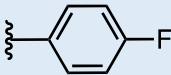
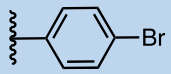
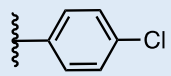
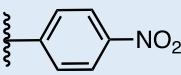
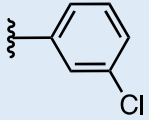
The group 2A pyrazolo[1,5- $\alpha$ ]pyrimidinones are such that the  $R^1$  substituent is a 1,3-bis(trifluoromethyl)phenyl and the  $R^2$  substituent is varied but must be a substituted aryl ring. The general structure of the group 2A compounds can be seen in Figure 2.6.

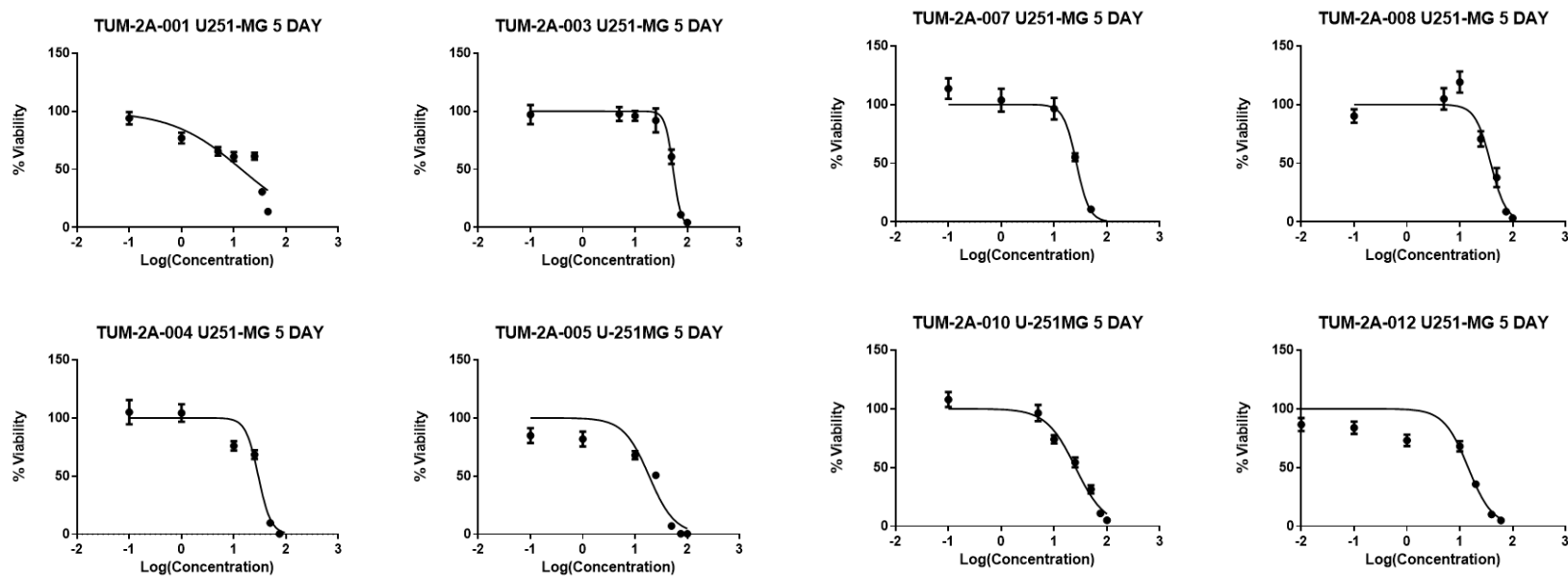


***Figure 2.6 General structure of group 2A analogue compounds whereby the  $R^1$  functional group consists of a 1,3-bis(trifluoromethyl)phenyl substituent and the  $R^2$  group consists of varied substituted aryl ring groups.***

Table 2-4 denotes the results obtained for the evaluation of group 2A pyrazolo[1,5- $\alpha$ ]pyrimidinones using the U251-MG cell line. A dose response curve was generated for all the group 2A compounds and are shown in Figure 2.7.

**Table 2-4 Results of U251-MG cell screen on group 2A compounds. U251-MG cell line and the MTT cell viability assay. Cells were analysed 5 days after treatment, N=3. X is denoted where an experimental value was not possible.**

Compound Name	R Group	IC <sub>50</sub> Value ( $\mu$ M)	IC <sub>50</sub> 95% CI ( $\mu$ M)	Hill Slope Value	Hill Slope 95% CI
TUM-2A-001		6.17	2.938 to 11.68	-0.4317	-0.6463 to -0.2740
TUM-2A-003		58.92	39.09 to 91.53	-2.886	X to - 1.081
TUM-2A-004		29.49	26.21 to 33.18	-3.613	-4.970 to - 2.256
TUM-2A-005		18.12	9.824 to 29.29	-3.136	X to - 1.508
TUM-2A-007		26.75	23.90 to 29.94	-4.101	-6.445 to - 1.757
TUM-2A-008		29.62	25.37 to 34.75	-3.232	-5.709 to - 2.284
TUM-2A-010		23.79	15.19 to 35.90	-1.166	-1.863 to - 0.7024
TUM-2A-012		21.72	7.456 to 90.95	-0.8800	-2.332 to - 0.3132



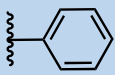
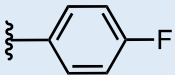
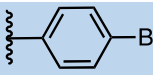
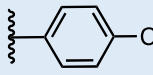
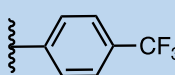
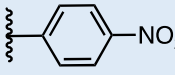
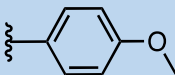
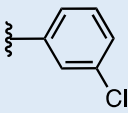
*Figure 2.7 Dose response curves for compounds in group 2A. U251-MG cell line and the MTT cell viability assay. Cells were analysed 5 days after treatment, N=3. Where the X axis denotes the logarithmic concentration of compound, and the Y axis denotes the % cell viability.*

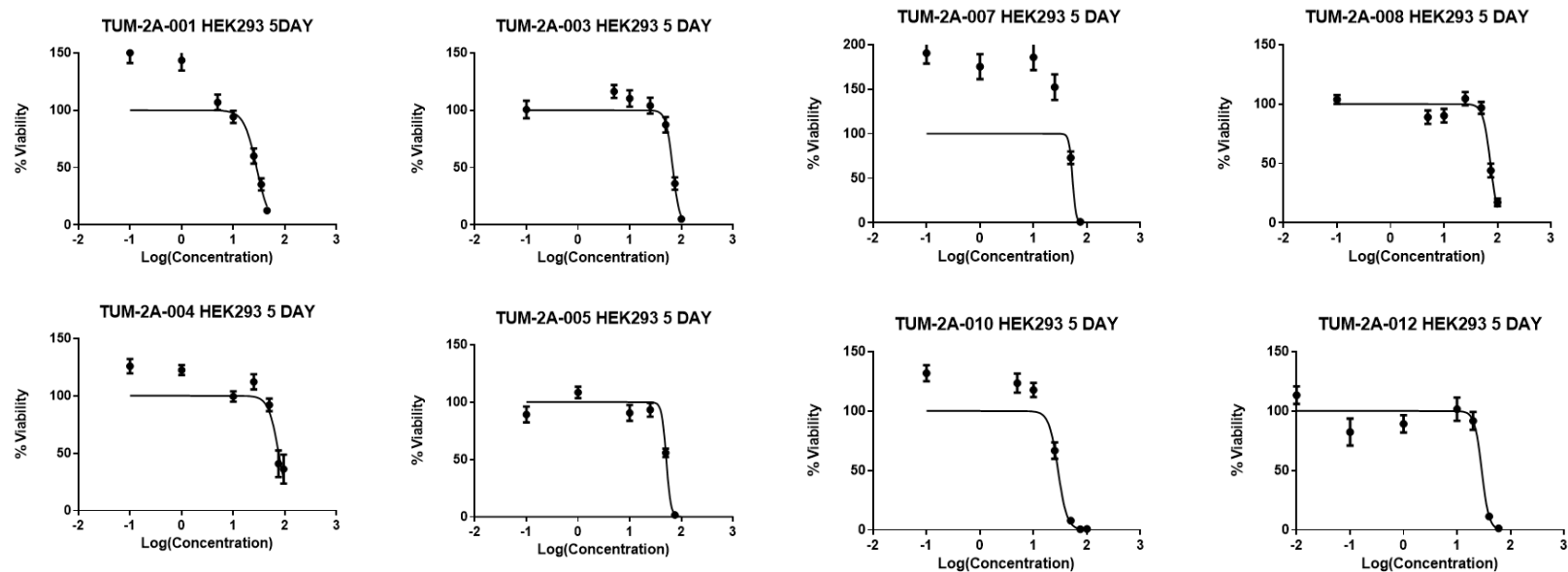


TUM-2A-003 has no biological effect on the U251-MG cell line as shown by the large experimental IC<sub>50</sub> value and the observed large IC<sub>50</sub> range. It was also not possible for a Hill slope range to be generated as denoted by X in Table 2-4. The remaining compounds in group 2A elicit a biological response as they have an IC<sub>50</sub> value of less than 50 µM. From the initial screen the compounds of most interest are TUM-2A-001 and TUM-2A-010, due to their low IC<sub>50</sub> values and narrow ranges. The Hill slope values for the aforementioned compounds are all close to -1.0, denoting a near perfect symmetrical sigmoidal shape as well as observed narrow Hill slope ranges.

The results of the group 2A compound screen on the HEK293 cell line can be observed in Table 2-5. Dose-response curves were generated for the compounds and are shown in Figure 2.8.

**Table 2-5 Results of HEK293 cell line screen on group 2A compounds. HEK293 cell line and the MTT cell viability assay. Cells were analysed 5 days after treatment, N=3. X is denoted where an experimental value was not possible.**

Compound Name	R Group	IC <sub>50</sub> Value (μM)	IC <sub>50</sub> 95% CI (μM)	Hill Slope Value	Hill Slope 95% CI
TUM-2A-001		15.47	13.55 to 17.56	-1.666	-2.002 to -1.394
TUM-2A-003		68.21	63.23 to 73.58	-6.575	-9.343 to -3.807
TUM-2A-004		60.34	X	-10.47	X to -6.875
TUM-2A-005		51.16	48.83 to 53.60	-9.993	-21.68 to 1.694
TUM-2A-007		51.52	48.47 to 56.63	-12.34	X to -5.245
TUM-2A-008		73.79	69.61 to 78.23	-6.309	-8.653 to -3.965
TUM-2A-010		28.85	25.34 to 32.85	-5.113	-8.523 to -1.703
TUM-2A-012		29.77	X	-6.565	X to -4.305

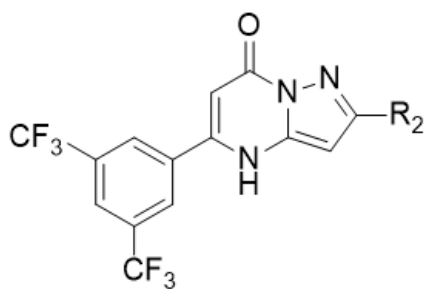


*Figure 2.8 Dose response curves for compounds in group 2A. Assay Conditions: HEK293 cell line and the MTT cell viability assay. Cells were analysed 5 days after treatment, N=3. Where the X axis denotes the logarithmic concentration of compound, and the Y axis denotes the % cell viability.*

The three compounds with IC<sub>50</sub> values < 50 µM in this group are TUM-2A-001, TUM-2A-010 and TUM-2A-012. The corresponding Hill slope values observed in both TUM-2A-010 and TUM-2A-012 are large, > 50 µM and the observed Hill slope ranges are large or unattainable as denoted by X in Table 2-5. TUM-2A-001 has both the lowest IC<sub>50</sub> value and a Hill slope value which is close to the ideal -1.0 value as observed in Table 2-4. It should be noted that each of the group 2A compounds showed potential selectivity for the cancerous cell line whereby lower IC<sub>50</sub> values were determined in the U251-MG cell line than those observed in the non-cancerous HEK293 cell line. Statistical analysis will be carried out in the next section of this chapter further evaluate the group 2A compounds.

### 2.3.1.3 Group 2B Pyrazolo[1,5-*a*]pyrimidinones

The pyrazolo[1,5-*a*]pyrimidinone consisting of a 1,3-bis(trifluoromethyl)phenyl as the R<sup>1</sup> substituent with a heterocyclic ring at the R<sup>2</sup> substituent is denoted as “group B” despite there being one compound in the aforementioned “group.” The compound was placed into a group subset for ease of use when describing the structural changes in the compounds. The general structure of the group 2B pyrazolo[1,5-*a*]pyrimidinone can be seen in Figure 2.9.

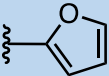


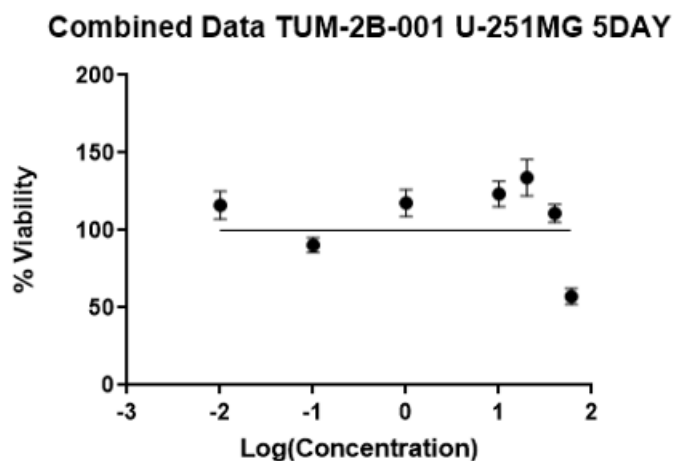
**Figure 2.9** General structure of group 2B compounds whereby the R<sup>1</sup> group consisted of a 1,3-bis(trifluoromethyl)phenyl substituent and the R<sup>2</sup> group consisted of a heterocyclic ring.

The results of the cell viability screen are shown on Table 2-6 and the dose-response curve generated is in

**Figure 2.10.** No IC<sub>50</sub> value was generated for this compound as it did not promote any cell death in the assay, where the concentration of compound used was (60-0.01)  $\mu$ M. It was also not possible to generate a slope which can be observed from the high Hill slope value and very wide Hill slope range. This compound is not biologically active against U251-MG cell line.

**Table 2-6 Results of U251-MG screen on Group 2B compounds. U251-MG cell line and the MTT cell viability assay. Cells were analysed 5 days after treatment, N=3. X is denoted where an experimental value was not possible.**

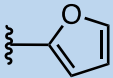
Compound Name	R Group	IC <sub>50</sub> Value ( $\mu$ M)	IC <sub>50</sub> 95% CI ( $\mu$ M)	Hill Slope Value	Hill Slope 95% CI
TUM-2B-001		X	X	X	X

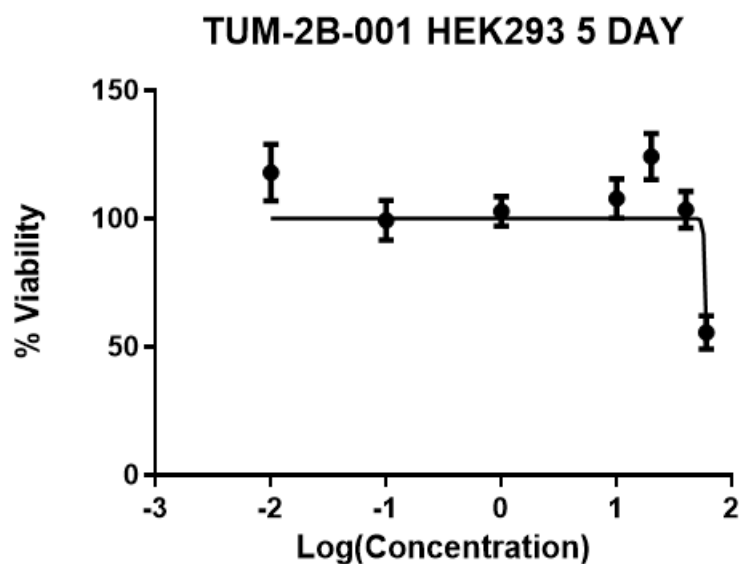


*Figure 2.10 Dose response curve for the compound in group 2B. U251-MG cell line and the MTT cell viability assay. Cells were analysed 5 days after treatment, N=3. Where the X axis denotes the logarithmic concentration of compound, and the Y axis denotes the % cell viability.*

The results of the group 2B compound screen on the HEK293 cell line can be observed in Table 2-7. A dose-response curve was generated for the compound and is shown at Figure 2.11. Upon observation of the dose-response curve, it can be said that this compound does not induce a biological response as there is no observed symmetrical sigmoidal curve whereby the Hill slope and Hill slope range is large and very wide respectively as per Table 2-7. The experimental  $IC_{50}$  value is also  $> 50 \mu M$  and no  $IC_{50}$  range could be determined.

**Table 2-7 Results of group 2B compound screen on HEK293 cell line. Assay Conditions: HEK293 cell line and the MTT cell viability assay. Cells were analysed 5 days after treatment, N=3. X is denoted where an experimental value was not possible.**

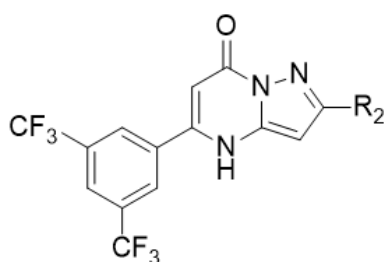
Compound Name	R Group	IC <sub>50</sub> Value (μM)	IC <sub>50</sub> 95% CI (μM)	Hill Slope Value	Hill Slope 95% CI
TUM-2B-001		60.31	X	X	X



**Figure 2.11 Dose response curve for the compound in group 2B. HEK293 cell line and the MTT cell viability assay. Cells were analysed 5 days after treatment, N=3. Where the X axis denotes the logarithmic concentration of compound, and the Y axis denotes the % cell viability.**

#### 2.3.1.4 Group 2C Pyrazolo[1,5- $\alpha$ ]pyrimidinones

The group 2C pyrazolo[1,5- $\alpha$ ]pyrimidinone has a 1,3-bis(trifluoromethyl)phenyl substituent at R<sup>1</sup> and the R<sup>2</sup> substituent consists of an alkyl chain. As observed previously in group 2B, group 2C also consists of one compound and cannot technically be a “group”. However, the compound was placed into a group subset for ease of use when describing the structural changes in the compound. The general structure of the group 2C pyrazolo[1,5- $\alpha$ ]pyrimidinone can be seen in Figure 2.12.



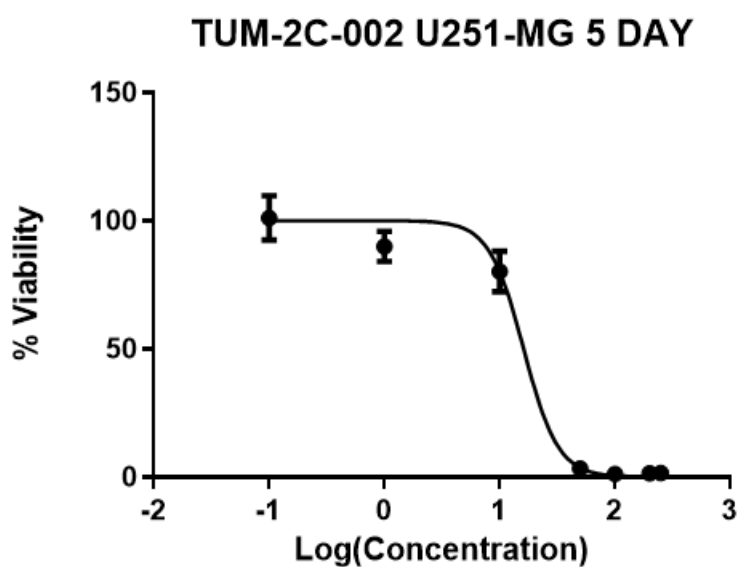
**Figure 2.12** General structure of group 2C compound whereby the R<sup>1</sup> group consisted of a 1,3-bis(trifluoromethyl)phenyl substituent-benzene group and the R<sup>2</sup> group consisted of an alkyl chain.

The results of the cell viability screen are shown in Table 2-8 and the dose-response curve generated is in Figure 2.13. An IC<sub>50</sub> of 16.16  $\mu$ M was calculated, alongside a narrow IC<sub>50</sub> range. A sigmoidal curve can be observed for this compound on Figure 2.13 and a narrow Hill slope range was also generated. It can be suggested from the data outlined in Table 2-8 that this compound elicits a biological response in the U251-MG cell line.



**Table 2-8 Results of U251-MG cell line screen on the group 2C compound. U251-MG cell line and the MTT cell viability assay. Cells were analysed 5 days after treatment, N=3. X is denoted where an experimental value was not possible.**

Compound	R Group	IC <sub>50</sub> Value (uM)	IC <sub>50</sub> 95% CI (uM)	Hill Slope Value	Hill Slope 95% CI
TUM-2C-002	CH <sub>3</sub>	16.16	11.75 to 22.22	-2.908	-4.655 to -1.161

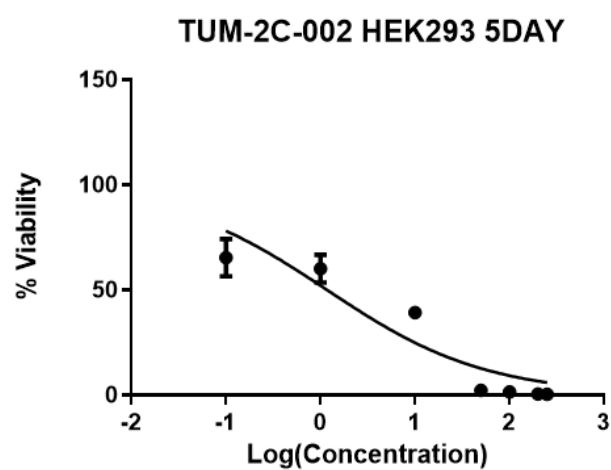


**Figure 2.13 Pooled data dose response curve for the compound in group 2C. U251-MG cell line and the MTT cell viability assay. Cells were analysed 5 days after treatment, N=3. Where the X axis denotes the logarithmic concentration of compound, and the Y axis denotes the % cell viability.**

The results of the cell viability screen for the HEK291 cell line are shown in table 2.8 and the dose-response curve generated by Figure 2.14. An IC<sub>50</sub> of 5.659 µM was calculated, alongside a narrow IC<sub>50</sub> range as per Table 2-9. The Hill slope value obtained is close to the ideal -1.0 value hence the observed sigmoidal curve on Figure 2.14. The Hill slope range is also very narrow as per Table 2-9. It can be said that TUM-2C-002 elicits a biological response on the HEK293 cell line.

***Table 2-9 Results of HEK293 cell line screen on the group 2C compound. HEK293 cell line and the MTT cell viability assay. Cells were analysed 5 days after treatment, N=3. X is denoted where an experimental value was not possible.***

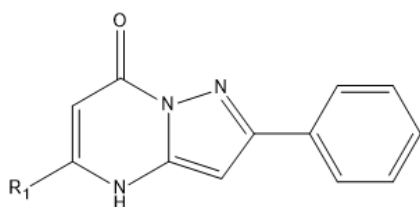
Compound Name	R Group	IC <sub>50</sub> Value (µM)	IC <sub>50</sub> 95% CI (µM)	Hill Slope Value	Hill Slope 95% CI
TUM-2C-002	CH <sub>3</sub>	5.66	3.623 to 8.720	-0.9410	-1.353 to -0.7261



*Figure 2.14 Pooled data dose response curve for the compound in group 2C. Assay Conditions: HEK293 cell line and the MTT cell viability assay. Cells were analysed 5 days after treatment, N=3. Where the X axis denotes the logarithmic concentration of compound, and the Y axis denotes the % cell viability.*

### 2.3.1.5 Group 3 Pyrazolo[1,5- $\alpha$ ]pyrimidinones

The group 3 pyrazolo[1,5- $\alpha$ ]pyrimidinones is such that the  $R^1$  substituent is varied and the  $R^2$  substituent is a phenyl ring. The general structure of the group 3 compounds can be seen in Figure 2.15.

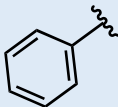


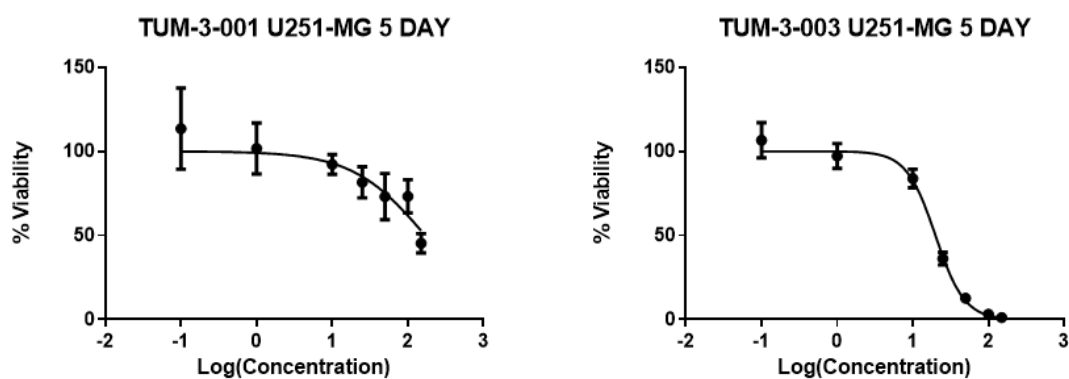
**Figure 2.15** General structure of group 3 compounds whereby the  $R^1$  group is consisted of varied functional groups and the  $R^2$  group is a phenyl ring.

A dose response curve was generated for all the compounds and can be seen in Figure 2.16. The results obtained for the group 3 compounds can be found in

Table 2-10. It can be confirmed that TUM-3-001 has no biological effect in the U251-MG cell line due to the large experimental  $IC_{50}$  value and the observed large  $IC_{50}$  range. Whereas TUM-3-003 does have an observed biological effect in the U251-MG cell line and there is also a narrow  $IC_{50}$  range.

**Table 2-10 Results of U251-MG cell line screen on group 3 compound. U251-MG cell line and the MTT cell viability assay. Cells were analysed 5 days after treatment, N=3. X is denoted where an experimental value was not possible.**

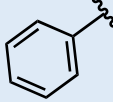
Compound Name	R1 Group	IC <sub>50</sub> Value (μM)	IC <sub>50</sub> 95 % CI (μM)	Hill Slope Value	Hill Slope Value 95 % CI
TUM-3-001	CH <sub>3</sub>	X	62.16 to 462.8	0.4437	-1.834 to 0.023556
TUM-3-003		19.96	16.96 to 23.50	0.3484	-2.979 to -1.546

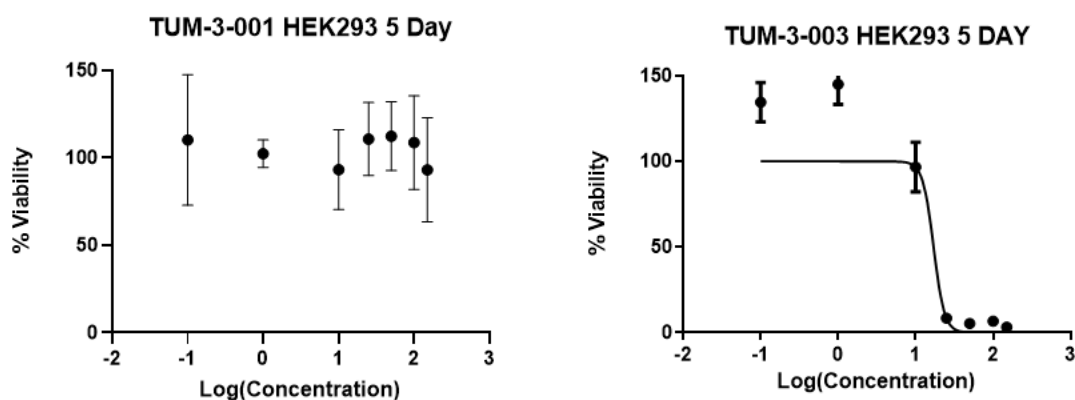


**Figure 2.16 Dose response curves for the compounds in group 3. U251-MG cell line and the MTT cell viability assay. Cells were analysed 5 days after treatment, N=3. Where the X axis denotes the logarithmic concentration of compound and the Y axis denotes % cell viability.**

The results of the cell viability screen for the HEK293 cell line are shown in table 2.11 and the dose-response curve generated by Figure 2.17. It can be observed that TUM-3-001 did not elicit a biological response as no IC<sub>50</sub> value could be generated for the compound. An IC<sub>50</sub> of 17.08 µM was calculated for TUM-3-003, alongside a narrow IC<sub>50</sub> range as per Table 2-11. It can be said that TUM-3-003 elicits a biological effect in the HEK293 cell line.

***Table 2-11 Results of HEK293 cell line screen on group 3 compounds. HEK293 cell line and the MTT cell viability assay. Cells were analysed 5 days after treatment, N=3. X is denoted where an experimental value was not possible.***

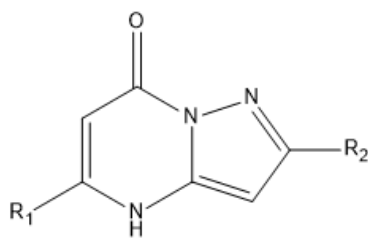
Compound Name	R1 Group	IC <sub>50</sub> Value (µM)	IC <sub>50</sub> 95% CI (µM)	Hill Slope Value	Hill Slope 95% CI
TUM-3-001	CH <sub>3</sub>	X	X	X	X
TUM-3-003		17.08	8.922 to 32.68	4.785	-16.04 to 3.637



**Figure 2.17** Dose response curves for the compounds in group 3. HEK293 cell line and the MTT cell viability assay. Cells were analysed 5 days after treatment,  $N=3$ . Where the  $X$  axis denotes the logarithmic concentration of compound, and the  $Y$  axis denotes the % cell viability.

#### 2.3.1.6 Group 4 Pyrazolo[1,5- $\alpha$ ]pyrimidinones

The group 4 pyrazolo[1,5- $\alpha$ ]pyrimidinones are such that both the  $R^1$  and  $R^2$  substituents are varied. The general structure of the group 4 compounds can be seen in Figure 2.18.

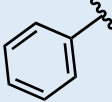


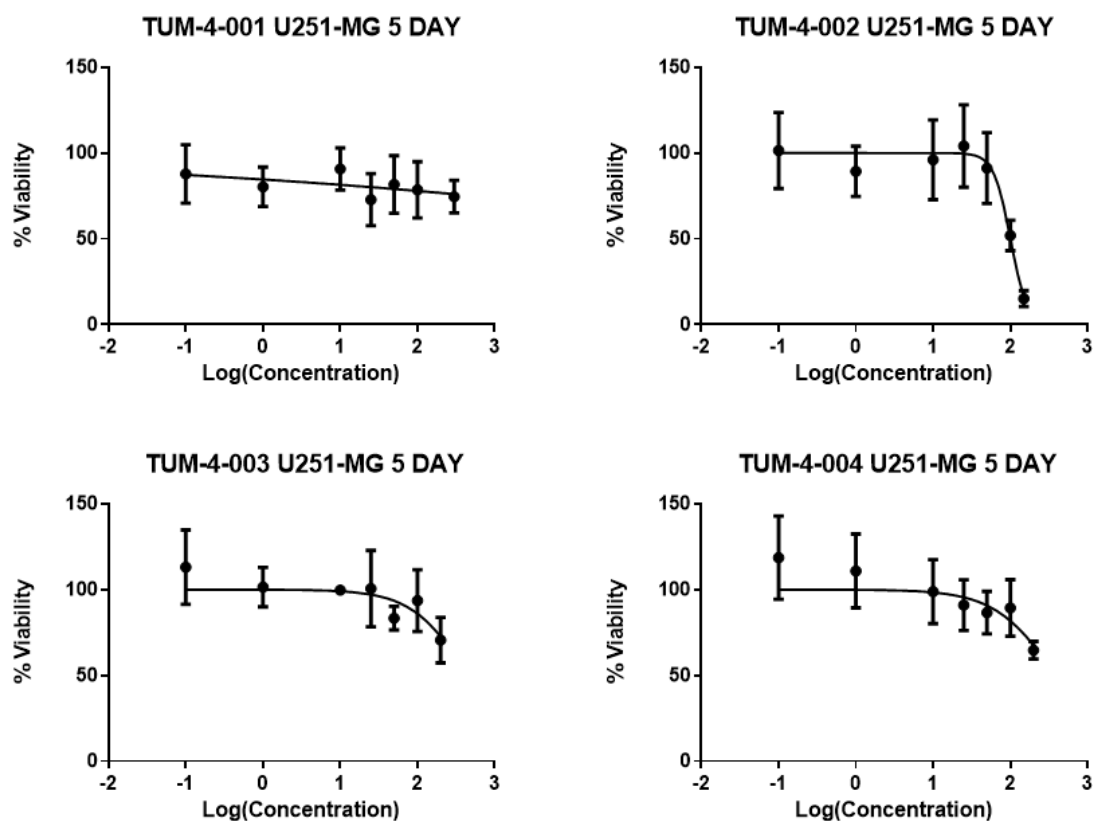
**Figure 2.18** General structure of group 4 compounds whereby the  $R^1$  substituent and the  $R^2$  substituent consists of varied functional groups.



The results of the compound screen can be seen in Table 2-12. A biological response in the U251-MG cell screen is defined as the compounds having an IC<sub>50</sub> value of < 50 µM. A dose response curve was generated for all the compounds and can be seen in Figure 2.19. It can be confirmed that none of the group 4 compounds have any biological effect towards the U251-MG cell line.

**Table 2-12 Results of U251-MG cell line screen on group 4 compounds. U251-MG cell line and the MTT cell viability assay. Cells were analysed 5 days after treatment, N=3. X is denoted where an experimental value was not possible.**

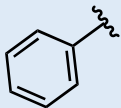
Compound Name	R <sup>1</sup> Group	R <sup>2</sup> Group	IC <sub>50</sub> Value (µM)	IC <sub>50</sub> 95% CI (µM)	Hill Slope Value	Hill Slope 95% CI
TUM-4-001	CH <sub>3</sub>	CH <sub>3</sub>	X	X	0.1375	-0.3836 to 0.1919
TUM-4-002		t-Bu	X	74.46 to 135.5	2.447	-9.113 to 1.131
TUM-4-003	i-Pr	i-Pr	X	38.66 to 5084	-1.218	-3.718 to 1.282
TUM-4-004	Et	i-Pr	X	41.02 to 3606	1.023	-3.257 to 1.026

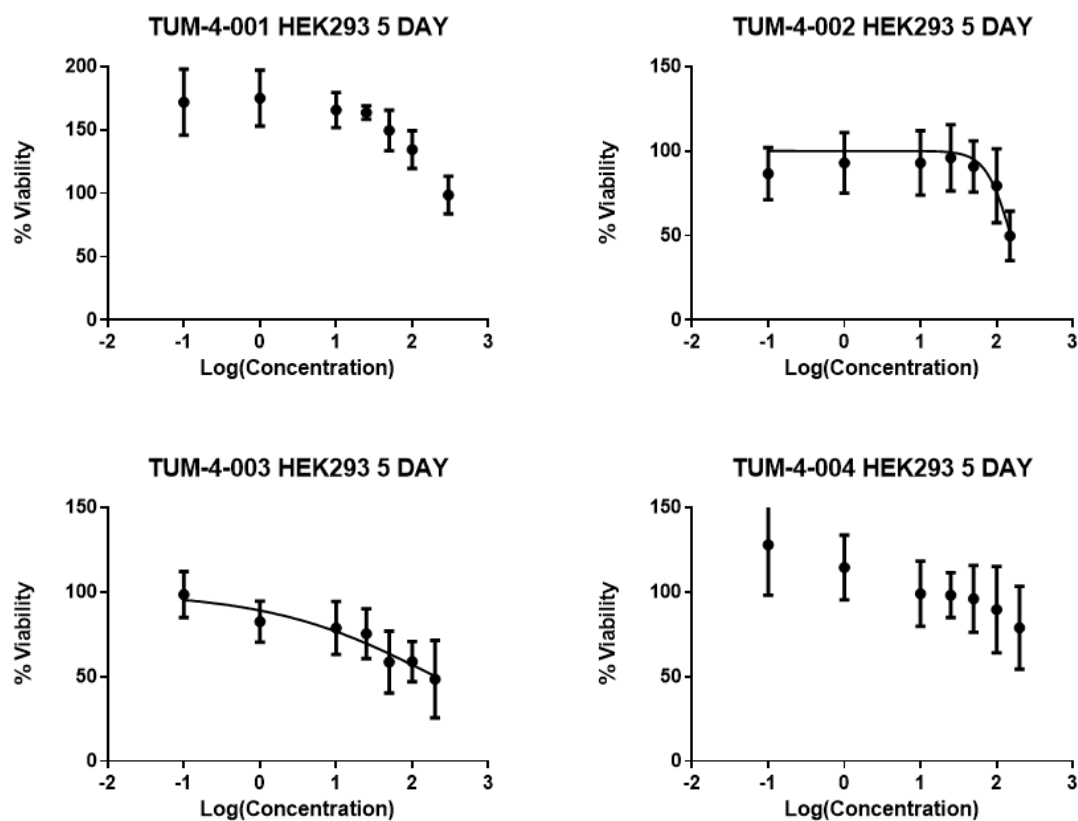


**Figure 2.19** Dose response curves for the compounds in group 4. U251-MG cell line and the MTT cell viability assay. Cells were analysed 5 days after treatment,  $N=3$ . Where the X axis denotes the logarithmic concentration of compound, and the Y axis denotes the % cell viability.

The results of the group 4 compound screen on the HEK293 cell line can be observed in Table 2-13. A dose-response curve was generated for the compound and is shown at Figure 2.20. Upon observation of the dose-response curves, this compound group does not induce a biological response as the experimental  $IC_{50}$  values are also  $> 50 \mu M$  and no  $IC_{50}$  range could be determined for two of the compounds and a large  $IC_{50}$  range was observed for the remaining compounds.

**Table 2-13 Results of HEK293 cell line screen on 4 compounds. HEK293 cell line and the MTT cell viability assay. Cells were analysed 5 days after treatment, N=3. X is denoted where an experimental value was not possible.**

Compound Name	R <sup>1</sup> Group	R <sup>2</sup> Group	IC <sub>50</sub> Value (μM)	IC <sub>50</sub> 95% CI (μM)	Hill Slope Value	Hill Slope 95% CI
TUM-4-001	CH <sub>3</sub>	CH <sub>3</sub>	X	X	X	X
TUM-4-002		t-Bu	X	92.10 to 257.3	2.086	-6.990 to 1.740
TUM-4-003	i-Pr	i-Pr	X	24.90 to 1648	0.2026	-0.8187 to 0.02947
TUM-4-004	Et	i-Pr	X	X	X	X



**Figure 2.20** Dose response curves for the compounds in group 4. Assay Conditions: HEK293 cell line and the MTT cell viability assay. Cells were analysed 5 days after treatment, N=3. Where the X axis denotes the logarithmic concentration of compound and the % cell viability.

### 2.3.2 Comparison of U251-MG and HEK293 Cell Line Results

The evaluation of the pyrazolo[1,5- $\alpha$ ]pyrimidinones was carried out on two cell lines, the U251-MG cell line and the HEK293 cell line. The experimental IC<sub>50</sub> values obtained are summarised and compared as shown in Table 2-14.

An ideal compound is one which is biologically active in the U251-MG cell line and generally biologically inactive or less active in the HEK293 cell line, so that the compounds are selective for the cancerous cell line and do not elicit a response in the non-cancerous cell line. To determine this, statistical analysis was carried out to see whether the experimentally obtained results were statistically significantly different. Statistical analysis was carried out using Prism software, method outlined in section 2.2.6.

The first type of statistical analysis carried out was curve fitting. The null hypothesis was such that if the U251-MG dose-response curve and the HEK293 dose-response curve fitted on one line the results were deemed statistically insignificant. The p value generated would also be  $\geq 0.05$ . Therefore, two separate curves are required for the results to be deemed statistically significant.

The IC<sub>50</sub> ranges for both the U251-MG cell line and HEK293 cell line were also compared to ascertain whether they can be deemed different with statistical significance. The null hypothesis was such that if the compound's IC<sub>50</sub> ranges for both cell lines overlapped then the difference in the results were deemed to be statistically insignificant. If the IC<sub>50</sub> ranges did not overlap, the difference in the results were determined to be statistically significant. The results from this analysis are shown in Table 2-14.

**Table 2-14 Comparison of IC<sub>50</sub> data generated to determine statistical significance. The null hypothesis was such that to be statistically significant the IC<sub>50</sub> values for both cell lines would have two separate curves, the p value generated must also be < 0.05 and both IC<sub>50</sub> ranges must not overlap. The initial compounds which are deemed statistically significant are shaded in blue.**

COMPOUND NAME	U251-MGIC <sub>50</sub> VALUE (μM)	HEK293 IC <sub>50</sub> VALUE (μM)	IC <sub>50</sub> STATISTICALLY DIFFERENT – YES/NO	P VALUE for IC <sub>50</sub>	IC <sub>50</sub> RANGE STATISTICALLY DIFFERENT – YES/NO
TUM-1-002	118.3	444.8	NO	0.1820	NO
TUM-1-003	20.69	9.992	NO	0.3803	NO
TUM-1-004	9.18	6.575	NO	0.2584	NO
TUM-1-005	14.90	7.447	YES	0.0006	YES
TUM-2A-001	6.17	15.47	YES	<0.0001	YES
TUM-2A-003	58.92	68.21	NO	0.4464	NO
TUM-2A-004	29.49	60.34	YES	<0.0001	YES
TUM-2A-005	18.12	51.16	YES	<0.0001	YES

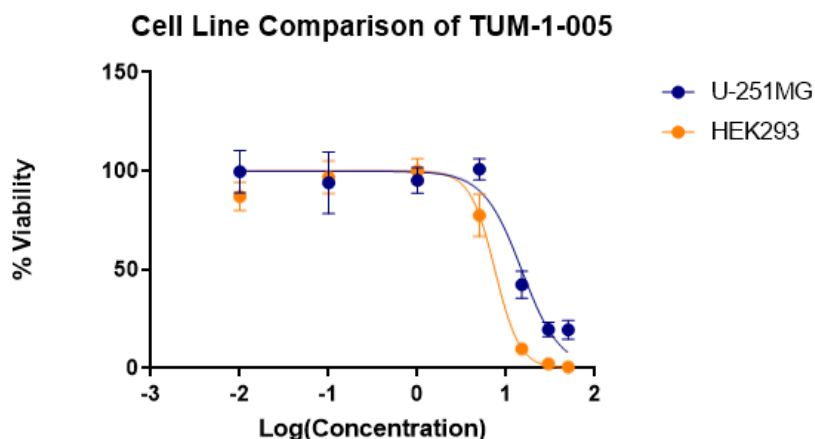
<b>TUM-2A-007</b>	26.75	51.52	YES	<0.0001	YES
<b>TUM-2A-008</b>	29.62	73.79	YES	<0.0001	YES
<b>TUM-2A-010</b>	23.79	28.85	YES	0.0033	NO
<b>TUM-2A-012</b>	21.72	29.77	YES	0.0018	NO
<b>TUM-2B-001</b>	N/A	60.31	NO	N/A	NO
<b>TUM-2C-002</b>	16.16	5.659	YES	<0.0001	YES
<b>TUM-3-001</b>	169.6	N/A	NO	N/A	NO
<b>TUM-3-003</b>	19.96	17.08	NO	0.0810	NO
<b>TUM-4-001</b>	N/A	N/A	NO	N/A	NO
<b>TUM-4-002</b>	100.50	153.9	NO	0.1663	NO
<b>TUM-4-003</b>	443.30	202.6	YES	0.0142	YES
<b>TUM-4-004</b>	384.60	N/A	N/A	N/A	NO

### ***2.3.2.1 Group 1 Pyrazolo[1,5- $\alpha$ ]pyrimidinones***

Upon analysis of the group 1 pyrazolo[1,5- $\alpha$ ]pyrimidinones, the one compound was shown to be statistically significant was TUM-1-005. TUM-2A-003 and TUM-2A-004 did exhibit a biological effect on both cell lines however the results are not statistically significant. Only one compound in this group, TUM-1-002 was considered biologically inactive due to the high experimental IC<sub>50</sub> values obtained.

TUM-1-005 was shown to have a biological effect in both the cancerous and non-cancerous cell lines. The experimental results from the two cell lines are statistically significant as two separate curves are observed and a p value of 0.0006 was calculated, therefore the null hypothesis was rejected. However, the results show that the compound is more selective towards the HEK293 cell line rather than the U251-MG cell line as denoted by the experimental IC<sub>50</sub> values whereby a lower IC<sub>50</sub> value is observed in the HEK293 cell line. It should be noted that the R<sup>1</sup> substituent that was used for the TUM-1-005 compound was a 1,3-bis(trifluoromethyl)phenyl substituent. This R<sup>1</sup> substituent is further explored as part of the group 2 compounds in an effort to improve the compounds selectivity. The cell line comparison for TUM-1-005 is shown in Figure 2.21.

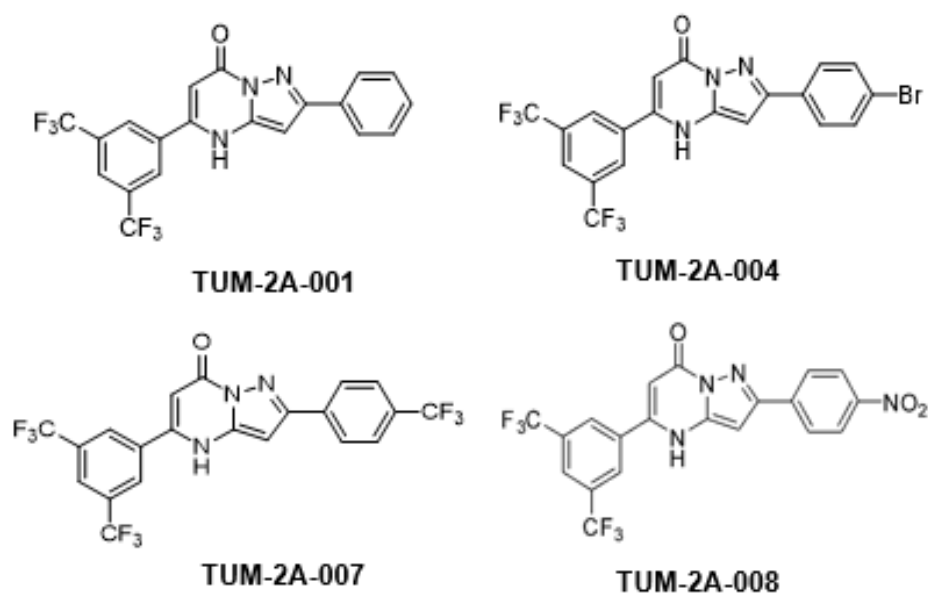




*Figure 2.21 Cell line comparison of TUM-1-005 whereby there is a different curve for each data set. The U251-MG cell line and HEK293 cell line are statistically significant.*

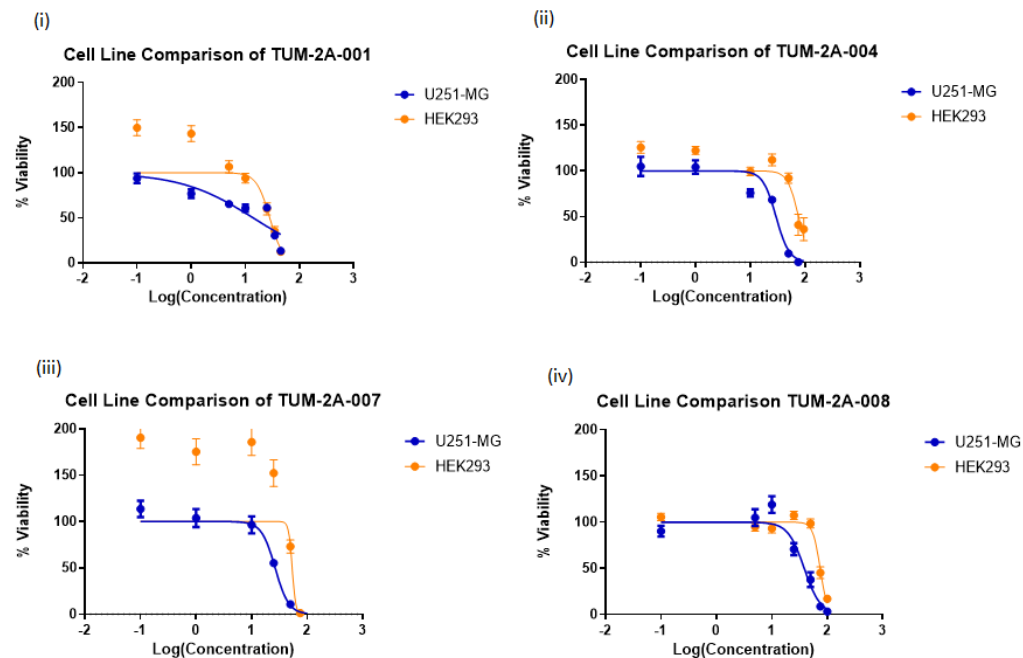
#### 2.3.2.2 Group 2A Pyrazolo[1,5-*a*]pyrimidinones

The IC<sub>50</sub> values were compared between the U251-MG cell line and the HEK293 cell line to ascertain whether they can be deemed different with statistical significance. There were four compounds in group 2A which were statistically significant and have p values  $\leq 0.001$ , these are as follows: TUM-2A-001, TUM-2A-004, TUM-2A-007 and TUM-2A-008. The structures are shown in Figure 2.22. It should be noted that each of the compounds contain the R<sup>1</sup> substituent that was used for the TUM-1-005 compound which was a 1,3-bis(trifluoromethyl)phenyl substituent. The R<sup>2</sup> substituents then comprised of a lipophilic, electron withdrawing group attached to the pyrazole phenyl ring. It can be said that the addition of said substituents has improved the overall selectivity of group 2A compounds.



***Figure 2.22 Structures of compounds: TUM-2A-001, TUM-2A-004, TUM-2A-007 and TUM-2A-008***

The dose-response graphs are shown in Figure 2.23. These compounds are of interest because the IC<sub>50</sub> values obtained for the U251-MG cell line are significantly lower than the values obtained for the HEK293 cell line. It can therefore be said that the compounds have selectivity towards the cancerous cell line over the healthy cell line



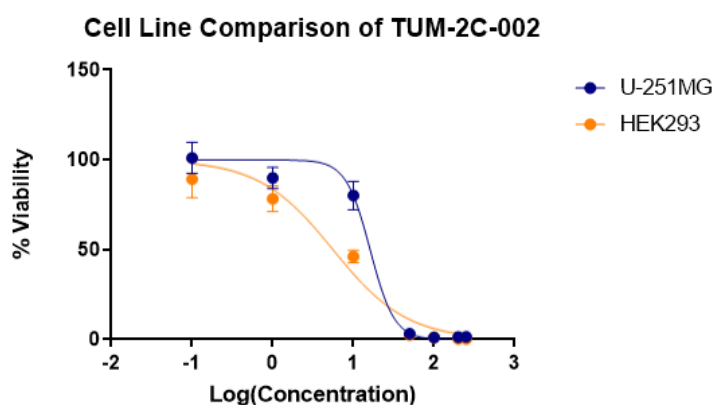
**Figure 2.23** Cell line comparison using both the U251-MG and HEK293 cell line whereby there is a different curve for each data set. The compounds shown are (i) TUM-2A-001, (ii) TUM-2A-004, (iii) TUM-2A-007 and (iv) TUM-2A-008 and are all statistically significant as there are two separate curves generated for both cell lines.

### 2.3.2.3 Group 2B Compounds

There was no statistical difference between the IC<sub>50</sub> values with the U251-MG cell line and the HEK293 cell line for the group 2B compounds as depicted in Table 2-13.

### 2.3.2.4 Group 2C Compounds

The graph depicting the group 2C cell line comparison for the U251-MG cell line and the HEK293 cell line is shown in Figure 2.24. There is a different curve for each data set and the p value obtained was  $\leq 0.005$ . However, despite the IC<sub>50</sub> results being statistically different the IC<sub>50</sub> value generated for the U251-MG cell line is greater than that of the HEK293 cell line and so will not be considered further here.



**Figure 2.24** Cell line comparison of TUM-2C-002 whereby there is a different curve for each data set. The U251-MG cell line and HEK293 cell line are statistically significant.

### 2.3.2.5 Group 3 and 4 Compounds

There was no statistical difference between the IC<sub>50</sub> values with the U251-MG cell line and the HEK293 cell line for the group 3 and 4 compounds as shown in Table 2-13.

### 2.3.3 Statistical Analysis

Statistical analysis was carried out to further determine whether there was a statistically significant difference between the cancerous U251-MG cell line and the non-cancerous HEK293 cell line when they are both treated with the same compound. The statistical test that was chosen to compare the two datasets was the two-way Analysis of Variance (ANOVA) statistical test. The two-way ANOVA test examines the effect of two factors on a dependant variable. In this case, the two factors were the cancerous U251-MG cell line and the non-cancerous HEK293 cell line, and the dependant variable was the compound. This statistical test further reinforces what compounds can be deemed statistically significant and so if the compound is significant across all three statistical tests, it can be referred to as a HIT compound. Table 2-15 depicts a summary of results obtained from the statistical analysis. The P value style used on prism was the GraphPad style whereby the P values are reported as per Table 2-1.

As per the ANOVA analysis shown in Table 2-15, there are five compounds in total which were determined to be statistically significant. From the five compounds, only four of these passed every statistical test and can be referred to as hit compounds and these are: TUM-2A-001, TUM-2A-004, TUM-2A-007 and TUM-2A-008. See Figure 2.22 for chemical structures. The p value for TUM-2A-001, TUM-2A-004 and TUM-2A-008 was denoted by two asterisks (\*\*) whereby this refers to a very significant result as per the statistical analysis outlined in Table 2-1. The most statistically significant compound was TUM-2A-007 whereby it was allocated a p value of four asterisks (\*\*\*\*) and is therefore deemed to be extremely significant. By carrying out three different statistical tests, it further narrows down potential hit compounds more effectively.

**Table 2-15 Summary of results from two-way ANOVA statistical analysis whereby the P values are reported as follows:  $\geq 0.05$  (ns), 0.01 to 0.05 (\*), 0.001 to 0.01 (\*\*), 0.001 to 0.01 (\*\*\*) and  $< 0.0001$  (\*\*\*\*). The initial compounds which are deemed statistically significant are shaded in blue.**

COMPOUND NAME	P VALUE SUMMARY	STATISTICALLY SIGNIFICANT (YES / NO)
TUM-1-002	Ns	No
TUM-1-003	Ns	No
TUM-1-004	Ns	No
TUM-1-005	Ns	No
TUM-2A-001	**	Yes
TUM-2A-003	Ns	No
TUM-2A-004	**	Yes
TUM-2A-005	Ns	No

<b>TUM-2A-007</b>	****	Yes
<b>TUM-2A-008</b>	**	Yes
<b>TUM-2A-010</b>	Ns	No
<b>TUM-2A-012</b>	*	Yes
<b>TUM-2B-001</b>	Ns	No
<b>TUM-2C-002</b>	Ns	No
<b>TUM-3-001</b>	Ns	No
<b>TUM-3-003</b>	Ns	No
<b>TUM-6-001</b>	Ns	No
<b>TUM-6-003</b>	Ns	No
<b>TUM-6-004</b>	Ns	No
<b>TUM-6-005</b>	Ns	No

### 2.3.4 Physicochemical Properties of the Hit Compounds

Properties such as lipophilicity, molecular weight, polar surface area and number of hydrogen bond donors and acceptors are important factors in terms of crossing the BBB. These properties have been calculated for the group 2A hit compounds using Lipinski's rule of five as a guide to determine their probability of crossing the BBB. Lipinski's rule of five has been discussed previously in section 1.5.1. A table showing the compounds as well as their properties is shown on Table 2-16 (Bioinformatics, 2022).

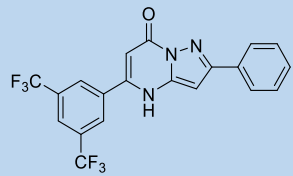
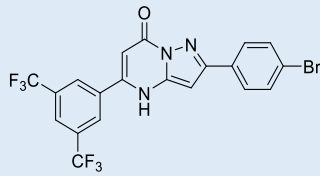
The logP coefficient was used to determine the optimum BBB permeation (1 - 5 range). Lipophilicity as well as permeability plays a role in determining the efficacy of a drug whereby high lipophilicity reduces aqueous solubility and can contribute to excessive volumes of distribution. The molecular weight of a drug targeting the CNS ideally will have a value above 500 Daltons as per the revised Lipinski rules.(Shultz, 2019) Polar surface area is used as a predictor for BBB penetration whereby ideally it has a value below (70 - 90) Å. The hydrogen bonding of a molecule is interlinked with its potential to cross the BBB and so the ideal number of hydrogen bond donors is no more than 1 and the ideal number of hydrogen bond acceptors can be a maximum of 13 as per the revised Lipinski rules (Shultz, 2019). It can be said that the compounds follow the majority of these rules in order to pass the BBB (Structural Properties – The Laboratory for Drug Discovery in Neurodegeneration, 2018).

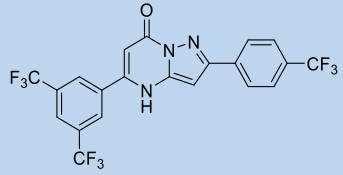
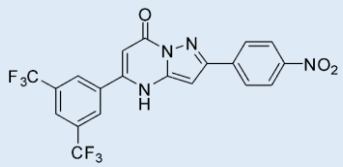
As per Table 2-16, it can be said that all the compounds do not exceed 600 g mol<sup>-1</sup> (Daltons) and have fewer than 5 hydrogen bond donors. The only hit compound which follows every rule in the revised “ideal” physicochemical model is TUM-2A-001. The observed LogP value for TUM-2A-004 one above the ideal number, the same can be said for TUM-2A-007 which also



has too many hydrogen bond acceptors. The polar surface area value for TUM-2A-008 is also just above the threshold. However, the guidelines for physicochemical properties for orally active drugs are constantly evolving and being updated. Each hit compound follows most of these rules and so further work will be done to evaluate the potential mode of action of the compounds and further determine whether they can work *in vivo* by carrying out 3D cell culture analysis.

**Table 2-16 Summary of Statistical Compounds of Interest including calculated molecular properties** (Bioinformatics, 2022).

Compound Name	Structure	Molecular Weight (g mol <sup>-1</sup> )	LogP	# H Bond Donor	# H Bond Acceptor	Polar Surface Area (Å <sup>2</sup> )
TUM-2A-001		423.32	5.30	1	8	50.17
TUM-2A-004		502.21	6.11	1	9	50.17

TUM-2A-007	 <chem>Cc1ccc(cc1)-c2nc3c(nc(=O)[nH]3)c(c2)c4cc(C(F)(F)F)cc4C(F)(F)F</chem>	491.31	6.20	1	14	50.17
TUM-2A-008	 <chem>O=[N+]([O-])c1ccc(cc1)-c2nc3c(nc(=O)[nH]3)c(c2)c4cc(C(F)(F)F)cc4C(F)(F)F</chem>	468.31	5.28	1	10	95.99

## 2.4. Discussion

Work previously carried out by (Conway, Curtin, & Howe, 2016), highlighted in section 1.9.3.4, showed that analogue compounds of TUM-1-005 were shown to have anticancer activity against the cancerous U251-MG cell line. This study began with the group 1 substituted pyrazolo[1,5- $\alpha$ ]pyrimidinones which includes analogue compounds of TUM-1-005 and the TUM-1-005 compound itself, see Figure 1.6. It was found that TUM-1-005 showed good efficacy against the U251-MG cell line with an  $IC_{50}$  value of 14.90  $\mu$ M. A SAR was carried out to discover more effective compounds which are also more selective for the cancerous U251-MG cell line over the non-cancerous HEK293 cell line.

To probe the SAR, the group1 pyrazolo[1,5- $\alpha$ ]pyrimidinones were evaluated. This was done by varying the  $R^1$  substituent and keeping the  $R^2$  isopropyl substituent unchanged. Biological activity was observed in TUM-1-003, TUM-1-004 and TUM-1-005 whereby the  $R^1$  substituent contained either a phenyl ring or a substituted phenyl ring. As previously mentioned, the group one compound which has the best statistical biological activity against the U251-MG cell line was TUM-1-005. This compound contains a 1,3-bis(trifluoromethyl)phenyl group at the  $R^1$  substituent (bis- $CF_3$ ). The bis  $CF_3$  group was replaced with methyl ( $CH_3$ ) groups as observed in TUM-1-004. The  $CH_3$  and  $CF_3$  groups are both lipophilic but differ in their electronic properties, where the  $CH_3$  group has an electron donating effect and the  $CF_3$  group has an electron withdrawing effect thanks to the role of the fluorine atoms. It was found that TUM-1-004 did yield the lowest  $IC_{50}$  value of 9.17  $\mu$ M in the U251-MG cell line screen. Despite this, TUM-1-004 was found to be non-selective for the cancerous U251-MG cell line as it yielded a lower  $IC_{50}$  value of 6.58  $\mu$ M in the non-cancerous HEK293 cell line. It was also deemed to be

statistically insignificant in both initial statistical tests observed in Table 2-14 and the ANOVA statistical analysis observed in Table 2-15.

The bis CF<sub>3</sub> groups observed in TUM-1-005 were replaced with H atoms to produce TUM-1-003 which had an R<sup>1</sup> substituent of an aromatic phenyl ring. This therefore removed the lipophilic and electronic effects that were previously observed in both TUM-1-004 and TUM-1-005. The IC<sub>50</sub> value generated by TUM-1-003 for the cancerous U251-MG cell line was 20.69 μM and the IC<sub>50</sub> value generated in the non-cancerous HEK293 cell line was 9.99 μM. It can therefore be said that TUM-1-003 is non-selective for the cancerous U251-MG cell line. Further to this, it was also deemed to be statistically insignificant in both initial statistical tests observed in Table 2-14 and the ANOVA statistical analysis observed in Table 2-15. The last compound that was screened as part of group 1 was TUM-1-002 whereby the R<sup>1</sup> substituent was a CH<sub>3</sub> group and so the phenyl ring was removed completely as observed in the previous compounds and replaced with a small lipophilic group. Both IC<sub>50</sub> values generated for this compound were much higher whereby the value for the cancerous cell line was 118.30 μM and the non-cancerous cell line was 444.80 μM, both denoted as X. From this screen it was determined that by removing the phenyl ring at the R<sup>1</sup> substituent, the biological activity and selectivity observed in the compounds decreased. It was found that the R<sup>1</sup> substituent needed to be lipophilic and electron withdrawing in nature as shown in TUM-1-005 for there to be biological activity and selectivity observed. It should be noted that while TUM-1-005 has been determined to be statistically significant as per Table 2-14 and the ANOVA statistical analysis observed in Table 2-15, the IC<sub>50</sub> value generated on the non-cancerous cell line was 7.45 μM. TUM-1-005 is therefore non-selective to the cancerous U251-MG cell line.

From this, the group 2 compounds were designed whereby the R<sup>1</sup> substituent was a bis-CF<sub>3</sub> phenyl group and the R<sup>2</sup> substituent was varied to determine if it was possible to maintain or increase efficacy and to improve the selectivity for the cancerous U251-MG cell line over the non-cancerous HEK293 cell line. Group 2 was split into three subgroups, namely 2A, 2B and 2C. In group 2A, the R<sup>2</sup> substituent used replaced the isopropyl substituent observed in group 1 with a series of substituted phenyl rings.

Group 2A consisted of 8 compounds in total. There was one compound, TUM-2A-003 which did not elicit any biological activity on the cancerous and non-cancerous cell lines. TUM-2A-003 contained an R<sup>2</sup> group which consisted of a substituted phenyl ring with a *para*-fluoro substituent. The remaining 7 compounds in group 2A all elicited biological activity whereby they were selective for the cancerous U251-MG cell line over the non-cancerous HEK293 cell line. The initial statistical tests that were carried out through the method of curve fitting outlined five compounds which were deemed to be statistically significant as per Table 2-14. ANOVA statistical analysis was then carried out as per Table 2-15 whereby each compound must be deemed statistically significant in all three tests to be deemed a hit compound. From this, four hit compounds were determined: TUM-2A-001, TUM-2A-004, TUM-2A-007 and TUM-2A-008. The most statistically significant compound was found to be TUM-2A-007 whereby it had an extremely significant p value denoted by \*\*\*\*. TUM-2A-001, TUM-2A-004 and TUM-2A-008 were determined to be equally very statistically significant with a p value denoted by \*\* as shown in Table 2-15. Each of the hit compounds contained R<sup>2</sup> substituents which were lipophilic and electron withdrawing in nature except for TUM-2A-008 which contained a strong electron withdrawing group but was not lipophilic.

Group 2B replaced the isopropyl substituent with a heterocycle, in this case a furan. It was found that no biological activity was observed in either cell line as per Table 2-14. Group 2C replaced the isopropyl group with alkyl chains. This allowed us to determine whether chain length had an effect on efficacy and selectivity in the cancerous U251-MG cell line. It was found that this compound was not selective for the cancerous cell line whereby the  $IC_{50}$  value obtained was 16.16  $\mu$ M and the  $IC_{50}$  value obtained for the non-cancerous cell line was much lower at 5.66  $\mu$ M. The results were also deemed to be statistically insignificant in the ANOVA analysis as per Table 2-15.

It was determined that TUM-2A-001 showed good efficacy and selectivity with an unsubstituted phenyl ring at the  $R^2$  substituent. From this, group 3 was established which consisted of TUM-3-001 and TUM-3-003. TUM-3-001 revisited having a  $CH_3$  group in the  $R^1$  position and TUM-3-003 contained an unsubstituted phenyl ring in the  $R^1$  position. It was determined that TUM-3-001 was biologically inactive in both cell lines as shown in Table 2-14 and so the compound was ruled out from future work. TUM-3-003 did yield a low  $IC_{50}$  value of 19.96  $\mu$ M in the cancerous U251-MG cell line however the  $IC_{50}$  value obtained in the non-cancerous cell line was lower at 17.08  $\mu$ M. The compound is therefore not selective towards the cancerous cell line. It was determined from this group that no hit compounds were found however to see an increase in biological activity, phenyl rings are necessary at both the  $R^1$  and  $R^2$  substituents.

Group 4 was established primarily to confirm that by removing phenyl rings at both the  $R^1$  and  $R^2$  substituents or just at one substituent, biological activity decreased. The use of small lipophilic groups such as  $CH_3$  were also used to depict a lack of biological activity and

selectivity towards the cancerous U251-MG cell line. There were no hit compounds determined in group 4 as shown in Table 2-14 as predicted.

It can be said that out of a total of 20 screened analogue compounds, four were determined to be hit compounds whereby they all belong to the 2A group. From this, their physicochemical properties were examined and determined that they have the potential to cross the blood-brain barrier. Further studies will be carried out as part of Chapter 3 where analogues of these hit compounds will be synthesised to determine whether selectivity can be improved and whether new hit compounds can be determined.

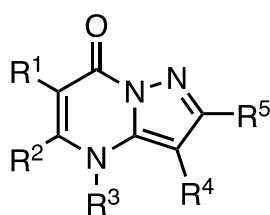


### **3. SYNTHESIS OF PYRAZOLO[1,5- $\alpha$ ]PYRIMIDINONE COMPOUNDS & *IN VITRO* EVALUATION AGAINST GBM**

### 3.1. Introduction

#### 3.1.1 Pyrazolopyrimidinones

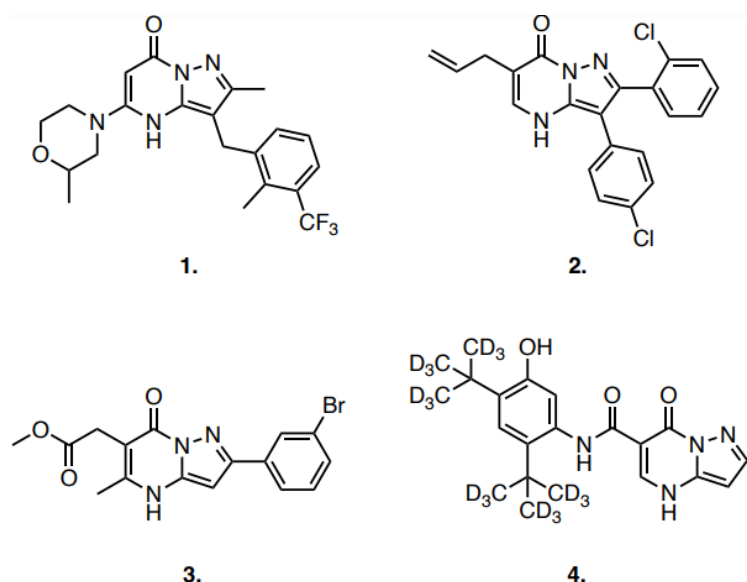
Pyrazolopyrimidinones play a role as a core scaffold in many bioactive pharmaceutical compounds. Pyrazolo[1,5- $\alpha$ ]pyrimidinones are comprised of two nitrogen containing heterocycles, a pyrazole ring fused to a pyrimidinone ring, and allows for substitution at several sites as seen in Figure 3.1 (Kelada *et al.*, 2018).



**Figure 3.1** General structure of a pyrazolopyrimidinone (Kelada *et al.*, 2018)

Substituted pyrazolo[1,5- $\alpha$ ]pyrimidinone derivatives have been used in the treatment of illnesses such as cancer, obesity, cystic fibrosis and viral infections. The structures of some bioactive pharmaceutical compounds can be seen in Figure 3.2 whereby each compound has the same core scaffold as observed in Figure 3.1 (Kelada *et al.*, 2018). Each of the aforementioned structures are covered under a patent and so there is very little to no information provided. Compound 1 is currently covered under patent by GlaxoSmithKline (identifier WO-2010120854-A1). It is stated under the patent that it is an inhibitor of pyruvate dehydrogenase kinase 1 (PDK1) and can be used in the treatment of disorders such as leukaemia and cancers of the breast, colon and lung (GlaxoSmithKline, 2015). Compound 2 is currently covered under patent by Pfizer to be used as an anti-obesity drug. As per the patent ID (US 20040157838 A1) the compound is used as a cannabinoid receptor ligand, in particular

CB1 receptor antagonists. The compound is therefore being used to treat conditions modulated by cannabinoid receptor antagonists (Pfizer, 2004). Compound 3 refers to a pyrazolopyrimidinone compound used to treat Human Immunodeficiency Virus (HIV) infection. The compound is currently protected via a patent (identifier US 9932356). (VIIV Healthcare, 2018) Compound 4 is a pyrazolopyrimidinone analogue of a cystic fibrosis drug, CTP656 which was bought by Vertex Pharmaceuticals and is covered under the same patent. This drug is a deuterated version of Vertex's own compound which is sold under the brand name Kalydeco. It is currently undergoing phase II clinical trials (identifier NCT02971839) (ClinicalTrials.gov, 2020).

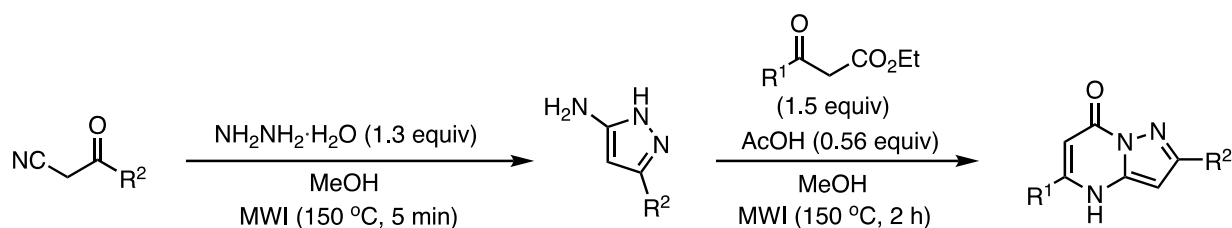


**Figure 3.2 Bioactive pyrazolo[1,5-a]pyrimidinones. 1. GSK anticancer drug. 2. Pfizer anti-obesity Drug. 3. BMS HIV intermediate. 4. Vertex cystic fibrosis regulator. (Kelada et al. 2018)**

### 3.1.2 Pyrazolopyrimidinones and Microwave Chemistry

A number of synthetic methods have been developed for the generation of pyrazolopyrimidinones with the majority of methods employing a two-step process and heating to reflux (Abdel-Jalil et al., 2005). The first step involves the formation of the 5-aminopyrazole. Typical methods reported for the synthesis of 5-aminopyrazoles involve the conventional heating of the appropriate  $\beta$ -ketonitrile in the presence of hydrazine. The second step of the synthesis involves reacting the 5-aminopyrazole with the appropriate  $\beta$ -ketoester and acetic acid under heated conditions (Kelada et al., 2018).

A simple one-pot method for the microwave assisted synthesis of substituted pyrazolo[1,5- $\alpha$ ]pyrimidinones was established by the Stephens research group in Maynooth University (Kelada et al., 2018). The conditions for the synthesis were established such that a solution of the  $\beta$ -ketonitrile in methanol was treated with hydrazine and heated to 150 °C under microwave irradiation for 5 minutes. The  $\beta$ -ketoester and acetic acid were then added to the pot and the reaction was heated to 150 °C under microwave irradiation for a further 2 hours. A reaction scheme for the general one-pot method is shown in Figure 3.3 (Kelada *et al.*, 2018). The traditional synthesis involves two 18 h reflux steps to produce the final substituted pyrazolo[1,5- $\alpha$ ]pyrimidinone product. It was shown by (Kelada et al., 2018) that the one-pot method also results in higher yields whereby a target pyrazolo[1,5- $\alpha$ ]pyrimidinone compound was isolated with an overall yield of 52 % whereby the same compound produced using reflux synthesis was isolated with an overall yield of 25 %.



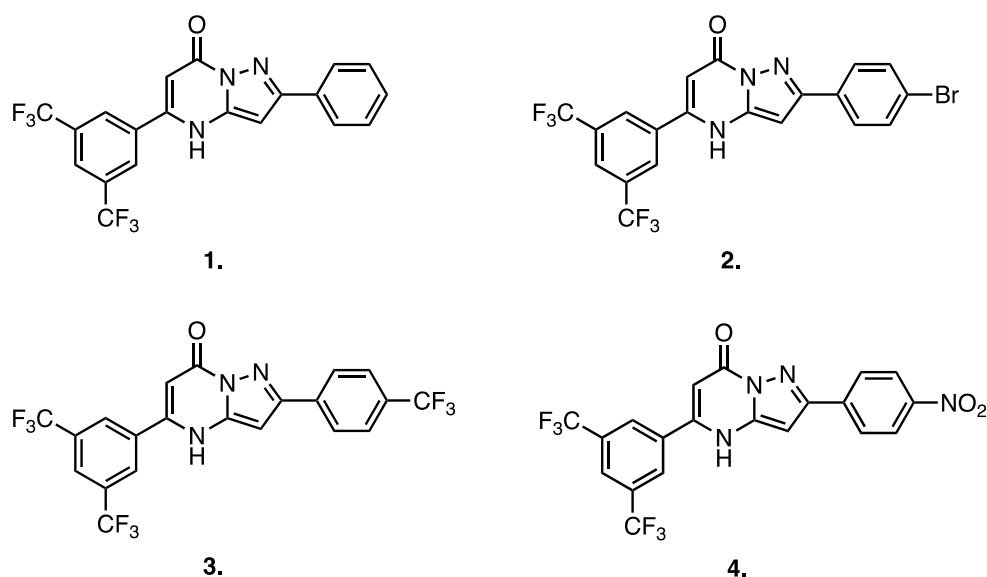
**Figure 3.3** *General one-pot method for the formation of pyrazolo[1,5-a]pyrimidinones (Kelada, 2018)*

### 3.1.3 Improving Biological Activity

In the absence of information on target structures, classic medicinal chemistry methods are usually applied whereby SARs are explored to reveal and assign pharmacophores which guide in the design of novel compounds (Guo, 2017). The term analogue has always been used to describe structural and functional similarities. When this term is applied to drugs, the term analogue implies that the analogue of the existing drug molecule shares structural and pharmacological similarities with the original compound (Ghorab et al., 2016). There are three types of analogue compounds. The first type is referred to as a direct analogue and so the analogues possess both chemical and pharmacological similarities. The second analogue type is a structural analogue whereby they possess structural similarities only. The third analogue type is referred to as a functional analogue whereby these are chemically different compounds which display structural similarities only (Ghorab et al., 2016).

An example of modifying an existing drug and examining its analogues for biological activity can be seen in the anticancer drug Paclitaxel. This drug is used to treat various types of cancer such as ovarian and breast cancer. Two analogues of this drug, Docetaxel and Cabazitaxel are also used as chemotherapeutic agents which are used in the treatment of stomach and prostate cancer as well as others (Guo, 2017). The generation and optimisation of active compounds plays a central role in medicinal chemistry. Hit to lead compound optimisation requires producing a series of structural analogues used to explore the SAR, to improve compound potency and to identify molecular regions most important for specific ligand-target interactions (Yoshimori & Bajorath, 2022).

The compounds synthesised as part of this chapter include the four hit compounds determined as part of Chapter 2 which are TUM-2A-001, TUM-2A-004, TUM-2A-007 and TUM-2A-008 as well as five designed analogues of these hit compounds: TUM-2A-013, TUM-2A-014, TUM-2A-015, TUM-2A-016 and TUM-2A-017. Each of the compounds synthesised contain the same core scaffold and belong to the 2A group whereby the R<sup>1</sup> substituent was a 1,3-bis(trifluoromethyl)phenyl group and the R<sup>2</sup> substituent group varied. The R<sup>2</sup> substituents that were found to be the most effective were those that were found to be electron withdrawing and lipophilic in nature except for TUM-2A-008 which contained a strong electron withdrawing group but was not lipophilic. The synthesised compounds are shown in Figure 3.4.



**Figure 3.4** *Hit compounds whereby the core scaffold and R1 substituent remain the same and the R2 substituent varies. 1. TUM-2A-001 2. TUM-2A-004 3. TUM-2A-007 4. TUM-2A-008*

Analogues of the hit compounds were then synthesised whereby the R<sup>2</sup> *para* substituent was changed to an *ortho* or a *meta* position. The analogues were synthesised to determine whether the structural changes in the compounds would increase or decrease their biological activity. The selectivity was also examined to determine whether the analogue compounds were selective for a cancerous U251-MG cell line over a non-cancerous HEK293 cell line.

A study was carried out by (Olender et al., 2018) whereby medicines containing a nitro or halogen group were modified to determine the efficacy of medicines, specifically benzodiazepine and how it can affect its pharmacology. An increase in the pharmacological effect of benzodiazepines was observed when the halogen group (Cl, Br) was modified whereby the substituent was moved to the *ortho* substituent of the phenyl group (Olender et al., 2018). The presence of the nitro group in benzodiazepine was also shown to enhance the therapeutic action of the drug whereby it is in the *para* position on the phenyl ring. The nitro

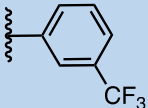
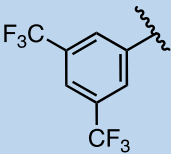
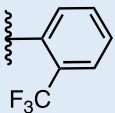
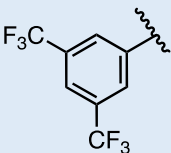
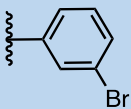
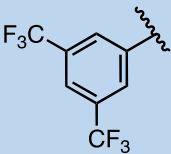
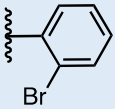
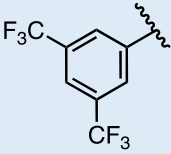
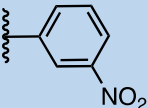
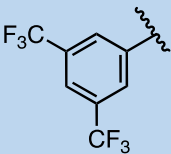
group is a chemical functional group containing two oxygen atoms bound to a nitrogen atom which connects the group to the rest of the molecule, as shown in TUM-2A-008. The nitro group has a strong electron withdrawing effect due to the resonance effect that causes the “pull” of electrons from the cyclic aromatic structure. It can also be said that the presence of the nitro group can also be responsible for the toxicity of some drugs, this is observed in chemotherapy drugs such as Nitroglycerin in the treatment of non-small cell lung cancer (Noriega et al., 2022)(Sukhatme et al., 2015).

The compounds synthesised as part of this chapter are such that the *para*-trifluoromethyl group observed in TUM-2A-007 will be moved to the *meta* and *ortho* positions and will be referred to as TUM-2A-013 and TUM-2A-014 respectively. The *para*-bromophenyl group observed in TUM-2A-004 will also be moved to the *meta* and *ortho* positions. The new compounds will be named TUM-2A-015 and TUM-2A-016 respectively. The *para*-nitrophenyl group observed in TUM-2A-008 will be moved to the *meta* position and will be referred to as TUM-2A-017. Table 3.1 highlights the analogue compounds which will be synthesised as part of this chapter. The analogue compounds will then be evaluated to determine whether there has been an increase or decrease in their biological activity. They will also be evaluated to determine whether they are selective for the cancerous U251-MG cell line over the non-cancerous HEK293 cell line. Potential hit compounds will also be identified from the biological evaluation of the analogue compounds.

It should be noted that as this is a medicinal chemistry project, the structure of Chapter 3 differs from Chapter 2 and Chapter 4. This is because Chapter 3 is a primarily chemistry-based chapter and so takes on the structure of a chemistry thesis.



**Table 3-1 Analogue compounds to be synthesised; R2 substituent remains unchanged where the only observed change in structure is observed in the R1 substituent.**

Compound	R1 Substituent	R2 Substituent
TUM-2A-013		
TUM-2A-014		
TUM-2A-015		
TUM-2A-016		
TUM-2A-017		

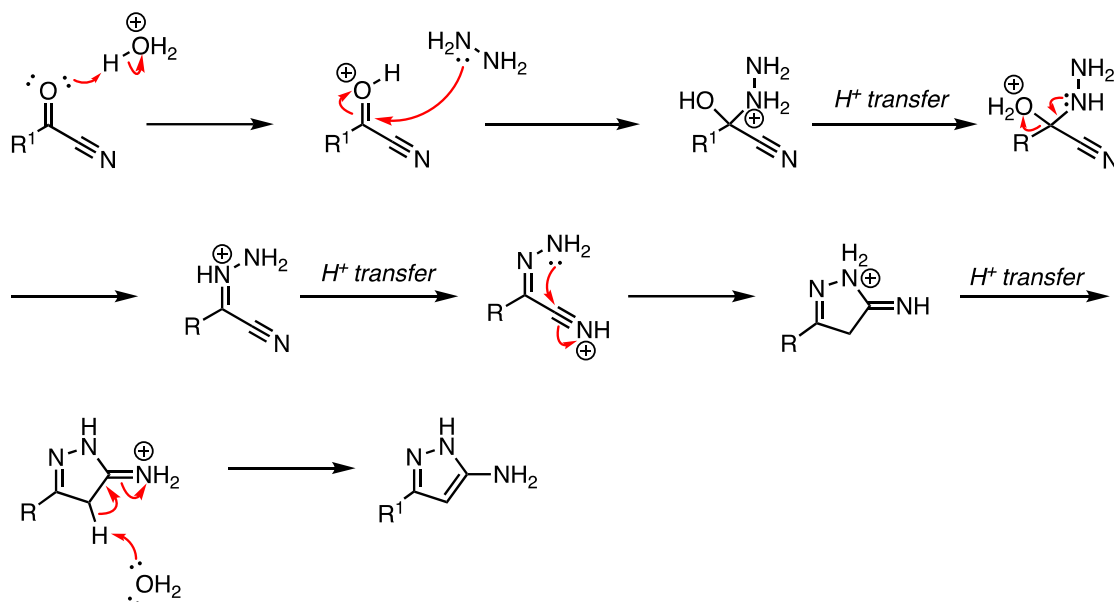
## 3.2. Results and Discussion

### 3.2.1 5-Aminopyrazoles

Pyrazole derivatives are a special class of *N*-heterocyclic compounds consisting of a heteroaromatic five membered ring with two adjacent nitrogen atoms where there is one pyrrole type (proton donor) and one pyridine type (proton acceptor). Pyrazoles can act as weak acids or bases where their strength is dependent on the nature of their substituent groups. Some fused pyrazoles have demonstrated different biological activities in many areas such as anticancer, anti-inflammatory and antibacterial activities. Many drugs which contain a pyrazole core have been reported such as the analgesic antipyrine and the non-steroid anti-inflammatory drugs (NSAIDs) Lonazolac and Rimonabant. Therefore, synthesising pyrazole derivatives efficiently and selectively is an important area of organic chemistry (Jasinski et al., 2022).

This chapter initially discusses the formation of the 5-aminopyrazole intermediate product. The classic synthesis for pyrazoles involves harsh reaction conditions, high temperatures, organic solvents which are often toxic and volatile and extensive reaction times. This long reaction time has significant energy waste and increases the final cost of the synthesis. As a result of this, protocols have been developed to improve the efficiency, cost, and time of this synthesis. One protocol that was developed was the use of microwave (MW) assisted synthesis whereby it reduces the overall reaction time, solvent quantity required and reaction purification needed (Jasinski et al., 2022) (Kelada et al., 2018).

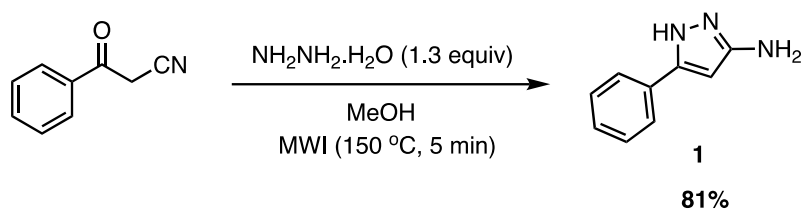
The majority of the 5-aminopyrazoles used as part of the synthesis were obtained commercially. Only one 5-aminopyrazole was synthesised, 3-phenyl-1H-pyrazol-5-amine, which was the TUM-2A-001 intermediate. This compound will be referred to as 5-aminopyrazole **1** throughout. A proposed mechanism for the synthesis of 5-aminopyrazoles is shown in Figure 3.5. Here the carbonyl oxygen of the ketonitrile is protonated followed by nucleophilic attack of hydrazine. A sequence of proton transfers, loss of water, and an intramolecular cyclisation occurs to form the aminopyrazole. The intramolecular cyclisation can be described as a favoured 5-exo-dig cyclisation according to Baldwin's rules.



**Figure 3.5** Proposed mechanism for the formation of 5-aminopyrazoles.

### 3.2.2 3.3.1.1 Synthesis of 5-Aminopyrazole 1

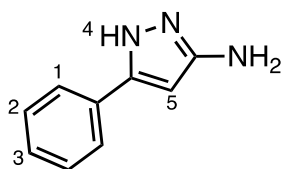
The  $\beta$ -ketonitrile, benzoylacetonitrile in this case, was treated with hydrazine monohydrate to generate the 5-aminopyrazole 1 in an 81% yield, see figure 3.6. Structural characterisation for 5-aminopyrazole 1 was carried out using  $^1\text{H}$  NMR spectroscopy, LC-MS, and FTIR analysis.



**Figure 3.6 Synthesis of 5-aminopyrazole 1.**

### 3.2.3 Structural Characterisation of 5-Aminopyrazole 1

The structure of the 5-aminopyrazole **1** is shown in **Error! Reference source not found.** with the protons numbered for structural characterisation.

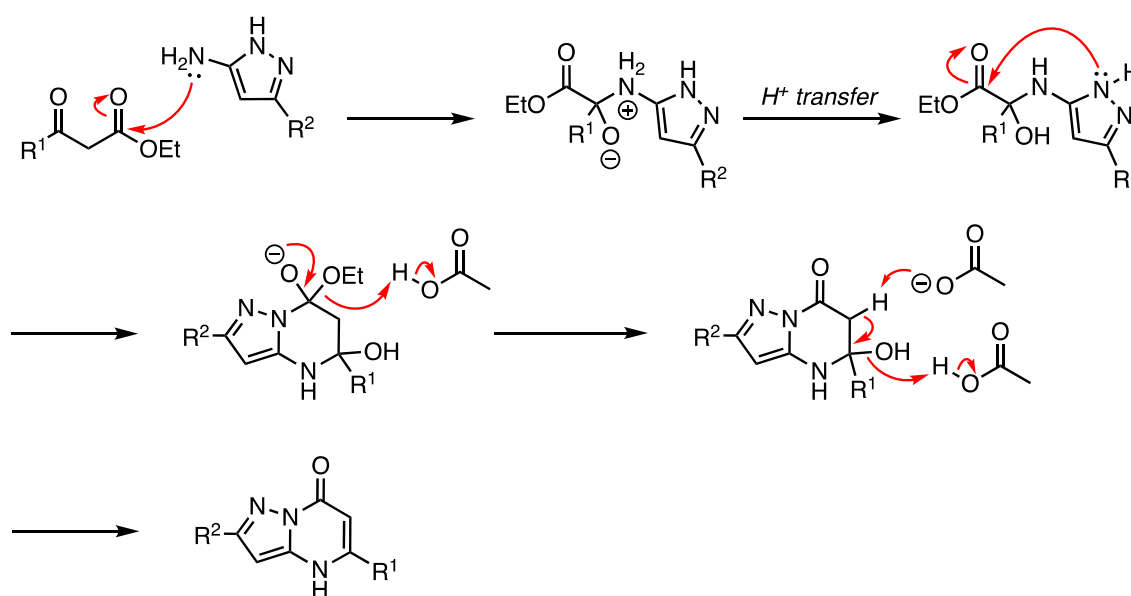


**Figure 3.7** Structure of 5-aminopyrazole **1** with protons numbered for structural characterisation.

The phenyl ring protons of 5-aminopyrazole **1** appear as three signals in the  $^1\text{H}$  NMR spectrum, a multiplet integrating for 2H at 7.64 ppm, a multiplet integrating for 2H at 7.37 ppm, and a multiplet integrating for 1H at 7.26 ppm. The pyrazole proton occurs as a singlet at 5.76 ppm. LCMS was carried out on 5-aminopyrazole **1** and showed the isolated material was 99 % pure by LC and a protonated mass obtained for  $\text{C}_9\text{H}_{10}\text{N}_3$ ,  $[\text{M} + \text{H}]^+$  at 160.3 m/z. The IR spectrum for 5-aminopyrazole **1** showed absorption band at  $3380\text{ cm}^{-1}$  and  $1569\text{ cm}^{-1}$  and are typically of those generated by an NH bond. The absorption band at  $3060\text{ cm}^{-1}$  can be assigned to the aromatic CHs. The  $^1\text{H}$  NMR spectrum, IR spectrum, and LCMS for 5-aminopyrazole **1** can be found in the Appendix A1.

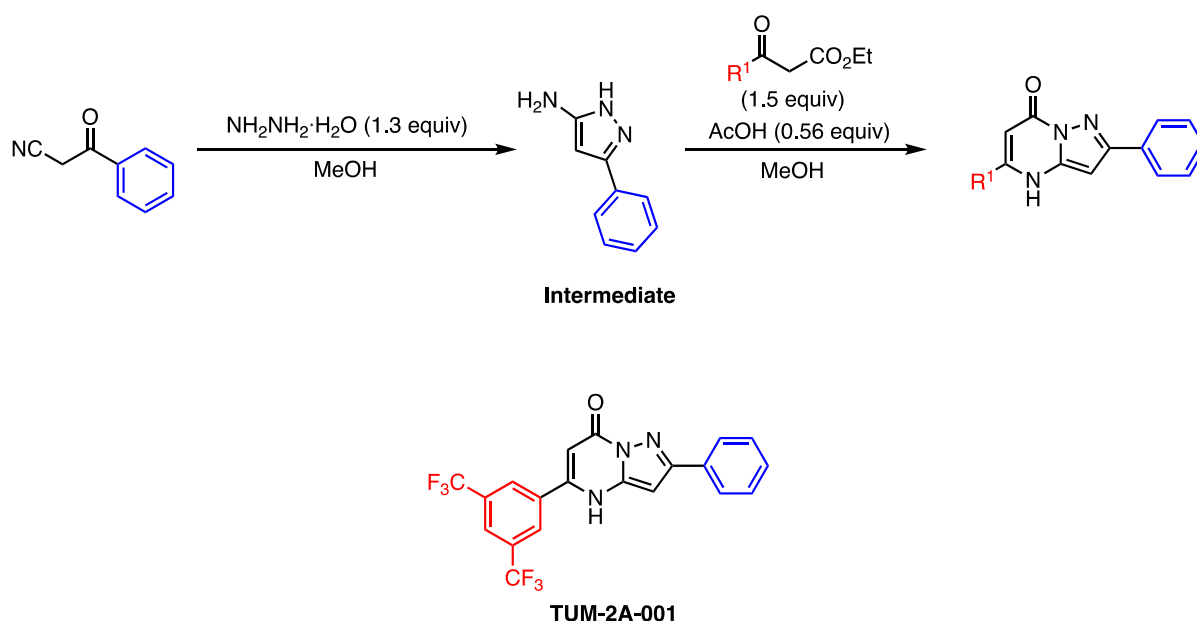
### 3.2.4 Synthesis of Pyrazolo[1,5- $\alpha$ ]pyrimidinones

A proposed mechanism for the synthesis of the pyrazolo[1,5- $\alpha$ ]pyrimidinones is shown in Figure 3.8. Here, nucleophilic attack by the primary amino group of the 5-aminopyrazole at the keto carbonyl group occurs. This is followed by a sequence of proton transfers, an intramolecular cyclisation, and loss of ethanol to give the pyrazolo[1,5- $\alpha$ ]pyrimidinone. The intramolecular cyclisation can be described as a favoured 6-exo-trig cyclisation according to Baldwin's rules.



**Figure 3.8** Proposed mechanism for the formation of pyrazolopyrimidinones.

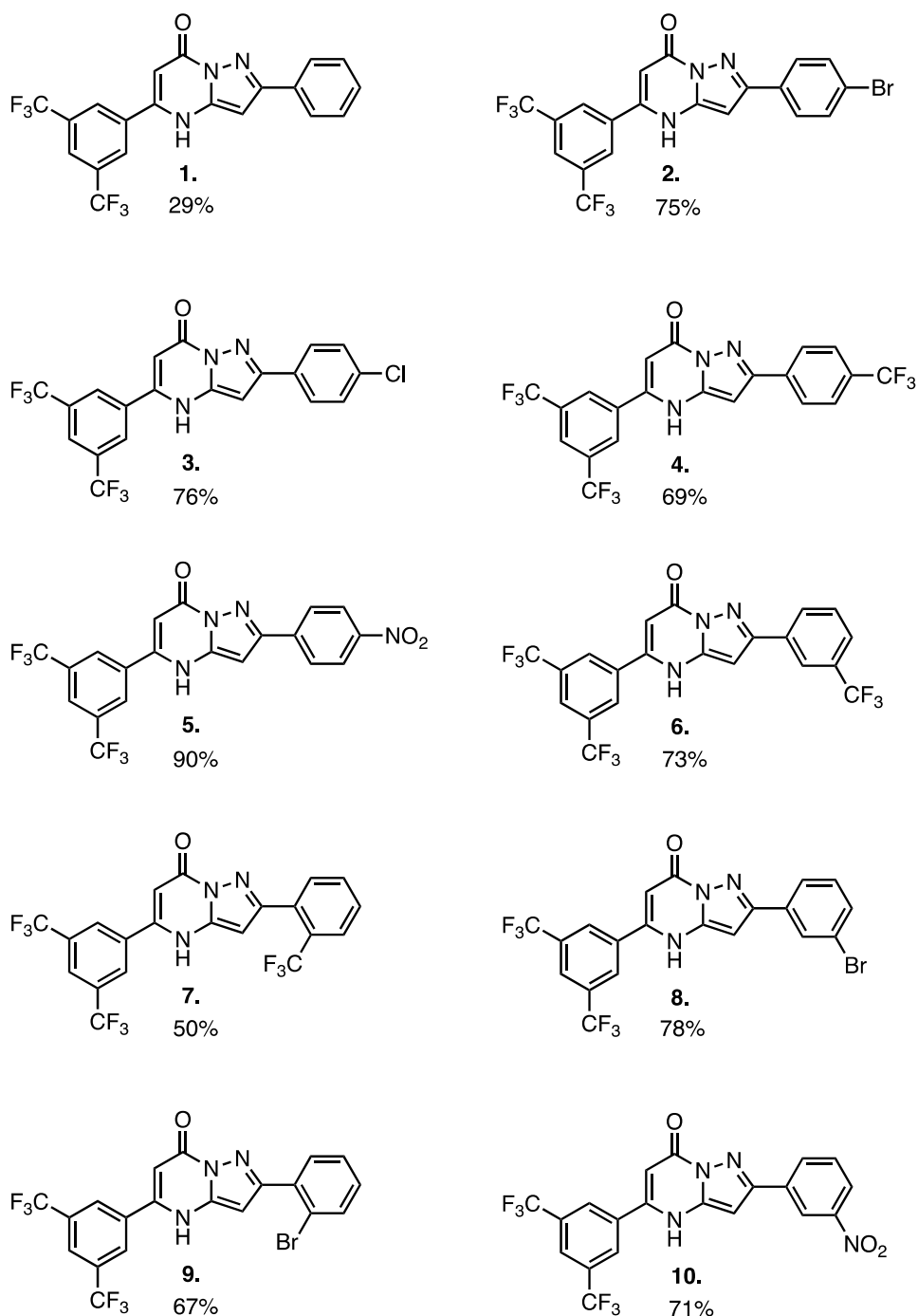
The method employed was based on the one-pot method developed by the Stephens research group. The times and temperatures used in the microwave synthesis are identical to those used in this work (Kelada *et al.*, 2018). The first step in the synthesis was to generate a pure 5-aminopyrazole product with a good yield. The required  $\beta$ -ketonitrile was reacted with excess hydrazine monohydrate in the presence of methanol. The excess hydrazine monohydrate (1.3 equivalents) was used to ensure the starting material was completely used up in the reaction. The desired 5-aminopyrazole was then isolated and purified using column chromatography in an 82 % yield. This approach was used when the 5-aminopyrazole was not commercially available. The second step in the synthesis involved generating the pyrazolo[1,5- $\alpha$ ]pyrimidinone. Figure 3.9 outlines the synthetic route used to generate TUM-2A-001. The chosen  $\beta$ -ketoester was used in excess (1.5 equivalents) in this step as it ensured all the 5-aminopyrazole was used up when generating the final product.



**Figure 3.9 Synthetic route to pyrazolo[1,5- $\alpha$ ]pyrimidinone TUM-2A-001.**

The retention factor ( $R_f$ ) for both the 5-aminopyrazole and the final product are similar ( $R_f = 0.1$ , 100 % EtOAc) and so by using up the 5-aminopyrazole in the reaction it makes the use of column chromatography in purification and isolation step easier. The remaining  $\beta$ -ketoester was easily removed due to its vastly different  $R_f$  value (0.91) when compared to the 5-aminopyrazole and the pyrazolopyrimidinone final product. The isolation and purification of the final product was carried out using column chromatography. The yields ranged from 29 – 90 % for the ten pyrazolo[1,5- $\alpha$ ]pyrimidinones synthesised, shown in Figure 3.10. Structural characterisation for pyrazolo[1,5- $\alpha$ ]pyrimidinones was carried out using  $^1\text{H}$  NMR spectroscopy, LC-MS, and FTIR analysis.



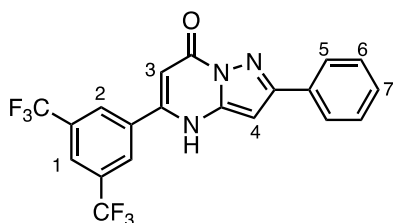


**Figure 3.10 Structures of the synthesised pyrazolo[1,5-a]pyrimidinones and their corresponding yields. 1. TUM-2A-001 2. TUM-2A-004 3. TUM-2A-005 4. TUM-2A-007 5. TUM-2A-008 6. TUM-2A-013 7. TUM-2A-014 8. TUM-2A-015 9. TUM-2A-016 10. TUM-2A-017.**

### 3.2.5 Structural Characterisation of Pyrazolo[1,5- $\alpha$ ]pyrimidinones

#### 3.2.5.1 TUM-2A-001

The structure of TUM-2A-001 with labelled hydrogen atoms is shown in Figure 3.11.



**Figure 3.11** Structure of TUM-2A-001 with labelled hydrogen atoms.

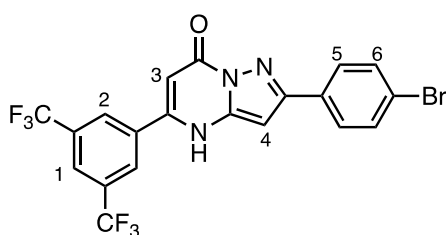
The most upfield signals appear as singlets with a chemical shift of 6.62 ppm which is assigned as the pyrazole proton shown at H4 and 6.24 ppm and assigned as the  $\alpha$ -proton at H3. Each singlet integrates for 1H. The signals in the range of 7.30 ppm to 7.97 ppm can be assigned to the protons associated with the phenyl ring at the  $\text{R}^2$  substituent. The most deshielded protons at 7.97 ppm are assigned to H5 where they appear as a doublet and integrate for 2H. H6 and H7 both appear as multiplets. H6 is assigned to 7.35 ppm and it integrates for 2H. H7 is assigned to the signal at 7.30 ppm integrating for 1H. The next two signals are assigned as the  $\text{CF}_3$  substituted aryl ring at the  $\text{R}^1$  substituent and are the most downfield signals observed. H2 is assigned to 8.63 ppm appears as a singlet with an integration for two protons. H1 is assigned to 8.14 ppm and appears as a singlet with an integration for one proton.

A  $^{13}\text{C}$  NMR spectrum was also taken where key signals observed are quaternary carbons and aromatic carbon signals in the 134.2 – 122.8 ppm region, which is expected. LCMS was carried out on TUM-2A-001 and showed the isolated material was 97 % pure by LC and a protonated

mass obtained for  $\text{C}_{20}\text{H}_{11}\text{F}_6\text{N}_3\text{O}$ ,  $[\text{M} + \text{H}]^+$  at 424 m/z. The IR spectrum for TUM-2A-001 showed an absorption band at  $3382\text{ cm}^{-1}$  which is indicative of an N-H bond. The absorption band at  $1660\text{ cm}^{-1}$  is typical of those generated by a C=O bond and the band at  $1600\text{ cm}^{-1}$  is typical of those generated by a C=C bond. The absorption band assigned at  $1275\text{ cm}^{-1}$  can be assigned to a C-N bond. All spectra can be found in Appendix A1.

### 3.2.5.2 TUM-2A-004

The structure of TUM-2A-004 with labelled hydrogen atoms is shown in Figure 3.12.



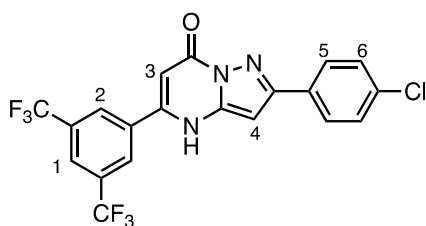
**Figure 3.12 Structure of TUM-2A-004 with labelled hydrogen atoms.**

The most upfield signals appear as singlets with a chemical shift of 6.75 ppm which represents the pyrazole proton shown at H4 and 6.41 ppm representing the  $\alpha$ -proton at H3. Each singlet integrates for 1H. The doublet at 7.70 ppm is assigned to H6 and the more downfield doublet at 8.00 ppm is assigned to H5. H6 and H5 are coupled and appear as a pair of doublets due to the splitting and the n+1 rule, where  $n = 1$  and  $n+1 = 2$  (a doublet), and each doublet integrates for two hydrogens. H2 is assigned to the signal at 8.54 ppm and appears as a singlet with an integration for two protons. H1 is assigned to 8.36 ppm and appears as a singlet with an integration for one proton.

A  $^{13}\text{C}$  NMR spectrum was also taken where key signals observed are quaternary carbons and aromatic carbon signals in the 150.4 – 120.3 ppm region, which is expected. LCMS was carried out on TUM-2A-004 and showed the isolated material was 96% pure by LC and a protonated mass obtained for  $\text{C}_{20}\text{H}_{10}\text{BrF}_6\text{N}_3\text{O}$ ,  $[\text{M} + \text{H}]^+$  at 503 m/z. The IR spectrum for TUM-2A-004 showed an absorption band at  $2922\text{ cm}^{-1}$  indicative of an N-H bond. The absorption band at  $1667\text{ cm}^{-1}$  is assigned as a C=O band and the band at  $1607\text{ cm}^{-1}$  is typical of one generated by a C=C bond. The absorption band assigned at  $1364\text{ cm}^{-1}$  can be assigned to a C-F bond and the absorption band at  $1275\text{ cm}^{-1}$  can be assigned to a C-N bond. All spectra can be found in Appendix A1.

### 3.2.5.3 TUM-2A-005

The structure of TUM-2A-005 with labelled hydrogen atoms is shown in Figure 3.13.



**Figure 3.13 Structure of TUM-2A-005 with labelled hydrogen atoms.**

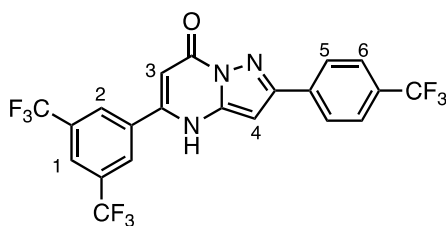
The most upfield signals appear as singlets with a chemical shift of 6.61 ppm which represents the pyrazole proton shown at H4 and 6.23 ppm representing the  $\alpha$ -proton at H3. Each singlet integrates for 1H. The doublet at 7.48 ppm is assigned to H6 and the more downfield doublet at 7.96 ppm is assigned to H5. H6 and H5 are coupled and appear as a pair of doublets due to the splitting and the n+1 rule, where  $n = 1$  and  $n+1 = 2$  (a doublet), and each doublet has an integrates for two hydrogens. The identical  $J$  value also shows that the hydrogens are coupled

to each other,  $J = 8.5$  Hz. H2 is assigned to 8.64 ppm appears as a singlet with an integration for two protons. H1 is assigned to 8.11 ppm and appears as a singlet with an integration for one proton.

A  $^{13}\text{C}$  NMR spectrum was also taken where key signals observed where the aromatic carbons were observed at 128.9 and 127.9 ppm respectively. There was not enough sample present to get a clearer spectrum and so baseline noise is observed on the spectrum. Due to the poor quality of the  $^{13}\text{C}$  NMR spectrum it is not included. LCMS was carried out on TUM-2A-005 and showed the isolated material was 98 % pure by LC and a protonated mass obtained for  $\text{C}_{20}\text{H}_{10}\text{ClF}_6\text{N}_3\text{O}$ ,  $[\text{M} + \text{H}]^+$  at 458 m / z. The IR spectrum for TUM-2A-005 showed an absorption band located at 3088  $\text{cm}^{-1}$  and 1543  $\text{cm}^{-1}$  which are indicative of an N-H bond. The absorption band at 1703  $\text{cm}^{-1}$  is typical of one generated by a C=O bond and the band at 1603  $\text{cm}^{-1}$  is typical of one generated by a C=C bond. The absorption band assigned at 1275  $\text{cm}^{-1}$  can be assigned to a C-N bond and the absorption band at 845  $\text{cm}^{-1}$  is assigned to a C-Cl bond. All spectra can be found in Appendix A1.

#### 3.2.5.4 TUM-2A-007

The structure of TUM-2A-007 with labelled hydrogen atoms is shown in Figure 3.14.



**Figure 3.14 Structure of TUM-2A-007 with labelled hydrogen atoms.**

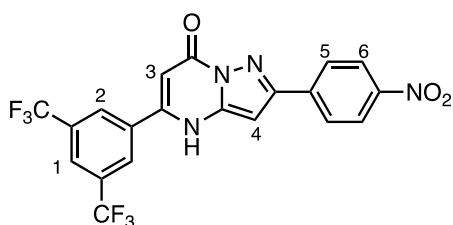
The most upfield signals appear as singlets with a chemical shift of 6.69 ppm which represents the pyrazole proton shown at H4 and 6.29 ppm representing the  $\alpha$ -proton at H3. Each singlet integrates for 1H. The doublet at 7.73 ppm is assigned to H6. The more downfield doublet is assigned to H5 at 8.11 ppm. H1 and H2 are assigned to the protons on the R<sup>1</sup> substituent. H2 is assigned to 8.65 ppm appears as a singlet with an integration for two protons. H1 is assigned to 8.13 ppm and appears as a singlet with an integration for one proton.

A <sup>13</sup>C NMR spectrum was also taken where key signals observed were a C=O signal at 207.5ppm and an aromatic carbon at 126.8 ppm. There was not enough sample present to get a clearer spectrum and so baseline noise is observed on the spectrum. Due to the poor quality of the <sup>13</sup>C NMR spectrum it is not included. LCMS was carried out on TUM-2A-007 and showed the isolated material was 99 % pure by LC and a protonated mass obtained for C<sub>21</sub>H<sub>10</sub>F<sub>9</sub>N<sub>3</sub>O, [M + H]<sup>+</sup> at 492 m/z. The IR spectrum for TUM-2A-007 showed an absorption band at 3093 cm<sup>-1</sup> and at 1549 cm<sup>-1</sup> which is indicative of an N-H bond. The absorption band at 1697 cm<sup>-1</sup> is typically generated by a C=O bond and the band at 1610 cm<sup>-1</sup> is typically generated by a C=C bond. The absorption band assigned at 1275 cm<sup>-1</sup> can be assigned to a C-N bond and

the absorption band at  $1168\text{ cm}^{-1}$  can be assigned to a C-F bond. All spectra can be found in Appendix A1.

### 3.2.5.5 TUM-2A-008

The structure of TUM-2A-008 with labelled hydrogen atoms is shown in Figure 3.15.



**Figure 3.15 Structure of TUM-2A-008 with labelled hydrogen atoms.**

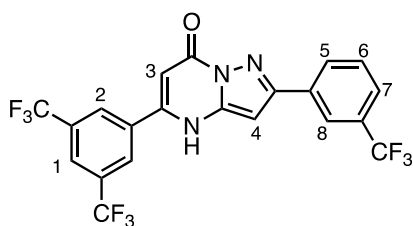
The most upfield signals appear as singlets with a chemical shift of 6.89 ppm which represents the pyrazole proton shown at H4 and 6.41 ppm representing the  $\alpha$ -proton at H3. Each singlet integrates for 1H. The doublet at 8.29 ppm is assigned to H6. H2 is assigned to 8.52 ppm appears as a singlet with an integration for two protons. There should be a doublet and singlet present to account for both H5 and H1 respectively, the two peaks were amalgamated through error however the integration at the 8.34 ppm mark accounts for the 3H's that should be present.

A  $^{13}\text{C}$  NMR spectrum was also taken where key signals observed are quaternary carbons and aromatic carbon signals in the  $148.0 - 124.6$  ppm region, which is expected. Furthermore, a carbonyl proton signal occurs at 207.5 ppm in the  $^{13}\text{C}$  NMR spectrum. LCMS was carried out on TUM-2A-008 and showed the isolated material was 100 % pure by LC and a protonated mass obtained for  $\text{C}_{20}\text{H}_{10}\text{F}_6\text{N}_4\text{O}_3$ ,  $[\text{M} + \text{H}]^+$  at 469 m / z. The IR spectrum for TUM-2A-008 showed an absorption band at  $3067\text{ cm}^{-1}$  and at  $1516\text{ cm}^{-1}$  which is indicative of an N-H bond. The absorption band at  $1669\text{ cm}^{-1}$  is typical of one generated by a C=O bond and the band at

1601  $\text{cm}^{-1}$  is of one generated by a C=C bond. The absorption band assigned at 1516  $\text{cm}^{-1}$  can be assigned to an N-O band and the absorption band at 1275  $\text{cm}^{-1}$  can be assigned to a C-N bond. The absorption band observed at 1142  $\text{cm}^{-1}$  can be assigned to a C-F bond. All spectra can be found in Appendix A1.

### 3.2.5.6 TUM-2A-013

The structure of TUM-2A-013 with labelled hydrogen atoms is shown in Figure 3.16.



**Figure 3.16 Structure of TUM-2A-013 with labelled hydrogen atoms.**

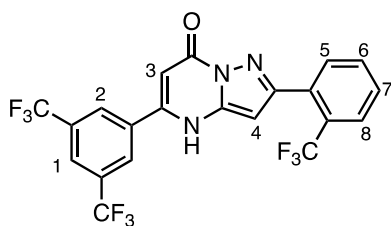
The most upfield signals appear as singlets with a chemical shift of 6.70 ppm which represents the pyrazole proton shown at H4 and 6.17 ppm representing the  $\alpha$ -proton at H3. Each singlet integrates for 1H. H2 is assigned to 8.58 ppm appears as a singlet with an integration for two hydrogens. H1 is assigned to 8.7 ppm and appears as a singlet with an integration for one hydrogen. H5, H6, H7 and H8 are labelled as the protons on the  $R^2$  substituent. H6 is assigned to 8.12 ppm as a doublet of doublets due to the splitting from H5 and H7. The H6 signal is split by H5 into one doublet and is also split by H7 to form a doublet hence the doublet of doublets signal. The remaining signals observed at 7.68 ppm, 8.32 ppm and 8.03 ppm are assigned as aromatic CH's on the  $\text{CF}_3$  substituted aryl ring.



The  $^{13}\text{C}$  NMR spectrum for TUM-2A-013 only picked up on one peak which was at 207.1 ppm and denotes a carbonyl proton bond. The spectrum was run several times however it was unable to determine peaks and there was baseline noise observed on the spectrum. It would be suggested that more scans over a longer period of time be carried out in future however this was not possible at the time. Due to the poor quality of the  $^{13}\text{C}$  NMR spectrum it is not included. LCMS was carried out on TUM-2A-013 and showed the isolated material was 96 % pure by LC and a protonated mass obtained for  $\text{C}_{21}\text{H}_{10}\text{F}_9\text{N}_3\text{O}$ ,  $[\text{M} + \text{H}]^+$  at 492 m/z. The IR spectrum for TUM-2A-013 showed an absorption band at  $3067\text{ cm}^{-1}$  and at  $1516\text{ cm}^{-1}$  which is indicative of an N-H bond. The absorption band at  $1669\text{ cm}^{-1}$  is typically generated by a C=O bond and the band at  $1601\text{ cm}^{-1}$  is typically generated by a C=C bond. The absorption band at  $1275\text{ cm}^{-1}$  can be assigned to a C-N bond. The absorption band observed at  $1142\text{ cm}^{-1}$  can be assigned to a C-F bond. All spectra can be found in Appendix A1.

### 3.2.5.7 TUM-2A-014

The structure of TUM-2A-014 with labelled hydrogen atoms is shown in Figure 3.17



**Figure 3.17 Structure of TUM-2A-014 with labelled hydrogen atoms.**

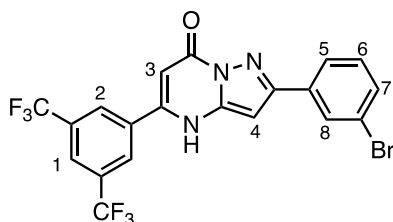
The most upfield signals appear as singlets with a chemical shift of 6.33 ppm which represents the pyrazole proton shown at H4 and 6.25 ppm representing the  $\alpha$ -proton at H3. Each singlet integrates for 1H. H2 is assigned to 8.62 ppm appears as a singlet with an integration for two hydrogens. H1 is assigned to 8.10 ppm and appears as a singlet with an integration for one hydrogen. The protons assigned to H5, H6, H7 and H8 all correspond to the R<sup>2</sup> substituent. H5 is observed as the expected doublet at 7.83 ppm and is located next to H6 at 7.62 ppm where both the *J* values are identical at 7.9 Hz. At protons H7 and H8 overlap to give a multiplet and integrate for 2 protons at 7.74 ppm.

A <sup>13</sup>C NMR spectrum was also taken where key signals observed are quaternary carbons and aromatic carbon signals in the 158.9 – 122.8 ppm region, which is expected. Furthermore, a carbonyl proton signal occurs at 207.5 ppm in the <sup>13</sup>C NMR spectrum. LCMS was carried out on TUM-2A-014 and showed the isolated material was 98 % pure by LC and a protonated mass obtained for C<sub>21</sub>H<sub>10</sub>F<sub>9</sub>N<sub>3</sub>O, [M + H]<sup>+</sup> at 492 m/z. The IR spectrum for TUM-2A-014 showed an absorption band at 3036 cm<sup>-1</sup> and at 1623 cm<sup>-1</sup> which is indicative of an N-H bond. The absorption band at 1635 cm<sup>-1</sup> is typical of that generated by a C=O bond and the band at 1607

cm<sup>-1</sup> is typical of that generated by a C=C bond. The absorption band at 1395 cm<sup>-1</sup> can be assigned to a C-N bond. The absorption band observed at 1230 cm<sup>-1</sup> can be assigned to a C-F bond. All spectra can be found in Appendix A1.

### 3.2.5.8 TUM-2A-015

The structure of TUM-2A-015 with labelled hydrogen atoms is shown in Figure 3.18.



**Figure 3.18 Structure of TUM-2A-015 with labelled hydrogen atoms.**

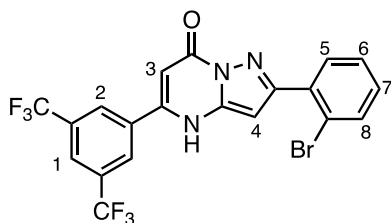
The most upfield signals appear as singlets with a chemical shift of 6.69 ppm which represents the pyrazole proton shown at H4 and 6.33 ppm representing the  $\alpha$ -proton at H3. Each singlet integrates for 1H. H2 is assigned to 8.65 ppm appears as a singlet with an integration for two hydrogens. H1 is assigned to 8.12 ppm and appears as a singlet with an integration for one hydrogen. H5, H6, H7 and H8 are labelled as the protons on the R<sup>2</sup> substituent. H5 is assigned 7.93 ppm and there is a doublet of triplets observed. The doublet of triplets is observed as there is long range coupling of H5 to H7 and H8 as well as  $3J$  coupling to H6. The predicted triplet is observed at H6 and is assigned 7.37 ppm. A doublet is observed at 7.51 ppm and is assigned to H7. H8 is a singlet assigned to 8.15 ppm.

A <sup>13</sup>C NMR spectrum was also taken where key signals observed are quaternary carbons and aromatic carbon signals in the 159.0 – 122.0 ppm region, which is expected. Furthermore, an alkenyl carbon signal occurs at 90.0 ppm and a carbonyl signal occurs at 207.0 ppm in the <sup>13</sup>C

NMR spectrum. LCMS was carried out on TUM-2A-015 and showed the isolated material was 95 % pure by LC and a protonated mass obtained for  $C_{20}H_{10}BrF_6N_3O$ ,  $[M + H]^+$  at 503 m/z. The IR spectrum for TUM-2A-015 showed an absorption band at  $3086\text{ cm}^{-1}$  and at  $1539\text{ cm}^{-1}$  which is indicative of an N-H bond. The absorption band at  $1668\text{ cm}^{-1}$  is typically generated by a C=O bond and the band at  $1603\text{ cm}^{-1}$  is typical of that generated by a C=C bond. The absorption band assigned at  $1276\text{ cm}^{-1}$  can be assigned to a C-N bond and the absorption band at  $680\text{ cm}^{-1}$  can be assigned to a C-Br bond. All spectra can be found in Appendix A1.

### 3.2.5.9 TUM-2A-016

The structure of TUM-2A-016 with labelled hydrogen atoms is shown in Figure 3.19.



**Figure 3.19 Structure of TUM-2A-016 with labelled hydrogen atoms.**

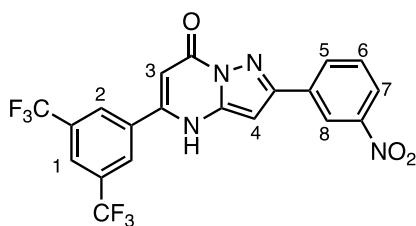
The most upfield signals appear as singlets with a chemical shift of 6.58 ppm which represents the pyrazole proton shown at H4 and 6.32 ppm representing the  $\alpha$ -proton at H3. Each singlet integrates for 1H. H2 is assigned to 8.64 ppm appears as a singlet with an integration for two hydrogens. H1 is assigned to 8.09 ppm and appears as a singlet with an integration for one hydrogen. H5, H6, H7 and H8 are assigned to the protons on the  $R^2$  substituent. The expected doublets were observed for H5 and H8. The expected triplets were observed for H6 and H7. The doublet observed at 7.75 ppm is coupled to the triplet observed at 7.37 ppm as they have the same  $J$  value. H5 is expected to be the most shielded proton and is allocated to 7.75 ppm

and the H6 proton is allocated to 7.37 ppm. H8 is assigned to the doublet at 7.68 ppm and is more shielded than the H7 triplet located at 7.25 ppm. Both H7 and H8 contain the same  $J$  value of 7.9 Hz and so the protons are coupled to each other.

A  $^{13}\text{C}$  NMR spectrum was also taken where key signals observed are quaternary carbons and aromatic carbon signals in the 159.0 – 122.0 ppm region, which is expected. Furthermore, an alkenyl carbon signal occurs at 90.0 ppm and a carbonyl signal occurs at 207.0 ppm in the  $^{13}\text{C}$  NMR spectrum. LCMS was carried out on TUM-2A-016 and showed the isolated material was 99 % pure by LC and a protonated mass obtained for  $\text{C}_{20}\text{H}_{10}\text{BrF}_6\text{N}_3\text{O}$ ,  $[\text{M} + \text{H}]^+$  at 503 m/z. The IR spectrum for TUM-2A-016 showed an absorption band at  $2930\text{ cm}^{-1}$  and at  $1538\text{ cm}^{-1}$  which is indicative of an N-H bond. The absorption band at  $1604\text{ cm}^{-1}$  is typical of that generated by a C=C bond and the band at  $1275\text{ cm}^{-1}$  is typical of that generated by a C=N bond. The absorption band assigned at  $680\text{ cm}^{-1}$  can be assigned to a C-Br bond. All spectra can be found in Appendix A1.

#### 3.2.5.10 TUM-2A-017

The structure of TUM-2A-017 with labelled hydrogen atoms is shown in Figure 3.20.



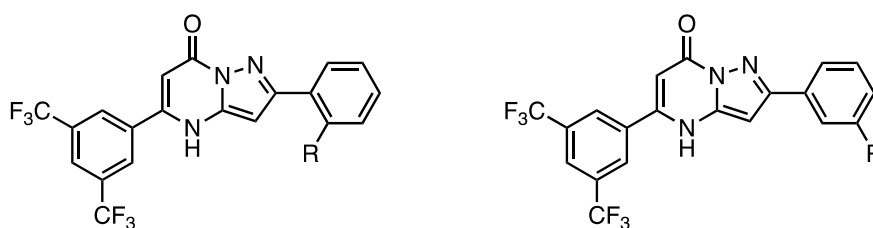
**Figure 3.20 Structure of TUM-2A-017 with labelled hydrogen atoms.**

The most upfield signals appear as singlets with a chemical shift of 6.65 ppm which represents the pyrazole proton shown at H4 and 6.22 ppm representing the  $\alpha$ -proton at H3. Each singlet integrates for 1H. H2 is assigned to 8.63 ppm appears as a singlet with an integration for two hydrogens. H1 is assigned to 8.15 ppm and appears as a singlet with an integration for one hydrogen. H5, H6, H7 and H8 are assigned to the protons on the R<sup>2</sup> substituent. There is an expected doublet and triplet present at 7.94 ppm and 7.40 ppm. Both signals are allocated to H7 and H6 respectively where the *J* values are identical showing the protons are coupled to each other. H8 is assigned to 8.09 ppm where it is observed as the expected singlet. The multiplet shown at 7.52 ppm is assigned to H5.

A <sup>13</sup>C NMR spectrum was also taken where key signals observed are quaternary carbons and aromatic carbon signals in the 131.2 – 122.5 ppm region, which is expected. Furthermore, a carbonyl signal occurs at 207.0 ppm in the <sup>13</sup>C NMR spectrum. LCMS was carried out on TUM-2A-017 and showed the isolated material was 97 % pure by LC and a protonated mass obtained for C<sub>20</sub>H<sub>10</sub>F<sub>6</sub>N<sub>4</sub>O<sub>3</sub>, [M + H]<sup>+</sup> at 469 m/z. The IR spectrum for TUM-2A-017 showed an absorption band at 3087 cm<sup>-1</sup> and at 1581 cm<sup>-1</sup> which is indicative of an N-H bond. The absorption band at 1606 cm<sup>-1</sup> is typically generated by a C=O bond and the band at 1581 cm<sup>-1</sup> is typically generated by a C=C bond. The absorption band assigned at 1516 cm<sup>-1</sup> can be assigned to an N-O band and the absorption band at 1275 cm<sup>-1</sup> can be assigned to a C-N bond. The absorption band observed at 1142 cm<sup>-1</sup> can be assigned to a C-F bond. All spectra can be found in Appendix A1.

### 3.2.6 Conclusions on the Synthesis of Pyrazolo[1,5- $\alpha$ ]pyrimidinones

A total of 10 substituted pyrazolo[1,5- $\alpha$ ]pyrimidinones were synthesised and structurally characterised using analytical chemistry techniques such as  $^1\text{H}$  NMR,  $^{13}\text{C}$  NMR, FTIR and LC-MS. TUM-2A-005 was the first compound that was synthesised and characterised as part of this study. The remaining synthesised compounds were as follows: the four hit compounds which were determined as part of Chapter 2 (TUM-2A-001, TUM-2A-004, TUM-2A-007 and TUM-2A-008) and analogues of those hit compounds (TUM-2A-013, TUM-2A-014, TUM-2A-015, TUM-2A-016 and TUM-2A-017). The hit compounds determined all contained a substituent in the *para* position of the phenyl ring. It was hypothesised that by moving this substituent into the *meta* and *ortho* positions it could potentially change the overall biological activity of the compounds thus either improving or hindering the activity. It was also hypothesised that by moving the substituent to the *meta* and *ortho* positions, selectivity for the cancerous cell line over the non-cancerous cell line could potentially be improved. Figure 3.21 shows the structure of the analogue 2A compounds where the functional group has been moved to the *ortho* or *meta* positions respectively.



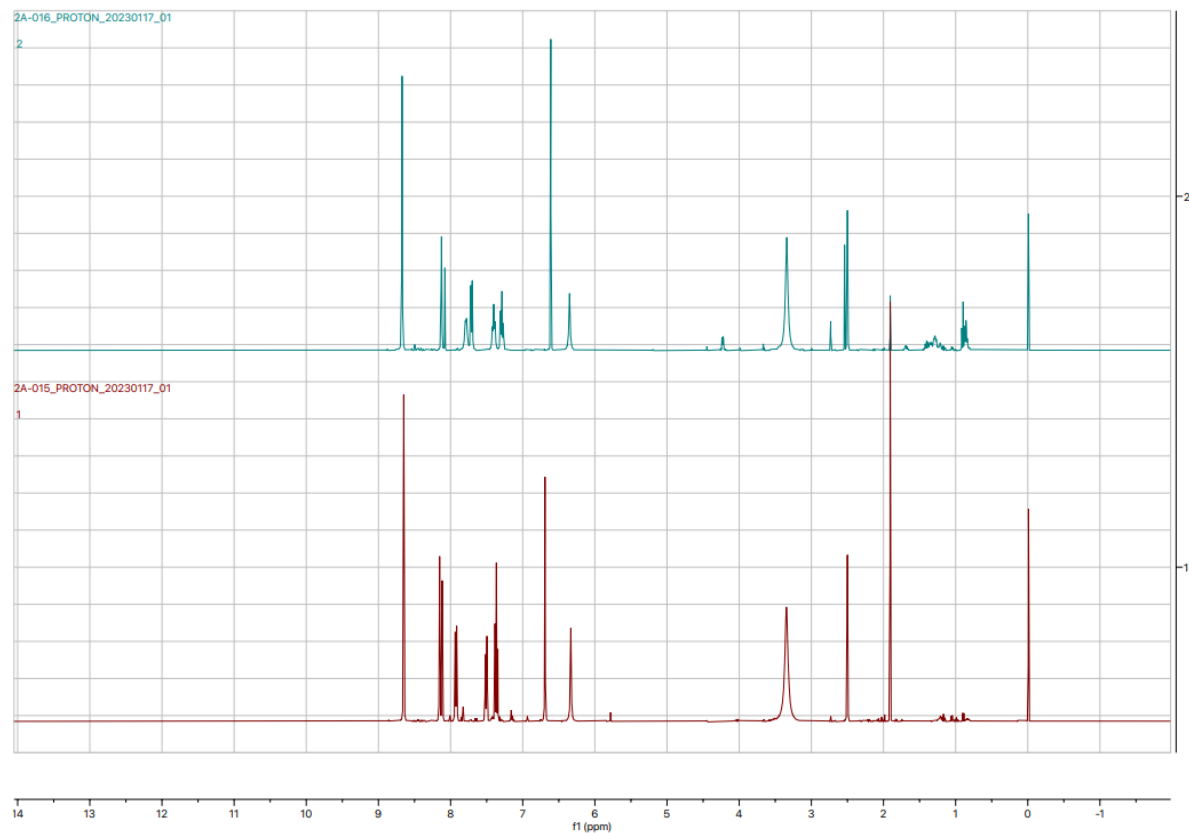
**Figure 3.21** Structure of group 2A analogue compounds whereby the  $R^1$  functional group consists of a 1,3-bis(trifluoromethyl)phenyl substituent and the  $R^2$  group consists of varied substituted aryl ring groups in the *ortho* or *meta* position respectively.

The synthesis of analogue compounds is very common in the field of medicinal chemistry as the goal is to strive to continuously synthesise new, more effective, more selective and less toxic drugs (Gensicka-Kowalewska et al., 2017). There are different ways in which this can be achieved whether it is manually synthesising analogue compounds in a lab setting or by carrying out molecular docking studies using computational chemistry. A study which was carried out focused on coumarin analogue compounds with anti-Alzheimer activities (Yusufzai et al., 2018). It was reported that the movement of the fluoro substituent from the *ortho* position to the *para* position resulted in a 4 time decrease in inhibition properties. Docking studies were carried out to confirm these observations whereby it was shown that fluoro substituent at the *ortho* position disrupted the  $\pi$  to  $\pi$  stacking interactions due to the rotation of the phenyl ring. The movement of the fluoro substituent to the *meta* position increased the inhibitory properties due to the proper stacking of the phenyl ring (Yusufzai et al., 2018). A similar approach will be taken as part of this study whereby an example would be the hit compound TUM-2A-004. The *para*-bromophenyl substituent was moved to the *meta* and *ortho* position to yield TUM-2A-015 and TUM-2A-016 respectively. However, to determine whether biological activity has been improved, the synthesised compounds must be initially characterised.



The first technique used to structurally characterise any of the compounds was proton nuclear magnetic resonance,  $^1\text{H}$  NMR spectroscopy. This is a technique used to determine the structure of the compounds and was a useful tool when determining the structure of the two analogue compounds TUM-2A-015 and TUM-2A-016. Figure 3.22 is an overlay of the TUM-2A-016 and the TUM-2A-015  $^1\text{H}$  NMR spectra. Both spectra are very similar bar the regions shown in the aromatic 7 – 8 ppm region where the splitting patterns change due to the movement of the Br substituent from the *ortho* to the *meta* position respectively.

For TUM-2A-015 where the bromo electron withdrawing group is in the meta position, it would be predicted that the splitting observed in the aromatic region of the  $^1\text{H}$  NMR would be such that a singlet, two doublets and a triplet. The actual observed peaks are such that a singlet at 8.15 ppm, a doublet at 7.51 ppm and a doublet triplet at 7.93 ppm where the predicted doublet and triplet peaks overlap. For TUM-2A-016 where the bromo substituent has been moved to the ortho position, the predicted splitting observed in the aromatic region of the  $^1\text{H}$  NMR would be doublet, triplet, doublet, triplet. The observed peaks in this spectrum were a doublet at 7.75 ppm located beside a triplet at 7.37 ppm and another doublet at 7.68 ppm beside a triplet at 7.25 ppm. It is known that the peaks are located beside one another due to the identical  $J$  values.

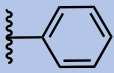
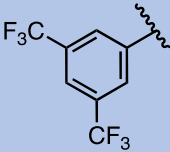
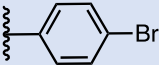
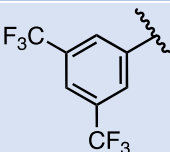

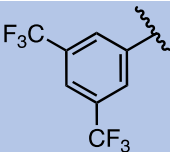


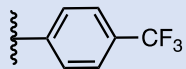
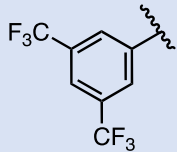
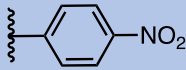
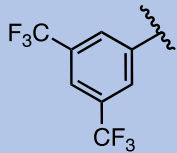
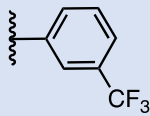
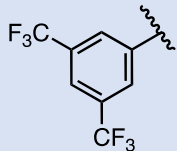
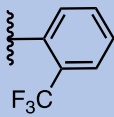
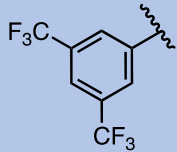
**Figure 3.22** An overlay of the <sup>1</sup>H NMR spectra where the upper spectrum refers to TUM-2A-016 and the lower spectrum refers to TUM-2A-015. Changes in the aromatic region shown 7 – 8 ppm allow the determination of whether the Br substituent was in the meta or ortho position.

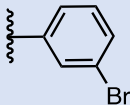
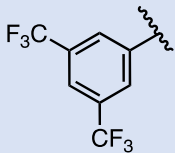
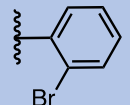
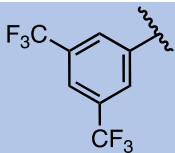
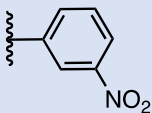
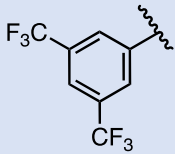
Carbon-13 nuclear magnetic resonance,  $^{13}\text{C}$  NMR was also used as part of this study. The presence of aromatic and quaternary carbons as well as a carbonyl carbon and alkenyl carbon were detected in the spectra for TUM-2A-015 and TUM-2A-016. It should be noted that not all the  $^{13}\text{C}$  NMR spectra could be assigned due to low quality spectra and baseline noise observed. Ideally, the compounds should be run with extra scans over a longer period of time however at the time this was not possible.

Fourier-transform infrared spectroscopy (FTIR) was also carried out for each compound. This technique shows the presence of functional groups in the compounds via absorption band however these band do not tell you where the functional group is located. It should also be noted that in order to test novel compounds for biological activity, the compounds must have a minimum purity value of 95 % according to the Royal Society of Chemistry (RSC, 2023). The purity was determined using liquid chromatography mass spectrometry (LC-MS). The mass of the compound +1 was searched to determine if the compound was present and when it was located the % purity value was also provided. A summary table of all the compounds synthesised as well as their purities and yields are shown in Table 3-2.

**Table 3-2** The synthesised HIT compounds and their analogues highlighting the substitutions made at the  $R^1$  and  $R^2$  positions. The % purity and % yield is also highlighted for each synthesised compound.

Compound	$R^1$	$R^2$	Purity %	Yield %
TUM-2A-001			97	29
TUM-2A-004			96	75
TUM-2A-005			97	76

TUM-2A-007			99	69
TUM-2A-008			99	90
TUM-2A-013			96	73
TUM-2A-014			98	50

TUM-2A-015			95	78
TUM-2A-016			99	67
TUM-2A-017			97	71

### **3.3. Experimental**

#### **3.3.1 General Experimental**

The synthesis of the 5-aminopyrazoles and the substituted pyrazolo[1,5- $\alpha$ ]pyrimidinones were prepared using modified literature procedures (Kelada *et al.*, 2018)(Devine *et al.*, 2014).

##### **3.3.1.1 Purification of Reagents and Solvents for Synthetic Work**

All reagents and solvents were obtained from approved commercial suppliers and did not require any further purification unless otherwise stated.

#### **3.3.2 Purification of Products**

##### **3.3.2.1 Thin Layer Chromatography**

Thin Layer Chromatography (TLC) was carried out using Silica Plates (Merck). The TLC plates are coated with fluorescent indicator UV254. The plates were analysed under 254 nm light to detect the synthesised compounds using the eluents specified.

##### **3.3.2.2 Flash Column Chromatography**

Flash column chromatography was carried out using ZEOPrep® 60 HYD 40 - 63 micron silica gel.

##### **3.3.2.3 Rotary Evaporator**

Excess solvent was removed *in vacuo* using a Büchi R114 rotary evaporator with B-480 heating bath where temperatures can reach up to 50 °C.

### 3.3.3 Analysis of Products

#### 3.3.3.1 Liquid Chromatography-Mass Spectrometry (LC-MS) Analysis

The LC-MS instrument used in the analysis was the 'Agilent Technologies 1200 Series.' Reverse phase chromatography was utilised in which the stationary phase was a non-polar silica column and the mobile phase used was acetonitrile with 0.1 % formic acid. (LC-MS grade solvent).

LC-MS Analysis of 5-aminopyrazoles: The required 5-aminopyrazole (0.001 g) was added to a vial of acetonitrile (1 mL).

LC-MS Analysis of pyrazolopyrimidinones: The required pyrazolopyrimidinone (0.030 g) was added to dimethyl sulfoxide (DMSO) (1000  $\mu$ L). The pyrazolopyrimidinone-DMSO solution (100  $\mu$ L) was then added to acetonitrile (1 mL).

#### 3.3.3.2 Nuclear Magnetic Resonance Spectroscopy (NMR) Analysis

NMR spectroscopic analysis was carried out using a 500 MHz Bruker DRX 500 Spectrometer. The compounds synthesised were analysed using  $^1\text{H}$  NMR,  $^{13}\text{C}$  NMR and 2D NMR spectroscopy. Chemical shifts ( $\delta$ ) are reported in parts per million (ppm) with reference to the residual solvent peaks. The references used were deuterated DMSO- $\text{d}_6$ , deuterated chloroform ( $\text{CDCl}_3$ ), or TMS which can be observed at 2.50 ppm, 7.26 ppm, and 0 ppm respectively for  $^1\text{H}$  NMR. The references for DMSO- $\text{d}_6$  and  $\text{CDCl}_3$  are observed at 77.16 ppm and 39.52 ppm respectively for  $^{13}\text{C}$  NMR (Fulmer *et al.*, 2010). Coupling constants ( $J$ ) are given in Hertz (Hz) with multiplicities abbreviated to (s) singlet, (d) doublet, (t) triplet, (m) multiplet or combinations of the above.



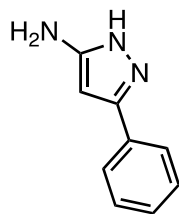
### 3.3.4 Materials and Methods for Biological Evaluation

The method employed in the biological evaluation of the analogue compounds is the same of that outlined in Chapter 2.

### 3.4. Synthesis of 5-Aminopyrazole Intermediates

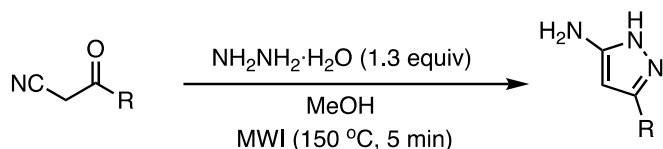
A solution of  $\beta$ -ketonitrile (2 mmol) and hydrazine monohydrate (126  $\mu$ L, 2.5 mmol) in MeOH (1 mL) was subjected to microwave irradiation (100 W, 150  $^{\circ}$ C) for 5 min. The resulting mixture was concentrated *in vacuo* and the residue was purified *via* column chromatography on silica gel to give the title compound.

The majority of the 5-aminopyrazoles needed were commercially available. The exception was 3-phenyl-1H-pyrazol-5-amine, the intermediate compound for TUM-2A-001. This compound will be referred to as 5-aminopyrazole **1**, see Figure 3.23.



**Figure 3.23 5-aminopyrazole 1: 3-Phenyl-1H-pyrazol-5-amine**

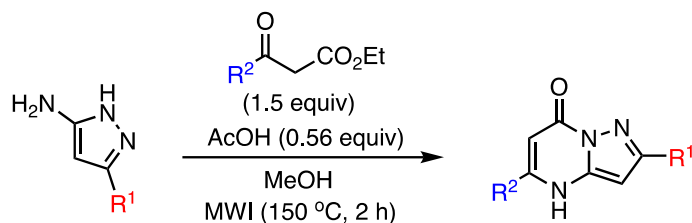
Following General Procedure A (Figure 3.24) using 3-oxo-3phenylpropanenitrile (0.145 g, 2.00 mmol) as the  $\beta$ -ketonitrile.



**Figure 3.24 General Procedure A for the Synthesis of 5-Aminopyrazole Intermediates**

The residue was purified *via* column chromatography (30:70 petroleum ether/EtOAc) on silica gel to yield the desired 5-aminopyrazole TUM-2A-001 intermediate as a pale pink solid (0.1308 g, 82 %). **R<sub>f</sub>**: 0.55 (70:30 EtOAc/pet. ether). **<sup>1</sup>H NMR** (500 MHz, DMSO-*d*<sub>6</sub>):  $\delta$  11.91 (s, 1H, NH), 7.65 (d, 2H, J = 7.6 Hz 2 x ArCH), 7.37 (t, 2H, J = 7.6 Hz 2 x ArCH), 7.26 (m, 1H, J = 7.6 Hz, ArCH), 5.76 (s, 1H). **LC-MS** (Acetonitrile, 1 % formic acid): R<sub>t</sub> = 1.18 min, [M + H]<sup>+</sup> 160, 100 % purity. **FTIR** 3149 (N-H), 1700w (C=N), 1507s (Ar C) cm<sup>-1</sup>.

### 3.5. Synthesis of Substituted Pyrazolo[1,5- $\alpha$ ]pyrimidinones

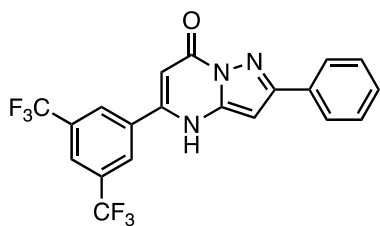


**Figure 3.25 General Procedure B for the Synthesis of Pyrazolo[1,5- $\alpha$ ]pyrimidinones**

The procedure for the synthesis of pyrazolo[1,5- $\alpha$ ]pyrimidinones is referred to as general procedure B and is shown in Figure 3.25. A microwave vial (2 mL) was charged with the required 5-aminopyrazole (0.45 mmol),  $\beta$ -ketoester (0.675 mmol), AcOH (14.3  $\mu$ L, 0.25 mmol) in MeOH (1 mL) were subjected to MW irradiation (100 W, 150 °C) for 2 h. The resulting mixture was concentrated under reduced pressure and the residue was purified *via* column chromatography or trituration to give the title compound.

### 3.5.1 5-(3,5-Bis(trifluoromethyl)phenyl)-2-phenylpyrazolo[1,5-a]pyrimidin-7(4H)-one

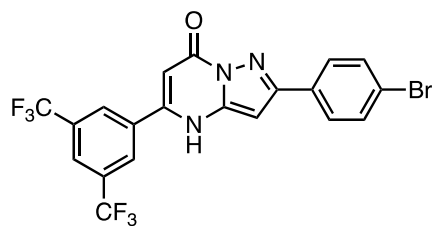
(TUM-2A-001)



The general procedure **B**, (Figure 3.25) was followed using 3-phenyl-1H-pyrazol-5-amine (0.07 g, 0.45 mmol) as the 5-aminopyrazole and ethyl 3-(3,5-bis(trifluoromethyl)phenyl)-3-oxopropanoate (0.22 g, 0.67 mmol) as the  $\beta$ -ketoester.

The resulting residue was purified *via* column chromatography (50:50 EtOAc/petroleum ether to 70:30 EtOAc/petroleum ether to 100% EtOAc) to yield the product as a pale-yellow solid (0.056 g, 29%). **R<sub>f</sub>**: 0.77 (1:1 EtOAc /pet. ether; 7:3 EtOAc /pet. ether; 100% EtOAc). **<sup>1</sup>H NMR** (500 MHz, DMSO):  $\delta$  8.63 (s, 2H, 2 x *H*2), 8.14 (s, 1H, *H*1), 7.97 (d, 2H, *J* = 7.3 Hz, 2 x *H*6), 7.45 (t, 2H, *J* = 7.6 Hz, 2 x *H*5), 7.45 (t, 1H, *J* = 7.3 Hz, *H*7), 7.35 (s, 1H, *H*4), 6.62 (s, 1H, *H*3). **<sup>13</sup>C NMR** (126 MHz, DMSO):  $\delta$  134.3, 131.1, 130.9, 128.9, 128.6, 127.5, 127.1, 126.6, 124.9, 122.8, 90.3. **LC-MS** (Acetonitrile, 1 % formic acid): *R<sub>t</sub>* = 1.18 min, [*M* + *H*]<sup>+</sup> 423.32, 96.7 % purity. **FTIR** 3382m (N-H), 1660m (C=O), 1600s (C=C), 1275s (C-N) cm<sup>-1</sup>.

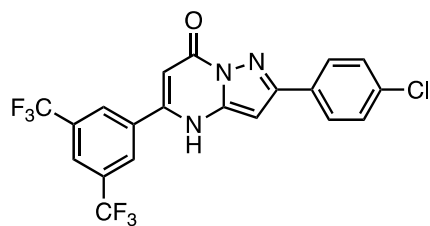
3.5.2 5-(3,5-Bis(trifluoromethyl)phenyl)-2-(4-bromophenyl)pyrazolo[1,5-a]pyrimidin-7(4H)-one (TUM-2A-004)



The general procedure **B** (Figure 3.25) was followed using 3-(4-bromophenyl)-1H-pyrazol-5-amine (0.12 g, 0.45 mmol) as the 5-aminopyrazole and ethyl 3-(3,5-bis(trifluoromethyl)phenyl)-3-oxopropanoate (0.164 g, 0.49 mmol) as the  $\beta$ -ketoester.

The resulting residue was placed in ice and was purified using trituration from MeOH (2 mL) to yield the product as a pale pink solid (0.17 g, 75 %). **R<sub>f</sub>**: 0.11 (70:30 pet. Ether / EtOAc) **<sup>1</sup>H NMR** (500 MHz, DMSO-*d*<sub>6</sub>):  $\delta$  12.89 (s, 1H, *NH*), 8.54 (s, 2H, 2 x *H*<sub>2</sub>), 8.36 (s, 1H, *H*<sub>1</sub>), 8.00 (d, 2H, 2 x *H*<sub>5</sub>), 7.70 (d, 2H, 2 x *H*<sub>6</sub>), 6.75 (s, 1H, *H*<sub>4</sub>), 6.41 (s, 1H, *H*<sub>3</sub>). **<sup>13</sup>C NMR** (126 MHz, DMSO-*d*<sub>6</sub>):  $\delta$  156.4, 152.9, 147.3, 143.5, 135.3, 132.2, 131.9, 131.7, 131.5, 131.2, 130.9, 129.0, 128.7, 126.8, 124.9, 124.6, 122.8, 122.4, 120.3, 96.5, 87.4 **LC-MS** (Acetonitrile, 1 % formic acid): *R<sub>t</sub>* = 1.18 min, [M + H]<sup>+</sup> 503, 96.4 % purity. **FTIR** 2922s (N-H), 1667s (C=O), 1607s (C=C), 1364m (C-F), 1275 (C-N) cm<sup>-1</sup>.

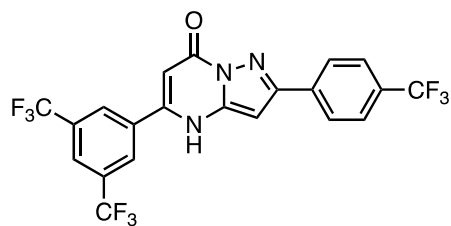
3.5.3 5-(3,5-Bis(trifluoromethyl)phenyl)-2-(4-chlorophenyl)pyrazolo[1,5-a]pyrimidin-7(4H)-one (TUM-2A-005)



The general procedure **B** (Figure 3.25) was followed using 3-(4-chlorophenyl)-1H-pyrazol-5-amine (0.09 g, 0.45 mmol) as the 5-aminopyrazole and ethyl 3-(3,5-bis(trifluoromethyl)phenyl)-3-oxopropanoate (0.22 g, 0.67 mmol) as the  $\beta$ -ketoester.

The resulting residue was purified *via* column chromatography (70:30 EtOAc/petroleum ether) and the product was isolated as dark yellow/green solid (0.156 g, 76 %). **R<sub>f</sub>**: 0.84 (7:3 petroleum ether/EtOAc). **<sup>1</sup>H NMR** (500 MHz, DMSO-*d*<sub>6</sub>):  $\delta$  8.64 (2s, 2H, 2 x *H*<sub>2</sub>), 8.11 (s, 1H, *H*<sub>1</sub>), 7.96 (d, 2H, *J* = 8.5 Hz, 2 x *H*<sub>5</sub>), 7.48 (d, 2H, *J* = 8.5 Hz, 2 x *H*<sub>6</sub>), 6.61 (s, 1H, *H*<sub>4</sub>) 6.23 (s, 1H, *H*<sub>3</sub>). **LC-MS** (Acetonitrile, 1 % formic acid): *R<sub>t</sub>* = 1.18 min, [*M* + *H*]<sup>+</sup> 458, 97.5 % purity. **FTIR**: 3088s (N-H), 1703m (C=O), 1603m (C=C), 1543m (N-H), 1275s (C-N), 845m (C-Cl) cm<sup>-1</sup>.

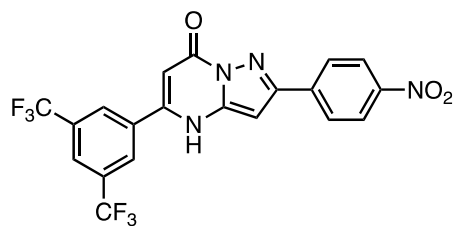
3.5.4 5-(3,5-Bis(trifluoromethyl)phenyl)-2-(4-(trifluoromethyl)phenyl)pyrazolo[1,5-a]pyrimidin-7(4H)-one (TUM-2A-007)



The general procedure **B** (Figure 3.25) was followed using 3-(4-(trifluoromethyl)phenyl)-1H-pyrazol-5-amine (0.10 g, 0.45 mmol) as the 5-aminopyrazole and ethyl 3-(3,5-bis(trifluoromethyl)phenyl)-3-oxopropanoate (0.22 g, 0.67 mmol) as the  $\beta$ -ketoester.

The resulting residue was purified *via* column chromatography (70:30 petroleum ether/EtOAc to 50:50 petroleum ether/EtOAc to 70:30 EtOAc/petroleum ether to 100% EtOAc) and the product was obtained as a pale-yellow solid (0.152 g, 69 %). **R<sub>f</sub>**: 0.1 (70:30 pet. ether / EtOAc) **<sup>1</sup>H NMR** (500 MHz, DMSO-*d*<sub>6</sub>):  $\delta$  8.65 (d, 2H, 2 x *H*<sub>2</sub>), 8.13 (s, 1H, *H*<sub>1</sub>), 8.11 (d, 2H, 2 x *H*<sub>5</sub>), 7.73 (d, 2H, *H*<sub>6</sub>) 6.69 (s, 1H, *H*<sub>4</sub>), 6.29 (s, 1H, *H*<sub>3</sub>). **LC-MS** (Acetonitrile, 1 % formic acid): *R*<sub>t</sub> = 1.18 min, [M + H]<sup>+</sup> 492, 98.8 % purity. **FTIR**: 3093s (N-H), 1697m (C=O), 1610m (C=C), 1549m (N-H), 1275s (C-N), 1168s (C-F) cm<sup>-1</sup>.

3.5.5 5-(3,5-Bis(trifluoromethyl)phenyl)-2-(4-nitrophenyl)pyrazolo[1,5-a]pyrimidin-7(4H)-one (TUM-2A-008)

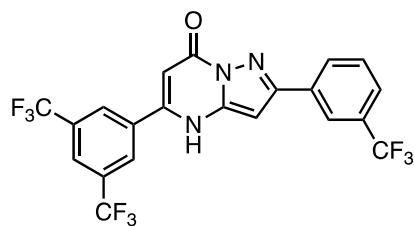


The general procedure **B** (Figure 3.25) was followed using 3-(4-nitrophenyl)-1H-pyrazol-5-amine (0.10 g, 0.45 mmol) as the 5-aminopyrazole and ethyl 3-(3,5-bis(trifluoromethyl)phenyl)-3-oxopropanoate (0.22 g, 0.67 mmol) as the  $\beta$ -ketoester.

The resulting residue was filtered under vacuum and purified using trituration from acetone (2 mL). The purified product was isolated as a pale-yellow solid (0.19 g, 90 %). **R<sub>r</sub>**: 0.08 (70:30 pet. ether /EtOAc) **<sup>1</sup>H NMR** (500 MHz, DMSO-*d*<sub>6</sub>):  $\delta$  8.52 (d, 2H, 2 x *H*<sub>2</sub>), 8.34 (m, 3H, 3 x *H*<sub>1</sub>, *H*<sub>5</sub>), 8.29 (d, 2H, 2 x *H*<sub>6</sub>), 6.89 (s, 1H, *H*<sub>4</sub>) 6.41 (s, 1H, *H*<sub>3</sub>). **<sup>13</sup>C NMR** (126 MHz, DMSO-*d*<sub>6</sub>)  $\delta$  207.5, 148.0, 129.0, 127.8, 124.6 (ArC) **LC-MS** (Acetonitrile, 1 % formic acid): *R*<sub>t</sub> = 1.18 min, [*M* + *H*]<sup>+</sup> 469, 100 % purity. **FTIR**: 3067s (N-H), 1669m (C=O), 1601m (C=C), 1516m (N-H), 1516s (N-O) 1275s (C-N), 1142s (C-F) cm<sup>-1</sup>.



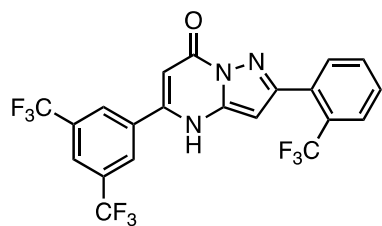
3.5.6 5-(3,5-Bis(trifluoromethyl)phenyl)-2-(3-(trifluoromethyl)phenyl)pyrazolo[1,5-a]pyrimidin-7(4H)-one (TUM-2A-013)



The general procedure **B** (Figure 3.25) was followed using 3-(3-(trifluoromethyl)phenyl)-1H-pyrazol-5-amine (0.10 g, 0.45 mmol) as the 5-aminopyrazole and ethyl 3-(3,5-bis(trifluoromethyl)phenyl)-3-oxopropanoate (0.22 g, 0.67 mmol) as the  $\beta$ -ketoester.

The resulting residue was purified *via* column chromatography (70:30 petroleum ether/EtOAc to 100% EtOAc) and the product was isolated as a pale-yellow solid (0.162 g, 73 %). **R<sub>r</sub>**: 0.4 (70:30 EtOAc /Pet Ether). **<sup>1</sup>H NMR** (500 MHz, DMSO-*d*<sub>6</sub>):  $\delta$  8.70 (s, 1H, *H1*), 8.58 (d, 2H, 2 x *H2*), 8.32 (s, 1H, Ar*CH*), 8.12 (ddd, 1H, *J* = 8 Hz, *H6*), 8.03 (s, 1H, Ar*H*), 7.68 (s, 1H, *J* = 8 Hz, Ar*H*), 6.70 (s, 1H, *H4*), 6.17 (s, 1H, *H3*). **LC-MS** (Acetonitrile, 1 % formic acid): *R<sub>t</sub>* = 1.18 min, [*M* + *H*]<sup>+</sup> 492, 95.5 % purity. **FTIR**: 3067s (N-H), 1669m (C=O), 1601m (C=C), 1516m (N-H), 1275s (C-N), 1142s (C-F) cm<sup>-1</sup>.

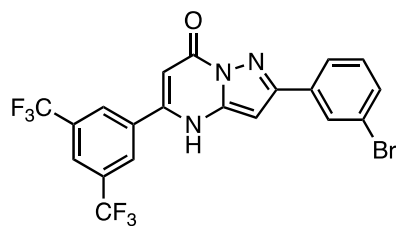
3.5.7 **5-(3,5-Bis(trifluoromethyl)phenyl)-2-(2-(trifluoromethyl)phenyl)pyrazolo[1,5-a]pyrimidin-7(4H)-one (TUM-2A-014)**



The general procedure **B** (Figure 3.25) was followed using 3-(2-(trifluoromethyl)phenyl)-1H-pyrazol-5-amine (0.11 g, 0.45 mmol) as the 5-aminopyrazole and ethyl 3-(3,5-bis(trifluoromethyl)phenyl)-3-oxopropanoate (0.22 g, 0.67 mmol) as the  $\beta$ -ketoester.

The resulting residue was purified *via* column chromatography (100% EtOAc to 95:5 EtOAc/MeOH) to yield the product as a dark green solid (0.110 g, 50 %). **R<sub>f</sub>**: 0.4 (100 EtOAc). **<sup>1</sup>H NMR** (500 MHz, DMSO-*d*<sub>6</sub>):  $\delta$  8.62 (d, 2H,  $J$  = 1.7 Hz, 2 x  $H_2$ ), 8.10 (s, 1H,  $H_1$ ), 7.83 (d, 1H,  $J$  = 7.9 Hz,  $H_5$ ), 7.74 (dt, 2H,  $J$  = 7.7 Hz,  $H_7$ ,  $H_8$ ), 7.62 (t, 1H,  $J$  = 7.6 Hz,  $H_6$ ), 6.33 (s, 1H,  $H_4$ ), 6.25 (s, 1H,  $H_3$ ). **<sup>13</sup>C NMR** (126 MHz, DMSO-*d*<sub>6</sub>)  $\delta$  207.5, 158.9, 151.3, 132.8, 132.6, 131.1, 130.8, 128.8, 127.3, 122.8, 89.7. **LC-MS** (Acetonitrile, 1 % formic acid):  $R_t$  = 1.18 min,  $[M + H]^+$  492, 98.4 % purity. **FTIR**: 3036s (N-H), 1635m (C=O), 1607m (C=C), 1623m (N-H), 1395s (C-N), 1230s (C-F)  $\text{cm}^{-1}$ .

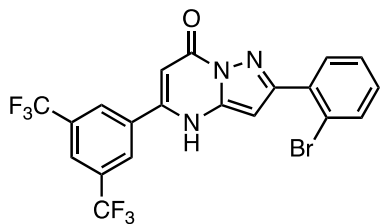
3.5.8 5-(3,5-Bis(trifluoromethyl)phenyl)-2-(3-bromophenyl)pyrazolo[1,5-a]pyrimidin-7(4H)-one (TUM-2A-015)



The general procedure **B** (Figure 3.25) was followed using 3-(3-bromophenyl)-1H-pyrazol-5-amine (0.11 g, 0.45 mmol) as the 5-aminopyrazole and ethyl 3-(3,5-bis(trifluoromethyl)phenyl)-3-oxopropanoate (0.22 g, 0.67 mmol) as the  $\beta$ -ketoester.

The resulting residue was purified *via* column chromatography (70:30 petroleum ether/EtOAc to 100% EtOAc) yielding the product as a pale yellow/white solid (0.176 g, 78 %). **R<sub>f</sub>**: 0.62 (100 EtOAc). **<sup>1</sup>H NMR** (500 MHz, DMSO-*d*<sub>6</sub>):  $\delta$  8.65 (s, 2H, 2 x *H*<sub>2</sub>), 8.15 (t, *J* = 1.8 Hz, 1H, *H*<sub>8</sub>), 8.12 (s, 1H, *H*<sub>1</sub>), 7.93 (dt, *J* = 7.9, 1.2 Hz, 1H, *H*<sub>7</sub>), 7.51 (ddd, *J* = 7.9, 1.8, 1.2 Hz, 1H, *H*<sub>5</sub>), 7.37 (t, *J* = 7.9 Hz, 1H, *H*<sub>6</sub>), 6.69 (s, 1H, *H*<sub>4</sub>), 6.33 (s, 1H, *H*<sub>3</sub>). **<sup>13</sup>C NMR** (126 MHz, DMSO-*d*<sub>6</sub>):  $\delta$  207.0, 131.0, 130.0, 127.0 **LC-MS** (Acetonitrile, 1 % formic acid): *R*<sub>t</sub> = 1.18 min, [*M* + *H*]<sup>+</sup> 503, 95.2 % purity. **FTIR**: 3086s (N-H), 1668m (C=O), 1603m (C=C), 1539m (N-H), 1276s (C-N), 680s (C-Br) cm<sup>-1</sup>.

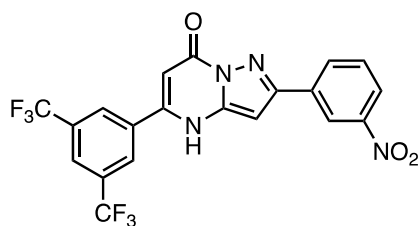
3.5.9 **5-(3,5-Bis(trifluoromethyl)phenyl)-2-(2-bromophenyl)pyrazolo[1,5-a]pyrimidin-7(4H)-one (TUM-2A-016)**



The general procedure **B** (Figure 3.25) was followed using 3-(2-bromophenyl)-1H-pyrazol-5-amine (0.11 g, 0.45 mmol) as the 5-aminopyrazole and ethyl 3-(3,5-bis(trifluoromethyl)phenyl)-3-oxopropanoate (0.22 g, 0.67 mmol) as the  $\beta$ -ketoester.

The resulting residue was purified *via* column chromatography (70:30 petroleum ether/EtOAc to 100% EtOAc) to yield the product as a yellow/green solid (0.152 g, 67 %). **R<sub>r</sub>**: 0.15 (70:30 EtOAc/pet. ether). **<sup>1</sup>H NMR** (500 MHz, DMSO-*d*<sub>6</sub>):  $\delta$  8.64 (s, 2H, 2 x *H*<sub>2</sub>), 8.09 (s, 1H, *H*<sub>1</sub>), 7.75 (d, *J* = 7.7 Hz, 1H, *H*<sub>5</sub>), 7.68 (d, *J* = 7.9 Hz, 1H, *H*<sub>8</sub>), 7.37 (t, *J* = 7.7 Hz, 1H, *H*<sub>6</sub>), 7.25 (t, *J* = 7.9, 1H, *H*<sub>8</sub>), 6.58 (s, 1H, *H*<sub>4</sub>), 6.32 (s, 1H, *H*<sub>3</sub>). **<sup>13</sup>C NMR** (126 MHz, DMSO-*d*<sub>6</sub>):  $\delta$  207.0, 159.0, 152.0, 134.0, 132.0, 131.0, 130.0, 128.0, 127.0, 125.0, 123.0, 122.0, 90.0 **LC-MS** (Acetonitrile, 1 % formic acid): *R*<sub>t</sub> = 1.18 min, [M + H]<sup>+</sup> 503, 99.4 % purity. **FTIR**: 2930s (N-H), 1604m (C=C), 1538m (N-H), 1275s (C-N), 680s (C-Br) cm<sup>-1</sup>.

3.5.10 5-(3,5-Bis(trifluoromethyl)phenyl)-2-(3-nitrophenyl)pyrazolo[1,5-a]pyrimidin-7(4H)-one (TUM-2A-017)

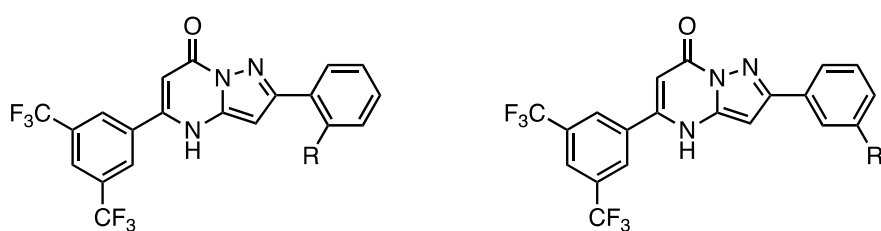


The general procedure **B** (Figure 3.25) was followed using 3-(3-nitrophenyl)-1H-pyrazol-5-amine (0.09 g, 0.44 mmol) as the 5-aminopyrazole and ethyl 3-(3,5-bis(trifluoromethyl)phenyl)-3-oxopropanoate (0.22 g, 0.67 mmol) as the  $\beta$ -ketoester.

The resulting residue was purified *via* column chromatography (70:30 petroleum ether/EtOAc) and the product was isolated as a dark yellow solid (0.149 g, 71 %). **R<sub>f</sub>**: 0.84 (70:30 EtOAc/pet. ether). **<sup>1</sup>H NMR** (500 MHz, DMSO-*d*<sub>6</sub>):  $\delta$  8.63 (d, 2H, 2 x *H*<sub>2</sub>), 8.15 (s, 1H, *H*<sub>1</sub>), 8.09 (s, 1H, *H*<sub>8</sub>), 7.94 (d, 1H, *J* = 7.8 Hz, *H*<sub>7</sub>), 7.52 (m, 1H, *H*<sub>5</sub>), 7.40 (t, 1H, *J* = 7.8 Hz, *H*<sub>6</sub>), 6.65 (s, 1H, *H*<sub>4</sub>), 6.22 (s, 1H, *H*<sub>3</sub>). **<sup>13</sup>C NMR** (126 MHz, DMSO-*d*<sub>6</sub>):  $\delta$  207.0, 131.2, 122.5 **LC-MS** (Acetonitrile, 1 % formic acid): *R*<sub>t</sub> = 1.18 min, [*M* + *H*]<sup>+</sup> 469, 97.1 % purity. **FTIR**: 3087s (N-H), 1606m (C=O), 1581m (C=C), 1581m (N-H), 1516s (N-O) 1275s (C-N), 1142s (C-F) cm<sup>-1</sup>.

### 3.6. Optimised HIT Compound Cell Viability Assays

The group 2A hit compounds were optimised and analogue compounds were generated. The group 2A analogue compounds are such that the  $R^1$  substituent is a 1,3-bis(trifluoromethyl)phenyl and the  $R^2$  substituent is varied but must be a substituted aryl ring. The structure of the group 2A compounds can be seen in Figure 3.26. The analogue hit compounds consist of the substituent on the aryl ring being moved to the *ortho* or *meta* positions.



**Figure 3.26** Structure of group 2A analogue compounds whereby the  $R^1$  functional group consists of a 1,3-bis(trifluoromethyl)phenyl substituent and the  $R^2$  group consists of varied substituted aryl ring groups in the *ortho* or *meta* position respectively.

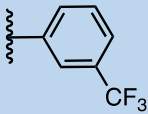
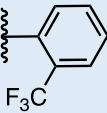
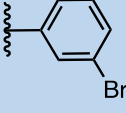
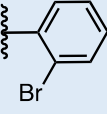
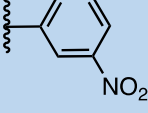
### **3.7. Results and Discussion of Biological Evaluation**

The analogue compounds were screened using a cancerous U251-MG cell line and a non-cancerous HEK293 cell line. The methods employed were those outlined in Chapter 2 whereby a compound with potential to cross the BBB must have an  $IC_{50}$  value less than 50  $\mu$ M and there must be statistical significance between the cancerous and non-cancerous cell line.

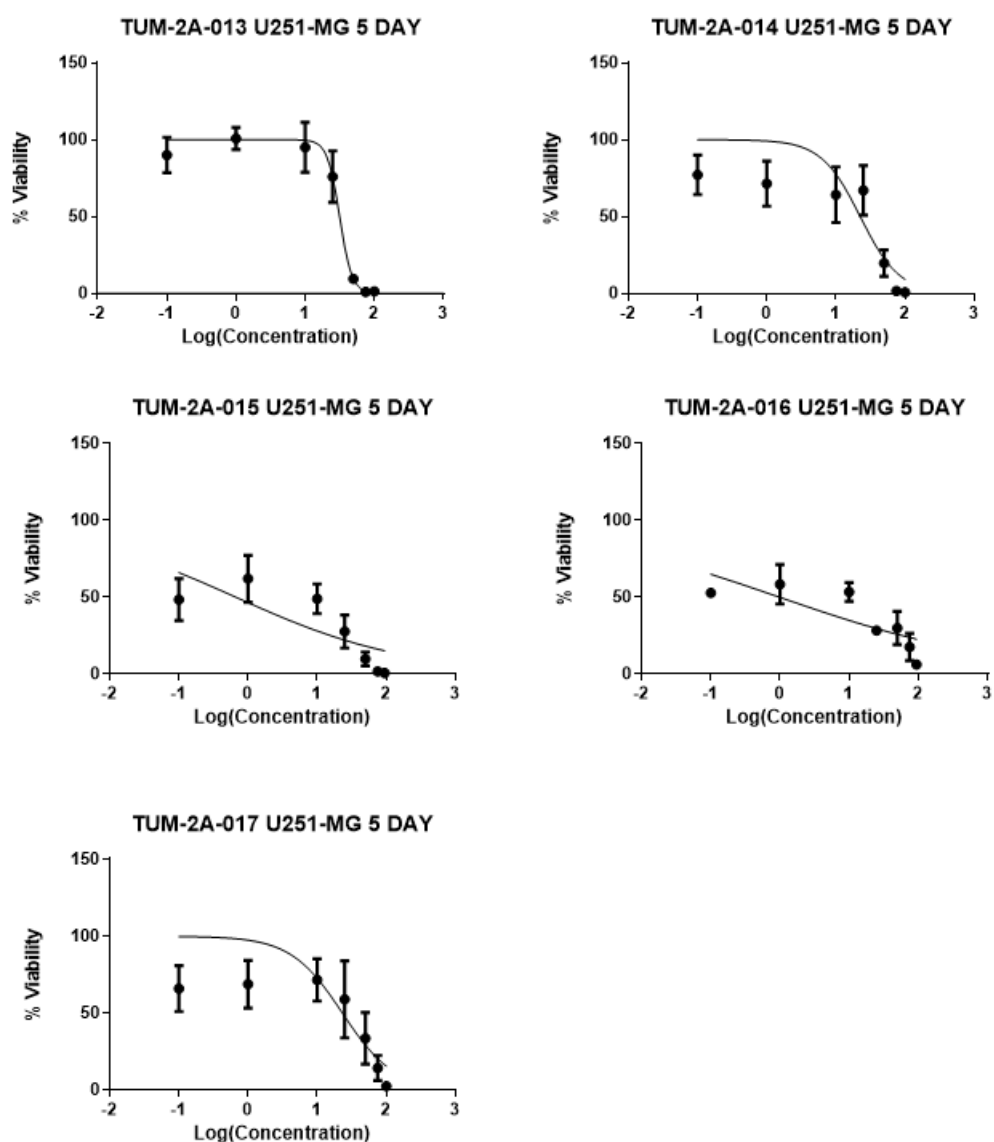
#### **3.7.1 U-251 MG Cell Line**

The results of the compound screen can be seen in Table 3-3. A biological response in the U251-MG cell screen is defined as the compounds having an  $IC_{50}$  value of < 50  $\mu$ M as previously discussed. A dose response curve was generated for all the compounds and is shown in Figure 3.27.

**Table 3-3 Results of U-251 MG cell screen on group 2A compound . Assay Conditions: U-251 MG cell line and the MTT cell viability assay. Cells were analysed 5 days after treatment, N=3**

Compound Name	R Group	IC <sub>50</sub> Value (μM)	IC <sub>50</sub> 95% CI (μM)	Hill Slope Value	Hill Slope 95% CI
TUM-2A-013		31.56	25.69 to 38.78	1.625	-8.275 to -1.471
TUM-2A-014		22.51	12.77 to 39.69	0.5705	-2.730 to -0.3415
TUM-2A-015		0.51	0.03464 to 7.459	0.1133	-0.5254 to -0.05108
TUM-2A-016		2.79	0.6168 to 12.61	0.07772	-0.4371 to -0.1118
TUM-2A-017		23.20	10.77 to 49.98	0.5085	-2.226 to -0.09778



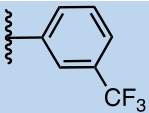
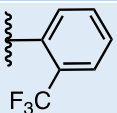
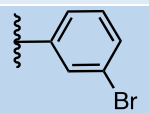
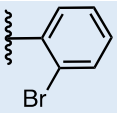
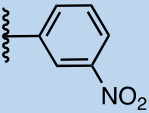


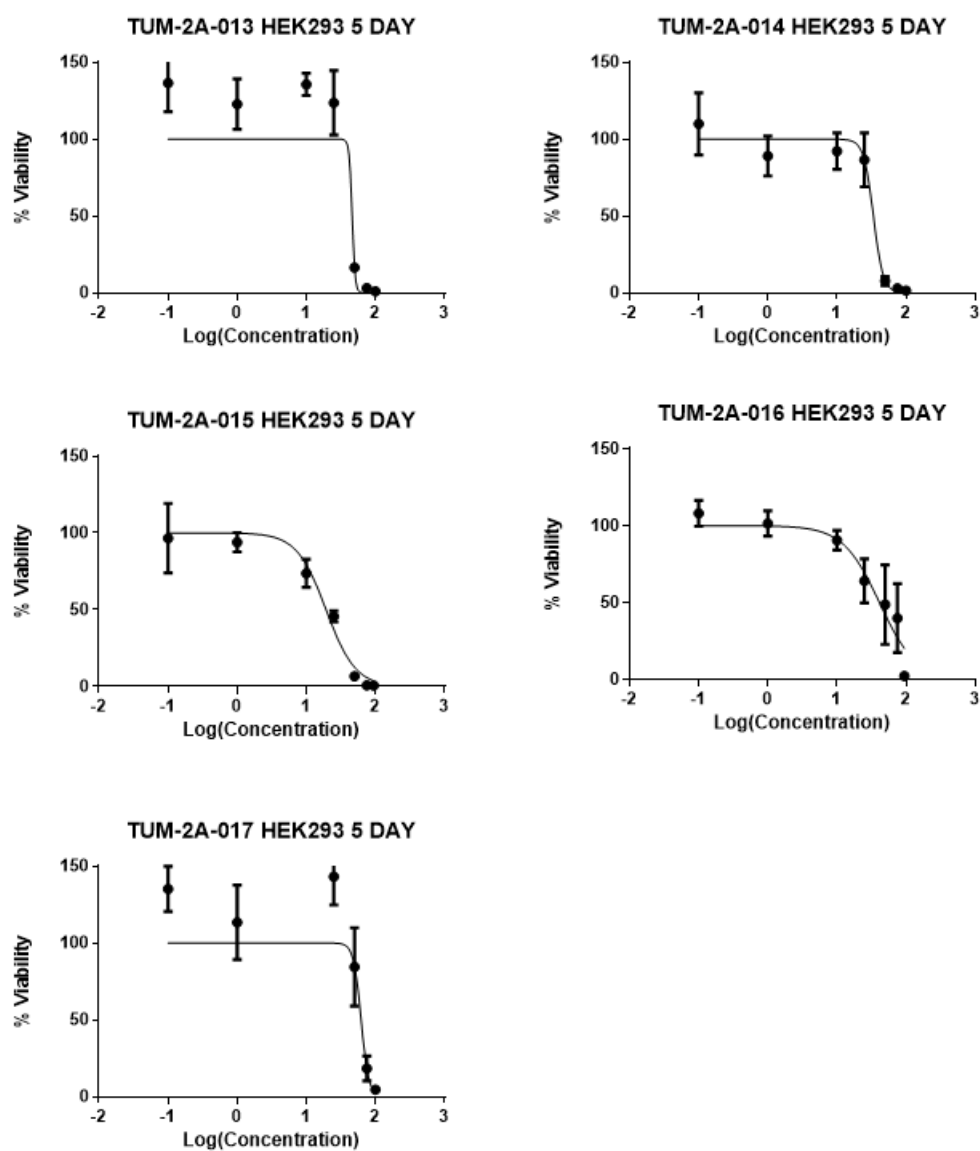
*Figure 3.27 Dose response curves for compounds in group 2A. Assay Conditions: U-251 MG cell line and the MTT cell viability assay. Cells were analysed 5 days after treatment, N=3. Where the X axis denotes the logarithmic concentration of compound, and the Y axis denotes the % cell viability.*

### 3.7.2 HEK293 Cell Line

The results of the group 2A compound screen on the HEK293 cell line can be observed in Table 3-4. Dose-response curves were generated for the compounds and are shown in Figure 3.28.

**Table 3-4 Results of HEK293 cell line screen on group 2A compounds. Assay Conditions: HEK293 cell line and the MTT cell viability assay. Cells were analysed 5 days after treatment, N=3. X is denoted where an experimental value was not possible.**

Compound Name	R Group	IC <sub>50</sub> Value (μM)	IC <sub>50</sub> 95% CI (μM)	Hill Slope Value	Hill Slope 95% CI
TUM-2A-013		46.16	X	X	X
TUM-2A-014		33.74	25.43 to 44.78	2.507	-11.40 to -0.9052
TUM-2A-015		18.64	13.64 to 25.49	0.3906	-2.576 to -0.9415
TUM-2A-016		67.03	50.09 to 89.71	1.978	-7.770 to 0.5075
TUM-2A-017		62.20	44.80 to 86.35	5.992	-20.44 to 4.645



**Figure 3.28** Dose response curves for compounds in group 2A. Assay Conditions: HEK293 cell line and the MTT cell viability assay. Cells were analysed 5 days after treatment, N=3. Where the X axis denotes the logarithmic concentration of compound, and the Y axis denotes the % cell viability.

### **3.7.3 Comparison of U-251 MG Cell Line and HEK293 Cell Line**

The analogue screen was carried out in two cell lines, the cancerous U251-MG cell line and the non-cancerous HEK293 cell line. As previously discussed as part of Chapter 2, an ideal compound is one which elicits a biological response in the cancerous cell line and does not elicit a response in the non-cancerous cell line i.e., has selectivity for the cancerous cell line. Statistical analysis was also carried out to determine whether the IC<sub>50</sub> results obtained can be deemed statistically significant. The first type of analysis carried out was curve fitting. The null hypothesis was that if the U251-MG dose response curve and the HEK293 dose response curve fitted on one line then the results are deemed statistically insignificant. The p value generated will also be  $\geq 0.05$ . Therefore, two separate curves are required for the result to be statistically significant. The IC<sub>50</sub> ranges for both dose-response curves were compared and if the ranges overlapped the results were also deemed statistically insignificant. The results from this analysis are shown in Table 3-5.

**Table 3-5 Comparison of IC<sub>50</sub> data generated to determine statistical significance.. The null hypothesis was such that to be statistically significant the IC<sub>50</sub> values for both cell lines would have two separate curves, the p value generated must also be < 0.05 and both IC<sub>50</sub> ranges must not overlap. The initial compounds which are deemed statistically significant are shaded in blue.**

COMPOUND NAME	U-251 MG IC <sub>50</sub> VALUE (μM)	HEK293 IC <sub>50</sub> VALUE (μM)	STATISTICALLY DIFFERENT YES/NO	STAT. DIFF. P VALUE	IC <sub>50</sub> RANGE STATISTICALLY DIFFERENT – YES/NO
TUM-2A-013	31.56	46.16	NO	N/A	NO
TUM-2A-014	22.51	33.74	NO	0.05	NO
TUM-2A-015	0.51	18.64	YES	0.0003	YES
TUM-2A-016	2.79	67.03	YES	<0.0001	YES
TUM-2A-017	23.20	62.20	YES	0.0259	NO

### 3.7.4 Statistical Analysis - ANOVA

The statistical test carried out to compare the two datasets was the two-way Analysis of Variance (ANOVA) statistical test. The two-way ANOVA test examines the effect of two factors on a dependant variable. In this case, the two factors were the cancerous U251-MG cell line and the non-cancerous HEK293 cell line, and the dependant variable was the compound. The null hypothesis was to see if there was a statistical difference between the two cell lines after being treated with the same compound. This statistical test further reinforces what compounds can be deemed statistically significant and so if the compound is significant across all three statistical tests, it can be referred to as a lead compound. Table 3-6 depicts a summary of results obtained from the statistical analysis. The P value style used on Prism is that outlined as per section 2.2.6.

***Table 3-6 Summary of results from two-way ANOVA statistical analysis whereby the P values are reported as follows:  $\geq 0.05$  (ns), 0.01 to 0.05 (\*), 0.001 to 0.01 (\*\*), 0.001 to 0.01 (\*\*\*) and  $< 0.0001$  (\*\*\*\*).***

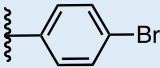
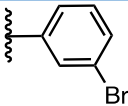
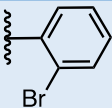
Compound	P Value Summary	Significant
<b>TUM-2A-013</b>	Ns	No
<b>TUM-2A-014</b>	Ns	No
<b>TUM-2A-015</b>	**	Yes
<b>TUM-2A-016</b>	***	Yes
<b>TUM-2A-017</b>	Ns	No

### 3.8. Biological Evaluation Discussion

The compounds that were screened as part of this chapter were analogue compounds of the previously determined hit compounds as per Chapter 2. It was found that each of the hit compounds contained R<sup>2</sup> substituents which were lipophilic and electron withdrawing in nature except for TUM-2A-008 which contained a strong electron withdrawing group but was not lipophilic. It was found that all five analogue compounds were selective for the cancerous cell line over the non-cancerous cell line however only two of these analogue compounds were determined to be statistically significant. The statistically significant compounds were TUM-2A-015 and TUM-2A-016 and are now termed hit compounds.

The new hit compounds contained a *meta* bromophenyl ring and an *ortho* bromophenyl substituent. It was found that by moving the bromo substituent from the *para* position as seen in TUM-2A-004 to the *meta* and *ortho* positions the IC<sub>50</sub> values were lowered significantly from 29.49 μM to 0.51 μM and 2.79 μM respectively. Thus, improving the selectivity and potency of the compounds as a smaller concentration of the compound is required to elicit cell death which would be ideal in a patient setting as there is a lower dose of a toxic compound being administered. By moving the bromo substituent from the *para* position to both the *meta* and *ortho* position, selectivity for the cancerous cell line was increased and the overall potency of the drugs were also increased. Table 3-7 highlights the different IC<sub>50</sub> values obtained when the bromo substituent is moved to different positions in the phenyl ring.

**Table 3-7** A comparison of the changes in the  $IC_{50}$  values for TUM-2A-004, TUM-2A-015 and TUM-2A-016 when the bromo substituent is moved to different positions in the phenyl ring.

Compound Name	R Group	$IC_{50}$ Value ( $\mu$ M)
TUM-2A-004		29.49
TUM-2A-015		0.51
TUM-2A-016		2.79

Further work will now be carried out as per Chapter 4 with the hit compounds to determine whether they are suitable for use as part of a potential co-treatment study with the current gold standard chemotherapeutic, TMZ. Flow cytometry will be utilised to determine whether the hit compounds are eliciting cell death and it will also confirm the cell death observed in the 2D cell viability assays carried out as per Chapter 2 and Chapter 3. A further look into the type of cell death being observed will be carried out via inhibitor studies. 3D cell culture will also be used to ascertain whether the hit compounds have the potential to induce cell death *in vivo* and if a lead compound can be identified.



**4. EVALUATION OF HIT COMPOUNDS FOR SUITABILITY IN A CO-TREATMENT  
STUDY FOR GBM AND DETERMINATION OF POTENTIAL MECHANISM OF  
ACTION OF HIT COMPOUNDS**

## **4.1. Introduction**

### **4.1.1 Co-Treatment Studies**

There are several factors which can be attributed to the difficulty in treating the grade IV cancer, GBM. One of the factors that makes GBM treatment so difficult is its tumour heterogeneity. Inter-tumour heterogeneity refers to the diversity within individual tumours whereby each tumour microenvironment has its own genetic alterations and is classified into different molecular subtypes (Friedmann-Morvinski, 2014). Single cell sequencing of five primary GBM tumours showed different gene expression in transcriptional programs associated with oncogenic signalling such as hypoxia, proliferation, and immune response (Mokhtari et al., 2017). The heterogenous environment can also make it very difficult to find a single chemotherapeutic agent which is effective in all of the tumour microenvironments (Friedmann-Morvinski, 2014). Another factor which causes difficulty in GBM treatment is delivering drugs to residual tumour cells where the BBB is less compromised which can lead to an insufficient therapeutic effect as well as sub optimal drug concentrations causing drug resistance. As a result of these challenges the use of combination therapy whereby drugs are combined that have different working mechanisms has gained popularity in recent years (Mokhtari et al., 2017).

Monotherapy can be defined as the use of one therapeutic to treat disease. Monotherapy is a very common approach used to treat different forms of cancer however it is deemed less successful than the combination therapy approach as monotherapy is more susceptible to drug resistance and is non-selective in targeting proliferating cells which can lead to the destruction of both healthy and cancerous cells (Ghosh et al., 2018). TMZ is the current gold standard drug used in the treatment of GBM however severe side effects such as toxic DNA damage, vomiting, fatigue, and drug resistance are common in patients. A potential approach to improve

the first-line treatment of GBM may be to explore a more effective combination regimen (Ghosh et al., 2018). The use of TMZ in combination with other chemotherapeutic agents have been outlined in Chapter 1, section 1.4.3 (Singh et al., 2021).

#### **4.1.2 Drug Co-Treatment**

Combination therapy or co-treatment studies can be defined as having two or more therapeutic approaches to treat disease. The success of combination therapy relies on three factors; the first factor is such that each component of therapy should have a single activity with no cross resistance. The second factor is that combination therapy should ideally work in an additive manner and the third factor is that each component should have separate safety criteria (Ghosh et al., 2018).

Combination therapy works in such a manner that lower doses of a combination of individual anti-cancer drugs are administered. The amalgamation of anti-cancer drugs enhances efficacy compared to the monotherapy approach because it targets key pathways in a synergistic or additive manner. This approach generally reduces drug resistance, provides therapeutic anti-cancer benefits such as slowing and reducing tumour growth and reduces drug toxicity to healthy cells (Mokhtari et al., 2017). Typically when lower doses of an individual drug, particularly antibiotics are administered leads to excessive drug use and ultimately leads to drug resistance (MacVane, 2017). Chemotherapeutic agents are toxic, however when they are used as part of combination therapy the toxicity to healthy cells is significantly less as different pathways will be targeted. This therefore works in a synergistic manner whereby a lower therapeutic dose of each treatment is administered (Mokhtari et al., 2017).

Combined strategies such as nanocarriers and co-treatments have been explored in an effort to combat TMZ resistance. An example of such a treatment is the use of antibodies nimotuzumab

and bevacizumab to block the effects of EGFR VIII, a mutated EGFR. The mutated EGFR is expressed in GBM cells and enhances tumorigenicity and drug resistance (C. Y. Lee, 2017). In mice, nimotuzumab enhanced the effect of TMZ in suppressing the growth of EGFR VIII expressed glioma cells (Nitta et al., 2016). The use of bevacizumab in conjunction with TMZ was studied in a phase II trial and was shown to improve the patient overall survival with a median value of 21.1 months and progression-free survival time with a median value of 14.2 months (Narita, 2015)(Lai et al., 2011).

Combination therapy using the hit compounds will be trialled as part of this chapter as there could potentially be a positive, synergistic effect when used in conjunction with the current gold standard therapeutic, TMZ.

### **4.1.3 Flow Cytometry**

#### ***4.1.3.1 Cell Death and Flow Cytometry***

Flow cytometry was used to confirm the MTT cell proliferation assay whereby cell death was observed when the cancerous cell line was treated with the hit compounds. Flow cytometry was also used to determine how the hit compounds are potentially eliciting cell death and so two very broad dyes were used; propidium iodide (PI) and JC-1. PI looks at cell death via loss of membrane integrity which is a common feature of regulated cell death. The principle of PI is such that it is a membrane impermeant dye. It is excluded from viable cells and emits green fluorescence however it can penetrate dead cells through loss of membrane integrity and stain DNA. The bound PI – DNA (stained DNA) emits bright red fluorescence. PI is therefore widely used to evaluate cell viability and measure the DNA content in cell cycle analysis (Crowley et al., 2016). The second dye used was the JC-1 dye whereby it looks at mitochondrial membrane depolarization whereby the mitochondria play key roles in activating apoptosis and other regulated cell death pathways in mammalian cells. The principle of the JC-1 dye is such that JC-1 can enter healthy mitochondria and form aggregates which change the fluorescent property of the dye, and these aggregates can then emit red fluorescence. Unhealthy or apoptotic cells do not form aggregates in the mitochondria and so exhibit green fluorescence. The higher the ratio of red to green fluorescence, the higher the polarisation of the mitochondrial membrane thus showing higher levels of apoptosis (Sivandzade et al., 2019).

Cell death, in particular apoptosis is one of the most widely studied areas in cell biology. Understanding apoptosis in disease is important as it can provide information on the pathogenesis of the disease and how the disease can be treated (Wong, 2011). The broad-spectrum cell death experiments could potentially narrow down a mechanism of action for the hit compounds.

Flow cytometry is a technique which allows for large scale, automated quantification of cells based on their optical parameters on a cell-by-cell basis (Maruccio et al., 2019). It is a powerful tool which has uses in immunology, molecular biology, cancer biology and infectious disease monitoring (McKinnon, 2018). Clinics and hospitals worldwide utilise this method as cell counting is a useful tool to determine the health of a patient. This is because blood is rich with cells and proteins which provide a wealth of information with regards to general health (Maruccio et al., 2019).

Flow cytometers use lasers as light sources which produce scattered and fluorescent signals. These signals are read by detectors which are then converted to electronic signals that are analysed by a computer (McKinnon, 2018). The data obtained provides information about the biochemical, biophysical, and molecular aspects of particles. Light scattering is directly related to the structural and morphological properties of the cell. Fluorescence emission derived from a fluorescent probe is proportional to the amount of fluorescent probe bound to the cell or cellular component (Adan et al., 2016).

Visible light scatter is measured in two directions, forward scatter (FSC) which can indicate the relative size of the cell and side scatter (SSC) which indicates the internal complexity or granularity of the cell. The most common lasers used in flow cytometers are 488 nm (blue), 405 nm (violet), 532 nm (green), 552 nm (green), 561 nm (green - yellow), 640 nm (red) and 355 nm (ultraviolet) (McKinnon, 2018). The principle of this technique therefore is such that the light absorption of certain markers can provide information such as qualitative or quantitative analysis of cell viability. Limitations of this technique include where dead cells can be shown as living cells when they are in the early stages of apoptosis (Hu et al., 2021).

“Gating” can be defined as the selection of subpopulations of cells for analysis in flow cytometry. It is usually performed manually by visually examining flow cytometry data. This is accomplished using flow cytometry software (CytExpert software version 2.4.0.28). This software allows for the identification of subsets of cells in a population and to assess the expression levels of markers of interest on those selected subsets. Gating is subjective and there can be substantial variation of the same data set when examined by different analysts. In addition to requiring analyst expertise, factors such as the quality of staining, sample integrity and fluorescence spill over can affect gating as it affects the cell population resolution (Staats et al., 2019).

A trigger gate can be defined as excluding events such as noise or excluding debris based on particle size. The most common trigger gate which excludes cellular debris based on size is the use of forward scatter (FSC). By using forward scatter, the trigger gate excludes events that are too small to be considered cells. An exclusion gate is used to remove unwanted cell populations before positive gating on markers of interest. Studying cell viability is an example of why exclusion gates are important, this is due to the fact that alive cells have an intact cell membrane and exclude the fluorescent dye from entering the cell and binding. An example of such a dye is propidium iodide (Staats et al., 2019).

#### ***4.1.3.2 Propidium Iodide***

PI is a small fluorescent molecule that binds to DNA but cannot pass through an intact cell membrane. PI uptake versus exclusion can be used to identify and quantify necrotic or late apoptotic cells whereby the plasma membrane becomes permeable regardless of the mechanism of cell death. PI is excited by wavelengths of 400 – 600 nm (green) and emits light between wavelengths of 600 – 700 nm (red). It is therefore compatible with lasers and photodetectors used in a flow cytometer (Crowley et al., 2016).

#### ***4.1.3.3 JC-1 Dye***

The JC-1 dye (5,5,6,6'-tetrachloro-1,1',3,3'-tetraethylbenzimidazolylcarbocyanine iodide) is a lipophilic, cationic dye which naturally emits green fluorescence. The principle of the JC-1 dye has been discussed previously in section 4.1.3.1. As the JC-1 dye utilises both red and green channels, corrections must be made for potential fluorescence spill over, this is termed “compensation”. Compensation is carried out to remove the signal from a fluorochrome from all detectors except for the one measuring the dye. The FITC fluorescence is predominant in the detector at 530 nm filter (green) and the PE fluorescence is predominant in the detector with a 595 nm filter (red). However, some FITC fluorescence can appear in the PE filter due to the emission overlap. This signal is termed spill over. It should be noted that when two dyes or channels are used that spill over will always occur. Proper compensation is when the centre of both populations aligns and can be seen in the quadrant graph (Roederer, 2002)(Perelman et al., 2012).



#### 4.1.4 Inhibitor Studies

Enzyme inhibitors and inactivators have transformed human medicine and are comprised of roughly half of all marketed drugs (Holdgate et al., 2018). Mechanistic enzymology is used in this study whereby three inhibitors were used in conjunction with the hit compounds to ascertain a potential mode of cell death observed in the compounds. The inhibitors used as part of this study are as follows: The E-64 inhibitor, SP600125 and the zVAD-fmk inhibitor. E-64 and zVAD-fmk are both used to prevent apoptosis and the SP600125 inhibitor is widely used to inhibit JNK activation and apoptosis (Wadhawan et al., 2014) (Li et al., 2019). JNK activation is linked to apoptosis as they can activate apoptotic signalling through the upregulation of genes or by varying mitochondrial pro and anti-apoptotic proteins through phosphorylation events (Lin et al., 2013) The three broad aforementioned inhibitors were chosen as they are broad inhibitors which look primarily at apoptosis and carry on from the flow cytometry work.

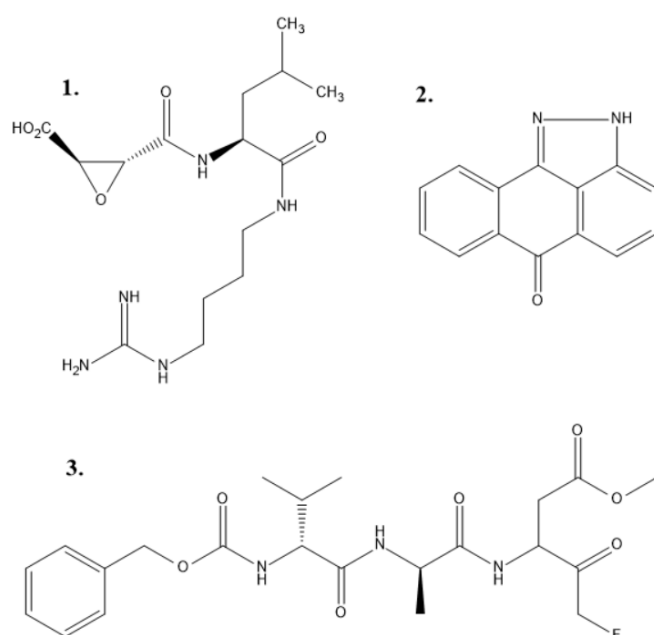
The two cysteine protease inhibitors that are used as part of the inhibitor studies are E64, an irreversible inhibitor of cysteine proteases and the irreversible pan-caspase inhibitor benzyloxycarbonyl-Val-Ala-Asp-fluoromethyl ketone (zVAD-fmk). E-64 is a potent irreversible inhibitor against general cysteine proteases such as papain, cathepsin B and cathepsin L. The main advantage of this inhibitor is its low toxicity and its high potency (Vidal-Albalat & González, 2016). E-64 is also an inhibitor against calpains which are a family of cysteine proteases that are calcium dependent (Y. Wang et al., 2020). It should be noted that E-64 does not irreversibly inhibit cysteine peptidases such as caspases (Vidal-Albalat & González, 2016).

zVAD-fmk was originally designed as an inhibitor for cysteine proteases but was subsequently found to efficiently inhibit the proteolytic activity of other enzymes in the caspase family

(Cordara et al., 2016). One of the main biochemical changes observed in apoptosis is the activation of caspases (cysteine aspartyl proteases) (Wong, 2011). Human caspases can be divided into two functional groups: those related to caspase which are involved in cytokine processing during inflammatory processes (caspase 1, 4, 5, 13 and 14) and caspases which play a central role in apoptosis (caspase 2, 3, 6, 7, 8, 9 and 10). The caspases which play a role in apoptosis can be further classified as either initiator caspases or effector caspases. Initiator caspases (caspase 2, 8, 9 and 10) are primarily responsible for the initiation of the apoptotic pathway. Effector caspases (caspase 3, 6 and 7) are responsible for the actual cleavage of cellular components during apoptosis (Wong, 2011)(Julien & Wells, 2017). The zVAD-fmk inhibitor is referred to as an irreversible pan caspase inhibitor whereby the term pan caspase refers to a broad-spectrum caspase inhibitor and has been shown to prevent apoptosis (Fransolet et al., 2019).

The c-Jun amino-terminal kinase (JNK) signalling pathway is a member of the large mitogen-activated protein kinase (MAPK) family. Upon activation, JNK has roles in cell growth, proliferation, apoptosis, and inflammatory responses. It has been suggested that JNK is implicated in the incidence and progression of cancer (Wu et al., 2020). It has become an important and promising target in diseases such as chronic inflammation, neurodegenerative diseases, and cancer progression (He et al., 2016)(Wu et al., 2020). JNK signalling is chronically altered in several tumours including glioblastoma (Jin et al., 2018). The JNK family is encoded by three genes: JNK1, JNK2 and JNK3 whereby JNK1 and JNK2 genes are expressed all over the body. The JNK3 gene is restricted to the brain, heart and testes (Wu et al., 2020). An example of a JNK inhibitor is the SP600125 (Anthrapyrazolone) reversible ATP-competitive inhibitor (Fan et al., 2021). SP600125 which is effective for JNK1, JNK2 and JNK3 proteins will be used in this study to determine whether the HIT compounds are involved

in JNK signalling. The structures of the three inhibitors used as part of this study are shown in Figure 4.1.



**Figure 4.1 Inhibitor Structures: 1. The structure of the E-64 inhibitor. 2. The structure of the SP600125 inhibitor. 3. The structure of the z-VAD-fmk inhibitor.**

#### 4.1.5 3D Cell Culture

Drug discovery is the most important aspect in the field of medicine and pharmacology. It requires extensive amounts of time and money and can yield low success rates in pre-clinical trials and in animal studies. Less than half of all drugs in phase II and phase III clinical trials are successful and so there is a need for new methods and technologies to improve the efficacy of drug discovery (Jensen & Teng, 2020).

3D cell culture has become an increasingly popular method used to bridge the gap between 2D cell culture and *in vivo* studies. 3D cell culture is widely used in cancer cell studies to evaluate cell differentiation, intracellular interactions and in the evaluation of substance toxicity and efficacy of potential drugs (Białkowska et al., 2020). When performing experiments using 3D cell culture, the cell environment can be manipulated to mimic that of a cell *in vivo* thus providing more accurate information about tumour characteristics and drug behaviour (Jensen & Teng, 2020). There are several formats and materials available which help the culturing of cells in 3D. A review was carried out by (Wanigasekara et al., 2023) which looks at the different 3D techniques that can be used as well as their advantages and disadvantages. A summary of this review is outlined on Table 4-1.

**Table 4-1 3D cell culture techniques such as hydrogel-based support, hanging drop plate, scaffold based, magnetic levitation, and microfluidic device as well as their advantages and disadvantages** (Wanigasekara et al., 2023).

3D Culture Method	Advantages	Disadvantages
<b>Hydrogel-Based Support</b>	Cells can be easily recovered for further analysis. Greater similarity to the in vivo conditions. Wide variety of polymers are available.	Low repeatability depending on the cell line. Batch to batch variation. Low optical transparency.
<b>Hanging Drop Plate</b>	Relative simplicity. Relative low cost. Uniform spheroid size control.	Smaller culture medium. Not suitable for drug testing. Smaller size of spheroids.
<b>Scaffold Based</b>	Greater similarity to the in vivo conditions. Compatibility with all cell types. Direct visualization.	Difficulty of cell retrieval. Expensive for large scale production. Not suitable for drug testing.
<b>Magnetic Levitation</b>	Relative simplicity. Efficient. Easy to collect spheroids and change media.	Magnetic beads need pre-treatment and can be expensive. Limited applications. Numerous cells attach to bottom of plate.
<b>Microfluidic Device</b>	Ability to control spheroid size and parameters. Commercially available. Larger amounts of data may be obtained from smaller samples.	High cost for microfabrication and devices. Requires expertise. Difficult to collect cells for further analysis.

Examples of 3D cell culture methods include hydrogel and scaffold methods. Disadvantages of 3D culture using these methods were found to be that the methods were not reproducible. It was found that the efficiency, life span and repeatability of work was poorer in these systems. This problem was solved by Vinci et al., where a spheroid based functional assay was developed using low attachment 96 well plates to create one spheroid per well. It was shown that the size of the spheroids was reproducible when compared to other methods (Kapałczyńska et al., 2018).

The method used in this study was the use of low adhesion plates. Low adhesion plates are specialised cell culture plates with an ultra-low attachment hydrophilic polymer coating which promotes cell aggregation to form spheroids. This coating can consist of poly-HEMA (poly-2-hydroxyethyl methacrylate), agarose, bovine serum, albumin or agar. The hydrophilic polymer coating prohibits protein adsorption to the culture surface which therefore minimises monolayer cell adhesion to the culture vessel. These low attachment plates promote aggregation of cells by cell to cell and cell to extracellular matrix (ECM) interactions. There are several advantages in using these low adhesion plates such as they are easier to handle with higher reproducibility and they have the ability to generate a wide range of tumour types. As with every method there are disadvantages associated with it, an example of such would be that it is a very labour intensive and time consuming method (Wanigasekara et al., 2023).

From this, it can be said that the final aims and objectives of Chapter 4 are to firstly evaluate the hit compounds and determine whether they would be suitable for use as part of a co-treatment study using the current gold-standard therapeutics. The second aim of this chapter was to determine whether the compounds were eliciting cell death, this was carried out using flow cytometry. The flow cytometry analysis will confirm the cell viability assays that were carried out as part of Chapter 2 and Chapter 3. The third aim of this chapter was to elicit a particular type of cell death that could be occurring by utilising inhibitor studies. Three inhibitors were used: E-64, SP600125 and zVAD-fmk. Each of the inhibitors utilised look at different common pathways which induce apoptosis. The final aim of this chapter was to utilise 3D cell culture to ascertain whether the hit compounds have the potential to induce cell death *in vivo* and if a lead compound can be identified.

## **4.2. Materials and Methods**

### **4.2.1 Co-Treatment Studies**

#### ***4.2.1.1 Preparation of Stock Solution for TMZ***

TMZ (Merck) was dissolved in DMSO to obtain stock concentrations whereby the solubility is 5 mg mL<sup>-1</sup> as per the safety data sheet. (Merck, 2021) The working stock solution of TMZ did not exceed a DMSO value of 0.05 %. This working solution was without any cytotoxic effects.

#### ***4.2.1.2 TMZ Combination Therapy***

TMZ (Merck, Ireland) is the gold standard drug for GBM and was used as part of combination therapy with the hit compounds; TUM-2A-001, TUM-2A-004, TUM-2A-007, TUM-2A-008, TUM-2A-015 and TUM-2A-016. TMZ was reconstituted in DMSO at a stock concentration of 128.75 µM and stored at -20 °C. TMZ working solutions (120, 100, 50, 25, 10, 1, 0.1) µM were then prepared. U251-MG cells were plated in 96 well plates (Sarstedt) at a seeding density of 2 x 10<sup>4</sup> cells per well (5 days) where the total volume per well was 100 µL. The cells were incubated for 24 hours and then equal aliquots of both the compound IC<sub>50</sub> and TMZ drug concentration were added to falcon tubes, mixed, and subsequently pipetted on the plate. Table 4-2 outlines the compound IC<sub>50</sub> values used in the treatments. The cell exposure time was a period of 5 days. Cell viability was assessed after 5 days using the MTT assay. Dose response curves were then plotted, and statistical analysis carried out using the GraphPad software version 8.0.0 for Windows, GraphPad Software, San Diego, California USA, [www.graphpad.com](http://www.graphpad.com) (GraphPad, 2020). Cells were also treated using controls whereby the



negative control used was untreated cells containing DMEM and 0.5 % DMSO and the positive control used was untreated cells containing DMEM and 20 % DMEM.

## **4.2.2 Flow Cytometry**

### **4.2.2.1 Propidium Iodide**

Stock solutions of propidium iodide (PI) dye (Merck, Ireland) were prepared at  $10\text{ }\mu\text{g mL}^{-1}$  in PBS and stored at  $-20\text{ }^{\circ}\text{C}$ . U251-MG cells were plated in 96 well plates (Sarstedt) at a seeding density of  $2 \times 10^4$  cells per well (5 days) where the total volume per well was  $100\text{ }\mu\text{L}$ . U251-MG cells were treated with fresh drug after 24 hours. The U251-MG cells were collected after the 5-day incubation period and pipetted into  $15\text{ mL}$  falcon tubes. A wash step was carried out whereby  $100\text{ }\mu\text{L}$  of PBS was pipetted into each well and was then collected and added to the corresponding falcon tube.  $50\text{ }\mu\text{L}$  of trypsin was added to each well and was incubated for a period of 6 minutes.  $100\text{ }\mu\text{L}$  of DMEM was then added to each well. Cell suspension was collected and added to the corresponding falcon tube. Cells were then centrifuged at  $1,200\text{ rpm}$  for 5 minutes. The supernatant was removed, and  $1\text{ mL}$  of sterile PBS was added to the falcon tube. Cells were then transferred to an Eppendorf tube. A PI working solution of  $2.5\text{ }\mu\text{g mL}^{-1}$  was made up in PBS. (Conway et al., 2016)  $10\text{ }\mu\text{L}$  of PI stain was added to the Eppendorf tubes and the tubes were incubated for a period of 15 minutes. Cells were also treated using controls whereby the negative control used was DMEM and 0.5 % DMSO and the positive control used was media and 20 % DMEM. It should be noted that 20 % DMEM was used as cells are still needed for the positive control and so to use 100 % DMEM, the cells would not be viable and so no cell count would be possible. The cells were then analysed using flow cytometry (Beckmann Coulter, CytExpert version 2.4.0.28). Fluorescence was measured using the FL2 channel. PI was detected in the red channel which is R-phycoerythrin (PE-Cy5). PE was used

206

in combination with fluorescein isothiocyanate (FITC) and is excited at a wavelength of 488 nm (McKinnon, 2018).

#### ***4.2.2.2 Propidium Iodide Analysis***

Necrosis and late apoptosis was detected by measuring the permeability of the plasma membrane to a normally impermeable fluorescent dye such as the DNA binding dye propidium iodide (Cummings et al., 2004). Gates were set for forward scatter (FSC) and side scatter (SSC) to ensure all cells are counted. The measurement of FSC allows the size of the cell to be determined, the higher the FSC intensity, the larger the cell. The measurement of SSC is used to identify cells with varying complexity such as granularity. This is referred to as P1. PI was detected in the red channel which is R-phycoerythrin (PE-Cy5). A graph of the fluorescence (PE) versus the cell count was then created. This determines which cells have high or low PI fluorescence. Living cells are larger (high FSC) and are less granular (low SSC) thus having low PI fluorescence whereas the opposite can be said for dead cells. P2 is allocated to living cells and P3 is allocated to dead cells.(Crowley et al., 2016) Samples were then analysed using quadrants whereby a graph is divided into four parts: the upper left quadrant (UL), the upper right (UR) quadrant, the lower left (LL) quadrant and the lower right (LR) quadrant. This graph will provide information about the cell cycle. Viable cells will remain in the LL quadrant as no stain entered these cells. Early-stage apoptotic cells are those with increased fluorescence intensity and are denoted in the LR quadrant. Necrotic cells are also associated with increased fluorescence intensity and are observed in the UL quadrant. Cells which are present in the UR quadrant indicate late-stage apoptosis when the membrane is no longer intact (Cummings et al., 2004)(Jafarlou et al., 2016).

A table outlining the concentrations of the drugs used is shown in Table 4-2. The highest toxic concentration is the concentration which was the maximum concentration the hit compound would allow in terms of solubility in DMSO, e.g., the highest concentration of TUM-2A-001 that could be prepared was 45  $\mu$ M due to its solubility in DMSO. The IC<sub>50</sub> values outlined are those determined as per Chapter 2 and 3. The highest non-toxic concentration of the hit compound used was determined via extrapolation of the initial dose response curves that were carried out as per Chapter 2 and 3. This is the highest concentration value on the dose-response curve in which the hit compound was not toxic to the cells, in general it was one of the lower concentration values used.

**Table 4-2 Hit compounds used for flow cytometry analysis, including the highest toxic concentrations, the IC<sub>50</sub> value and the highest non-toxic drug concentration.**

Compound Name	Highest Toxic Concentration (μM)	IC <sub>50</sub> Value (μM)	Highest Non-Toxic Concentration (HNT) (μM)
<b>TUM-2A-001</b>	45	6.17	0.1
<b>TUM-2A-004</b>	50	29.49	1
<b>TUM-2A-007</b>	50	26.75	10
<b>TUM-2A-008</b>	50	29.62	5
<b>TUM-2A-015</b>	50	0.66	1
<b>TUM-2A-016</b>	50	2.79	1

#### ***4.2.2.3 Propidium Iodide Flow Cytometry Analysis***

The data obtained via the flow cytometry CytExpert software was then exported via MS excel and analysed using the software GraphPad Prism version 8.0.0 for Windows, GraphPad Software, San Diego, California USA, [www.graphpad.com](http://www.graphpad.com) (GraphPad, 2020). A graph of the % dead cells was then produced whereby the total number of dead cells (P3) was divided by the total cell population (P1) which is shown on the y axis verses the cell treatment which is shown on the x axis. This procedure was carried out for each hit compound.

#### ***4.2.2.4 JC-1 Dye***

Stock solutions of JC-1 dye (Merck, Ireland) were prepared at  $1 \text{ mg mL}^{-1}$  in DMSO and stored at  $-20^\circ \text{C}$ . U251-MG cells were plated in 6 well plates (Sarstedt) at a seeding density of  $2 \times 10^4$  cells per well (5 days) where the total volume per well was  $1000 \mu\text{L}$ . Cells were collected after the incubation period and pipetted into falcon tubes. Cells were then harvested by trypsinisation, incubated for a period of 6 minutes, and pelleted at 1200 rpm for 5 minutes. A JC-1 working solution of  $2 \mu\text{g mL}^{-1}$  was made up in DMEM and was light protected. The cell pellet was resuspended and stained with  $2 \mu\text{g mL}^{-1}$  JC-1 dye and incubated and protected from the light for a period of 10 minutes (Conway et al., 2016). Cells were then centrifuged at 1200 rpm for 5 minutes. The supernatant was removed, and cells were washed with 1 mL of sterile PBS. This was repeated twice. The cells were resuspended in sterile PBS where the cell pellet was observed to be red in colour. Cells were also treated using controls whereby the negative control used was DMEM and 0.5 % DMSO and the positive control used was media and 20 % DMEM. The cells were then analysed using flow cytometry (Beckmann Coulter, CytExpert version 2.4.0.28). Fluorescence was measured using FL1 (FITC) (530 nm) and FL2 (PE) (595 nm) channels with emission.

#### ***4.2.2.5 JC-1 Dye Analysis***

When carrying out the analysis of the data, the ratio of monomers / aggregates was investigated, i.e., green / red fluorescence = unhealthy cells / healthy cells. Therefore, an increase in the green / red ratio indicates mitochondrial depolarisation whereby a loss of mitochondrial membrane potential is associated with apoptosis (Perelman et al., 2012). The mean FITC fluorescence was divided by the mean PE fluorescence which is termed the green / red fluorescence ratio. The higher ratio observed equates to apoptotic cells and the lower the ratio observed equates to viable cells. Compensation was also carried out to ensure the centre of both populations aligns and is shown in the quadrant graph. The compensation was carried out whereby in the FITC channel PE was allocated 10 % compensation and in the PE channel FITC was allocated 80 % compensation. This compensation was used throughout the thesis for JC-1 dye analysis.

#### ***4.2.2.6 JC-1 Dye Flow Cytometer Analysis***

The data from the flow cytometry CytExpert software was exported via excel and analysed using the software GraphPad Prism version 8.0.0 for Windows, GraphPad Software, San Diego, California USA, [www.graphpad.com](http://www.graphpad.com) (GraphPad, 2020). A graph of the fluorescence ratios was determined whereby the mean fluorescence values for FITC and PE were divided against one another and were plotted on the y axis against the controls and substance treatment which is shown on the x axis. This procedure was carried out for each hit compound.

### **4.2.3 Inhibitor Studies**

#### ***4.2.3.1 E-64 Inhibitor***

The irreversible cysteine protease inhibitor E-64 (Fisher Scientific) was used to determine whether cysteine proteases play a role in cell death in U251-MG cells. E-64 was reconstituted in DMSO at a stock concentration of 1 mM and stored at -20 °C. Cells were pre-treated with a 10 µM working solution of E-64 for a period of one hour as per the inhibitor protocol (Conway et al., 2016) (Fisher Scientific). E-64 was then removed from each well and replaced with the IC<sub>50</sub> of the fresh drug. Cell viability was assessed after 5 days using the MTT assay. Cells were also treated using controls whereby the negative control used was media and 0.5 % DMSO and the positive control used was 1.5 µM and 2 µM Ionomycin (Merck, Ireland) (Conway et al., 2016).

#### ***4.2.3.2 SP600125 Inhibitor***

SP600125 is a reversible JNK inhibitor commonly associated with apoptosis. SP600125 (Fisher Scientific) was reconstituted in DMSO at a stock concentration of 25 mM and stored at -20 °C. Cells were pre-treated with 100 µL of 12.5 µM working solution SP600125 for a period of one hour as per the inhibitor protocol this was done by aspirating the old media and replacing it with the working solution (Conway et al., 2016) (Fisher Scientific). 90 µL of SP600125 was then removed by pipetting and the IC<sub>50</sub> of the fresh drug was then pipetted into each well where 96 well plates were used (Merck, Ireland). Cell viability was assessed after 5 days using the MTT assay. Cells were also treated using controls whereby the negative control used was DMEM and 0.5 % DMSO and the positive control used was UV irradiation (Conway et al., 2016).

#### **4.2.3.3 zVAD-fmk Inhibitor**

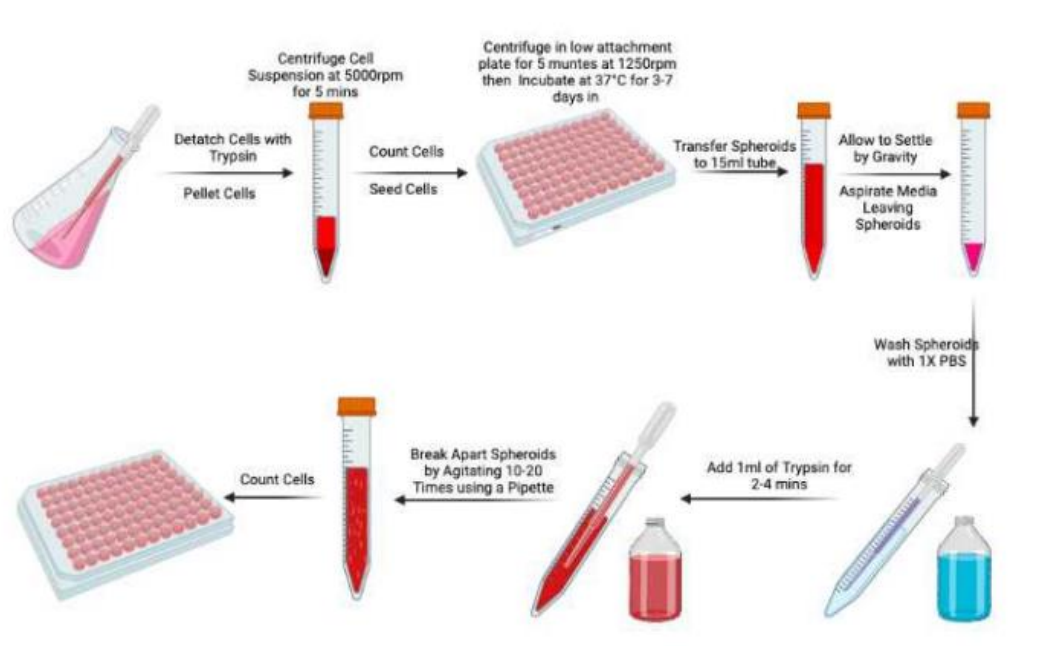
The irreversible general caspase inhibitor zVAD-fmk (Fisher Scientific) was used to determine whether caspases play a role in cell death in U251-MG cells. zVAD-fmk was reconstituted in DMSO at a stock concentration of 10 mM and stored at -20 °C. Cells were pre-treated with a 25 µM working solution zVAD-fmk for a period of one hour as per the inhibitor protocol (Conway et al., 2016) Fisher Scientific). This was done by aspirating the old media and replacing it with 100 µL of working solution into each well. zVAD-fmk was then removed from each well and replaced with the IC<sub>50</sub> of the fresh drug. Cell viability was assessed after 5 days using the MTT assay. Cells were also treated using controls whereby the negative control used was DMEM and 0.5 % DMSO and the positive control used was UV irradiation (Conway et al., 2016).

#### **4.2.4 3D Cell Culture Low Attachment Plate Method**

U251-MG cells were used to generate tumour spheroids. The single cell suspensions were centrifuged at 5000 rpm for 5 mins, the supernatant was removed, and the cell pellet was re-suspended in DMEM high glucose with 10 % FBS and 1 % penicillin-streptomycin. The single cell suspensions at the desired seeding density of  $1 \times 10^4$  cells cm<sup>-2</sup> were transferred to a sterile reservoir and were seeded into Nunclon™ Sphera™ low attachment 96 well plates (Thermo Fischer Scientific). The low attachment plates were centrifuged at 1250 rpm for 5 minutes (Eppendorf Centrifuge, Fisher Scientific) followed by a period of incubation. The media was replenished after 24 hr of incubation. 100 µL of media was removed without disrupting the tumourspheres and 100 µL of fresh media was added into each well and was incubated. It should be noted that the sides of each well should be used to add or remove media to avoid disruption to spheroids. Tumour spheroid formation was observed within 4 days and was



visually confirmed using Optika XDS-2 trinocular inverse microscope equipped with a camera ISH500. The mean diameters were analysed using “ImageJ version 1.53.e” software (Wanigasekara et al., 2022). The cells were seeded in the Nunclon™ Sphera™ low attachment plates for a period of 14 days. Fresh media was added every third day by removing the old media in the wells without disturbing the tumour spheroids. The spheroid formation and growth were monitored daily by using an inverted phase-contrast microscope and the sizes of the spheroids were measured as outlined above for at least three independent experiments. Figure 4.2 outlines the method carried out to grow the tumour spheroids. The tumour spheroids were grown and treated by Janith Manohara Wanigasekara (TU Dublin) as part of a collaboration.



**Figure 4.2** A visual representation of the 3D cell culture method using low adhesion plates (Wanigasekara et al., 2022).

#### **4.2.4.1 Spheroid Cell Viability Analysis**

The alamarBlue™ cell viability reagent (Thermo Fisher Scientific) was used to analyse the spheroid cell viability post treatment with hit compounds. Tumourspheres were washed with sterile PBS, trypsinised using a 0.25 % w / w trypsin-EDTA solution and incubated for 3 h at 37 °C with a 10 % Alamar Blue solution. Fluorescence was measured using an excitation wavelength of 530 nm and an emission wavelength of 590 nm with a Varioskan Lux multiplate reader (Thermo Fisher Scientific). The fluorescence signals were normalised by spheroid size (diameter) where a higher ratio indicates healthier spheroids as discussed in section 4.2.2.2. The experiment consisted of three independent tests where at least nine spheroids were measured throughout three biological repeats. It should be noted that the alamarBlue™ cell viability reagent was used instead of the MTT assay as it was specified in the protocol developed by (Wanigasekara et al., 2022).

#### **4.2.5 Spectrophotometer Data Analysis**

The absorbance unit values were extracted for viability calculations using the statistical analyses software GraphPad Prism version 8.0.0 for Windows, GraphPad Software, San Diego, California USA, [www.graphpad.com](http://www.graphpad.com) (GraphPad, 2020). All experiments were performed a minimum of three independent times with a minimum of six technical replicates per experiment. Cell viability was calculated by removing any background absorbance from the MTT blank reading. The mean absorbance value was calculated from each test per plate. Six technical replicates were carried out for each individual experiment which was repeated three independent times,  $n = 3$ .

#### 4.2.6 Statistical Analysis

Statistical analysis was carried out using the GraphPad Prism version 8.0.0 for Windows, GraphPad Software, San Diego, California USA, [www.graphpad.com](http://www.graphpad.com) (GraphPad, 2020). The statistical analysis performed was such that the IC<sub>50</sub> values for the compounds were determined and analysis of variance (ANOVA) was performed. One-way ANOVA was carried out whereby each treatment was compared to the negative control to determine statistical significance; this is referred to as Dunnett's T3 multiple comparisons test. The P value style used on Prism was the GraphPad style which reports the P values as per Table 4-3 (GraphPad, 2020).

***Table 4-3 Prism statistical significance values, significance level and summary.***

P Value	Wording	Summary
<b>&lt;0.0001</b>	Extremely Significant	****
<b>0.0001 to 0.001</b>	Extremely Significant	***
<b>0.001 to 0.01</b>	Very Significant	**
<b>0.01 to 0.05</b>	Significant	*
<b>≥ 0.05</b>	Not Significant	ns

### **4.3. Results**

#### **4.3.1 Co-Treatment Study**

Previously, six hit compounds were identified: TUM-2A-001, TUM-2A-004, TUM-2A-007, TUM-2A-008, TUM-2A-015 and TUM-2A-016 as there was a statistically significant difference in the IC<sub>50</sub> values between the cancerous and non-cancerous cell line. All six hit compounds also have IC<sub>50</sub> values < 50 µM for the U251-MG cell line. An IC<sub>50</sub> cut-off value of 50 µM was used when carrying out the initial analysis, this is due to the fact that current chemotherapeutic agents used to treat GBM on the U251-MG cell line do not exceed this value (Gao et al., 2019). This cut-off value can be modified when more studies and future research has been carried out, but it serves as a good marker for the initial studies. There are four previously discussed therapeutics used in the treatment of GBM (as per Chapter 1): Lomustine (CCNU); Carmustine Wafers (CW); Procarbazine, Lomustine and Vincristine Sulphate (PCV); and TMZ. The IC<sub>50</sub> values for the current chemotherapeutic agents are outlined in Table 4-4. The IC<sub>50</sub> values obtained for the chemotherapeutic agents were all taken after a 24-hour period bar TMZ which was taken after 6 days. A 5-day timepoint was the value obtained when optimisation studies were conducted in the lab at the start of the research project. The information regarding the 6-day period at that time was unknown.

**Table 4-4 Chemotherapeutic agents currently used in the treatment of GBM and their corresponding IC<sub>50</sub> values for the U-251MG cell line.**

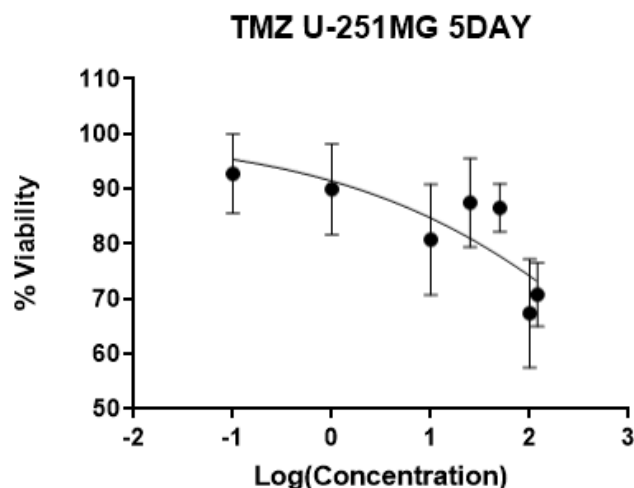
Chemotherapeutic Agent	Co-Treatment IC <sub>50</sub> Value (μM)	Reference
<b>Lomustine (CCNU)</b>	15 (24 hr)	(Armand et al., 2007)
<b>Carmustine Wafers (CW)</b>	32.3 (24 hr)	(Ene et al., 2016)
<b>Procarbazine, Lomustine and Vincristine Sulphate (PCV)</b>	30-50 (24 hr)	(Badrudjoja et al., 2000)
<b>TMZ</b>	28 (6 days)	(Conway et al., 2016)

#### **4.3.1.1 TMZ Analysis**

The U-251MG cell line was treated with TMZ over a 5-day period (120 hours) and the dose-response curve obtained is shown at Figure 4.3. The TMZ was dissolved in DMSO and so the maximum concentration used in this study was 120 μM. Solubility data was obtained from MSDS (Merck, Ireland). No accurate IC<sub>50</sub> value was calculated under these conditions as the value generated by Prism exceeds the maximum concentration used. The high IC<sub>50</sub> value obtained correlates with the literature whereby TMZ has been shown to be resistant to the U251-MG GBM cell lines (Perazzoli et al., 2015)(S. Y. Lee, 2016).

The high IC<sub>50</sub> value for TMZ can be attested to the role of the p53 tumour suppressor gene. Glioma cell lines can express a normal wildtype or mutant p53 gene; examples of such would include the U87 and U251-MG cell lines, respectively (Zhu et al., 2021). TMZ has been shown to have a substantially increased cytotoxicity at a shorter time-point in wild-type cell lines (Dinca et al., 2008). The poor cytotoxicity observed in the U251-MG cell line is consistent with that of the literature due to the fact it has the mutant p53 gene (Dinca et al., 2008). It was also found that TMZ does not induce apoptosis in GBM cells until after 120 hours of treatment and so the experimental result matches the literature (Shervington et al., 2020).

It can therefore be said that the hit compounds have either a much lower IC<sub>50</sub> value than the current marketed chemotherapeutic agents such as TUM-2A-001 or that the hit compounds fall within the acceptable range for GBM therapeutics, < 50 µM (Gao et al., 2019). It was determined that TMZ is not effective on its own over a short incubation period and with the U251-MG cell line. However, it was hypothesised that TMZ and the hit compounds could potentially be used as part of a co-treatment strategy as there could be a potential observed synergistic effect.



**Figure 4.3** *TMZ screen. Assay Conditions: U-251MG cell line and the MTT cell viability assay. Cells were analysed 5 days after treatment, N=3. Where the X axis denotes the logarithmic concentration of compound, and the Y axis denotes the % cell viability.*

#### **4.3.1.2 TMZ Co-Treatment**

The IC<sub>50</sub> of each hit compound, see Table 4-5 was combined with a concentration range of TMZ (120, 100, 50, 25, 10, 1)  $\mu\text{M}$  to assess whether the compounds would be suitable for use as part of a co-treatment study. The TMZ concentration range was determined as per the solubility of TMZ in DMSO (5 mg mL<sup>-1</sup>). The compounds were tested as per the method section outlined in 4.2.1.2 and dose-response curves for the co-treatment study are shown on Figure 4.4. No IC<sub>50</sub> values could be generated for any of the compounds that were used in conjunction with TMZ as the values all exceeded 120  $\mu\text{M}$ . It could be suggested that the use of TMZ had an inhibitory effect on the hit compounds. The compounds are therefore not suitable to be used as part of a co-treatment study with TMZ when using the U251-MG cell

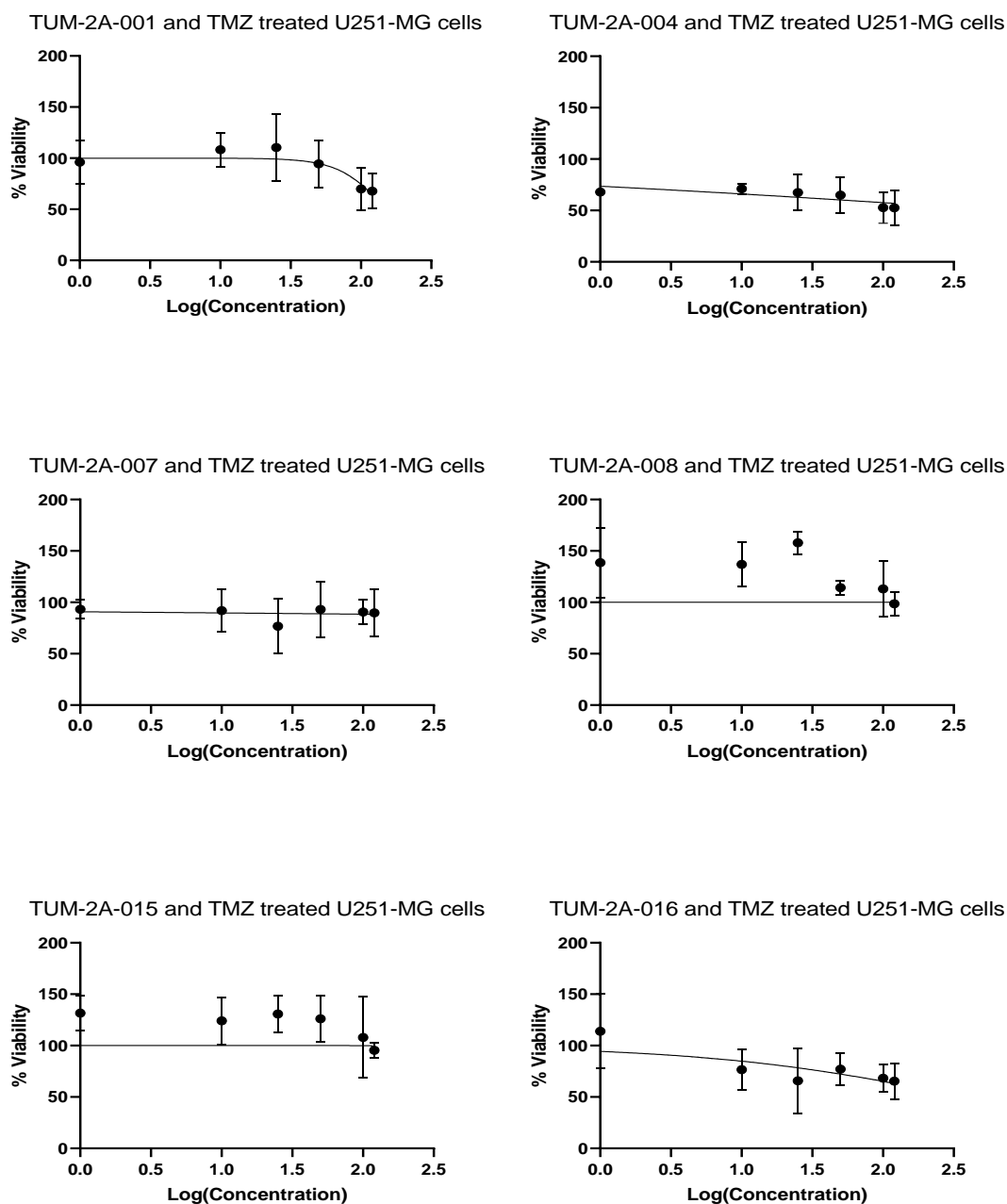
line over a 5-day period. It would be suggested to repeat the TMZ co-treatment studies using a wildtype U87 cell line over a longer period of time as part of future work.

***Table 4-5 Table outlining the hit Compounds and their corresponding IC<sub>50</sub> values for use as part of the co-treatment studies.***

Name of Compound	IC <sub>50</sub> Value (μM)
<b>TUM-2A-001</b>	6.17
<b>TUM-2A-004</b>	29.49
<b>TUM-2A-007</b>	26.75
<b>TUM-2A-008</b>	29.62
<b>TUM-2A-015</b>	0.51
<b>TUM-2A-016</b>	2.79



## TMZ & HIT Compound Co-Treatment



**Figure 4.4** Dose response curves for a combined treatment of TMZ and the hit compounds. Assay Conditions: U251-MG cell line and the MTT cell viability assay. Cells were analysed 5 days after treatment, N=3. Where the X axis denotes the logarithmic concentration of compound, and the Y axis denotes the % cell viability.

### 4.3.2 Flow Cytometry

Flow cytometry was used to determine whether the compounds were eliciting cell death and will also confirm the cell death observed in the 2D cell viability assays which were carried out as part of Chapter 2 and Chapter 3.

#### 4.3.2.1 *TUM-2A-001 PI Analysis*

The hit compound used as part of the PI analysis shown is TUM-2A-001. The graphs shown in Figure 4.5 are for the negative control whereby the first part shows FSC versus SSC which is used to collect the cell population and remove any debris or dust that could be present. The second graph in Figure 4.5 is used to distinguish viable cells from dead cells, in this case 96.33 % of the cells are viable and 2.96 % of the cells are dead. The third graph as part Figure 4.5 is the gating strategy used divides the cell population into quadrants to denote what stage of the cell cycle they are in however further discussion is not required as it is not needed as part of this analysis.

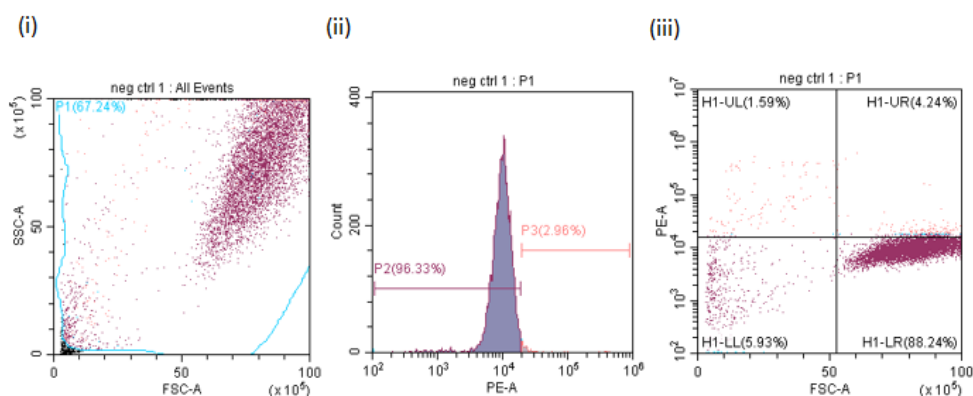
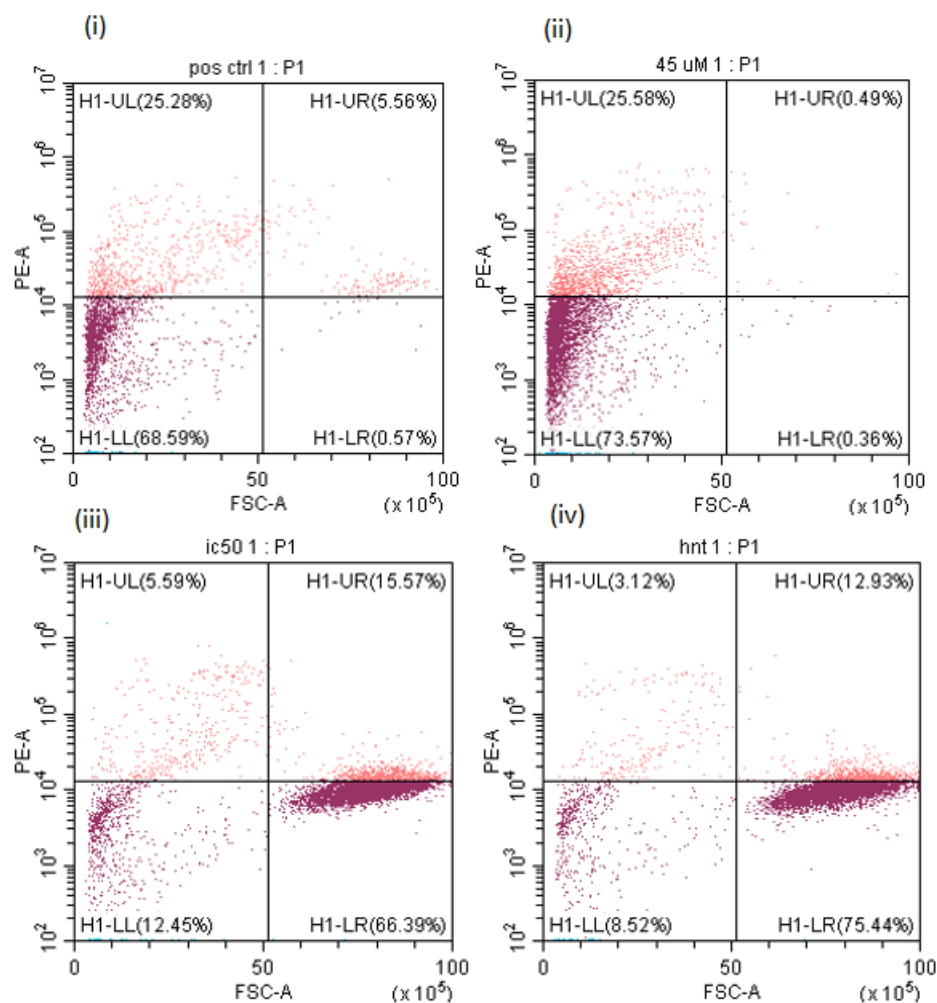


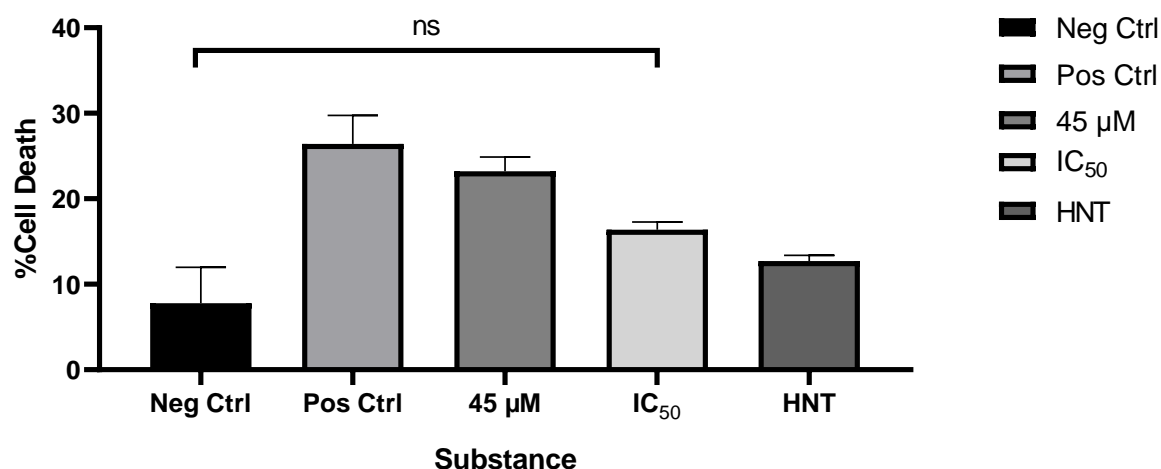
Figure 4.5 PI dye used on TUM-2A-001 hit compound using U251-MG cells. (i) **Graph showing total cell population excluding cellular debris.** (ii) **Graph distinguishing the viable cell population P2 from the dead cell population P3.** (iii) **Quadrant graph for cell cycle analysis for TUM-2A-001**

The quadrant graphs obtained for the positive control, highest toxic control of TUM-2A-001, the IC<sub>50</sub> of TUM-2A-001 and highest non-toxic concentration of TUM-2A-001 are shown in Figure 4.6. The data from these quadrant graphs was then expedited into an excel file and analysed as per the method outlined in 4.2.2.3 to determine the overall % cell death observed for TUM-2A-001. The graph obtained is shown below in Figure 4.7.



**Figure 4.6** Quadrant graphs of forward scatter (FSC-A) verses PE-A were plotted of TUM-2A-001 treated U251-MG cells for a 5-day incubation period whereby then the U251-MG cells were treated with PI and analysed using flow cytometry. The four graphs denote the following (i) positive control (ii) highest toxic concentration of TUM-2A-001 (iii) TUM-2A-001 IC<sub>50</sub> concentration (iv) highest non-toxic concentration of TUM-2A-001.

### TUM-2A-001 PI Cell Death



*Figure 4.7 TUM-2A-001 and PI treated controls as well as the highest toxic concentration (45 µM), the IC<sub>50</sub> value (6.17 µM) and the highest non-toxic drug concentration. Assay Conditions: U251-MG cell line. Cells were treated with fresh drug IC<sub>50</sub>. Cells were analysed 5 days after treatment, N=3 using flow cytometry. Where the X axis denotes the substance or treatment used, and the Y axis denotes the % cell death. The statistical significance shown is only that of the negative control and the IC<sub>50</sub>.*

Statistical analysis was then performed whereby the null hypothesis was such that: there is no statistical significance between the negative control and the other treatments. A one-way ANOVA was carried out whereby each treatment was compared to the negative control to determine statistical significance. Dunnett's T3 multiple comparisons test was used, and a summary of the results are shown in Table 4-6. It can be said that the TUM-2A-001 IC<sub>50</sub> treatment did not induce cell death by cell wall permeabilization as the % necrotic cells observed was not statistically significant when compared to the negative control as per Figure

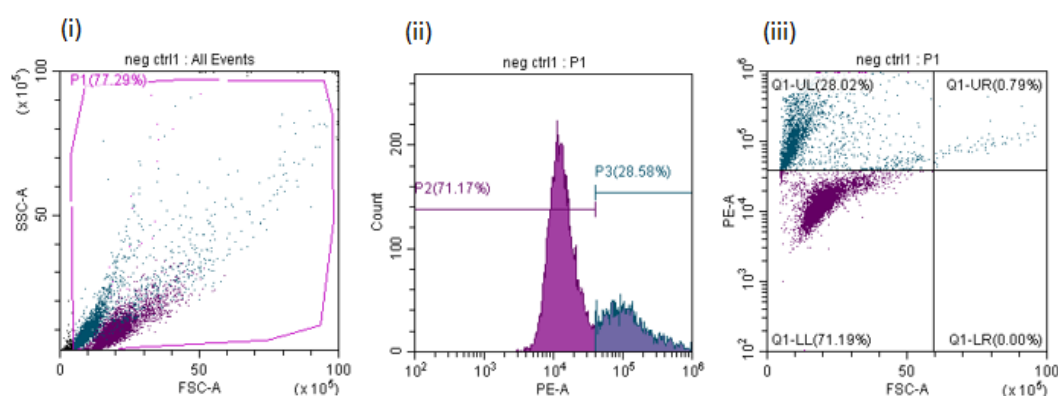
4.7. There was also no statistical difference between the negative control and the highest non-toxic concentration of TUM-2A-001.

**Table 4-6 Summary of results from one-way ANOVA statistical analysis for TUM-2A-001 whereby the P values are reported as follows:  $\geq 0.05$  (ns), 0.01 to 0.05 (\*), 0.001 to 0.01 (\*\*), 0.001 to 0.01 (\*\*\*) and  $< 0.0001$  (\*\*\*\*).**

Comparison	Summary	P Value
Neg Ctrl v Pos Ctrl	*	0.0123
Neg Ctrl v 45 $\mu$ M	*	0.0337
Neg Ctrl v IC <sub>50</sub>	Ns	0.1440
Neg Ctrl v HNT	Ns	0.3617

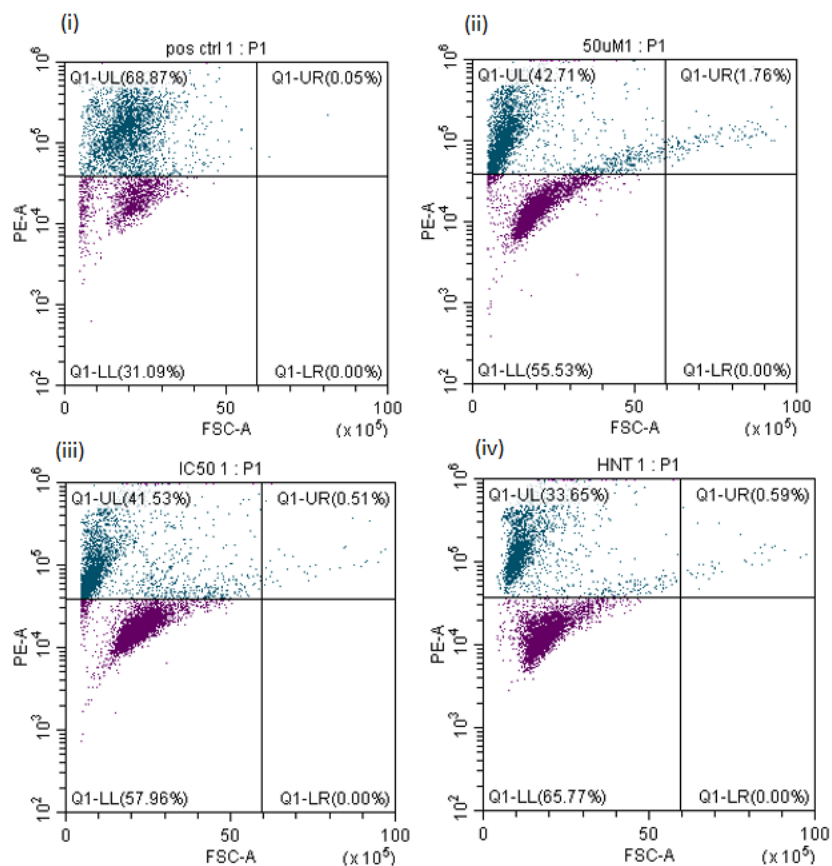
#### 4.3.2.2 TUM-2A-004 PI Analysis

The graphs shown in Figure 4.8 are for the negative control whereby the first part shows FSC verses SSC which is used to collect the cell population and remove any debris or dust that could be present. The second graph in Figure 4.9 is used to distinguish viable cells from dead cells. It can be said that 71.17 % of the cell population is viable and 28.58 % of the cell population is dead. The third graph is a quadrant graph highlighting the gating strategy used to divide the cell population into quadrants to denote what stage of the cell cycle they are in however further discussion is not required as it is not needed as part of this analysis.



**Figure 4.8 (i) Graph showing total TUM-2A-004 cell population excluding cellular debris. (ii) Graph distinguishing the viable cell population P2 from the dead cell population P3. (iii) Gating strategy used to determine the % of cell population in different cell cycle stages.**

The quadrant graphs for the positive control, highest toxic control of TUM-2A-004, the IC<sub>50</sub> of TUM-2A-004 and highest non-toxic concentration of TUM-2A-004 are shown in Figure 4.9. The data from these quadrant graphs was then expedited into an excel file and analysed. The bar chart of results for TUM-2A-004 are shown in Figure 4.18.

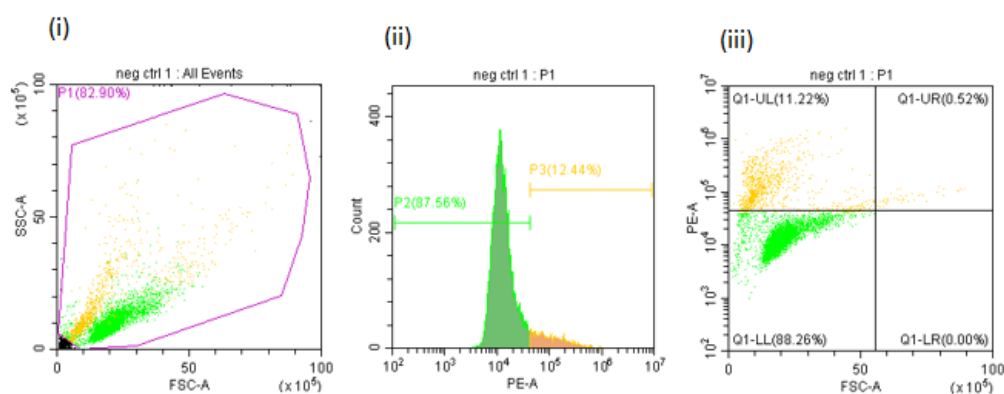


**Figure 4.9** TUM-2A-004 Quadrant graphs of forward scatter (FSC-A) verses PE-A were plotted of TUM-2A-004 whereby the cells were treated with PI and analysed using flow cytometry. The four graphs denote the following (i) positive control (ii) highest toxic concentration of TUM-2A-004 (iii) TUM-2A-004 IC<sub>50</sub> concentration (iv) highest non-toxic concentration of TUM-2A-004.

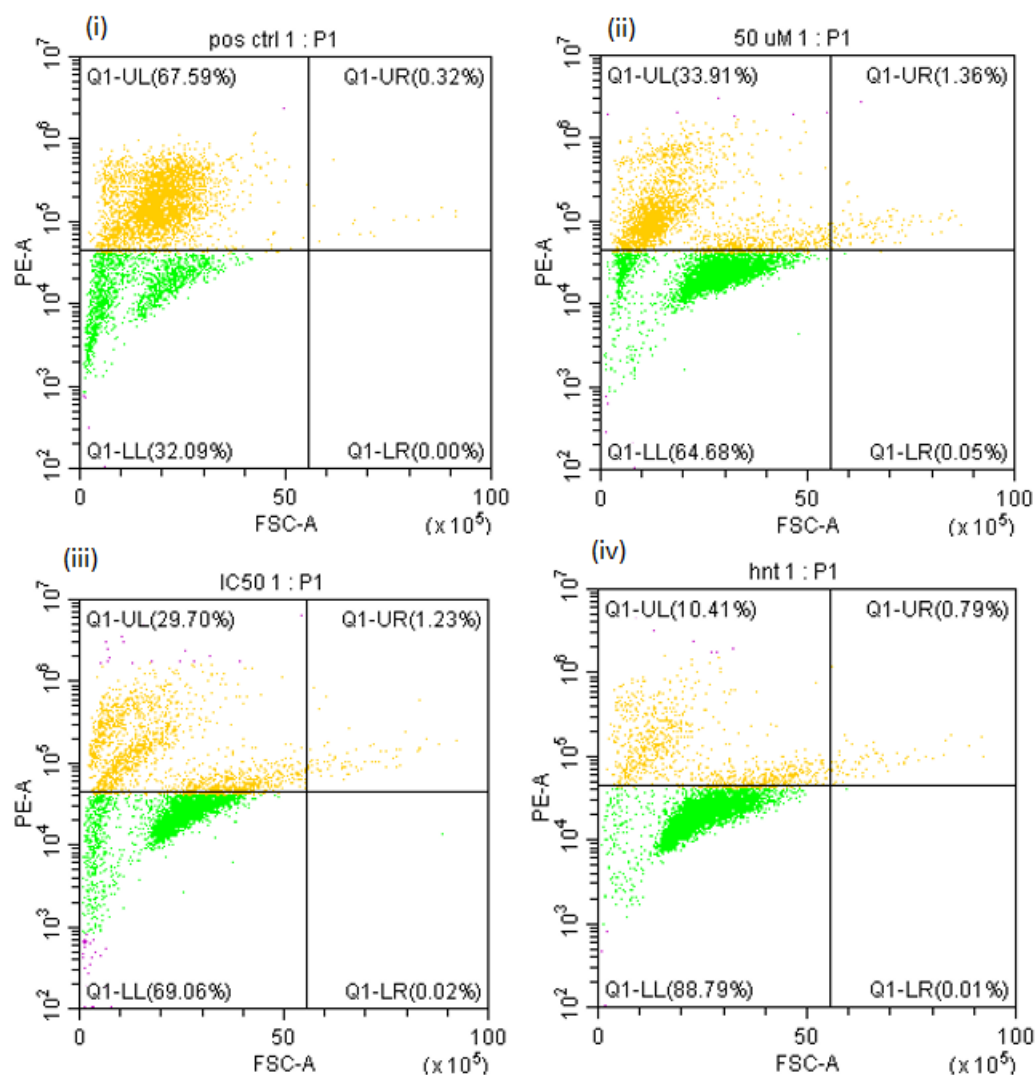


#### 4.3.2.3 TUM-2A-007 PI Analysis

Propidium Iodide cell population analysis remains the same for all hit compounds as per TUM-2A-001. The PI cell population analysis graphs are shown in Figure 4.10. It should be noted that 87.56 % of the cell population is deemed viable and 12.44 % of the cell population are non-viable as per Figure 4.10. The quadrant graphs for the positive control, highest toxic control of TUM-2A-007, the IC<sub>50</sub> of TUM-2A-007 and highest non-toxic concentration of TUM-2A-007 are shown in Figure 4.11. The data from these quadrant graphs was then expedited into an excel file and analysed. The bar chart of results for TUM-2A-007 are shown in Figure 4.18.



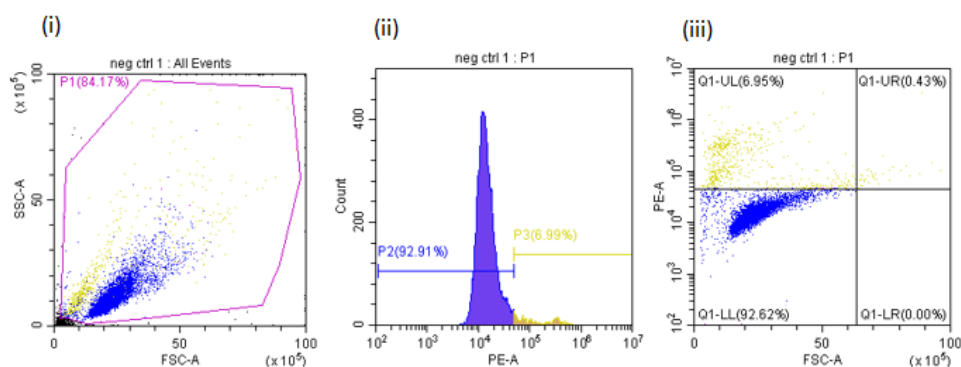
**Figure 4.10 (i) Graph showing total TUM-2A-007 cell population excluding cellular debris. (ii) Graph distinguishing the viable cell population P2 from the dead cell population P3. (iii) Gating strategy used to determine the % of cell population in different cell cycle stages.**



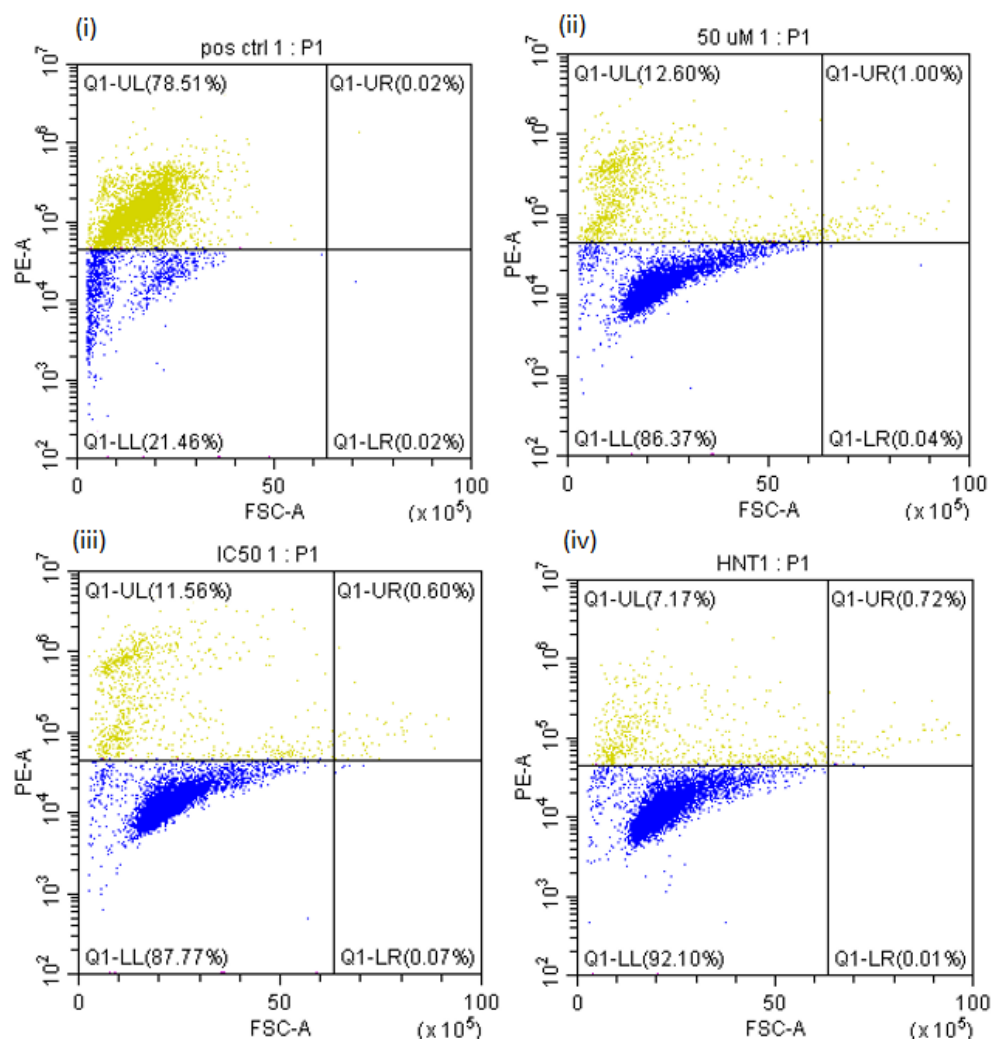
**Figure 4.11** TUM-2A-007 Quadrant graphs of forward scatter (FSC-A) verses PE-A were plotted of TUM-2A-007 whereby the cells were treated with PI and analysed using flow cytometry. The four graphs denote the following (i) positive control (ii) highest toxic concentration of TUM-2A-007 (iii) TUM-2A-007 IC<sub>50</sub> concentration (iv) highest non-toxic concentration of TUM-2A-007.

#### 4.3.2.4 TUM-2A-008 PI Analysis

Propidium Iodide cell population analysis remains the same for all hit compounds as per TUM-2A-001. The PI cell population analysis graphs are shown in Figure 4.12. It should be noted that 92.91 % of the cell population is deemed viable and 6.99 % of the cell population are non-viable as per Figure 4.12. The quadrant graphs for the positive control, highest toxic control of TUM-2A-008, the IC<sub>50</sub> of TUM-2A-008 and highest non-toxic concentration of TUM-2A-008 are shown in Figure 4.13. The data from these quadrant graphs was then expedited into an excel file and analysed. The bar chart of results for TUM-2A-008 are shown in Figure 4.18.



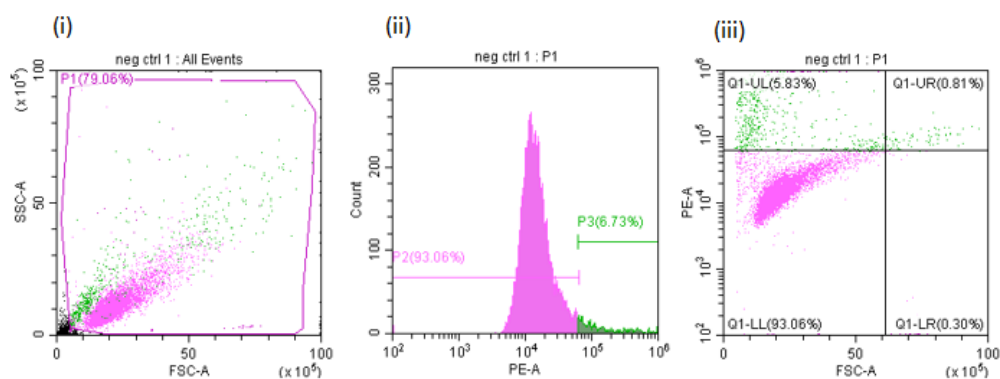
**Figure 4.12** (i) Graph showing total TUM-2A-008 cell population excluding cellular debris. (ii) Graph distinguishing the viable cell population P2 from the dead cell population P3. (iii) Gating strategy used to determine the % of cell population in different cell cycle stages.



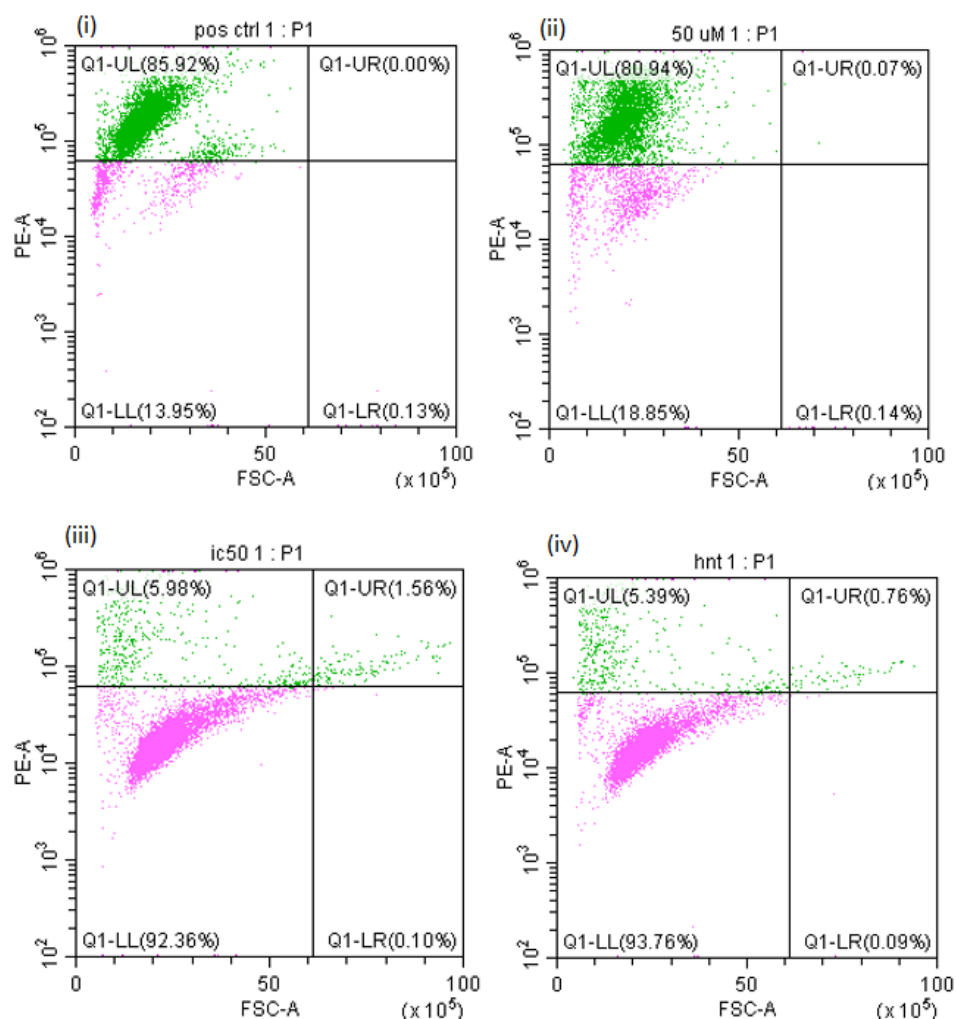
**Figure 4.13** TUM-2A-008 Quadrant graphs of forward scatter (FSC-A) verses PE-A were plotted of TUM-2A-008 whereby the cells were treated with PI and analysed using flow cytometry. The four graphs denote the following (i) positive control (ii) highest toxic concentration of TUM-2A-008 (iii) TUM-2A-008 IC<sub>50</sub> concentration (iv) highest non-toxic concentration of TUM-2A-008.

#### 4.3.2.5 TUM-2A-015 PI Analysis

Propidium Iodide cell population analysis remains the same for all hit compounds as per TUM-2A-001. The PI cell population analysis graphs are shown in Figure 4.14. It should be noted that 93.06 % of the cell population is deemed viable and 6.73 % of the cell population are non-viable as per Figure 4.14. The quadrant graphs for the positive control, highest toxic control of TUM-2A-015, the IC<sub>50</sub> of TUM-2A-015 and highest non-toxic concentration of TUM-2A-015 are shown in Figure 4.15. The data from these quadrant graphs was then expedited into an excel file and analysed. The bar chart of results for TUM-2A-015 are shown in Figure 4.18.



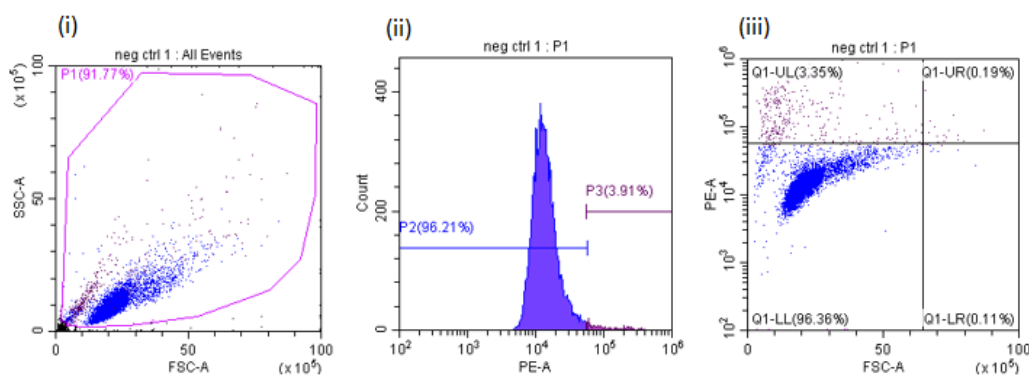
**Figure 4.14 (i) Graph showing total TUM-2A-015 cell population excluding cellular debris. (ii) Graph distinguishing the viable cell population P2 from the dead cell population P3. (iii) Gating strategy used to determine the % of cell population in different cell cycle stages.**



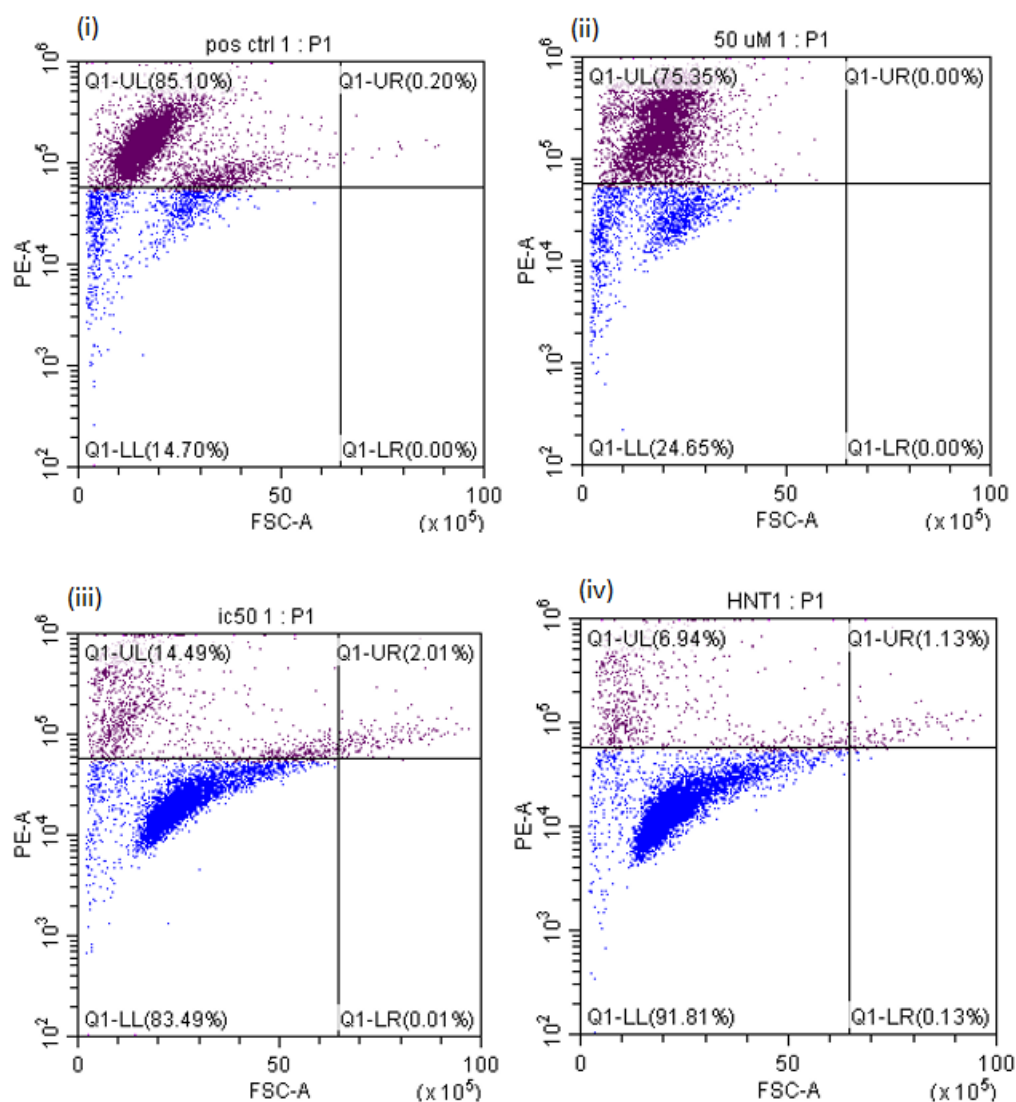
**Figure 4.15** TUM-2A-015 Quadrant graphs of forward scatter (FSC-A) verses PE-A were plotted of TUM-2A-015 whereby the cells were treated with PI and analysed using flow cytometry. The four graphs denote the following (i) positive control (ii) highest toxic concentration of TUM-2A-015 (iii) TUM-2A-015 IC<sub>50</sub> concentration (iv) highest non-toxic concentration of TUM-2A-015.

#### 4.3.2.6 TUM-2A-016 PI Analysis

Propidium Iodide cell population analysis remains the same for all hit compounds as per TUM-2A-001. The PI cell population analysis graphs are shown in Figure 4.16. It should be noted that 96.21 % of the cell population is deemed viable and 3.91 % of the cell population are non-viable as per Figure 4.16. The quadrant graphs for the positive control, highest toxic control of TUM-2A-016, the IC<sub>50</sub> of TUM-2A-016 and highest non-toxic concentration of TUM-2A-016 are shown in Figure 4.17. The data from these quadrant graphs was then expedited into an excel file and analysed. The bar chart of results for TUM-2A-016 are shown in Figure 4.18.



**Figure 4.16 (i) Graph showing total TUM-2A-016 cell population excluding cellular debris. (ii) Graph distinguishing the viable cell population P2 from the dead cell population P3. (iii) Gating strategy used to determine the % of cell population in different cell cycle stages.**

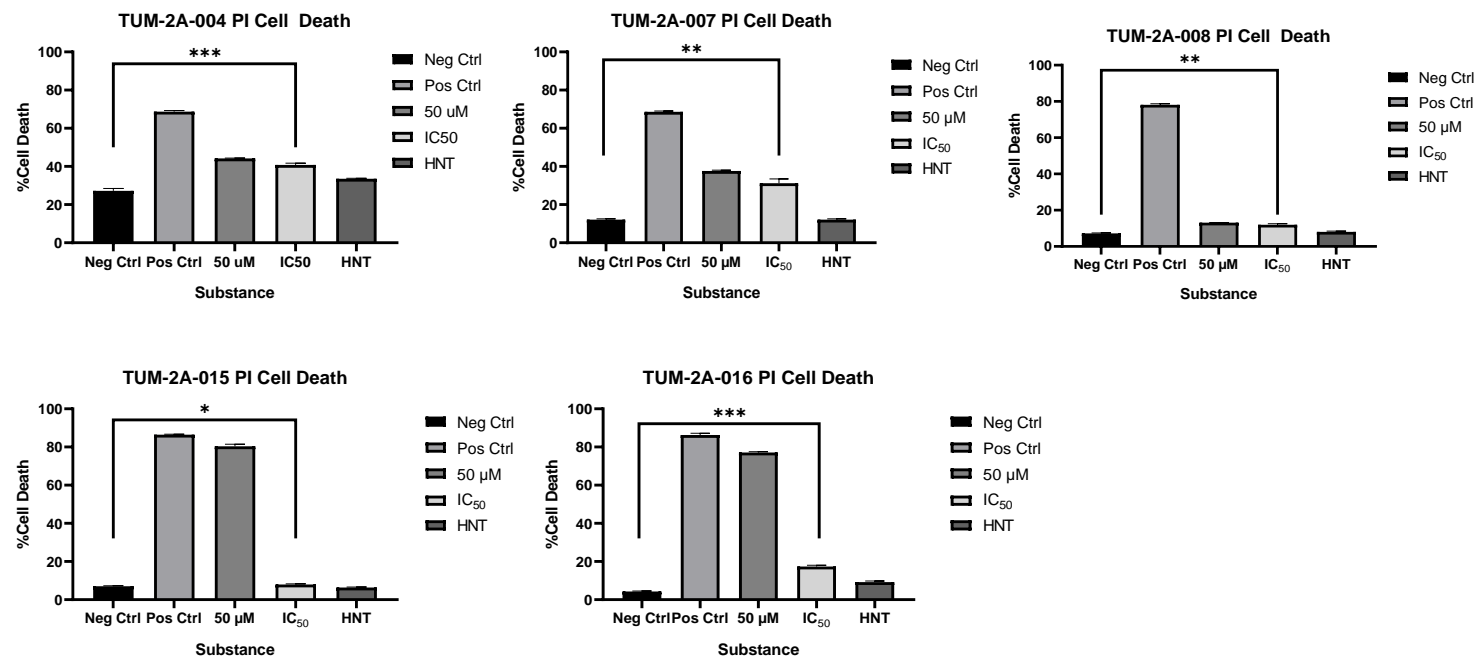


**Figure 4.17** TUM-2A-016 Quadrant graphs of forward scatter (FSC-A) verses PE-A were plotted of TUM-2A-016 whereby the cells were treated with PI and analysed using flow cytometry. The four graphs denote the following (i) positive control (ii) highest toxic concentration of TUM-2A-016 (iii) TUM-2A-016 IC<sub>50</sub> concentration (iv) highest non-toxic concentration of TUM-2A-016.



#### **4.3.2.7 HIT Compound Propidium Iodide Analysis**

The graphs obtained via flow cytometry were generated and analysed as per TUM-2A-001 using the method outlined in section 4.2.2.3. The graphed data is shown in Figure 4.18**Error! Reference source not found.** whereby the negative control was compared to the positive control, highest toxic concentration, highest non-toxic concentration and the IC<sub>50</sub> value. A one-way ANOVA was carried out whereby each treatment was compared to the negative control to determine statistical significance. Dunnett's T3 multiple comparisons test was used, and a summary of the results are shown in **Error! Reference source not found.** It should be noted that the graph shown in Figure 4.18**Error! Reference source not found.** only highlights the statistical significance of the negative control when compared to the IC<sub>50</sub> value, this is deemed to be statistically significant as per the three asterisks shown for each hit compound. TUM-2A-004 and TUM-2A-016 have three asterisks of statistical significance and so it can be deduced that there is a greater possibility of these hit compounds inducing cell death by cell membrane permeabilization. TUM-2A-007, TUM-2A-008 and TUM-2A-015 are also deemed to be statistically significant and may induce cell death by cell membrane permeabilization – this can be deemed as either necrosis or apoptosis. A second dye, the JC-1 dye was used as a continuation from this work to further deduce whether apoptosis is the main mode of cell death the compounds are eliciting.



**Figure 4.18 Hit Compounds, TUM-2A-004, TUM-2A-007, TUM-2A-008, TUM-2A-015 and TUM-2A-016 were treated with PI using their highest toxic concentration, the IC<sub>50</sub> value and the highest non-toxic drug concentration. Statistical significance only shown between hit Compound IC<sub>50</sub> value and negative control. Assay Conditions: U251-MG cell line. Cells were treated with fresh drug IC<sub>50</sub>. Cells were analysed 5 days after treatment, N=3 using flow cytometry. Where the X axis denotes the substance or treatment used, and the Y axis denotes the % cell death.**

**Table 4-7 Summary of results from one-way ANOVA statistical analysis for PI treated HIT Compounds TUM-2A-004, TUM-2A-007, TUM-2A-008, TUM-2A-015 and TUM-2A-016 whereby the P values are reported as follows:  $\geq 0.05$  (ns), 0.01 to 0.05 (\*), 0.001 to 0.01 (\*\*), 0.001 to 0.01 (\*\*\*) and  $<0.0001$  (\*\*\*\*). The negative control was compared with the positive control, highest toxic concentration, IC<sub>50</sub> value and the lowest toxic concentration using Dunnett's T3 multiple comparisons statistical test.**

HIT Compound	Comparison	Summary	P Value
<b>TUM-2A-004</b>	Neg Ctrl v Pos Ctrl	****	<0.001
<b>TUM-2A-004</b>	Neg Ctrl v 50 $\mu$ M	**	0.0034
<b>TUM-2A-004</b>	Neg Ctrl v IC <sub>50</sub>	***	0.0005
<b>TUM-2A-004</b>	Neg Ctrl v HNT	*	0.0216
<b>TUM-2A-007</b>	Neg Ctrl v Pos Ctrl	****	<0.001
<b>TUM-2A-007</b>	Neg Ctrl v 50 $\mu$ M	****	<0.001
<b>TUM-2A-007</b>	Neg Ctrl v IC <sub>50</sub>	**	0.084
<b>TUM-2A-007</b>	Neg Ctrl v HNT	Ns	>0.9999

<b>TUM-2A-008</b>	Neg Ctrl v Pos Ctrl	****	<0.0001
<b>TUM-2A-008</b>	Neg Ctrl v 50 $\mu$ M	***	0.0005
<b>TUM-2A-008</b>	Neg Ctrl v IC <sub>50</sub>	**	0.0048
<b>TUM-2A-008</b>	Neg Ctrl v HNT	Ns	0.1976
<b>TUM-2A-015</b>	Neg Ctrl v Pos Ctrl	****	<0.001
<b>TUM-2A-015</b>	Neg Ctrl v 50 $\mu$ M	****	<0.001
<b>TUM-2A-015</b>	Neg Ctrl v IC <sub>50</sub>	*	0.0327
<b>TUM-2A-015</b>	Neg Ctrl v HNT	Ns	0.0979
<b>TUM-2A-016</b>	Neg Ctrl v Pos Ctrl	****	<0.0001
<b>TUM-2A-016</b>	Neg Ctrl v 50 $\mu$ M	****	<0.0001
<b>TUM-2A-016</b>	Neg Ctrl v IC <sub>50</sub>	***	0.0002
<b>TUM-2A-016</b>	Neg Ctrl v HNT	**	0.0012

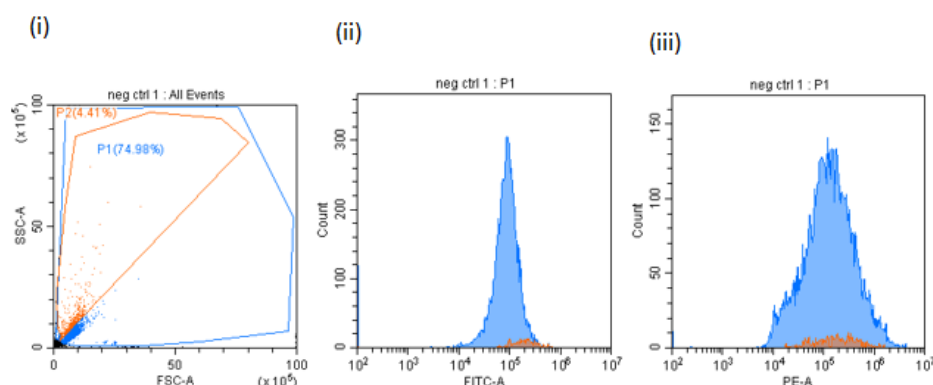
A summary of the results from the PI flow cytometry analysis can be found on **Error! Reference source not found.** The null hypothesis was such that there was no statistical significance between the negative control and the IC<sub>50</sub> of the hit compound. It can be said that there was statistical significance observed in every hit compound bar TUM-2A-001. The results pertain to the statistical significance observed rather than the % levels of necrosis observed. PI staining was a useful tool to show that there is cell death happening however it is not necessarily necrosis or apoptosis. As a result of this, the use of the JC-1 dye was employed to further explore the hit compounds and apoptosis.

**Table 4-8 PI flow cytometry analysis of results from one-way ANOVA statistical analysis whereby the P values are reported as follows:  $\geq 0.05$  (ns), 0.01 to 0.05 (\*), 0.001 to 0.01 (\*\*), 0.001 to 0.01(\*\*\*), and  $< 0.0001$ (\*\*\*\*).**

Compound Name	IC <sub>50</sub> Statistical Significance	Cell Membrane Permeabilised
<b>TUM-2A-001</b>	Ns	No
<b>TUM-2A-004</b>	***	Yes
<b>TUM-2A-007</b>	**	Yes
<b>TUM-2A-008</b>	**	Yes
<b>TUM-2A-015</b>	*	Yes
<b>TUM-2A-016</b>	***	Yes

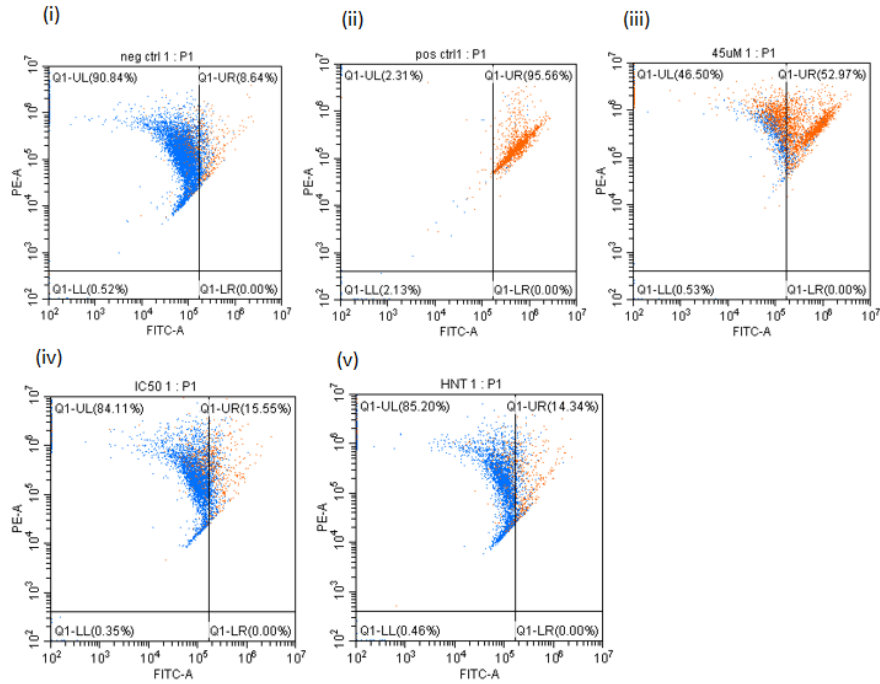
#### ***4.3.2.8 TUM-2A-001 JC-1 Dye Analysis***

The hit compound used as part of the JC-1 dye analysis shown is TUM-2A-001. The remaining hit compounds were analysed in the same manner. The cell population was determined using the same methods carried out using PI as per the first graph shown in **Error! Reference source not found..** As per the first graph shown in **Error! Reference source not found.** it should be noted that the dead cell population is shown in orange and the remaining cells shown in blue are viable. For reference, cells shown above the diagonal line are dead as per graph (i). The cells were then counted in both the green FITC, and red PE channels and compensation was added to ensure there was an overlap between the two channels. It should be noted that there was increased green fluorescence observed in the dead cell population as per **Error! Reference source not found..** The compensation was carried out whereby in the FITC channel PE was allocated 10 % compensation and in the PE channel FITC was allocated 80 % compensation. This compensation was used throughout the thesis for JC-1 dye analysis.



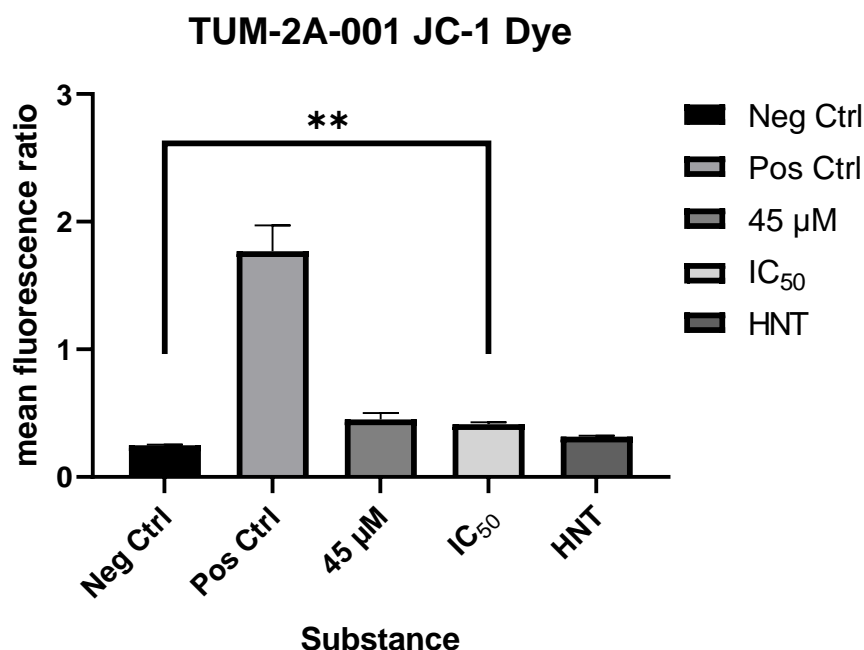
**Figure 4.19 TUM-2A-001 and JC-1 Dye Analysis** (i) Graph showing total cell population excluding cellular debris. (ii) Graph distinguishing the cell population in the green FITC channel (iii) Graph distinguishing the cell population in the red PE channel.

The controls were then checked when the compensation was added, it can be observed that there is an overlap of cells from the two channels. It is shown in **Error! Reference source not found.** that there is little cell death observed in the negative control (8.64 %) and the majority of cell death is observed in the positive control (95.56 %). From this, a quadrant graph of PE v FITC was made whereby the two overlaid cell populations can be seen. In the case of TUM-2A-001, the orange cells are deemed apoptotic whereby they are located in the upper right (UR) quadrant as shown in **Error! Reference source not found..** The data from the CytExpert software was extracted to an excel file whereby the method used is outlined in section 4.2.2.6. The bar chart of results for TUM-2A-001 can be seen as per Figure 4.21**Error! Reference source not found..**



**Figure 4.20 JC-1 and TUM-2A-001** (i) 8.64 % apoptotic cell population observed in negative control for TUM-2A-001. (ii) 95.56 % apoptotic cell population observed in positive control for TUM-2A-001 (iii) 52.97 % apoptosis observed in highest toxic concentration of TUM-2A-001 (iv) 15.55 % apoptosis observed in TUM-2A-001 IC<sub>50</sub> (v) 14.34 % apoptosis observed in highest non-toxic concentration of TUM-2A-001.





*Figure 4.21 TUM-2A-001 and JC-1 treated highest toxic concentration (45 µM), the IC<sub>50</sub> value (6.17 µM) and the highest non-toxic drug concentration (0.1 µM). Assay Conditions: U251-MG cell line. Cells were treated with fresh drug IC<sub>50</sub>. Cells were analysed 5 days after treatment, N=3 using flow cytometry. Where the X axis denotes the substance or treatment used, and the Y axis denotes the % cell death.*

Statistical analysis was then performed whereby the null hypothesis was such that: there is no statistical significance between the negative control and the positive control and between the negative control and the hit compound treatments. A one-way ANOVA was carried out whereby each treatment was compared to the negative control to determine statistical significance. Dunnett's T3 multiple comparisons test was used, and a summary of the results are shown in **Error! Reference source not found.** below. It can be said that there is statistical significance between the negative control and the IC<sub>50</sub> of the hit compound which is deemed very significant as per a p value of \*\* shown on **Error! Reference source not found.** . It can

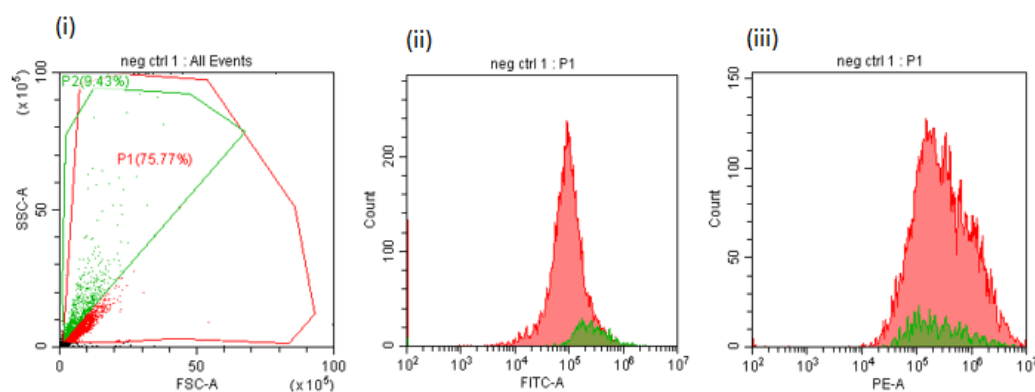
be inferred that TUM-2A-001 is eliciting enough apoptosis to be deemed statistically significant.

***Table 4-9 JC-1 dye flow cytometry analysis of results from one-way ANOVA statistical analysis whereby the P values are reported as follows:  $\geq 0.05$  (ns), 0.01 to 0.05 (\*), 0.001 to 0.01 (\*\*), 0.001 to 0.01 (\*\*\*) and  $< 0.0001$  (\*\*\*\*).***

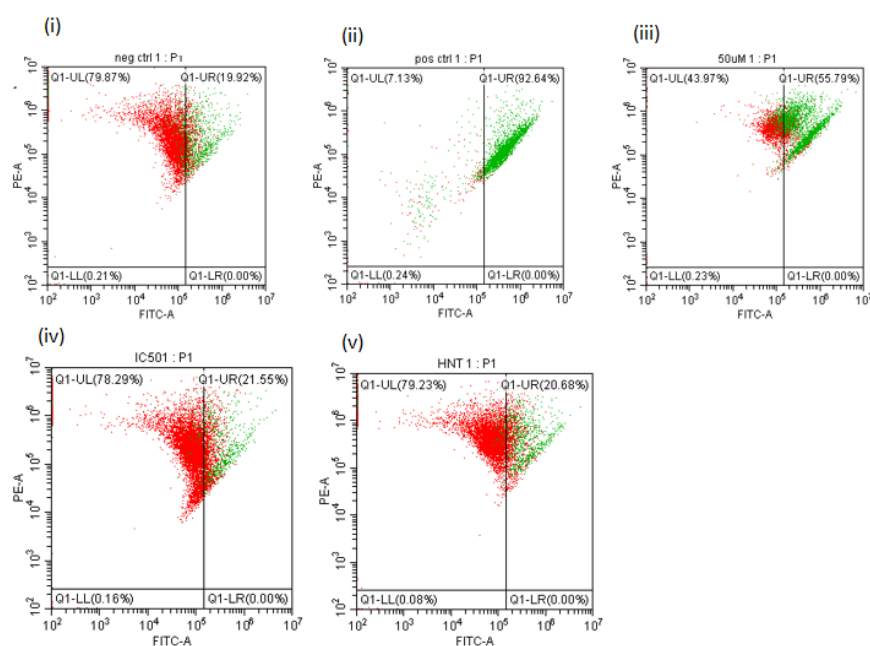
Comparison	Summary	P Value
<b>Neg Ctrl v Pos Ctrl</b>	*	0.0129
<b>Neg Ctrl v 50 <math>\mu</math>M</b>	*	0.0420
<b>Neg Ctrl v IC<sub>50</sub></b>	**	0.0051
<b>Neg Ctrl v HNT</b>	**	0.0010

#### 4.3.2.9 TUM-2A-004 JC-1 Dye Analysis

JC-1 dye cell population analysis and compensation remains the same for all hit compounds as per TUM-2A-001. **Figure 4.22** highlights the graphs which were generated to show total cellular population excluding the cellular debris as well as the cell population in both the green and red channel. Quadrant graphs for each control and HIT compound treatment were prepared and are shown in Figure 4.23.



**Figure 4.22** Graph showing total cell population excluding cellular debris. (ii) Graph distinguishing the cell population in the green FITC channel (iii) Graph distinguishing the cell population in the red PE channel.

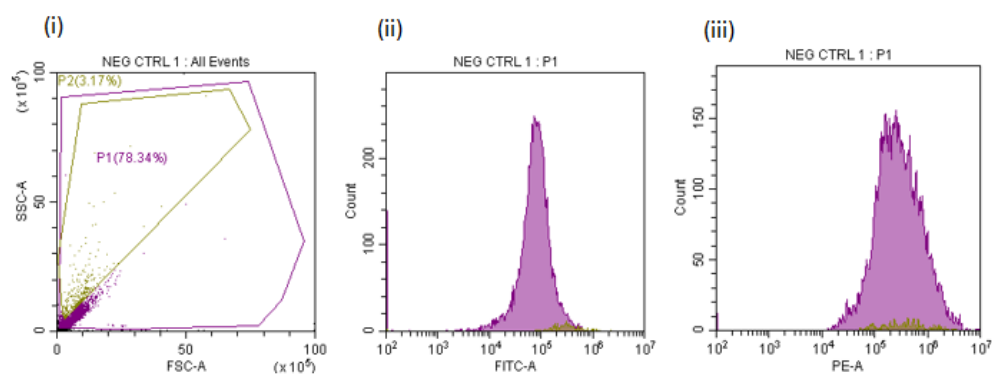


**Figure 4.23 (i) 19.92 % apoptotic cell population observed in negative control for TUM-2A-004. (ii) 92.64 % apoptotic cell population observed in positive control for TUM-2A-004 (iii) 55.79 % apoptosis observed in highest toxic concentration of TUM-2A-004 (iv) 21.55 % apoptosis observed in TUM-2A-004 IC<sub>50</sub> (v) 20.68 % apoptosis observed in highest non-toxic concentration of TUM-2A-004.**

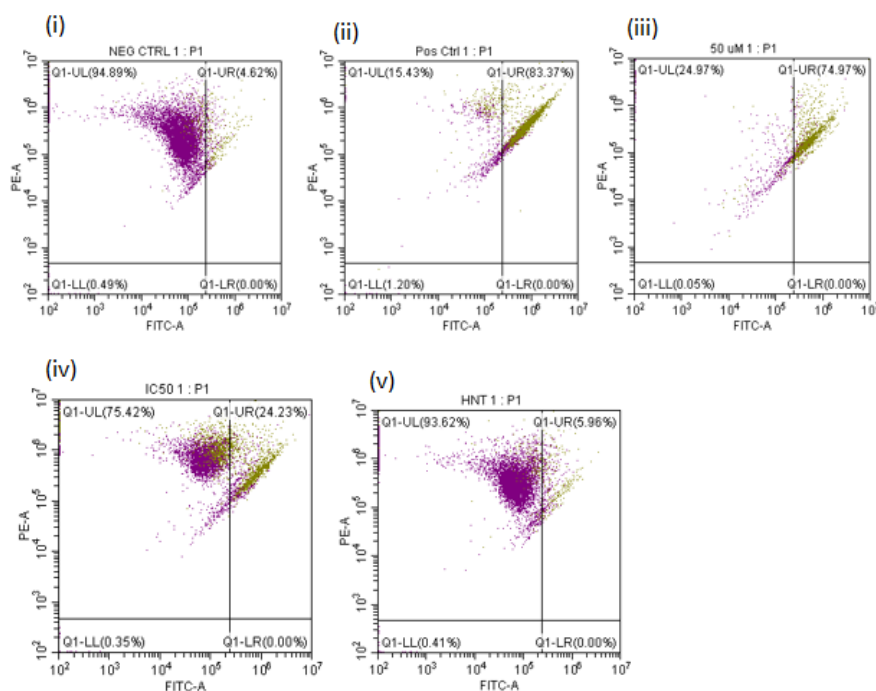
From this, a quadrant graph of PE v FITC was made whereby the two overlaid cell populations can be seen. In the case of TUM-2A-004, the green cells are deemed apoptotic whereby they are located in the upper right (UR) quadrant. The data from the CytExpert software was extracted to an excel file. The fluorescence ratios were determined whereby the mean fluorescence values for FITC and PE were divided against one another and were plotted against the controls and substance treatment. The bar chart of results for TUM-2A-004 are shown in Figure 4.32.

#### 4.3.2.10 TUM-2A-007 JC-1 Dye Analysis

JC-1 dye cell population analysis and compensation remains the same for all hit compounds as per JC-1 dye analysis carried out for TUM-2A-001. TUM-2A-007 cell population analysis is shown in Figure 4.24. Quadrant analysis carried out also utilises the same technique as TUM-2A-001 and is shown in Figure 4.25.



**Figure 4.24** Graph showing total cell population excluding cellular debris. (ii) Graph distinguishing the cell population in the green FITC channel (iii) Graph distinguishing the cell population in the red PE channel.

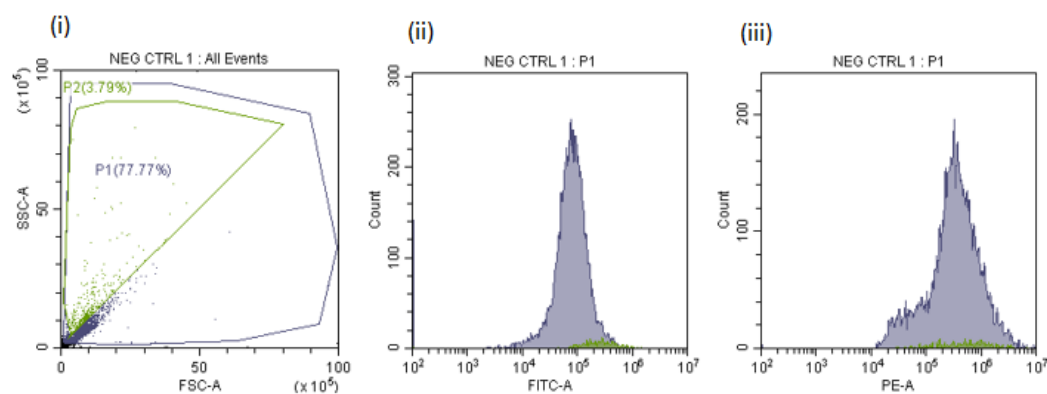


**Figure 4.25** (i) 4.62 % apoptotic cell population observed in negative control for TUM-2A-007. (ii) 83.37 % apoptotic cell population observed in positive control for TUM-2A-007 (iii) 74.97 % apoptosis observed in highest toxic concentration of TUM-2A-007 (iv) 24.23 % apoptosis observed in TUM-2A-007  $IC_{50}$  (v) 5.96 % apoptosis observed in highest non-toxic concentration of TUM-2A-007.

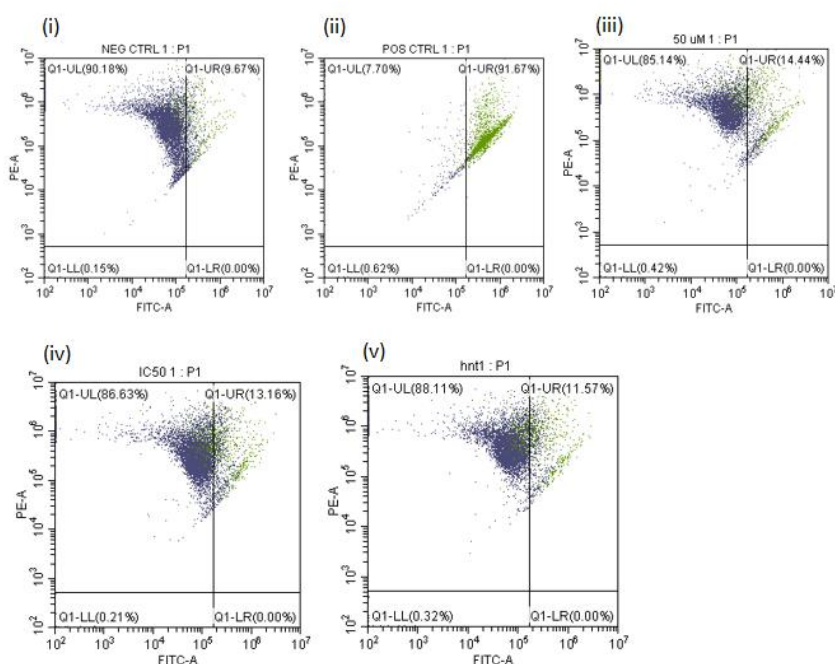
From this, a quadrant graph of PE v FITC was made whereby the two overlaid cell populations can be seen. In the case of TUM-2A-007, the brown cells are deemed apoptotic whereby they are located in the upper right (UR) quadrant. The data from the CytExpert software was extracted to an excel file. The fluorescence ratios were determined whereby the mean fluorescence values for FITC and PE were divided against one another and were plotted against the controls and substance treatment. The bar chart of results for TUM-2A-007 are shown in Figure 4.32.

#### 4.3.2.11 TUM-2A-008 JC-1 Dye Analysis

JC-1 dye cell population analysis and compensation remains the same for all hit compounds as per JC-1 dye analysis carried out for TUM-2A-001. TUM-2A-008 cell population analysis is shown in Figure 4.26. Quadrant analysis carried out also utilises the same technique as TUM-2A-001 and is shown in Figure 4.27.



**Figure 4.26 (i) Graph showing total cell population excluding cellular debris. (ii) Graph distinguishing the cell population in the green FITC channel (iii) Graph distinguishing the cell population in the red PE channel.**



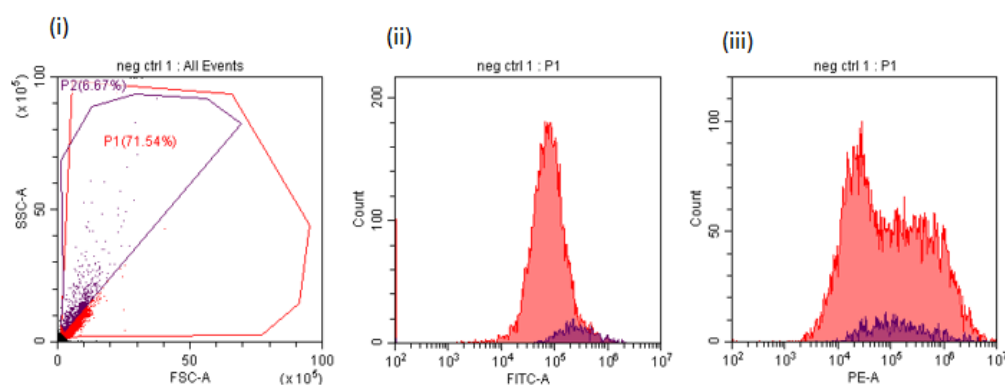
**Figure 4.27 (i) 9.67 % apoptotic cell population observed in negative control for TUM-2A-008. (ii) 91.67 % apoptotic cell population observed in positive control for TUM-2A-008 (iii) 14.44 % apoptosis observed in highest toxic concentration of TUM-2A-008 (iv) 13.16 % apoptosis observed in TUM-2A-008 IC<sub>50</sub> (v) 11.57 % apoptosis observed in highest non-toxic concentration of TUM-2A-008.**

From this, a quadrant graph of PE v FITC was made whereby the two overlaid cell populations can be seen. In the case of TUM-2A-008, the green cells are deemed apoptotic whereby they are located in the upper right (UR) quadrant. The data from the CytExpert software was extracted to an excel file. The fluorescence ratios were determined whereby the mean fluorescence values for FITC and PE were divided against one another and were plotted against the controls and substance treatment. The bar chart of results for TUM-2A-008 are shown in Figure 4.32.

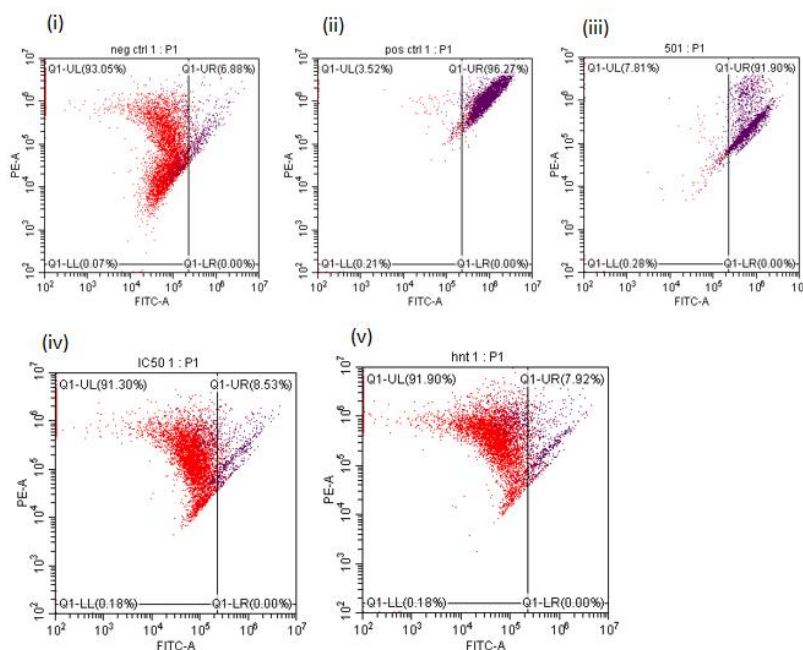


#### 4.3.2.12 TUM-2A-015 JC-1 Dye Analysis

JC-1 dye cell population analysis and compensation remains the same for all hit compounds as per JC-1 dye analysis carried out for TUM-2A-001. TUM-2A-015 cell population analysis is shown in Figure 4.28. Quadrant analysis carried out also utilises the same technique as TUM-2A-001 and is shown in Figure 4.29.



**Figure 4.28** (i) Graph showing total cell population excluding cellular debris. (ii) Graph distinguishing the cell population in the green FITC channel (iii) Graph distinguishing the cell population in the red PE channel.

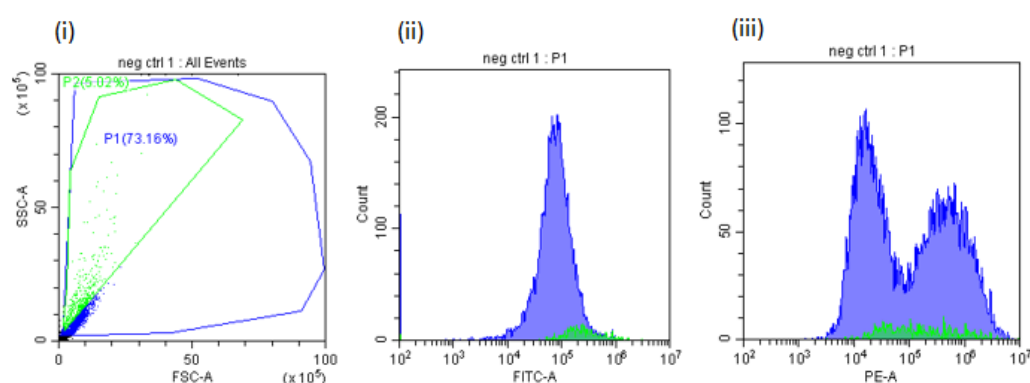


**Figure 4.29** (i) 6.88 % apoptotic cell population observed in negative control for TUM-2A-015. (ii) 96.27 % apoptotic cell population observed in positive control for TUM-2A-015 (iii) 91.90 % apoptosis observed in highest toxic concentration of TUM-2A-015 (iv) 8.53 % apoptosis observed in TUM-2A-015 IC<sub>50</sub> (v) 7.92 % apoptosis observed in highest non-toxic concentration of TUM-2A-015.

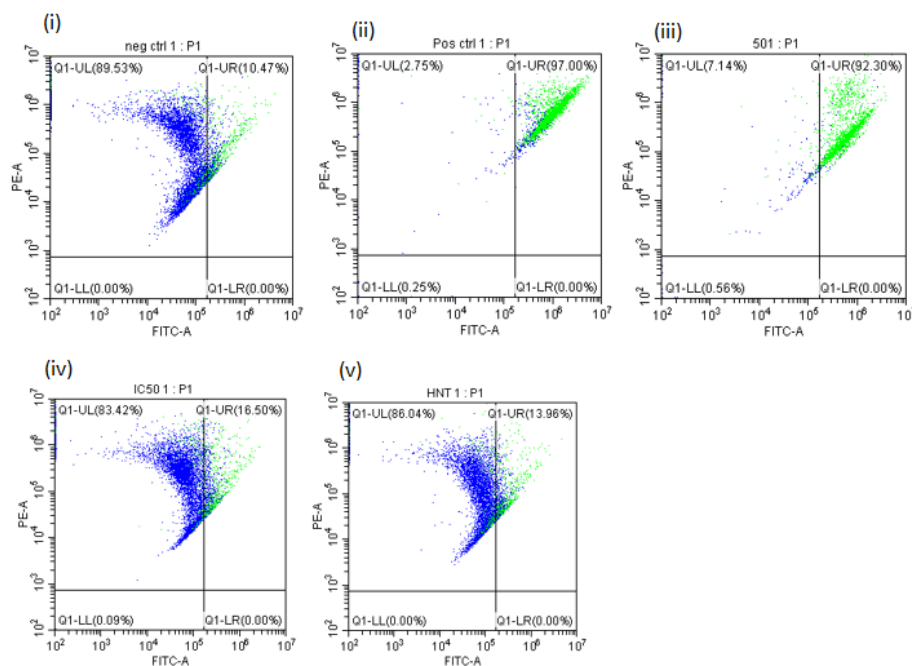
From this, a quadrant graph of PE v FITC was made whereby the two overlaid cell populations can be seen. In the case of TUM-2A-015, the purple cells are deemed apoptotic whereby they are located in the upper right (UR) quadrant. The data from the CytExpert software was extracted to an excel file. The fluorescence ratios were determined whereby the mean fluorescence values for FITC and PE were divided against one another and were plotted against the controls and substance treatment. The bar chart of results for TUM-2A-015 are shown in Figure 4.32.

#### 4.3.2.13 TUM-2A-016 JC-1 Dye Analysis

JC-1 dye cell population analysis and compensation remains the same for all hit compounds as per JC-1 dye analysis carried out for TUM-2A-001. TUM-2A-016 cell population analysis is shown in Figure 4.30. Quadrant analysis carried out also utilises the same technique as TUM-2A-001 and is shown in Figure 4.31.



**Figure 4.30 (i) Graph showing total cell population excluding cellular debris. (ii) Graph distinguishing the cell population in the green FITC channel (iii) Graph distinguishing the cell population in the red PE channel.**

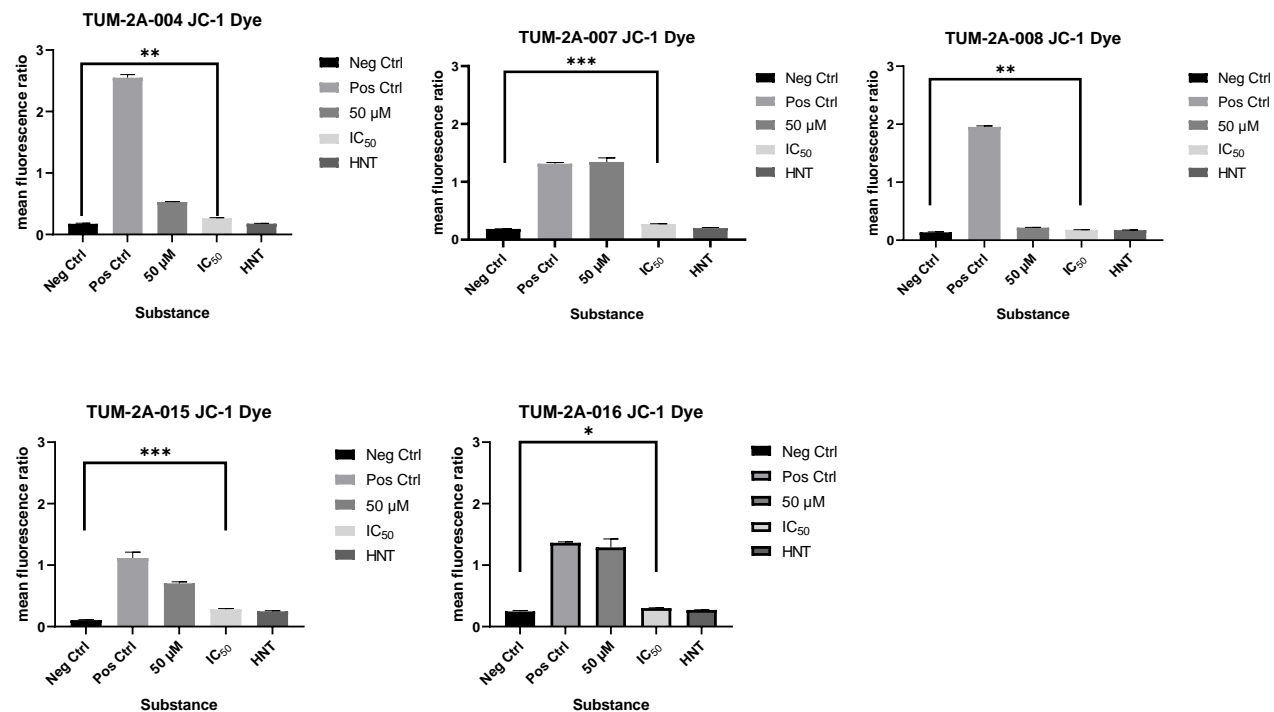


**Figure 4.31 (i) 10.47 % apoptotic cell population observed in negative control for TUM-2A-016. (ii) 97.00 % apoptotic cell population observed in positive control for TUM-2A-016 (iii) 92.30 % apoptosis observed in highest toxic concentration of TUM-2A-016 (iv) 16.50 % apoptosis observed in TUM-2A-016 IC<sub>50</sub> (v) 13.96 % apoptosis observed in highest non-toxic concentration of TUM-2A-016.**

From this, a quadrant graph of PE v FITC was made whereby the two overlaid cell populations can be seen. In the case of TUM-2A-016, the green cells are deemed apoptotic whereby they are located in the upper right (UR) quadrant. The data from the CytExpert software was extracted to an excel file. The fluorescence ratios were determined whereby the mean fluorescence values for FITC and PE were divided against one another and were plotted against the controls and substance treatment. The bar chart of results for TUM-2A-016 are shown in Figure 4.32.

#### 4.3.2.14 *HIT Compound JC-1 Dye Analysis*

JC-1 dye cell population analysis and compensation remains the same for all hit compounds as per TUM-2A-001. Statistical analysis was then performed on the hit compounds whereby the null hypothesis was such that: there is no statistical significance between the negative control and the other treatments. A one-way ANOVA was carried out whereby each treatment was compared to the negative control to determine statistical significance. Dunnett's T3 multiple comparisons test was used, and a summary of the results are shown in the **Error! Reference source not found.** Figure 4.32**Error! Reference source not found.** shows the statistical significance of the negative control when compared to the IC<sub>50</sub> value of the compound treated with the JC-1 dye. The most statistically significant compounds are observed to be TUM-2A-007 and TUM-2A-015 whereby the p value shows they have three asterisks of significance. It can therefore be inferred there is a change in the mitochondrial membrane potential which is indicative of apoptosis. TUM-2A-004 and TUM-2A-008 can also be deemed statistically significant therefore it could be assumed that there is a change in the mitochondrial membrane potential which is indicative of apoptosis. There is also statistical significance observed in TUM-2A-016 which is denoted via a p value of one asterisk.



**Figure 4.32 Hit Compounds, TUM-2A-004, TUM-2A-007, TUM-2A-008, TUM-2A-015 and TUM-2A-016 were treated with JC-1 Dye using their highest toxic concentration, the IC<sub>50</sub> value and the highest non-toxic drug concentration. Assay Conditions: U251-MG cell line. Cells were treated with fresh drug IC<sub>50</sub>. Cells were analysed 5 days after treatment, N=3 using flow cytometry. Where the X axis denotes the substance or treatment used, and the Y axis denotes the % cell death.**

**Table 4-10 Summary of results from one-way ANOVA statistical analysis for JC-1 Dye treated hit Compounds TUM-2A-004, TUM-2A-007, TUM-2A-008, TUM-2A-015 and TUM-2A-016 whereby the P values are reported as follows:  $\geq 0.05$  (ns), 0.01 to 0.05 (\*), 0.001 to 0.01 (\*\*), 0.001 to 0.01 (\*\*\*) and  $<0.0001$  (\*\*\*\*). The negative control was compared with the positive control, highest toxic concentration, IC<sub>50</sub> value and the lowest toxic concentration using Dunnett's T3 multiple comparisons statistical test.**

HIT Compound	Comparison	Summary	P Value
<b>TUM-2A-004</b>	Neg Ctrl v Pos Ctrl	***	0.0002
<b>TUM-2A-004</b>	Neg Ctrl v 50 $\mu$ M	****	$<0.0001$
<b>TUM-2A-004</b>	Neg Ctrl v IC <sub>50</sub>	**	0.0021
<b>TUM-2A-004</b>	Neg Ctrl v HNT	Ns	0.9867
<b>TUM-2A-007</b>	Neg Ctrl v Pos Ctrl	***	0.0002
<b>TUM-2A-007</b>	Neg Ctrl v 50 $\mu$ M	**	0.0028
<b>TUM-2A-007</b>	Neg Ctrl v IC <sub>50</sub>	***	0.0007
<b>TUM-2A-007</b>	Neg Ctrl v HNT	Ns	0.2912

<b>TUM-2A-008</b>	Neg Ctrl v Pos Ctrl	****	<0.0001
<b>TUM-2A-008</b>	Neg Ctrl v 50 $\mu$ M	***	0.0004
<b>TUM-2A-008</b>	Neg Ctrl v IC <sub>50</sub>	**	0.0075
<b>TUM-2A-008</b>	Neg Ctrl v HNT	*	0.0191
<b>TUM-2A-015</b>	Neg Ctrl v Pos Ctrl	**	0.0062
<b>TUM-2A-015</b>	Neg Ctrl v 50 $\mu$ M	***	0.0006
<b>TUM-2A-015</b>	Neg Ctrl v IC <sub>50</sub>	***	0.0005
<b>TUM-2A-015</b>	Neg Ctrl v HNT	***	0.0002
<b>TUM-2A-016</b>	Neg Ctrl v Pos Ctrl	****	<0.0001
<b>TUM-2A-016</b>	Neg Ctrl v 50 $\mu$ M	*	0.0116
<b>TUM-2A-016</b>	Neg Ctrl v IC <sub>50</sub>	*	0.0408
<b>TUM-2A-016</b>	Neg Ctrl v HNT	Ns	0.2188



A summary table of the results from the JC-1 dye flow cytometry analysis are shown as per **Error! Reference source not found.** The null hypothesis was such that there is no statistical significance when the negative control is compared to the IC<sub>50</sub> of the hit compounds. Each of the hit compounds was found to be statistically significant and so it can be said that each of the hit compounds is exhibiting a loss of mitochondrial membrane potential. This is an indicator that the hit compounds are potentially exhibiting cell death in the form of apoptosis. The results obtained via flow cytometry have shown that the hit compounds are eliciting cell death in the U251-MG cell line. This confirms the MTT cell viability assay results that were carried as per chapter 2 and 3. Inhibitor studies will now be carried out to further investigate whether a specific type of cell death can be determined or not.

**Table 4-11 Summary of results from one-way ANOVA statistical analysis for flow cytometry using the JC-1 dye whereby the P values are reported as follows:  $\geq 0.05$  (ns), 0.01 to 0.05 (\*), 0.001 to 0.01 (\*\*), 0.001 to 0.01 (\*\*\*) and  $< 0.0001$  (\*\*\*\*).**

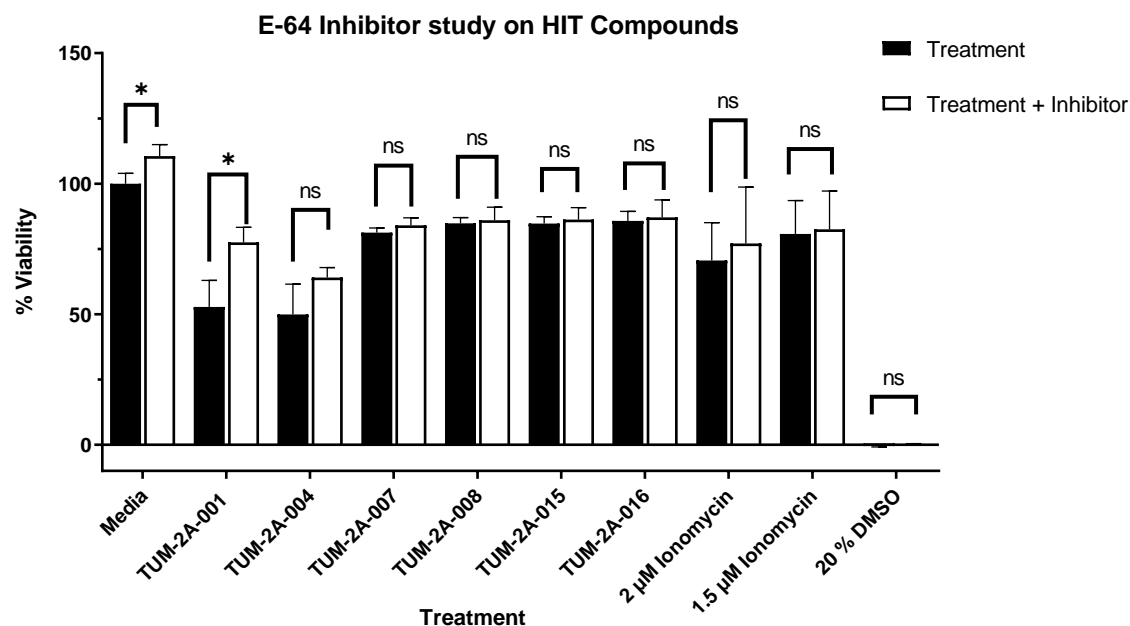
Compound Name	IC <sub>50</sub> Significance	Loss of Membrane Potential
<b>TUM-2A-001</b>	**	Yes
<b>TUM-2A-004</b>	**	Yes
<b>TUM-2A-007</b>	***	Yes
<b>TUM-2A-008</b>	**	Yes
<b>TUM-2A-015</b>	***	Yes
<b>TUM-2A-016</b>	*	Yes

### **4.3.3 Inhibitor Studies**

#### ***4.3.3.1 E-64 Inhibitor***

The negative control used in this study was DMEM and 0.5 % DMSO. The positive controls used in this study were Ionomycin and 20 % DMSO. DMSO induces cell death and so another positive control was also used, ionomycin which is a protease inhibitor. 2  $\mu$ M of this solution was used as well as 1.5  $\mu$ M as per the methods section 4.2.3.1. This was carried out to ascertain whether there would be a significant difference between the two concentrations (Conway et al., 2016).

Each of the hit compounds were treated with the E-64 inhibitor as per Figure 4.33. There is an increase in the % viability when the inhibitor was added, and so statistical analysis was carried out to ascertain whether the % increase in viability can be deemed statistically significant. The data was grouped whereby one set of data was not treated with the E-64 inhibitor and the second set of data was treated with the inhibitor. Multiple t tests were carried out to see if there was a statistically significant difference between the untreated and treated groups and the results are shown as per Table 4-12. None of the hit compounds bar TUM-2A-001 were deemed to be statistically significant. The p value obtained for TUM-2A-001 was 0.048644 and so the result is just about deemed to be significant as the cut off value is 0.05. It can be said that it is unlikely the HIT compounds are working via cysteine proteases except for potentially TUM-2A-001 this could be due to the inhibitor working on other pathways or enzymes.



*Figure 4.33 Bar chart highlighting the changes in % cell viability when controls and hit compounds are treated with E-64 inhibitor. Assay Conditions: U251-MG cell line and the MTT cell viability assay. Cells were treated with E-64 inhibitor for a period of one hour, the inhibitor was removed, and then corresponding treatment was added. Cells were analysed 5 days after treatment, N=3. Where the X axis denotes the treatment used, and the Y axis denotes the % cell viability.*

**Table 4-12 Summary of results from one-way ANOVA statistical analysis for the hit compounds & E-64 inhibitor treated hit compounds whereby the P values are reported as follows:  $\geq 0.05$  (ns), 0.01 to 0.05 (\*), 0.001 to 0.01 (\*\*), 0.001 to 0.01(\*\*\*) and  $<0.0001$ (\*\*\*\*).**

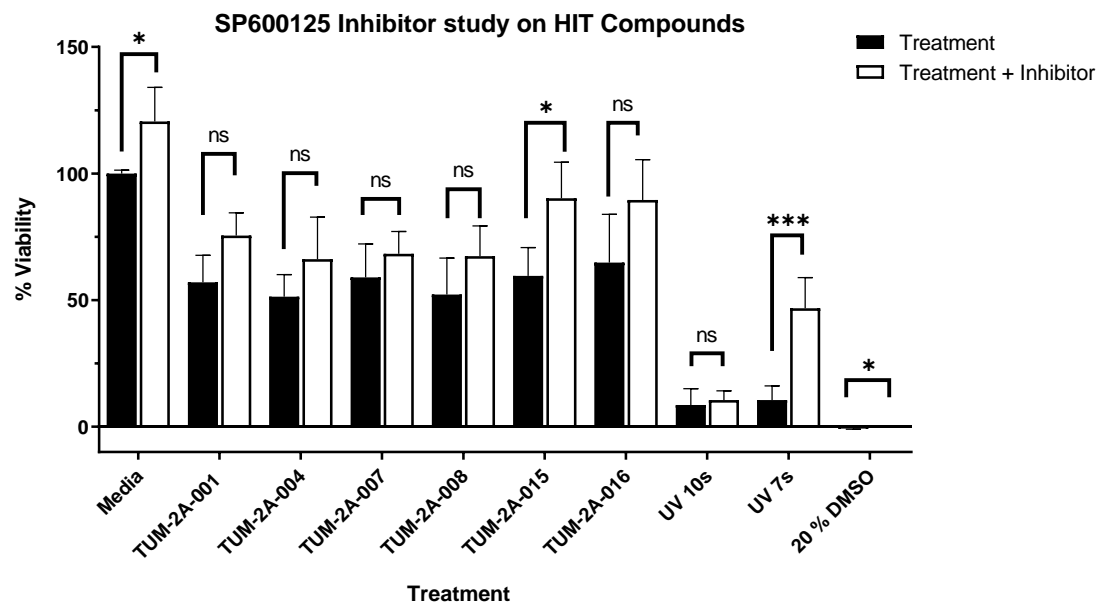
Compound Name	Summary	P Value
<b>Media &amp; Media + Inhibitor</b>	*	0.014041
<b>TUM-2A-001 &amp; TUM-2A-001 + Inhibitor</b>	*	0.048644
<b>TUM-2A-004 &amp; TUM-2A-004 + Inhibitor</b>	Ns	0.332064
<b>TUM-2A-007 &amp; TUM-2A-007 + Inhibitor</b>	Ns	0.389514
<b>TUM-2A-008 &amp; TUM-2A-008 + Inhibitor</b>	Ns	0.965794
<b>TUM-2A-015 &amp; TUM-2A-015+ Inhibitor</b>	Ns	0.965794
<b>TUM-2A-016 &amp; TUM-2A-016 + Inhibitor</b>	Ns	0.965794
<b>2 <math>\mu</math>M Ionomycin &amp; 2 <math>\mu</math>M Ionomycin + Inhibitor</b>	Ns	0.965794
<b>1.5 <math>\mu</math>M Ionomycin &amp; 1.5 <math>\mu</math>M Ionomycin + Inhibitor</b>	Ns	0.965794
<b>DMSO &amp; DMSO + Inhibitor</b>	Ns	0.389514

#### **4.3.3.2 SP600125 Inhibitor**

The negative control used in this study was DMEM and 0.5 % DMSO. The positive control used in this study was 20 % DMSO and UV Irradiation. DMSO induces cell death and so another positive control was also used, UV irradiation. Exposing mammalian cells to UV IR irradiation has been shown to activate JNK signalling, however the exact mechanism by which UV induces JNK activation is not yet known (Song & Lee, 2007). The timepoints used were 10 s and 7 s. It should be noted that Paclitaxel, an established chemotherapeutic drug used to treat ovarian cancer could also be used as a positive control for the SP600125 inhibitor. (Renlund et al., 2008). This was not used as part of this study due to Paclitaxel having P-gp mediated resistance to U251-MG cells . Each of the hit compounds were treated with the SP600125 inhibitor as per Figure 4.34.

It was found that the combination of the hit compounds with 10 s of UV irradiation killed the cells too efficiently and that there was greater significance observed when 7 s of UV irradiation was used. Each of the hit compounds and controls were treated with the SP600125 inhibitor as per Figure 4.34. There is an observed increase in the % viability when the inhibitor was added, and so statistical analysis was carried out to ascertain whether the % increase in viability can be deemed statistically significant. The data was grouped whereby one set of data was not treated with the SP600125 inhibitor and the second set of data was treated with the inhibitor. Multiple t tests were carried out to see if there was a statistically significant difference between the untreated and treated groups and the results are shown as per Table 4-13. It can be said that the addition of the SP600125 inhibitor was only deemed statistically significant on the TUM-2A-015 hit compound. The SP600125 JNK inhibitor is associated with apoptosis and so it can be

suggested that the potential mode of action for the aforementioned hit compound is apoptosis.



**Figure 4.34** Bar chart highlighting the changes in % cell viability when controls and hit compounds are treated with SP600125 inhibitor. Assay Conditions: U251-MG cell line and the MTT cell viability assay. Cells were treated with SP600125 inhibitor for a period of one hour and then corresponding treatment was added leaving 10 ml of the inhibitor in each well. Cells were analysed 5 days after treatment, N=3. Where the X axis denotes the treatment used, and the Y axis denotes the % cell viability.



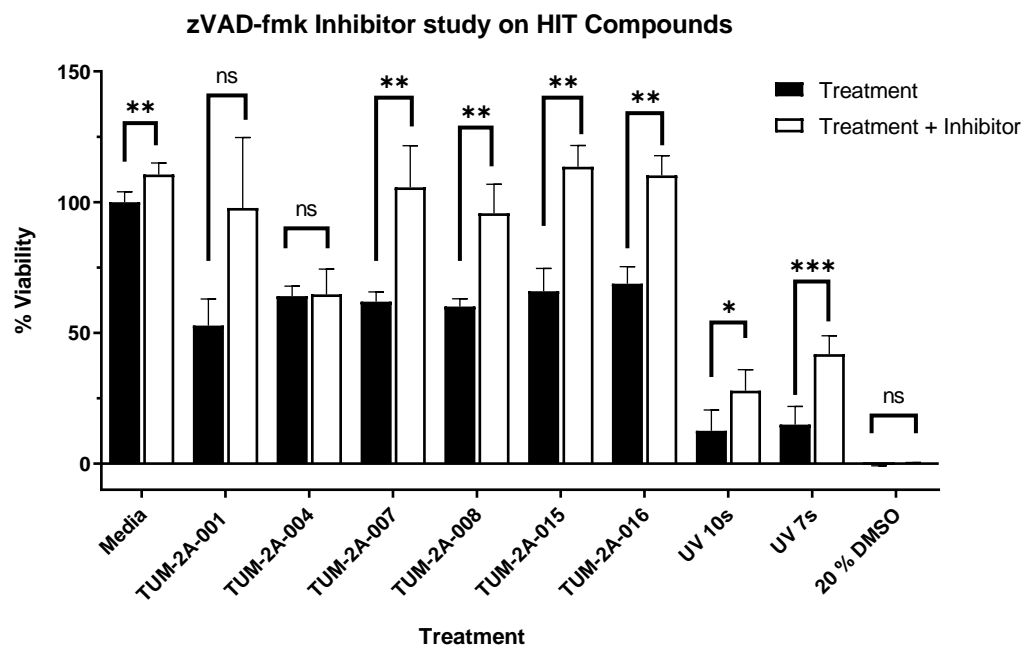
**Table 4-13 Summary of results from one-way ANOVA statistical analysis for the hit compounds & SP600125 inhibitor treated hit compounds whereby the P values are reported as follows:  $\geq 0.05$  (ns), 0.01 to 0.05 (\*), 0.001 to 0.01 (\*\*), 0.001 to 0.01(\*\*\*) and  $<0.0001$ (\*\*\*\*).**

Compound Name	Summary	P Value
<b>Media &amp; Media + Inhibitor</b>	*	0.027353
<b>TUM-2A-001 &amp; TUM-2A-001 + Inhibitor</b>	Ns	0.051578
<b>TUM-2A-004 &amp; TUM-2A-004 + Inhibitor</b>	Ns	0.264330
<b>TUM-2A-007 &amp; TUM-2A-007 + Inhibitor</b>	Ns	0.329027
<b>TUM-2A-008 &amp; TUM-2A-008 + Inhibitor</b>	Ns	0.264330
<b>TUM-2A-015 &amp; TUM-2A-015+ Inhibitor</b>	*	0.016017
<b>TUM-2A-016 &amp; TUM-2A-016 + Inhibitor</b>	Ns	0.161927
<b>10 s UV &amp; 10 s UV + Inhibitor</b>	Ns	0.540131
<b>7 s UV &amp; 7 s UV + Inhibitor</b>	***	0.000558
<b>DMSO &amp; DMSO + Inhibitor</b>	*	0.014860

#### **4.3.3.3 zVAD-fmk Inhibitor**

The negative control used in this study was DMEM and 0.5 % DMSO. The positive controls used in this study were 20 % DMSO and UV irradiation. DMSO induces cell death too readily and so there was no observable difference between DMSO and DMSO + inhibitor. As a result of this, another positive control was also used, UV IR irradiation. Each of the hit compounds and controls were treated with the zVAD-fmk inhibitor as per Figure 4.35. There is an observed increase in the % viability when the inhibitor was added, and so statistical analysis was carried out to ascertain whether the % increase in viability can be deemed statistically significant. The data was grouped whereby one set of data was not treated with the zVAD-fmk inhibitor and the second set of data was treated with the inhibitor. Multiple t tests were carried out to see if there was a statistically significant difference between the untreated and treated groups and the results are shown as per Table 4-14.

The pan caspase inhibitor, zVAD-fmk has been shown to prevent apoptosis in different cell types (Li et al., 2019). The addition of zVAD-fmk inhibitor showed statistical significance in four out of the six hit compounds where the only compounds not deemed to be statistically significant were TUM-2A-001 and TUM-2A-004. It can therefore be suggested that the following hit compounds are inducing cell death via apoptosis: TUM-2A-007, TUM-2A-008, TUM-2A-015 and TUM-2A-016.



**Figure 4.35** Bar chart highlighting the changes in % cell viability when controls and hit compounds are treated with the zVAD-fmk inhibitor. Assay Conditions: U251-MG cell line and the MTT cell viability assay. Cells were treated with the zVAD-fmk inhibitor for a period of one hour, was removed and then corresponding treatment was added. Cells were analysed 5 days after treatment, N=3. Where the X axis denotes the treatment used, and the Y axis denotes the % cell viability.

**Table 4-14 Summary of results from one-way ANOVA statistical analysis for the hit compounds & zVAD-fmk inhibitor treated hit compounds whereby the P values are reported as follows:  $\geq 0.05$  (ns), 0.01 to 0.05 (\*), 0.001 to 0.01 (\*\*), 0.001 to 0.01(\*\*\*) and  $< 0.0001$ (\*\*\*\*).**

Compound Name	Summary	P Value
<b>Media &amp; Media + Inhibitor</b>	**	0.008449
<b>TUM-2A-001 &amp; TUM-2A-001 + Inhibitor</b>	Ns	0.060771
<b>TUM-2A-004 &amp; TUM-2A-004 + Inhibitor</b>	Ns	0.907769
<b>TUM-2A-007 &amp; TUM-2A-007 + Inhibitor</b>	**	0.008914
<b>TUM-2A-008 &amp; TUM-2A-008 + Inhibitor</b>	**	0.005573
<b>TUM-2A-015 &amp; TUM-2A-015 + Inhibitor</b>	**	0.001610
<b>TUM-2A-016 &amp; TUM-2A-016 + Inhibitor</b>	**	0.001422
<b>10 s UV &amp; 10 s UV + Inhibitor</b>	*	0.030287
<b>7 s UV &amp; 7 s UV + Inhibitor</b>	***	0.000560
<b>DMSO &amp; DMSO + Inhibitor</b>	Ns	0.139144

#### **4.3.4 3D Cell Culture**

2D cell culture was carried out which allowed for a selection of hit compounds to be identified as per Chapter 2 and then be further developed as per Chapter 3. The limitations of 2D cell culture have been discussed whereby they are unable to mimic the physiological environment of complex organs thus limiting the drug-response predictions (Wang et al., 2021). A better representation of human physiology is needed in order to obtain a more accurate drug-response prediction and so the 3D cell culture method was utilised.

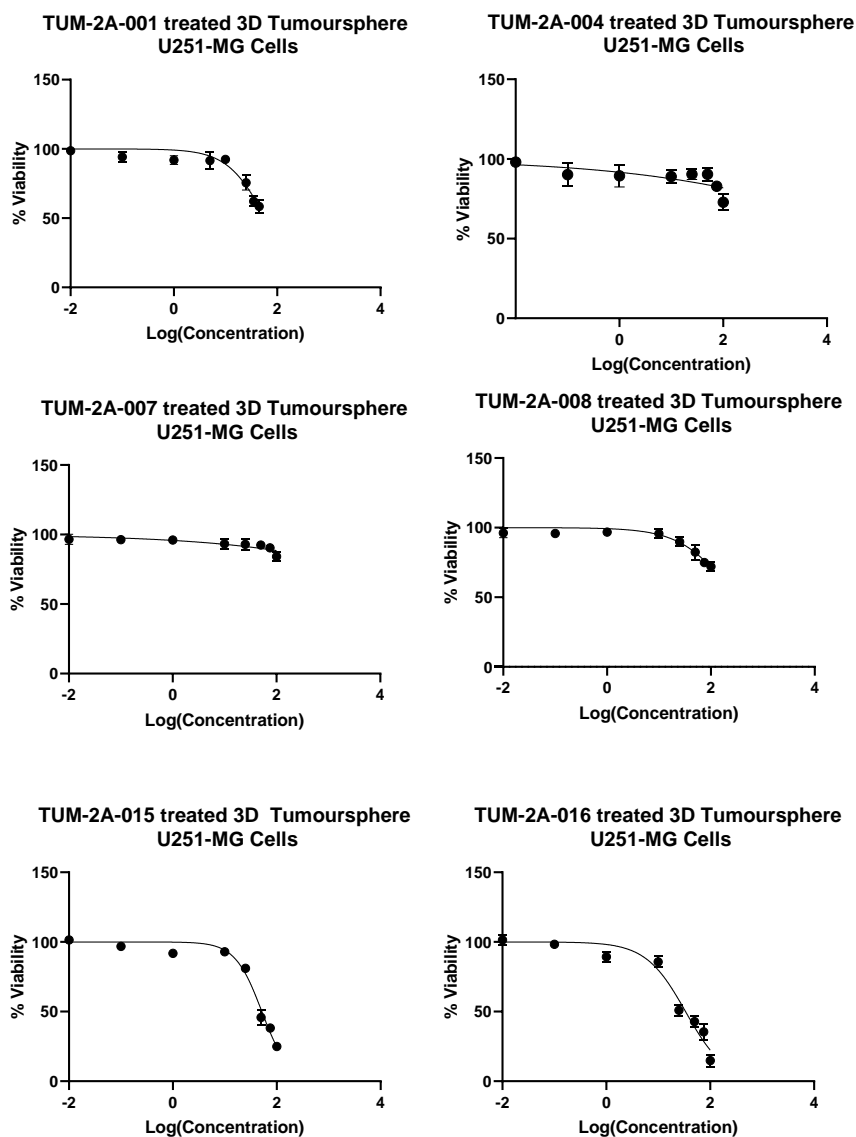
##### **4.5.2.1 Cell Viability Assay**

3D tumourspheres were grown and treated with the hit compounds to ascertain whether the drugs could potentially have a response *in vivo*. Dose response curves were generated for each 3D tumoursphere that was treated with the hit compound as shown in Figure 4.36. The IC<sub>50</sub> values for the 3D tumourspheres can be seen in Table 4-15. The results obtained where the hit compounds: TUM-2A-004, TUM-2A-007 and TUM-2A-008 did show potential activity in the initial MTT assay carried out as per chapter 2 yet they did not produce IC<sub>50</sub> values using the 3D culture method as shown in Table 4-15. It can be inferred that these compounds are not suitable to be used as a potential treatment for GBM. TUM-2A-016 demonstrated activity in the U251-MG cell line in the original MTT assay that was carried out as per Chapter 3. This was then confirmed using flow cytometry and has now demonstrated further activity using the more sophisticated 3D cell culture method.

As previously discussed in the co-treatment study section, the recommended threshold for drugs treating GBM is  $< 50 \mu\text{M}$  and for the purpose of this initial study, this was the threshold used (Gao et al., 2019). As per Table 4-15, only one HIT compound, TUM-2A-016 elicited a response that meets the criteria to treat GBM whereby the  $\text{IC}_{50}$  value obtained was  $33.55 \mu\text{M}$ . For the purpose of this study, TUM-2A-016 will be referred to as a lead compound as there is good probability that this compound would work *in vivo*. TUM-2A-015 is also borderline with respect to these criteria and so should also be considered as a potential lead compound whereby the  $\text{IC}_{50}$  obtained was  $51.72 \mu\text{M}$ . It should also be noted that as per the threshold for this study it is not probable that TUM-2A-001 will work *in vivo* as the experimental  $\text{IC}_{50}$  value obtained was  $59.50 \mu\text{M}$  which exceeds the  $50 \mu\text{M}$  criteria.

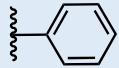
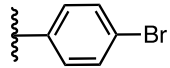
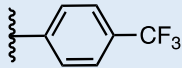
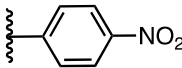
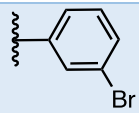
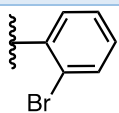
A recommendation would be to carry out a Transwell assay which models the BBB *in vivo* using both TUM-2A-015 and TUM-2A-016. The assay is based on a static apparatus where a confluent monolayer of epithelial cells is grown on top of the membrane filter (apical) and secondary cultures are seeded on the bottom of the membrane filter (basolateral). There is a membrane leak present which represents the tight junctions in the BBB as tight junctions do not form between cells and plastic (Williams-Medina et al., 2021). Through measuring the transport of the cells from the apical to the basolateral chambers, information can be provided about the mechanisms behind drug transport and whether the existing and newly identified hit compounds pass the BBB or not. This experiment could provide more insight and act as a confirmation assay as to whether the two compounds will pass the BBB and can be used as potential lead compounds for the treatment of GBM.

### 3D Tumourspheres treated with HIT Compound



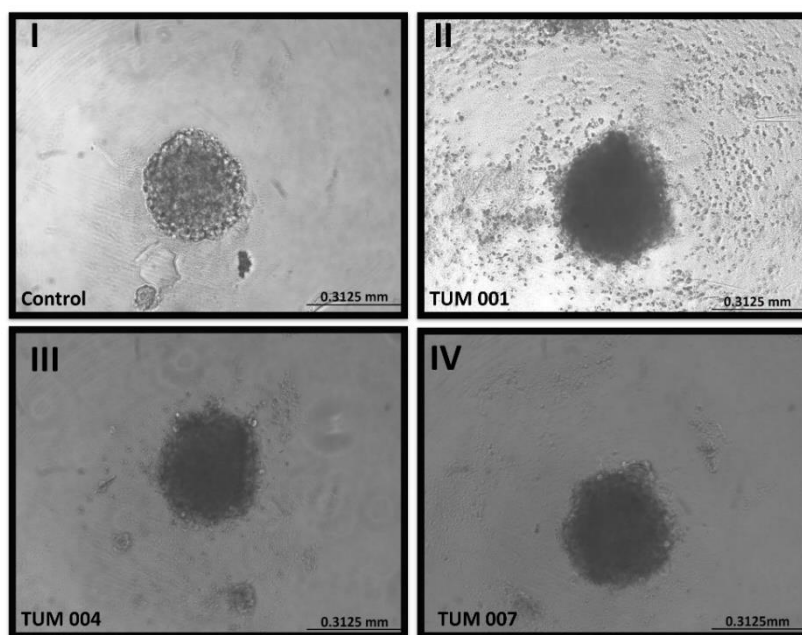
**Figure 4.36 Results of 3D cell line screen on hit compounds. Assay Conditions: U251-MG cell line and the alamarBlue™ cell viability assay. Cells were analysed 5 days after treatment, N=3. Where the X axis denotes the logarithmic concentration of hit compound, and the Y axis denotes the % cell viability.**

**Table 4-15 Results of 3D tumoursphere screen on hit compounds. Assay Conditions: U251-MG cell line and the alamarBlue™ cell viability assay. Cells were analysed 5 days after treatment, N=3. X is denoted where an experimental value was not possible.**

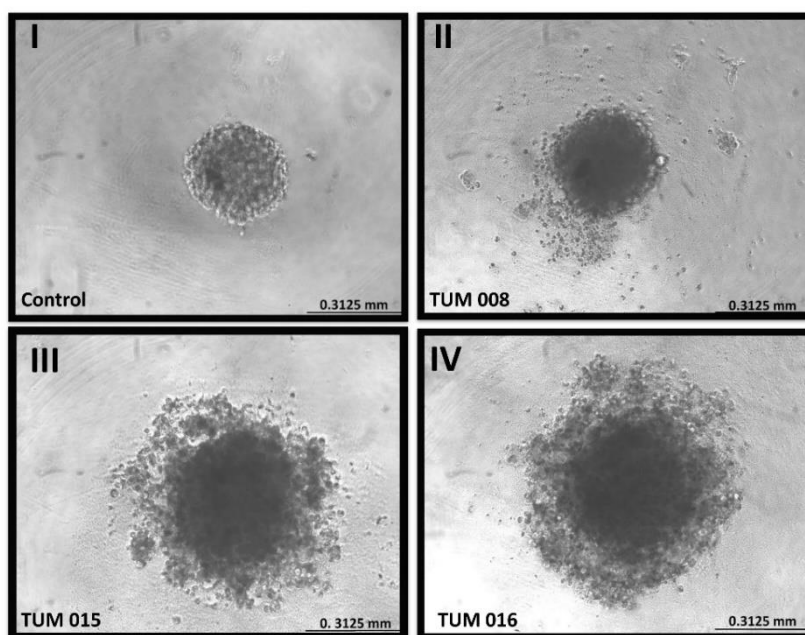
Compound Name	R Group	IC <sub>50</sub> Value (μM)	IC <sub>50</sub> 95 % CI (μM)	Hill Slope Value	Hill Slope 95 % CI
<b>TUM-2A-001</b>		59.50	52.16 to 71.31	-1.170	-1.440 to 0.9425
<b>TUM-2A-004</b>		X	X	-0.1924	-0.3072 to -0.1177
<b>TUM-2A-007</b>		X	X	-0.2355	-0.3763 to 0.1502
<b>TUM-2A-008</b>		X	X	-0.8725	-1.054 to 0.7113
<b>TUM-2A-015</b>		51.72	49.32 to 54.20	-1.679	1.693 to 1.734
<b>TUM-2A-016</b>		33.55	30.44 to 36.82	-1.136	-1.291 to 0.9930



Images were taken of the hit Compound treated tumourspheres using a regular laboratory optical microscope as per Figure 4.37 and Figure 4.38 . The images were taken on day 5 of treatment, ahead of the cell viability assay being carried out. The control used was an untreated U251-MG tumoursphere. There is no observed cell death in TUM-2A-001, TUM-2A-004, TUM-2A-007 and TUM-2A-008 which corresponds with the cell viability data previously discussed. There is observed cell death in the tumourspheres which were treated with both TUM-2A-015 and TUM-2A-016. This observed cell death can be seen in Figure 4.38 whereby the outer layers of the cell appear to shed, and the cell is visibly larger in both TUM-2A-015 and TUM-2A-016 than that of TUM-2A-008 which is shown in the same image. The compounds shown in Figure 4.37 can also be compared to that of TUM-2A-008 shown in Figure 4.38 .



***Figure 4.37 Development of 3D tumoursphere U251-MG cells in 3D cell culture model. 5-day time period used, tumourspheres treated with IC<sub>50</sub> concentration of hit compound. (i) Image of 3D tumoursphere with no treatment (ii) Image of 3D tumoursphere treated with TUM-2A-001 (iii) Image of 3D tumoursphere treated with TUM-2A-004 (iv) Image of 3D tumoursphere treated with TUM-2A-007. No observable cell death is shown. Image taken using an optical microscope.***



**Figure 4.38 Development of 3D tumoursphere U251-MG cells in 3D cell culture model. 5-day time period used, tumourspheres treated with  $IC_{50}$  concentration of hit compound. (i) Image of 3D tumoursphere with no treatment (ii) Image of 3D tumoursphere treated with TUM-2A-008 (iii) Image of 3D tumoursphere treated with TUM-2A-015 (iv) Image of 3D tumoursphere treated with TUM-2A-016. No observable cell death shown in TUM-2A-008. Cell death observed in TUM-2A-015 and TUM-2A-016. Image taken using an optical microscope.**

A summary table highlighting the results obtained from the chapter is shown in Chapter 4 of this study is divided into four subsections. The first part of this chapter looks at whether the hit compounds have the potential to be used as part of a co-treatment study. This was done by treating the hit compounds with the gold standard chemotherapeutic drug TMZ. The U251-MG cell line was treated with TMZ at the beginning of the research project (2018), and it was then later determined that TMZ is resistant to the U251-MG cell line (Shervington et al., 2020). It was also shown that TMZ does not respond to

treatment till after 120 hours whereby the timepoint used in this study was exactly 120 hours. Despite this, the hit compounds were tested in conjunction with TMZ to determine whether a synergistic effect would be observed. Unfortunately, no experimental IC<sub>50</sub> values could be obtained, and it could be suggested that TMZ had an inhibitory effect on the hit compounds. Recommendations would be such that this work could be carried out as part of future work with a different cell line such as the U87 cell line and by also carrying out the work using 3D culture models to see if there is an improved combination effect.

Flow cytometry was utilised to determine whether the hit compounds had the ability to elicit cell death. This technique was also used to confirm the 2D cell culture cell viability analysis. The two dyes used as part of the flow cytometry study were PI and the JC-1 dye. The dyes were used to confirm that the IC<sub>50</sub> values of the hit compounds were eliciting cell death and if so, was this cell death mediated via necrosis, apoptosis, autophagy or something else? Flow cytometry analysis confirmed that cell death was being observed when treated with the IC<sub>50</sub> of the hit compounds. It was found that the compounds did potentially elicit cell death via necrosis, apoptosis, or potentially other mechanisms of cell death such as autophagy as the experimental results were shown to be statistically significant.

Following the flow cytometry results, inhibitor studies were utilised in an effort to further narrow down apoptosis as a mode of cell death. As per the results from the inhibitor studies it was found that statistical significance was only observed for TUM-2A-001 for the E-64 cysteine protease inhibitor. TUM-2A-015 was observed to be statistically

significant in both the SP600125 JNK inhibitor and the zVAD-fmk caspase inhibitor. Four of the six hit compounds (TUM-2A-007, TUM-2A-008, TUM-2A-015 and TUM-2A-016) were found to be statistically significant in the caspase zVAD-fmk inhibitor. It is well known that E-64 protects cells from apoptosis, the JNK inhibitor is an indicator of apoptosis and the zVAD-fmk inhibitor is used as a broad test for apoptosis. Cell death regulated by apoptosis has been classified into an extrinsic pathway which is initiated by death receptors and an intrinsic pathway initiated by mitochondrial events.

E-64 has been shown to inhibit cathepsin B which then generates oxidative stress followed by mitochondrial mediated apoptosis (Wadhawan et al., 2014). JNK has been shown to play a role in apoptotic as well as non-apoptotic cell death mechanisms including necroptosis, ferroptosis and autophagy to name a few. It has been shown that JNK signalling is involved in the regulation of both the extrinsic and intrinsic pathways in apoptotic cell death (Dhanasekaran & Premkumar Reddy, 2017). It can be said that four of the six compounds are potentially eliciting apoptosis via caspase activation however additional studies would be required as confirmation. Caspases involved in apoptosis can be divided into two subclasses depending on their mechanism of action: initiator caspases (caspase 8 and 9) and executioner caspases (caspase 3, 6 and 7). Initiator caspases activate executioner caspases which coordinate their activities in demolishing structural proteins and activating other enzymes. Apoptosis pathways can be divided into extrinsic pathways and intrinsic pathways. The extrinsic pathway is activated through the binding of a ligand to a death receptor which in turn leads to recruitment, dimerization and activation of caspase 8. This then initiates apoptosis directly by cleaving and activating the executioner caspases or by activating the intrinsic pathway to induce cell

death. The intrinsic or mitochondrial apoptosis pathway can be activated through various cellular stresses which can lead to cytochrome c release from the mitochondria thus activating caspase 9. Active caspase 9 then initiates apoptosis by cleaving and activating executioner caspases (McIlwain et al., 2013). It can therefore be said that the hit compounds could potentially be eliciting cell death via the apoptosis mechanism as suggested in the flow cytometry study and in the inhibitor studies. Further studies would be required to confirm this theory. Apoptosis is a promising target for anticancer therapy as it is the cells natural mechanism for death (Pfeffer & Singh, 2018).

3D cell culture was carried out to determine if any of the hit compounds have the potential to elicit cell death *in vivo*. This is because the 3D model best mimics the tumour micro-environment as opposed to the 2D cell culture which was carried out in the early screening stages. It was found that four of the six hit compounds did not elicit cell death in the tumourspheres: TUM-2A-001, TUM-2A-004, TUM-2A-007 and TUM-2A-008. The IC<sub>50</sub> value generated was either too high (> 50 µM) as seen in TUM-2A-001 or there was no IC<sub>50</sub> value generated at all as shown in the compounds. The concentration threshold given for the compounds was < 50 µM, this is because none of the current marketed drugs exceed this value. This threshold has been used throughout this research project as a cut-off guideline for the initial studies. It was found that TUM-2A-016 was the only compound to obtain an IC<sub>50</sub> value below this amount, 33.55 µM. TUM-2A-015 was also shown to exhibit a cytotoxic effect where its IC<sub>50</sub> value is slightly above the 50 µM threshold (51.72 µM). Images were taken of all the treated 3D tumourspheres where both TUM-2A-015 and TUM-2A-016 were the only compounds that showed death in the tumoursphere.

. It can be concluded that from the six hit compounds, there are potentially two lead compounds (TUM-2A-015 and TUM-2A-016) that can be used in the treatment of GBM based off the experimental results gathered.

**Table 4-16** Summary table of results obtained from co-treatment studies, flow cytometry, inhibitor studies and 3D cell culture highlighting statistical significance whereby the *P* values are reported as follows:  $\geq 0.05$  (ns), 0.01 to 0.05 (\*), 0.001 to 0.01 (\*\*), 0.001 to 0.01 (\*\*\*) and  $< 0.0001$  (\*\*\*\*). The compounds which are deemed statistically significant are those shaded in green.

Compound Name	TMZ Co-Treatment	Necrosis PI Stain	Apoptosis JC-1 Stain	E-64 Inhibitor	SP600125 Inhibitor (JNK)	zVAD-fmk Inhibitor (Apoptosis)	3D Cell Culture IC <sub>50</sub> (μM)	3D Cell Culture Image Cell Death
<b>TUM-2A-001</b>	ns	ns	**	*	ns	ns	59.50	No
<b>TUM-2A-004</b>	ns	****	**	ns	ns	ns	X	No
<b>TUM-2A-007</b>	ns	**	****	ns	ns	**	X	No
<b>TUM-2A-008</b>	ns	**	**	ns	ns	**	X	No
<b>TUM-2A-015</b>	ns	*	****	ns	*	**	<b>51.72</b>	<b>Yes</b>
<b>TUM-2A-016</b>	ns	****	*	ns	ns	**	<b>33.55</b>	<b>Yes</b>



#### **4.4. Discussion**

Chapter 4 of this study is divided into four subsections. The first part of this chapter looks at whether the hit compounds have the potential to be used as part of a co-treatment study. This was done by treating the hit compounds with the gold standard chemotherapeutic drug TMZ. The U251-MG cell line was treated with TMZ at the beginning of the research project (2018), and it was then later determined that TMZ is resistant to the U251-MG cell line (Shervington et al., 2020). It was also shown that TMZ does not respond to treatment till after 120 hours whereby the timepoint used in this study was exactly 120 hours. Despite this, the hit compounds were tested in conjunction with TMZ to determine whether a synergistic effect would be observed. Unfortunately, no experimental  $IC_{50}$  values could be obtained, and it could be suggested that TMZ had an inhibitory effect on the hit compounds. Recommendations would be such that this work could be carried out as part of future work with a different cell line such as the U87 cell line and by also carrying out the work using 3D culture models to see if there is an improved combination effect.

Flow cytometry was utilised to determine whether the hit compounds had the ability to elicit cell death. This technique was also used to confirm the 2D cell culture cell viability analysis. The two dyes used as part of the flow cytometry study were PI and the JC-1 dye. The dyes were used to confirm that the  $IC_{50}$  values of the hit compounds were eliciting cell death and if so, was this cell death mediated via necrosis, apoptosis, autophagy or something else? Flow cytometry analysis confirmed that cell death was being observed when treated with the  $IC_{50}$  of the hit compounds. It was found that the compounds did

potentially elicit cell death via necrosis, apoptosis, or potentially other mechanisms of cell death such as autophagy as the experimental results were shown to be statistically significant.

Following the flow cytometry results, inhibitor studies were utilised in an effort to further narrow down apoptosis as a mode of cell death. As per the results from the inhibitor studies it was found that statistical significance was only observed for TUM-2A-001 for the E-64 cysteine protease inhibitor. TUM-2A-015 was observed to be statistically significant in both the SP600125 JNK inhibitor and the zVAD-fmk caspase inhibitor. Four of the six hit compounds (TUM-2A-007, TUM-2A-008, TUM-2A-015 and TUM-2A-016) were found to be statistically significant in the caspase zVAD-fmk inhibitor. It is well known that E-64 protects cells from apoptosis, the JNK inhibitor is an indicator of apoptosis and the zVAD-fmk inhibitor is used as a broad test for apoptosis. Cell death regulated by apoptosis has been classified into an extrinsic pathway which is initiated by death receptors and an intrinsic pathway initiated by mitochondrial events.

E-64 has been shown to inhibit cathepsin B which then generates oxidative stress followed by mitochondrial mediated apoptosis (Wadhawan et al., 2014). JNK has been shown to play a role in apoptotic as well as non-apoptotic cell death mechanisms including necroptosis, ferroptosis and autophagy to name a few. It has been shown that JNK signalling is involved in the regulation of both the extrinsic and intrinsic pathways in apoptotic cell death (Dhanasekaran & Premkumar Reddy, 2017). It can be said that four of the six compounds are potentially eliciting apoptosis via caspase activation however additional studies would be required as confirmation. Caspases involved in

apoptosis can be divided into two subclasses depending on their mechanism of action: initiator caspases (caspase 8 and 9) and executioner caspases (caspase 3, 6 and 7). Initiator caspases activate executioner caspases which coordinate their activities in demolishing structural proteins and activating other enzymes. Apoptosis pathways can be divided into extrinsic pathways and intrinsic pathways. The extrinsic pathway is activated through the binding of a ligand to a death receptor which in turn leads to recruitment, dimerization and activation of caspase 8. This then initiates apoptosis directly by cleaving and activating the executioner caspases or by activating the intrinsic pathway to induce cell death. The intrinsic or mitochondrial apoptosis pathway can be activated through various cellular stresses which can lead to cytochrome c release from the mitochondria thus activating caspase 9. Active caspase 9 then initiates apoptosis by cleaving and activating executioner caspases (McIlwain et al., 2013). It can therefore be said that the hit compounds could potentially be eliciting cell death via the apoptosis mechanism as suggested in the flow cytometry study and in the inhibitor studies. Further studies would be required to confirm this theory. Apoptosis is a promising target for anticancer therapy as it is the cells natural mechanism for death (Pfeffer & Singh, 2018).

3D cell culture was carried out to determine if any of the hit compounds have the potential to elicit cell death *in vivo*. This is because the 3D model best mimics the tumour micro-environment as opposed to the 2D cell culture which was carried out in the early screening stages. It was found that four of the six hit compounds did not elicit cell death in the tumourspheres: TUM-2A-001, TUM-2A-004, TUM-2A-007 and TUM-2A-008. The IC<sub>50</sub> value generated was either too high (> 50 µM) as seen in TUM-2A-001 or there was no

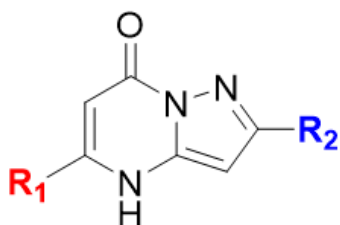
IC<sub>50</sub> value generated at all as shown in the compounds. The concentration threshold given for the compounds was < 50 µM, this is because none of the current marketed drugs exceed this value. This threshold has been used throughout this research project as a cut-off guideline for the initial studies. It was found that TUM-2A-016 was the only compound to obtain an IC<sub>50</sub> value below this amount, 33.55 µM. TUM-2A-015 was also shown to exhibit a cytotoxic effect where its IC<sub>50</sub> value is slightly above the 50 µM threshold (51.72 µM). Images were taken of all the treated 3D tumourspheres where both TUM-2A-015 and TUM-2A-016 were the only compounds that showed death in the tumoursphere.

## **5. GENERAL DISCUSSION**

GBM is considered to be the most common and aggressive type of brain tumour with a median survival rate of 15 months (Grochans et al., 2022). The current gold standard treatment for GBM is referred to as the “Stupp Protocol” and involves the use of maximal safe surgical resection, radiotherapy and the use of the chemotherapeutic agent TMZ (Adegboyega et al., 2021). This protocol has not changed in 18 years, it offers a modest prognosis and is associated with side effects and an array of limitations (Stupp et al., 2005). There are several factors which attest to the difficulty in treating GBM one being the BBB. The delivery of drugs is limited by the BBB where about 98 % of small molecules and almost all macromolecule drugs such as monoclonal antibodies cannot enter the CNS to exert a therapeutic effect. This leads to the failure of many drugs in clinical trials (Tang et al., 2021). The rapid proliferation and drug resistance of tumour cells further increase the difficulty of treatment. It is therefore evident that there is an urgent need for further drug discovery to be carried out (Poon et al., 2021). This thesis focused on the development of novel therapeutic compounds and tries to provide a better understanding surrounding cell death in GBM in response to these compounds. It also looks at their potential ability to work *in vivo* and as part of a co-treatment study with the current state of the art treatments.

The 20 pyrazolo[1,5- $\alpha$ ]pyrimidinone compounds used as part of the initial screen were those developed by the Stephens research group in Maynooth University. The compounds that were developed are structurally different but have a similar biological effect to anti-diabetic drug Metformin. Metformin has been repurposed as it has demonstrated an ability to reduce cancer incidence and mortality, specifically in gliomas. It has been shown to inhibit proliferation of human glioma cells in the U251-MG cell line and has

also affected tumour growth in mice models through the regulation of AMPK (Seliger et al., 2019). Preliminary results carried out by (Conway et al., 2016) showed that these compounds did elicit a cytotoxic effect against the U251-MG cell line. The 20 substituted pyrazolo[1,5- $\alpha$ ]pyrimidinones were separated based on structural variations and a SAR study was carried out. Four analogues of TUM-1-005 were tested whereby the core scaffold remained unchanged and the  $R^1$  substituent on the pyrimidine ring and an  $R^2$  substituent on the pyrazole ring were modified as shown in Figure 5.1.



**Figure 5.1** Structure of the analogue compound whereby there is an  $R^1$  substituent group on the pyrimidine ring and there is an  $R^2$  substituent group on the pyrazole ring.

The 20 pyrazolo[1,5- $\alpha$ ]pyrimidinone compounds were screened using the MTT cell proliferation assay against a cancerous U251-MG cell line and a non-cancerous HEK293 cell line. A total of 4 hit compounds were determined whereby they all belonged to the group 2A, where the  $R^1$  substituent is a 1,3-bis(trifluoromethyl)phenyl and the  $R^2$  substituent is varied but must be a substituted aryl ring. The four identified hit compounds were as follows: TUM-2A-001, TUM-2A-004, TUM-2A-007 and TUM-2A-008. Each of the hit compounds contained  $R^2$  substituents which were lipophilic and electron withdrawing in nature except for TUM-2A-008 which contained a strong electron

withdrawing group but was not lipophilic. They were deemed to be statistically significant as there was a significant difference in the IC<sub>50</sub> values between the cancerous and non-cancerous cell line. The IC<sub>50</sub> values obtained for the hit compounds were 6.17 µM, 29.49 µM, 26.75 µM and 29.62 µM respectively. Each of the hit compounds obtained an IC<sub>50</sub> value of < 50 µM which is the threshold for current chemotherapeutics used in the treatment of GBM (Gao et al., 2019). The compounds were then evaluated using Lipinski's physicochemical modified "rule of 5" as a guide to ascertain whether they have potential to cross the BBB (Shultz, 2019). It was found that each hit compound determined as part of Chapter 2 had a high probability of crossing the BBB as well as a low IC<sub>50</sub> value and could therefore be used in further studies to evaluate their suitability as a treatment for GBM.

A SAR study was carried out whereby the hit compounds were re-synthesised as part of Chapter 3 as well as synthesising additional analogue compounds of the hit compounds. The hit compounds were modified to determine whether this would enhance or decrease their biological activity and selectivity. The modification of functional groups and their position is very common practise in the field of medicinal chemistry as it can increase or decrease the selectivity of the drug. An example of such is that a study was carried out by (Liew et al., 2020) on isocoumarin compounds which found that an anti-metastatic effect was observed when fluoro groups were added to the *meta* and *para* positions of the phenyl ring. Coumarins have very significant anti-tumour abilities and anti-tumour mechanisms such as targeting mTOR signalling pathways and inducing cell apoptosis protein activation (Wu et al., 2020).



The four previously identified hit compounds (TUM-2A-001, TUM-2A-004, TUM-2A-007 and TUM-2A-008) all contain a *para* substituted phenyl ring and the synthesised analogues contained *meta* and *ortho* substituents. The analogues were screened in the same manner as observed in Chapter 2. From this, a further two hit compounds were then determined (TUM-2A-015 and TUM-2A-016). The new hit compounds contained a *meta* bromophenyl ring and an *ortho* bromophenyl substituent. It was found that by moving the bromo substituent from the *para* position to the *meta* and *ortho* positions the IC<sub>50</sub> values were lowered significantly from 29.49 µM to 0.51 µM and 2.79 µM respectively. Thus, improving the selectivity and potency of the compounds as a smaller concentration of the compound is required to elicit cell death which would be ideal in a patient setting as there is a lower dose of a toxic compound being administered. By moving the bromo substituent from the *para* position to both the *meta* and *ortho* position, selectivity for the cancerous cell line was increased and the overall potency of the drugs were also increased.

Chapter 4 of this study was broken into four subsections. The use of a co-treatment study was carried out using the gold standard chemotherapeutic as per the “Stupp Protocol.” It was found that current gold standard treatment, TMZ does not elicit cell death as a standalone treatment on the U251-MG cell line. Further to this it was found that none of the compounds were suitable for use in conjunction with TMZ. It can therefore be inferred that the hit compounds are suitable for use as a stand-alone treatment when used against the U251-MG mutant cell line. The effect of TMZ is not comparable across GBM cell lines and it would be therefore be recommended that this work be repeated as part of the future work using a wildtype U87 cell line that is not TMZ resistant.(Poon et al., 2021) It

is a common occurrence where not all therapeutic treatments are suitable for use for every subtype of cancer. Sorafenib is an oral multi kinase inhibitor which can be used in the treatment of breast cancer (Zafrakas et al., 2016). The use of Sorafenib is not suitable and not comparable for all types of breast cancer treatment. Sorafenib is not suitable for use when overexpression of human epidermal growth factor receptor 2 (HER2) is observed however it is suitable for treatment in triple negative breast cancer (Jaeger et al., 2015).

The second study carried out as per Chapter 4 was the use of flow cytometry. Flow cytometry confirmed the results from the 2D MTT cell proliferation assays that were carried out as per Chapter 2 and Chapter 3. It was found that the compounds did potentially elicit cell death via necrosis, apoptosis, autophagy or potentially other cell death mechanisms as the experimental results were shown to be statistically significant.

The third study carried out as per Chapter 4 was the use of inhibitors to further narrow down a particular mode of cell death. The E-64 cysteine protease inhibitor, the JNK SP600125 inhibitor and the zVAD-fmk caspase inhibitor were used as part of this study. E-64 and zVAD-fmk are both used to prevent apoptosis and the SP600125 inhibitor is widely used to inhibit JNK activation and apoptosis (Wadhawan et al., 2014) (Li et al., 2019). It was determined that that four of the compounds (TUM-2A-007, TUM-2A-008, TUM-2A-015 and TUM-2A-016) potentially elicited caspase activated cell death via the zVAD-fmk inhibitor, one compound (TUM-2A-015) potentially elicited cell death via SP600125 JNK activation, and one compound (TUM-2A-001) potentially elicited cell death via E-64 cysteine protease activation. It should be noted that TUM-2A-004 was not statistically significant for any of the inhibitors used. It can therefore be said that the hit

compounds are potentially eliciting cell death via the apoptosis mechanism as suggested in the flow cytometry study and in the inhibitor studies. Further work is required to confirm this hypothesis.

Apoptosis is a promising target for anticancer therapy as it is the cells natural mechanism for death. The apoptotic pathway is usually inhibited in cancer and can be done through the over expression of proteins or the under expression of proteins. These changes can then cause resistance to chemotherapeutics. Promising new anticancer therapies are said to be compounds that exhibit anticancer activity through the apoptotic pathway (Pfeffer & Singh, 2018). A suggestion would be to carry out future work investigating the modes of cell death particularly intrinsic apoptosis due to the preliminary results obtained from the MTT cell viability assays, the flow cytometry results and the inhibitor studies that were carried out.

The final 3D cell culture study described in Chapter 4 was carried out to determine if any of the hit compounds have the potential to elicit cell death in models which best represent conditions *in vivo*. 2D cell culture was carried out as per Chapter 2 and Chapter 3. While the 2D cell culture technique was ideal for the initial biological screening, it is not representative of the physiological conditions of the cells in the tumour micro-environment. This discrepancy is thought to be a significant contributor to the high failure rate in drug discovery, in which only a low percentage of drugs pass the development stage. 3D cell culture is now being pursued as it more closely resembles the *in vivo* cell environment and allows for higher precision in drug discovery (Langhans, 2018). Two compounds, TUM-2A-015 and TUM-2A-016 both obtained an experimental IC<sub>50</sub> value

of 0.51  $\mu\text{M}$  and 2.79  $\mu\text{M}$  in the 2D cell culture studies respectively. The  $\text{IC}_{50}$  values obtained for TUM-2A-015 and TUM-2A-016 as part of the 3D cell culture studies were below the 50  $\mu\text{M}$  threshold or were only slightly above this value: 33.55  $\mu\text{M}$  and 51.72  $\mu\text{M}$  respectively. There is an increase in the  $\text{IC}_{50}$  values obtained in the 3D cell culture assay, however, this value is more representative of the compounds behaviour *in vivo*. Images were also taken of all the treated 3D tumourspheres in which both TUM-2A-015 and TUM-2A-016 were the only compounds that confirmed death in the tumoursphere. This is observed whereby the outer layers of the tumoursphere appear to shed and the tumoursphere is visibly larger in size. It can therefore be inferred that out of all the hit compounds, TUM-2A-015 and TUM-2A-016 are the only compounds which have the potential to work *in vivo*. The other four compounds could potentially work *in vivo* but the method of drug delivery would need to be altered. For example, the hit compounds could be placed directly into the brain during surgery as observed in Carmustine wafers. This removes the obstacle of the drug needing to pass the BBB. This thesis provides some promising results whereby two lead compounds (TUM-2A-015 and TUM-2A-016) have been identified which have the potential to be used as a therapeutic for the treatment of GBM.

## **6. FUTURE WORK**

Recommended future work would be to employ computational chemistry methods to develop a pharmacophore and quantitative structure-activity relationship (QSAR) model. QSAR is a computational modelling method used to reveal relationships between structural properties of chemical compounds and their biological activities (Kwon et al., 2019). *In silico* methods have the advantage that they can make fast predictions for a large set of compounds in high throughput mode. Another advantage of using computational methods is that predictions can be made based on the structure of the compound without having to synthesise it (Amberg, 2013). This would be ideal when trying to further modify the compounds structure and could potentially identify new structures that do not belong to the 2A group. Computational chemistry can also be used to predict whether the compounds have the ability to pass the BBB. Based on the current findings, ideally more substituted pyrazolo[1,5- $\alpha$ ]pyrimidinone compounds in group 2A could be identified as well as other analogues that do not have the same structure as group 2A. The identified compounds could then be synthesised in the lab and biologically screened using 3D cell culture. This allows for a quicker and more efficient way to determine if the new compounds can potentially work *in vivo* thus being more time and cost effective.

The initial co-treatment studies, flow cytometry work and inhibitor studies work with the hit compounds and potential new compounds would be repeated using 3D cell culture. The initial studies were carried out using 2D cell culture which does not accurately reflect the tumour microenvironment. It is also suggested that the U87 wildtype GBM cell line be used in conjunction with the current hit compounds to assess their suitability for use as part of a co-treatment study as TMZ is not resistant to the U87 wildtype cell line (Zhu et al., 2021). As a continuation of this work, it would be recommended that the BBB be

modelled *in vitro*. Modelling the BBB *in vitro* has become increasingly more important for the advances of neuroscience research. The most common *in vitro* model of the BBB is based on the Transwell assay (Linville & Searson, 2021). The information gathered from this assay would therefore allow us to determine whether the compounds would potentially cross the BBB thus being a suitable candidate for use as a treatment for GBM. Further mechanistic work is also required as part of future work. The preliminary results obtained from the MTT cell viability assay, the flow cytometry work and inhibitor studies were very broad and so more in-depth studies would be required. Dyes such as Annexin V / PI could be used to differentiate between apoptotic and necrotic cell populations. Cells could also be stained with a fluorescently labelled autophagy marker specific for autophagic processes e.g., LC3-II. Caspase activity and reactive oxygen species (ROS) could also be measured as they are useful markers for identifying apoptotic cell populations. Gene expression analysis could also potentially be employed such as real time quantitative PCR or RNA sequencing to investigate the expression levels of genes associated with apoptosis. This would allow for the assessment of changes in the transcriptional regulation of apoptotic genes. Electron microscopy could also be a useful tool to carry out mechanistic work. Transmission electron microscopy (TEM) can provide ultrastructural evidence of apoptotic features such as condensed chromatin and mitochondrial changes. Examination of cells by TEM can confirm the occurrence of apoptosis and provide detailed morphological information (Hu et al., 2021).

## 7. REFERENCES

- Abdel-Jalil, R. J., Khanfar, M., Abu-Safieh, K., Al-Gharabli, S., El-Abadelah, M., & Voelter, W. (2005). An Efficient One-Pot Synthesis of Pyrazolopyrimidines, Intermediates for Potential Phosphodiesterase Inhibitors. *Monatshefte Für Chemie - Chemical Monthly*, 136(4), 619–624. <https://doi.org/10.1007/s00706-004-0252-0>
- Adegboyega, G., Kanmounye, U. S., Petrinic, T., Ozair, A., Bandyopadhyay, S., Kuri, A., Zolo, Y., Marks, K., Ramjee, S., Baticulon, R. E., Vaqas, B., & Collaborative, on behalf of I. U. (2021). Global Landscape of Glioblastoma Multiforme Management in the Stupp Protocol Era: Systematic Review Protocol. *International Journal of Surgery Protocols*, 25(1), 108. <https://doi.org/10.29337/IJSP.148>
- Agarwala, S. S., & Kirkwood, J. M. (2000). Temozolomide, a Novel Alkylating Agent with Activity in the Central Nervous System, May Improve the Treatment of Advanced Metastatic Melanoma; Temozolomide, a Novel Alkylating Agent with Activity in the Central Nervous System, May Improve the Treatment of Advanced Metastatic Melanoma. In *The Oncologist* (Vol. 5). <https://doi.org/10.1634/theoncologist.5-2-144>
- Al-Okaili, R. N., Krejza, J., Wang, S., Woo, J. H., & Melhem, E. R. (2006). Advanced MR imaging techniques in the diagnosis of intraaxial brain tumors in adults. In *Radiographics* (Vol. 26, Issue SPEC. ISS.). Radiological Society of North America . <https://doi.org/10.1148/rg.26si065513>
- Amberg, A. (2013). In silico methods. *Drug Discovery and Evaluation: Safety and Pharmacokinetic Assays, Second Edition*, 1273–1296. [https://doi.org/10.1007/978-3-642-25240-2\\_55/COVER](https://doi.org/10.1007/978-3-642-25240-2_55/COVER)



- Armand, J. P., Ribrag, V., Harrousseau, J. L., & Abrey, L. (2007). Reappraisal of the use of procarbazine in the treatment of lymphomas and brain tumors. In *Therapeutics and Clinical Risk Management* (Vol. 3, Issue 2, pp. 213–224). Dove Press. <https://doi.org/10.2147/tcrm.2007.3.2.213>
- ATCC. (2023). *Certified Reference Material* / ATCC. <https://www.atcc.org/cell-products/human-cells/certified-reference-materials#t=productTab&numberOfResults=24>
- Atlee, J. (2007). *Complications in Anesthesia* (2nd ed.). Elsevier.
- Ayob, A. Z., & Ramasamy, T. S. (2018). Cancer stem cells as key drivers of tumour progression. *Journal of Biomedical Science*, 25(1), 20. <https://doi.org/10.1186/s12929-018-0426-4>
- Bale, T. A., & Rosenblum, M. K. (2022). The 2021 WHO Classification of Tumors of the Central Nervous System: An update on pediatric low-grade gliomas and glioneuronal tumors. *Brain Pathology*, 32(4), e13060. <https://doi.org/10.1111/BPA.13060>
- Banday, A. H., & Abdalla, M. (2022). Immune Checkpoint Inhibitors: Recent clinical advances and future prospects. *Current Medicinal Chemistry*, 29. <https://doi.org/10.2174/0929867329666220819115849>
- Barciszewska AM, Gurda D, Glodowicz P, Nowak S, N.-B. M. (2015). A new epigenetic mechanism of temozolomide action in glioma cells. *PLOS One*. <https://doi.org/https://doi.org/10.1371/journal.pone.0136669>
- Bausart, M., Pr  at, V., & Malfanti, A. (2022). Immunotherapy for glioblastoma: the

- promise of combination strategies. *Journal of Experimental & Clinical Cancer Research* 2022 41:1, 41(1), 1–22. <https://doi.org/10.1186/S13046-022-02251-2>
- Benet, L. Z., Hosey, C. M., Ursu, O., & Oprea, T. I. (2016). BDDCS, the Rule of 5 and drugability. In *Advanced Drug Delivery Reviews* (Vol. 101, pp. 89–98). Elsevier B.V. <https://doi.org/10.1016/j.addr.2016.05.007>
- Bilous, R; Donnelly, R. (2010). *Handbook of Diabetes* (4th ed.). Wiley-Blackwell.
- Bioinformatics, S. I. of. (2022). *SwissADME*. <http://www.swissadme.ch/index.php>
- Bolen S, Tseng E, Huftless S, Segal JB, Suarez-Cuervo C, Berger Z, Wilson LM, Chu Y, Lyoha E, M. N. (2016). Diabetes Medications for Adults with Type 2 Diabetes: An Update. *Comparative Effectiveness Reviews*, 173.
- Bradley, C. A., Taghibiglou, C., Collingridge, G. L., & Yu, T. W. (2008). Mechanisms involved in the reduction of GABAA receptor  $\alpha 1$ -subunit expression caused by the epilepsy mutation A322D in the trafficking-competent receptor. *Journal of Biological Chemistry*, 283(32), 22043–22050. <https://doi.org/10.1074/jbc.M801708200>
- Bradshaw, A., Wickremsekera, A., Tan, S. T., Peng, L., Davis, P. F., & Itinteang, T. (2016). Cancer Stem Cell Hierarchy in Glioblastoma Multiforme. *Frontiers in Surgery*, 3, 21. <https://doi.org/10.3389/fsurg.2016.00021>
- Butowski, N. A. (2015). Epidemiology and diagnosis of brain tumors. In *CONTINUUM Lifelong Learning in Neurology* (Vol. 21, Issue 2, pp. 301–313). Lippincott Williams and Wilkins. <https://doi.org/10.1212/01.CON.0000464171.50638.fa>
- Cai, X., & Sughrue, M. E. (2018). Glioblastoma: new therapeutic strategies to address cellular and genomic complexity. *Oncotarget*, 9(10), 9540–9554.

- <https://doi.org/10.18632/oncotarget.23476>
- Chaput, G., & Regnier, L. (2021). Radiotherapy: Clinical pearls for primary care. *Canadian Family Physician*, 67(10), 753. <https://doi.org/10.46747/CFP.6710753>
- Chowdhary, S. A., Ryken, T., & Newton, H. B. (2015). Survival outcomes and safety of carmustine wafers in the treatment of high-grade gliomas: a meta-analysis. *Journal of Neuro-Oncology*, 122(2), 367–382. <https://doi.org/10.1007/s11060-015-1724-2>
- Chowdhury, S., Hasan Bappy, M., Clocchiatti-Tuozzo, S., Cheeti, S., Chowdhury, S., & Patel, V. (2021). *Current Advances in Immunotherapy for Glioblastoma Multiforme and Future Prospects*. <https://doi.org/10.7759/cureus.20604>
- ClinicalTrials.gov. (2020). *Study to Evaluate the Safety and Efficacy of CTP-656 in Patients With Cystic Fibrosis With CFTR Gating Mutations*. <https://clinicaltrials.gov/ct2/show/NCT02971839>
- Colvin, M. (2003). Alkylating Agents. In R. Kuffe, DW; Pollock, RE; Weichselbaum (Ed.), *Holland-Frei Cancer Medicine* (6th ed.). BC Decker.
- Comelli, I., Lippi, G., Campana, V., Servadei, F., & Cervellin, G. (2017). Clinical presentation and epidemiology of brain tumors firstly diagnosed in adults in the Emergency Department: A 10-year, single center retrospective study. *Annals of Translational Medicine*, 5(13). <https://doi.org/10.21037/ATM.2017.06.12>
- Conway, G., Curtin, J. F., & Howe, O. (2016). *Novel Therapeutic Approaches to Induce Autophagy in Brain Cancer* [Dublin Institute of Technology]. <https://doi.org/10.21427/D7632V>
- Cook, A. M., Morgan Jones, G., Hawryluk, G. W. J., Mailloux, P., McLaughlin, D.,

- Papangelou, A., Samuel, S., Tokumaru, S., Venkatasubramanian, C., Zacko, C., Zimmermann, L. L., Hirsch, K., & Shutter, L. (2020). Guidelines for the Acute Treatment of Cerebral Edema in Neurocritical Care Patients. *Neurocritical Care*, 32(3), 647–666. <https://doi.org/10.1007/S12028-020-00959-7/METRICS>
- Cordara, G., Van Eerde, A., Grahn, E. M., Winter, H. C., Goldstein, I. J., & Krengel, U. (2016). An Unusual Member of the Papain Superfamily: Mapping the Catalytic Cleft of the *Marasmius oreades* agglutinin (MOA) with a Caspase Inhibitor. *PLOS ONE*, 11(2). <https://doi.org/10.1371/journal.pone.0149407>
- Crowley, L. C., Scott, A. P., Marfell, B. J., Boughaba, J. A., Chojnowski, G., & Waterhouse, N. J. (2016). Measuring cell death by propidium iodide uptake and flow cytometry. *Cold Spring Harbor Protocols*, 2016(7), 647–651. <https://doi.org/10.1101/PDB.PROT087163>
- Currie, G. M. (2018). Pharmacology, Part 1: Introduction to Pharmacology and Pharmacodynamics. *Journal of Nuclear Medicine Technology*, 46(2), 81–86. <https://doi.org/10.2967/JNMT.117.199588>
- Das, S., Sahgal, A., & Perry, J. R. (2020). Commentary: Lomustine-temozolomide combination therapy versus standard temozolomide therapy in patients with newly diagnosed glioblastoma with methylated MGMT promoter (CeTeG/NOA-09): a randomised, open-label, phase 3 trial. *Frontiers in Oncology*, 10, 678–688. <https://doi.org/10.3389/fonc.2020.00066>
- Davies, D. C. (2002). Blood-brain barrier breakdown in septic encephalopathy and brain tumours. In *Journal of Anatomy* (Vol. 200, Issue 6, pp. 639–646). Wiley-Blackwell. <https://doi.org/10.1046/j.1469-7580.2002.00065.x>

- de Gooijer, M. C., de Vries, N. A., Buckle, T., Buil, L. C. M., Beijnen, J. H., Boogerd, W., & van Tellingen, O. (2018). Improved Brain Penetration and Antitumor Efficacy of Temozolomide by Inhibition of ABCB1 and ABCG2. *Neoplasia (New York, N.Y.)*, 20(7), 710–720. <https://doi.org/10.1016/j.neo.2018.05.001>
- Devine, R., Kelada, M., Leonard, S., Martin, D. S. D., Walsh, J. M. D., Breen, C. J., Driver, R. B., Kinsella, G. K., Findlay, J. B. C., & Stephens, J. C. (2014). Design, synthesis, and biological evaluation of aryl piperazines with potential as antidiabetic agents via the stimulation of glucose uptake and inhibition of NADH:ubiquinone oxidoreductase. *European Journal of Medicinal Chemistry*, 202, 112416. <https://doi.org/10.1016/j.ejmech.2020.112416>
- Dhanasekaran, D. N., & Premkumar Reddy, E. (2017). JNK-signaling: A multiplexing hub in programmed cell death. *Genes & Cancer*, 8(9–10), 682–694. <https://doi.org/10.18632/GENESANDCANCER.155>
- Di Martino, A., Kucharczyk, P., Capakova, Z., Humpolicek, P., & Sedlarik, V. (2017). Enhancement of temozolomide stability by loading in chitosan-carboxylated polylactide-based nanoparticles. *Journal of Nanoparticle Research*, 19(2), 1–16. <https://doi.org/10.1007/s11051-017-3756-3>
- Dumitru, C. A., Sandalcioglu, I. E., & Karsak, M. (2018). Cannabinoids in Glioblastoma Therapy: New Applications for Old Drugs. *Frontiers in Molecular Neuroscience*, 11, 159. <https://doi.org/10.3389/fnmol.2018.00159>
- Ene, C., Nerva, J., Morton, R., Barkley, A., Barber, J., Ko, A., & Silbergeld, D. (2016). Safety and efficacy of carmustine (BCNU) wafers for metastatic brain tumors.

- Surgical Neurology International*, 7(Suppl 11), S295–S299.  
<https://doi.org/10.4103/2152-7806.181987>
- Fedele, M., Cerchia, L., Pegoraro, S., Sgarra, R., & Manfioletti, G. (2019). Proneural-mesenchymal transition: Phenotypic plasticity to acquire multitherapy resistance in glioblastoma. In *International Journal of Molecular Sciences* (Vol. 20, Issue 11). MDPI AG. <https://doi.org/10.3390/ijms20112746>
- Ferlay, J., Colombet, M., Soerjomataram, I., Parkin, D. M., Piñeros, M., Znaor, A., & Bray, F. (2021). Cancer statistics for the year 2020: An overview. *International Journal of Cancer*, 149(4), 778–789. <https://doi.org/10.1002/IJC.33588>
- Fernandes, C., Costa, A., Osoria, L., Lago, R. C., LINHARES, P., CARVALHO, B., & CAEIRO, C. (2017). Current Standards of Care in Glioblastoma Therapy. In *Glioblastoma* (pp. 197–241). Codon Publications. <https://doi.org/10.15586/codon.glioblastoma.2017.ch11>
- Findlay, J. B. C., Martin, D. S. D., Leonard, S., Devine, R., Redondo, C., Kinsella, G. K., Breen, C. J., McEneaney, V., Rooney, M. F., Munsey, T. S., Porter, R. K., Sivaprasadarao, A., Stephens, J. C., & Findlay, J. B. C. (2016). Novel mitochondrial complex I inhibitors restore glucose-handling abilities of high-fat fed mice. *Journal of Molecular Endocrinology*, 56(3), 261–271. <https://doi.org/10.1530/JME-15-0225>
- Friedmann-Morvinski, D. (2014). Glioblastoma Heterogeneity and Cancer Cell Plasticity. *Critical Reviews & Trade in Oncogenesis*, 19(5), 327–336. <https://doi.org/10.1615/CRITREVONCOG.2014011777>
- Gabathuler, R. (2009). *Approaches to transport therapeutic drugs across the blood-brain barrier to treat brain diseases*. <https://doi.org/10.1016/j.nbd.2009.07.028>

- Gao, L., Huang, shichao, Zhang, H., Hua, W., Xin, shunmei, Cheng, L., Guan, W., Yu, Y., Mao, Y., & pei, G. (2019). *suppression of glioblastoma by a drug cocktail reprogramming tumor cells into neuronal like cells*. <https://doi.org/10.1038/s41598-019-39852-5>
- Gensicka-Kowalewska, M., Cholewí, G., & Dzierzbicka, K. (2017). *Recent developments in the synthesis and biological activity of acridine/acridone analogues*. <https://doi.org/10.1039/c7ra01026e>
- Ghasemi, M., Turnbull, T., Sebastian, S., & Kempson, I. (2021). The mtt assay: Utility, limitations, pitfalls, and interpretation in bulk and single-cell analysis. *International Journal of Molecular Sciences*, 22(23). <https://doi.org/10.3390/IJMS222312827/S1>
- Ghorab, M. M., Alsaid, M. S., Al-Ansary, G. H., Abdel-Latif, G. A., & Abou El Ella, D. A. (2016). Analogue based drug design, synthesis, molecular docking and anticancer evaluation of novel chromene sulfonamide hybrids as aromatase inhibitors and apoptosis enhancers. *European Journal of Medicinal Chemistry*, 124, 946–958. <https://doi.org/10.1016/j.ejmech.2016.10.020>
- GlaxoSmithKline. (2015). *Chemical compounds - Patent WO-2010120854-A1 - PubChem*. <https://pubchem.ncbi.nlm.nih.gov/patent/WO-2010120854-A1>
- Gonzalez, H., Hagerling, C., & Werb, Z. (2018). Roles of the immune system in cancer: from tumor initiation to metastatic progression. *Genes & Development*, 32(19–20), 1267. <https://doi.org/10.1101/GAD.314617.118>
- Goodarzi MO, B.-A. M. (2005). Metformin revisited: re-evaluation of its properties and role in the pharmacopoeia of modern anti diabetic agents. *Diabetes Obesity*

- Metabolism*, 7(6), 654–665.
- GraphPad. (2020). *GraphPad Prism 7 Curve Fitting Guide - Equation: [Inhibitor] vs. normalized response -- Variable slope*.  
[https://www.graphpad.com/guides/prism/7/curve-fitting/reg\\_dr\\_inhibit\\_normalized\\_variable\\_2.htm](https://www.graphpad.com/guides/prism/7/curve-fitting/reg_dr_inhibit_normalized_variable_2.htm)
- Grochans, S., Cybulska, A. M., Simińska, D., Korbecki, J., Kojder, K., Chlubek, D., & Baranowska-Bosiacka, I. (2022). Epidemiology of Glioblastoma Multiforme—Literature Review. *Cancers* 2022, Vol. 14, Page 2412, 14(10), 2412. <https://doi.org/10.3390/CANCERS14102412>
- Guo, Z. (2017). The modification of natural products for medical use. *Acta Pharmaceutica Sinica B*, 7(2), 119–136.  
<https://doi.org/10.1016/J.APSB.2016.06.003>
- Hanif, F., Muzaffar, K., Perveen, K., Malhi, S. M., & Simjee, S. U. (2017). Glioblastoma multiforme: A review of its epidemiology and pathogenesis through clinical presentation and treatment. In *Asian Pacific Journal of Cancer Prevention* (Vol. 18, Issue 1, pp. 3–9). Asian Pacific Organization for Cancer Prevention.  
<https://doi.org/10.22034/APJCP.2017.18.1.3>
- Hao, Z., & Sadek, I. (2016). Sunitinib: the antiangiogenic effects and beyond. *OncoTargets and Therapy*, 9, 5495. <https://doi.org/10.2147/OTT.S112242>
- Harder, B. G., Blomquist, M. R., Wang, J., Kim, A. J., Woodworth, G. F., Winkles, J. A., Loftus, J. C., & Tran, N. L. (2018). Developments in Blood-Brain Barrier Penetrance and Drug Repurposing for Improved Treatment of Glioblastoma. *Frontiers in Oncology*, 8, 462. <https://doi.org/10.3389/fonc.2018.00462>



- Hardie, D. (2013). Metformin-acting through cyclic AMP as well as AMP. *Cell Metabolism*, 17(3), 313–314.
- Hauser, P. (2021). Classification and Treatment of Pediatric Gliomas in the Molecular Era. *Children*, 8(9). <https://doi.org/10.3390/CHILDREN8090739>
- Herrlinger, U., Tzaridis, T., Mack, F., Steinbach, J. P., Schlegel, U., Sabel, M., Hau, P., Kortmann, R. D., Krex, D., Grauer, O., Goldbrunner, R., Schnell, O., Bähr, O., Uhl, M., Seidel, C., Tabatabai, G., Kowalski, T., Ringel, F., Schmidt-Graf, F., ... Glas, M. (2019). Lomustine-temozolomide combination therapy versus standard temozolomide therapy in patients with newly diagnosed glioblastoma with methylated MGMT promoter (CeTeG/NOA–09): a randomised, open-label, phase 3 trial. *The Lancet*, 393(10172), 678–688. [https://doi.org/10.1016/S0140-6736\(18\)31791-4](https://doi.org/10.1016/S0140-6736(18)31791-4)
- Holdsworth, S. J., & Bammer, R. (2008). Magnetic resonance imaging techniques: FMRI, DWI, and PWI. In *Seminars in Neurology* (Vol. 28, Issue 4, pp. 395–406). NIH Public Access. <https://doi.org/10.1055/s-0028-1083697>
- Holland, E. C. (2000). Glioblastoma multiforme: the terminator. *Proceedings of the National Academy of Sciences of the United States of America*, 97(12), 6242–6244. <http://www.ncbi.nlm.nih.gov/pubmed/10841526>
- Holt T, K. S. (2010). *ABC of Diabetes*. Wiley-Blackwell.
- Howell, J. J., Hellberg, K., Turner, M., Talbott, G., Kolar, M. J., Ross, D. S., Hoxhaj, G., Saghatelian, A., Shaw, R. J., & Manning, B. D. (2017). Metformin Inhibits Hepatic mTORC1 Signaling via Dose-Dependent Mechanisms Involving AMPK and the

- TSC Complex. *Cell Metabolism*, 25(2), 463–471.  
<https://doi.org/10.1016/j.cmet.2016.12.009>
- Hu, X. M., Li, Z. X., Lin, R. H., Shan, J. Q., Yu, Q. W., Wang, R. X., Liao, L. S., Yan, W. T., Wang, Z., Shang, L., Huang, Y., Zhang, Q., & Xiong, K. (2021). Guidelines for Regulated Cell Death Assays: A Systematic Summary, A Categorical Comparison, A Prospective. *Frontiers in Cell and Developmental Biology*, 9, 634690. <https://doi.org/10.3389/FCELL.2021.634690/BIBTEX>
- Hua, H., Kong, Q., Zhang, H., Wang, J., Luo, T., & Jiang, Y. (2019). Targeting mTOR for cancer therapy. In *Journal of Hematology and Oncology* (Vol. 12, Issue 1, pp. 1–19). BioMed Central Ltd. <https://doi.org/10.1186/s13045-019-0754-1>
- Huang, J., Chaudhary, R., Cohen, A. L., Fink, K., Goldlust, S., Boockvar, J., Chinnaiyan, P., Wan, L., Marcus, S., & Campian, J. L. (2019). A multicenter phase II study of temozolomide plus disulfiram and copper for recurrent temozolomide-resistant glioblastoma. *Journal of Neuro-Oncology*, 142(3), 537–544.  
<https://doi.org/10.1007/s11060-019-03125-y>
- Jaafari, O., Gallagher, H., Alshehri, M., Hakami, K., & AlShammari, M. (2021). Diagnostic Value of Perfusion-Weighted Magnetic Resonance Imaging as an Adjunct to Routine Magnetic Resonance Protocols for Adults Presenting with Acute Ischemic Stroke. *Reports in Medical Imaging, Volume 14*, 79–89.  
<https://doi.org/10.2147/RMI.S331876>
- Jaeger, S., Duran-Frigola, M., & Aloy, P. (2015). Drug sensitivity in cancer cell lines is not tissue-specific. *Molecular Cancer*, 14(1), 1–4. <https://doi.org/10.1186/S12943-015-0312-6/FIGURES/1>

- Jäkel, S., & Dimou, L. (2017). Glial cells and their function in the adult brain: A journey through the history of their ablation. In *Frontiers in Cellular Neuroscience* (Vol. 11). Frontiers Research Foundation. <https://doi.org/10.3389/fncel.2017.00024>
- Jang, S. J., Gardner, J. M., & Ro, J. Y. (2011). Diagnostic approach and prognostic factors of cancers. In *Advances in Anatomic Pathology* (Vol. 18, Issue 2, pp. 165–172). <https://doi.org/10.1097/PAP.0b013e31820cb39e>
- Jasinski, R., O'doherty, G., Ríos, M.-C., & Portilla, J. (2022). Recent Advances in Synthesis and Properties of Pyrazoles. *Chemistry 2022, Vol. 4, Pages 940-968*, 4(3), 940–968. <https://doi.org/10.3390/CHEMISTRY4030065>
- Jessen, K. R. (2004). Glial cells. In *International Journal of Biochemistry and Cell Biology* (Vol. 36, Issue 10, pp. 1861–1867). Elsevier Ltd. <https://doi.org/10.1016/j.biocel.2004.02.023>
- Jesús Naveja, J., Dueñas-González, A., & Medina-Franco, J. L. (2016). Drug Repurposing for Epigenetic Targets Guided by Computational Methods. In *Epi-Informatics: Discovery and Development of Small Molecule Epigenetic Drugs and Probes* (pp. 327–357). Elsevier Inc. <https://doi.org/10.1016/B978-0-12-802808-7.00012-5>
- Jin, D., Le, S., Deng, C., Chen, D., Sebastian, M., Thomas, N., Nguyen, D., Tran, D., Ganguly, A., Yu, H., Ghosh, S., Komarova, S., Daisuke, Y., Yamaguchi, S., Nam, D.-H., Nakano, I., Maria, A., De La Rocha, A., Rodriguez-Silva, M., ... Bar, E. (2018). STEM-18. THE c-Jun N-TERMINAL KINASE (JNK) IS A CRUCIAL COMPONENT OF MAINTENANCE IN GLIOBLASTOMA STEM-LIKE

CELLS. *Neuro-Oncology*, 20(suppl\_6), vi247–vi247.  
<https://doi.org/10.1093/NEUONC/NOY148.1025>

Karen Tsui, Amar Gajjar, Chenghong Li, Deokumar Srivastava, Alberto Broniscer, Cynthia Wetmore, Larry E. Kun, Thomas E. Merchant, David W. Ellison, Brent A. Orr, Frederick A. Boop, Paul Klimo, Jordan Ross, Leslie L. Robison, & Gregory T. Armstrong. (2018). Subsequent neoplasms in survivors of childhood central nervous system tumors: risk after modern multimodal therapy. *Neuro-Oncology*, 17(3), 448–456. <https://doi.org/10.1093/NEUONC>

Kato, S., Okamura, R., Marebina, M., Lee, S., Goodman, A., Patel, S. P., Fanta, P. T., Schwab, R. B., Vu, P., Raymond, V. M., Lanman, R. B., Sicklick, J. K., Lippman, S. M., & Kurzrock, R. (2019). Revisiting Epidermal Growth Factor Receptor (EGFR) Amplification as a Target for Anti-EGFR Therapy: Analysis of Cell-Free Circulating Tumor DNA in Patients With Advanced Malignancies. *JCO Precision Oncology*, 3(3), 1–14. <https://doi.org/10.1200/PO.18.00180>

Katrina Kan, L., Drummond, K., Hunn, M., Williams, D., O, T. J., & Monif, M. (2020). Potential biomarkers and challenges in glioma diagnosis, therapy and prognosis. *BMJ Neurol Open*, 2, 69. <https://doi.org/10.1136/bmjno-2020-000069>

Katzung B, Masters S, T. A. (2012). *Basic and Clinical Pharmacology* (12th ed.). McGraw-Hill.

Kelada, M., Walsh, J. M. D., Devine, R. W., McArdle, P., & Stephens, J. C. (2018). Synthesis of pyrazolopyrimidinones using a “one-pot” approach under microwave irradiation. *Beilstein Journal of Organic Chemistry*, 14, 122–1228. <https://doi.org/10.3762/bjoc.14.104>

- Kim K-W, Roh JK, Wee H-J, K. C. (2016). *Cancer drug discovery* (1st ed.). Springer.
- Komori, T. (2015). Pathology and Genetics of Diffuse Gliomas in Adults. *Neurologia Medico-Chirurgica*, 55(1), 28. <https://doi.org/10.2176/NMC.RA.2014-0229>
- Kumari, S., Ahsan, S. M., Kumar, J. M., Kondapi, A. K., & Rao, N. M. (2017). Overcoming blood brain barrier with a dual purpose Temozolomide loaded Lactoferrin nanoparticles for combating glioma (SERP-17-12433). *Scientific Reports*, 7(1), 6602. <https://doi.org/10.1038/s41598-017-06888-4>
- Kwon, S., Bae, H., Jo, J., & Yoon, S. (2019). Comprehensive ensemble in QSAR prediction for drug discovery. *BMC Bioinformatics*, 20(1), 521. <https://doi.org/10.1186/s12859-019-3135-4>
- Langhans, S. A. (2018). Three-dimensional in vitro cell culture models in drug discovery and drug repositioning. In *Frontiers in Pharmacology* (Vol. 9, Issue JAN, p. 6). Frontiers Media S.A. <https://doi.org/10.3389/fphar.2018.00006>
- Lee, C. Y. (2017). Strategies of temozolomide in future glioblastoma treatment. *OncoTargets and Therapy*, 10, 265. <https://doi.org/10.2147/OTT.S120662>
- Li, X., Yao, X., Zhu, Y., Zhang, H., Wang, H., Ma, Q., Yan, F., Yang, Y., Zhang, J., Shi, H., Ning, Z., Dai, J., Li, Z., Li, C., Su, F., Xue, Y., Meng, X., Dong, G., & Xiong, H. (2019). The Caspase Inhibitor Z-VAD-FMK Alleviates Endotoxic Shock via Inducing Macrophages Necroptosis and Promoting MDSCs-Mediated Inhibition of Macrophages Activation. *Frontiers in Immunology*, 10, 1824. <https://doi.org/10.3389/FIMMU.2019.01824/BIBTEX>
- Liew, S. K., Malagobadan, S., Arshad, N. M., & Nagoor, N. H. (2020). A Review of the

- Structure–Activity Relationship of Natural and Synthetic Antimetastatic Compounds. *Biomolecules* 2020, Vol. 10, Page 138, 10(1), 138. <https://doi.org/10.3390/BIOM10010138>
- Lin, Y., Zhang, B., Liang, H., Lu, Y., Ai, X., Zhang, B., & Chen, X. (2013). JNK inhibitor SP600125 enhances TGF- $\beta$ -induced apoptosis of RBE human cholangiocarcinoma cells in a Smad-dependent manner. *Molecular Medicine Reports*, 8(6), 1623–1629. <https://doi.org/10.3892/MMR.2013.1711/HTML>
- Linville, R. M., & Searson, P. C. (2021). Next-generation in vitro blood–brain barrier models: benchmarking and improving model accuracy. *Fluids and Barriers of the CNS*, 18(1), 56. <https://doi.org/10.1186/s12987-021-00291-y>
- Lisa Iorio, A., da Ros, M., Fantappiè, O., Lucchesi, M., Facchini, L., Stival, A., Becciani, S., Guidi, M., Favre, C., de Martino, M., Genitori, L., & Sardi, I. (2016). Blood-Brain Barrier and Breast Cancer Resistance Protein: A Limit to the Therapy of CNS Tumors and Neurodegenerative Diseases. *Anti-Cancer Agents in Medicinal Chemistry*, 16(7), 810–815. <https://doi.org/10.2174/1871520616666151120121928>
- Ljubimova, J. Y., Sun, T., Mashouf, L., Ljubimov, A. V., Israel, L. L., Ljubimov, V. A., Falahatian, V., & Holler, E. (2017). Covalent nano delivery systems for selective imaging and treatment of brain tumors. In *Advanced Drug Delivery Reviews* (Vol. 113, pp. 177–200). Elsevier B.V. <https://doi.org/10.1016/j.addr.2017.06.002>
- Louis, D. N., Perry, A., Wesseling, P., Brat, D. J., Cree, I. A., Figarella-Branger, D., Hawkins, C., Ng, H. K., Pfister, S. M., Reifenberger, G., Soffietti, R., Von Deimling, A., & Ellison, D. W. (2021). The 2021 WHO Classification of Tumors of the Central Nervous System: a summary. *Neuro-Oncology*, 23(8), 1231–1251.

<https://doi.org/10.1093/NEUONC/NOAB106>

- Lu, C. T., Zhao, Y. Z., Wong, H. L., Cai, J., Peng, L., & Tian, X. Q. (2014). Current approaches to enhance CNS delivery of drugs across the brain barriers. In *International Journal of Nanomedicine* (Vol. 9, Issue 1, pp. 2241–2257). Dove Medical Press Ltd. <https://doi.org/10.2147/IJN.S61288>
- Ludwig, P. E., & Varacallo, M. (2019). Neuroanatomy, Central Nervous System (CNS). In *StatPearls*. StatPearls Publishing. <http://www.ncbi.nlm.nih.gov/pubmed/28723039>
- Lyne, S. B., & Yamini, B. (2021). An Alternative Pipeline for Glioblastoma Therapeutics: A Systematic Review of Drug Repurposing in Glioblastoma. *Cancers*, 13(8). <https://doi.org/10.3390/CANCERS13081953>
- Ma, Y., Wang, Q., Dong, Q., Zhan, L., & Zhang, J. (2019). How to differentiate pseudoprogression from true progression in cancer patients treated with immunotherapy. *American Journal of Cancer Research*, 9(8), 1546–1553. <http://www.ncbi.nlm.nih.gov/pubmed/31497342>
- MacVane, S. H. (2017). Antimicrobial Resistance in the Intensive Care Unit: A Focus on Gram-Negative Bacterial Infections. *Journal of Intensive Care Medicine*, 32(1), 25–37. <https://doi.org/10.1177/0885066615619895>
- Mannas, J. P., Lightner, D. D., DeFrates, S. R., Pittman, T., & Villano, J. L. (2014). Long-term treatment with temozolomide in malignant glioma. *Journal of Clinical Neuroscience*, 21(1), 121–123. <https://doi.org/10.1016/J.JOCN.2013.03.039>
- Manrique-Guzman, S., Herrada-Pineda, T., & Revilla-Pacheco, F. (2017). Surgical

- Management of Glioblastoma. In *Glioblastoma* (pp. 243–261). Codon Publications.  
<https://doi.org/10.15586/codon.glioblastoma.2017.ch12>
- McDermott, J., Sturtevant, D., Kathad, U., Varma, S., Zhou, J., Kulkarni, A., Biyani, N., Schimke, C., Reinhold, W. C., Elloumi, F., Carr, P., Pommier, Y., & Bhatia, K. (2022). Artificial intelligence platform, RADR®, aids in the discovery of DNA damaging agent for the ultra-rare cancer Atypical Teratoid Rhabdoid Tumors. *Frontiers in Drug Discovery*, 2, 31. <https://doi.org/10.3389/FDDSV.2022.1033395>
- McIlwain, D. R., Berger, T., & Mak, T. W. (2013). Caspase Functions in Cell Death and Disease. *Cold Spring Harbor Perspectives in Biology*, 5(4), 1–28.  
<https://doi.org/10.1101/CSHPERSPECT.A008656>
- Mesfin, F. B., & Al-Dhahir, M. A. (2022). Gliomas. *Frontiers in Oncology*, 2. <https://doi.org/10.3389/FONC.2012.00205>
- Michinaga, S., & Koyama, Y. (2015). Pathogenesis of brain edema and investigation into anti-edema drugs. In *International Journal of Molecular Sciences* (Vol. 16, Issue 5, pp. 9949–9975). MDPI AG. <https://doi.org/10.3390/ijms16059949>
- Molitch, M. (1990). *Clinical Methods: The History, Physical and Laboratory Examinations*. Butterworths.
- Moody CL, W. R. (2014). The Medicinal Chemistry of Imidazotetrazine Prodrugs. *Pharmaceuticals*, 7(7), 797–838.
- Nam, L., Coll, C., Erthal, L. C. S., de la Torre, C., Serrano, D., Martínez-Máñez, R., Santos-Martínez, M. J., & Ruiz-Hernández, E. (2018). Drug delivery nanosystems for the localized treatment of glioblastoma multiforme. In *Materials* (Vol. 11, Issue 5). MDPI AG. <https://doi.org/10.3390/ma11050779>



- National Cancer Registry Ireland. (2020). *Cancer in Ireland with Estimates for 2018-2020*. <https://www.mendeley.com/reference-manager/reader/105d1a8e-1490-3131-8f3c-332be14d44c3/61052a41-2116-e0b5-4a08-01172b6cb2ed/>
- NCI. (2023). *Definition of telomerase*. NCI Dictionary of Cancer Terms. <https://www.cancer.gov/publications/dictionaries/cancer-terms/def/telomerase>
- Nehring, S. M., Tadi, P., & Tenny, S. (2022). Cerebral Edema. *StatPearls*. <https://www.ncbi.nlm.nih.gov/books/NBK537272/>
- Noriega, S., Cardoso-Ortiz, J., López-Luna, A., Cuevas-Flores, M. D. R., & Flores De La Torre, J. A. (2022). The Diverse Biological Activity of Recently Synthesized Nitro Compounds. *Pharmaceuticals* 2022, Vol. 15, Page 717, 15(6), 717. <https://doi.org/10.3390/PH15060717>
- Olar, A., & Aldape, K. D. (2014). Using the molecular classification of glioblastoma to inform personalized treatment. In *Journal of Pathology* (Vol. 232, Issue 2, pp. 165–177). NIH Public Access. <https://doi.org/10.1002/path.4282>
- Olender, D., Żwawiak, J., & Zaprutko, L. (2018). Multidirectional Efficacy of Biologically Active Nitro Compounds Included in Medicines. *Pharmaceuticals* 2018, Vol. 11, Page 54, 11(2), 54. <https://doi.org/10.3390/PH11020054>
- Omuro, A., & DeAngelis, L. M. (2013). Glioblastoma and Other Malignant Gliomas. *JAMA*, 310(17), 1842. <https://doi.org/10.1001/jama.2013.280319>
- PA, M. A. H. R. P. G. M. (2017). The Role of Hypoxia in Glioblastoma Invasion. *Cells*. <https://doi.org/doi:10.3390>
- Pardridge, W. M. (2012). Drug transport across the blood-brain barrier. In *Journal of*

- Cerebral Blood Flow and Metabolism* (Vol. 32, Issue 11, pp. 1959–1972). SAGE Publications. <https://doi.org/10.1038/jcbfm.2012.126>
- Parodi, A., Rudzińska, M., Deviatkin, A. A., Soond, S. M., Baldin, A. V., & Zamyatnin, A. A. (2019). Established and emerging strategies for drug delivery across the blood-brain barrier in brain cancer. In *Pharmaceutics* (Vol. 11, Issue 5). MDPI AG. <https://doi.org/10.3390/pharmaceutics11050245>
- Penfold, C., Joannides, A. J., Bell, J., & Walter, F. M. (2017). Diagnosing adult primary brain tumours: Can we do better? In *British Journal of General Practice* (Vol. 67, Issue 659, pp. 278–279). Royal College of General Practitioners. <https://doi.org/10.3399/bjgp17X691277>
- Pfeffer, C. M., & Singh, A. T. K. (2018). Apoptosis: A Target for Anticancer Therapy. *International Journal of Molecular Sciences*, 19(2). <https://doi.org/10.3390/IJMS19020448>
- Pfizer. (2004). *US2004157838A1*. <https://worldwide.espacenet.com/patent/search/family/032851028/publication/US2004157838A1?q=pn%3DUS2004157838>
- Poon, M. T. C., Bruce, M., Simpson, J. E., Hannan, C. J., & Brennan, P. M. (2021). Temozolomide sensitivity of malignant glioma cell lines-a systematic review assessing consistencies between in vitro studies. *BMC Cancer*, 21(1240). <https://doi.org/10.1186/s12885-021-08972-5>
- Pulgar, V. M. (2019). Transcytosis to cross the blood brain barrier, new advancements and challenges. *Frontiers in Neuroscience*, 13(JAN), 1019. <https://doi.org/10.3389/fnins.2018.01019>

- Pushpakom, S., Iorio, F., Eyers, P. A., Escott, K. J., Hopper, S., Wells, A., Doig, A., Williams, T., Latimer, J., McNamee, C., Norris, A., Sanseau, P., Cavalla, D., & Pirmohamed, M. (2018). Drug repurposing: Progress, challenges and recommendations. In *Nature Reviews Drug Discovery* (Vol. 18, Issue 1, pp. 41–58). Nature Publishing Group. <https://doi.org/10.1038/nrd.2018.168>
- Rena G, Hardie DG, P. E. (2017). The mechanisms of action of metformin. *Diabetologia*, 60(9), 1577–1585.
- Richter EA, R. N. (2010). AMPK and the biochemistry of exercise: implications for human health and disease. *Journal of Biochemistry*, 261–275.
- RSC. (2023). *Characterising / Royal Society Open Science*. <https://royalsocietypublishing.org/rsos/chemical-compounds>
- Sahu, M., & Suryawanshi, H. (2021). *Immunotherapy: The future of cancer treatment*. <https://doi.org/10.4103/0973-029X.325257>
- Schirmacher, V. (2019). From chemotherapy to biological therapy: A review of novel concepts to reduce the side effects of systemic cancer treatment (Review). *International Journal of Oncology*, 54(2), 407–419. <https://doi.org/10.3892/ijo.2018.4661>
- Seelig, A. (2020). P-Glycoprotein: One Mechanism, Many Tasks and the Consequences for Pharmacotherapy of Cancers. *Frontiers in Oncology*, 10, 1989. <https://doi.org/10.3389/FONC.2020.576559/BIBTEX>
- Seliger, C., & Hau, P. (2018). Drug repurposing of metabolic agents in malignant glioma. In *International Journal of Molecular Sciences* (Vol. 19, Issue 9). MDPI AG.

<https://doi.org/10.3390/ijms19092768>

- Seliger, C., Lubner, C., Gerken, M., Schaertl, J., Proescholdt, M., Riemenschneider, M. J., Meier, C. R., Bogdahn, U., Leitzmann, M. F., Klinkhammer-Schalke, M., & Hau, P. (2019). Use of metformin and survival of patients with high-grade glioma. *International Journal of Cancer*, 144(2), 273–280. <https://doi.org/10.1002/ijc.31783>
- Seo, Y.-S., Ko, I. O., Park, H., Jeong, Y. J., Park, J.-A., Kim, K. S., Park, M.-J., & Lee, H.-J. (2019). Radiation-Induced Changes in Tumor Vessels and Microenvironment Contribute to Therapeutic Resistance in Glioblastoma. *Frontiers in Oncology*, 9. <https://doi.org/10.3389/fonc.2019.01259>
- Shah, J. L., Li, G. H., & Soltys, S. G. (2021). Glioblastoma Multiforme. *CyberKnife Stereotactic Radiosurgery: Brain*, 1, 85–98. <https://doi.org/10.22290/jbnc.v24i1.1481>
- Shapira-Furman, T., Serra, R., Gorelick, N., Doglioli, M., Tagliaferri, V., Cecia, A., Peters, M., Kumar, A., Rottenberg, Y., Langer, R., Brem, H., Tyler, B., & Domb, A. J. (2019). Biodegradable wafers releasing Temozolomide and Carmustine for the treatment of brain cancer. *Journal of Controlled Release*, 295, 93–101. <https://doi.org/10.1016/j.jconrel.2018.12.048>
- Sharma, H. (2018). Development of Novel Therapeutics Targeting Isocitrate Dehydrogenase Mutations in Cancer. *Current Topics in Medicinal Chemistry*, 18(6), 505–524. <https://doi.org/10.2174/1568026618666180518091144>
- Shultz, M. D. (2019). Two Decades under the Influence of the Rule of Five and the Changing Properties of Approved Oral Drugs. *Journal of Medicinal Chemistry*, 62(4), 1701–1714.

[https://doi.org/10.1021/ACS.JMEDCHEM.8B00686/SUPPL\\_FILE/JM8B00686\\_SI\\_002.CSV](https://doi.org/10.1021/ACS.JMEDCHEM.8B00686/SUPPL_FILE/JM8B00686_SI_002.CSV)

- Simanshu, D. K., Nissley, D. V., & McCormick, F. (2017). RAS Proteins and Their Regulators in Human Disease. In *Cell* (Vol. 170, Issue 1, pp. 17–33). Cell Press.  
<https://doi.org/10.1016/j.cell.2017.06.009>
- Singh, N., Miner, A., Hennis, L., & Mittal, S. (2021). Mechanisms of temozolomide resistance in glioblastoma - a comprehensive review. *Cancer Drug Resistance*, 4(1), 17–43. <https://doi.org/10.20517/CDR.2020.79>
- Song, J. J., & Lee, Y. J. (2007). Differential activation of the JNK signal pathway by UV irradiation and glucose deprivation. *Cellular Signalling*, 19(3), 563–572.  
<https://doi.org/10.1016/J.CELLSIG.2006.08.016>
- Steponaitis, G., & Tamasauskas, A. (2021). Mesenchymal and Proneural Subtypes of Glioblastoma Disclose Branching Based on GSC Associated Signature. *International Journal of Molecular Sciences* 2021, Vol. 22, Page 4964, 22(9), 4964.  
<https://doi.org/10.3390/IJMS22094964>
- Stupp, R., Mason, W. P., van den Bent, M. J., Weller, M., Fisher, B., Taphoorn, M. J. B., Belanger, K., Brandes, A. A., Marosi, C., Bogdahn, U., Curschmann, J., Janzer, R. C., Ludwin, S. K., Gorlia, T., Allgeier, A., Lacombe, D., Cairncross, J. G., Eisenhauer, E., & Mirimanoff, R. O. (2005). Radiotherapy plus concomitant and adjuvant temozolomide for glioblastoma. *The New England Journal of Medicine*, 352(10), 987–996. <https://doi.org/10.1056/NEJMOA043330>
- Sukhatme, V., Bouche, G., Meheus, L., Sukhatme, V. P., & Pantziarka, P. (2015).

- Repurposing Drugs in Oncology (ReDO)—nitroglycerin as an anti-cancer agent. *Ecancermedicalscience*, 9. <https://doi.org/10.3332/ECANCER.2015.568>
- Sung, H., Ferlay, J., Siegel, R. L., Laversanne, M., Soerjomataram, I., Jemal, A., & Bray, F. (2021). Global Cancer Statistics 2020: GLOBOCAN Estimates of Incidence and Mortality Worldwide for 36 Cancers in 185 Countries. *CA: A Cancer Journal for Clinicians*, 71(3), 209–249. <https://doi.org/10.3322/CAAC.21660>
- Tang, L., Feng, Y., Gao, S., Mu, Q., & Liu, C. (2021). Nanotherapeutics Overcoming the Blood-Brain Barrier for Glioblastoma Treatment. *Frontiers in Pharmacology*, 12, 3418. <https://doi.org/10.3389/FPHAR.2021.786700/BIBTEX>
- Taylor, O. G., Brzozowski, J. S., & Skelding, K. A. (2019). Glioblastoma multiforme: An overview of emerging therapeutic targets. In *Frontiers in Oncology* (Vol. 9, Issue SEP, p. 963). Frontiers Media S.A. <https://doi.org/10.3389/fonc.2019.00963>
- Torsvik, A., Stieber, D., Enger, P. O., Golebiewska, A., Molven, A., Svendsen, A., Westermarck, B., Niclou, S. P., Olsen, T. K., Chekenya Enger, M., & Bjerkvig, R. (2014). U-251 revisited: Genetic drift and phenotypic consequences of long-term cultures of glioblastoma cells. *Cancer Medicine*, 3(4), 812–824. <https://doi.org/10.1002/cam4.219>
- Vagvala, S., Guenette, J. P., Jaimes, C., & Huang, R. Y. (2022). Imaging diagnosis and treatment selection for brain tumors in the era of molecular therapeutics. *Cancer Imaging 2022 22:1*, 22(1), 1–14. <https://doi.org/10.1186/S40644-022-00455-5>
- Verhaak R.G., H. K. A. . P. E. . W. V. Q. Y. . W. M. D. . M. C. R. . D. L. G. T. . M. J. P. . A. G. (2011). TCGA Scientists discover four distinct subtypes of glioblastoma distinguished by gene expression patterns and clinical characteristics. *Cancer Cell*,

17(1), 98–110.

Vidal-Albalat, A., & González, F. V. (2016). Natural Products as Cathepsin Inhibitors.

*Studies in Natural Products Chemistry*, 50, 179–213. <https://doi.org/10.1016/B978-0-444-63749-9.00006-2>

VIIIV Healthcare. (2018). US9932356.

<https://worldwide.espacenet.com/patent/search/family/052595439/publication/US9932356B2?q=pn%3DUS9932356>

Wadhawan, M., Singh, N., & Rathaur, S. (2014). Inhibition of Cathepsin B by E-64

Induces Oxidative Stress and Apoptosis in Filarial Parasite. *PLOS ONE*, 9(3). <https://doi.org/10.1371/journal.pone.0093161>

Waghray, D., & Zhang, Q. (2018). Inhibit or Evade Multidrug Resistance P-glycoprotein

in Cancer Treatment. *Journal of Medicinal Chemistry*, 61(12), 5108. <https://doi.org/10.1021/ACS.JMEDCHEM.7B01457>

Wang, D., Wang, C., Wang, L., & Chen, Y. (2019). A comprehensive review in

improving delivery of small-molecule chemotherapeutic agents overcoming the blood-brain/brain tumor barriers for glioblastoma treatment. *Drug Delivery*, 26(1), 551–565. <https://doi.org/10.1080/10717544.2019.1616235>

Wang, Y., Liu, Y., Bi, X., & Baudry, M. (2020). Calpain-1 and Calpain-2 in the Brain:

New Evidence for a Critical Role of Calpain-2 in Neuronal Death. *Cells*, 9(12), 2698. <https://doi.org/10.3390/cells9122698>

Wanigasekara, J., Barcia, C., Cullen, P. J., Tiwari, B., & Curtin, J. F. (2022). Plasma

induced reactive oxygen species-dependent cytotoxicity in glioblastoma 3D

- tumourspheres. *Plasma Processes and Polymers*, 19(4), 2100157.  
<https://doi.org/10.1002/PPAP.202100157>
- Wanigasekara, J., Cullen, P. J., Bourke, P., Tiwari, B., & Curtin, J. F. (2023). Advances in 3D culture systems for therapeutic discovery and development in brain cancer. *Drug Discovery Today*, 28(2). <https://doi.org/10.1016/J.DRUDIS.2022.103426>
- Warwick, G. (1963). The Mechanism of Action of Alkylating Agents. *Cancer Research*, 23(1), 1315–1333.
- Weller, M., Cloughesy, T., Perry, J. R., & Wick, W. (2013). Standards of care for treatment of recurrent glioblastoma-are we there yet? *Neuro-Oncology*, 15(1), 4–27.  
<https://doi.org/10.1093/neuonc/nos273>
- Wesseling, P., & Capper, D. (2018). WHO 2016 Classification of gliomas. *Neuropathology and Applied Neurobiology*, 44(2), 139–150.  
<https://doi.org/10.1111/nan.12432>
- Wick, W., Osswald, M., Wick, A., & Winkler, F. (2018). Treatment of glioblastoma in adults. *Therapeutic Advances in Neurological Disorders*, 11, 175628641879045.  
<https://doi.org/10.1177/1756286418790452>
- Williams-Medina, A., Deblock, M., & Janigro, D. (2021). In vitro Models of the Blood–Brain Barrier: Tools in Translational Medicine. *Frontiers in Medical Technology*, 2, 30. <https://doi.org/10.3389/FMEDT.2020.623950>
- Wu, Y., Xu, J., Liu, Y., Zeng, Y., & Wu, G. (2020). A Review on Anti-Tumor Mechanisms of Coumarins. *Frontiers in Oncology*, 10.  
<https://doi.org/10.3389/FONC.2020.592853>
- Würth, R., Pattarozzi, A., Gatti, M., Bajetto, A., Corsaro, A., Parodi, A., Sirito, R.,



- Massollo, M., Marini, C., Zona, G., Fenoglio, D., Sambuceti, G., Filaci, G., Daga, A., Barbieri, F., & Florio, T. (2013). Metformin selectively affects human glioblastoma tumor-initiating cell viability: A role for metformin-induced inhibition of Akt. *Cell Cycle*, 12(1), 145–156. <https://doi.org/10.4161/cc.23050>
- Yadavalli, S., Yenugonda, V. M., & Kesari, S. (2019). Repurposed Drugs in Treating Glioblastoma Multiforme. *The Cancer Journal*, 25(2), 139–146. <https://doi.org/10.1097/PPO.0000000000000365>
- Yamada, E., Lee, T. W. A., Pessin, J. E., & Bastie, C. C. (2010). Targeted therapies of the LKB1/AMPK pathway for the treatment of insulin resistance. In *Future Medicinal Chemistry* (Vol. 2, Issue 12, pp. 1785–1796). <https://doi.org/10.4155/fmc.10.264>
- Yancovitz, M., Litterman, A., Yoon, J., Ng, E., Shapiro, R. L., Berman, R. S., Pavlick, A. C., Darvishian, F., Christos, P., Mazumdar, M., Osman, I., & Polsky, D. (2012). Intra- and Inter-Tumor Heterogeneity of BRAFV600EMutations in Primary and Metastatic Melanoma. *PLoS ONE*, 7(1), 29336. <https://doi.org/10.1371/JOURNAL.PONE.0029336>
- Yang, H., Ye, D., Guan, K. L., & Xiong, Y. (2012). IDH1 and IDH2 mutations in tumorigenesis: Mechanistic insights and clinical perspectives. In *Clinical Cancer Research* (Vol. 18, Issue 20, pp. 5562–5571). NIH Public Access. <https://doi.org/10.1158/1078-0432.CCR-12-1773>
- Yoshimori, A., & Bajorath, J. (2022). Computational analysis, alignment and extension of analogue series from medicinal chemistry. *Future Science OA*, 8(7).

<https://doi.org/10.2144/FSOA-2022->

0033/ASSET/IMAGES/LARGE/FIGURE1.JPEG

- Yusufzai, S. K., Khan, M. S., Sulaiman, O., Osman, H., & Lamjin, D. N. (2018). Molecular docking studies of coumarin hybrids as potential acetylcholinesterase, butyrylcholinesterase, monoamine oxidase A/B and  $\beta$ -amyloid inhibitors for Alzheimer's disease. *Chemistry Central Journal* 2018 12:1, 12(1), 1–57. <https://doi.org/10.1186/S13065-018-0497-Z>
- Zafrakas, M., Papasozomenou, P., & Emmanouilides, C. (2016). Sorafenib in breast cancer treatment: A systematic review and overview of clinical trials. *World Journal of Clinical Oncology*, 7(4), 331. <https://doi.org/10.5306/WJCO.V7.I4.331>
- Zhang, J., F.G. Stevens, M., & D. Bradshaw, T. (2011). Temozolomide: Mechanisms of Action, Repair and Resistance. *Current Molecular Pharmacology*, 5(1), 102–114. <https://doi.org/10.2174/1874467211205010102>
- Zhang, Y., Chen, Y., Yang, C., Seger, N., Hesla, A. C., Tsagkozis, P., Larsson, O., Lin, Y., & Haglund, F. (2021). TERT promoter mutation is an objective clinical marker for disease progression in chondrosarcoma. *Modern Pathology*, 34(November 2021), 2020–2027. <https://doi.org/10.1038/s41379-021-00848-0>
- Zhu, G., Yang, S., Wang, R., Lei, J., Ji, P., Wang, J., Tao, K., Yang, C., Ge, S., & Wang, L. (2021). *P53/miR-154 Pathway Regulates the Epithelial-Mesenchymal Transition in Glioblastoma Multiforme Cells by Targeting TCF12*. <https://doi.org/10.2147/NDT.S273578>

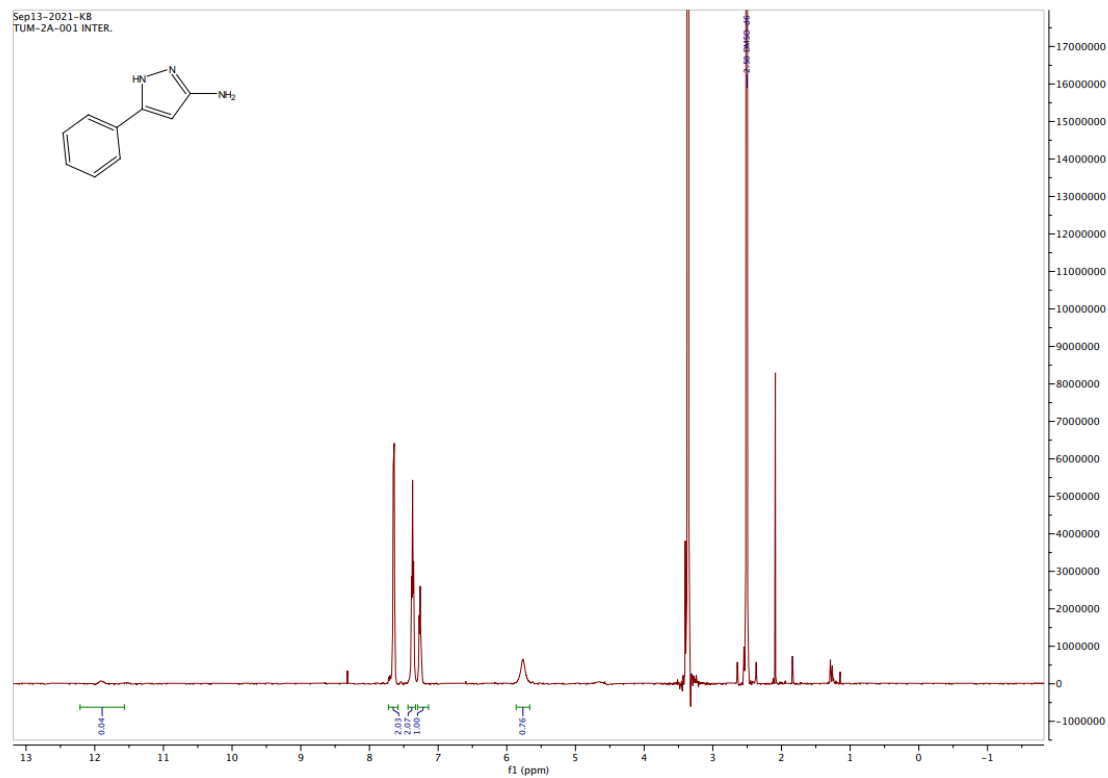


# APPENDICES

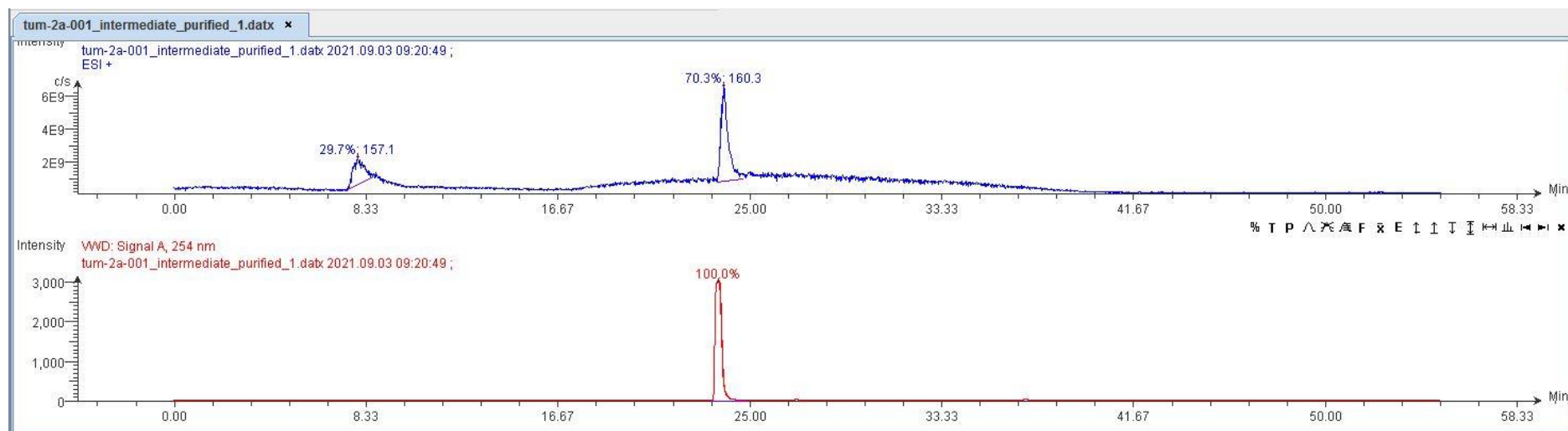
## **A1. CHEMISTRY**

## 1.1.1 TUM-2A-001 Intermediate

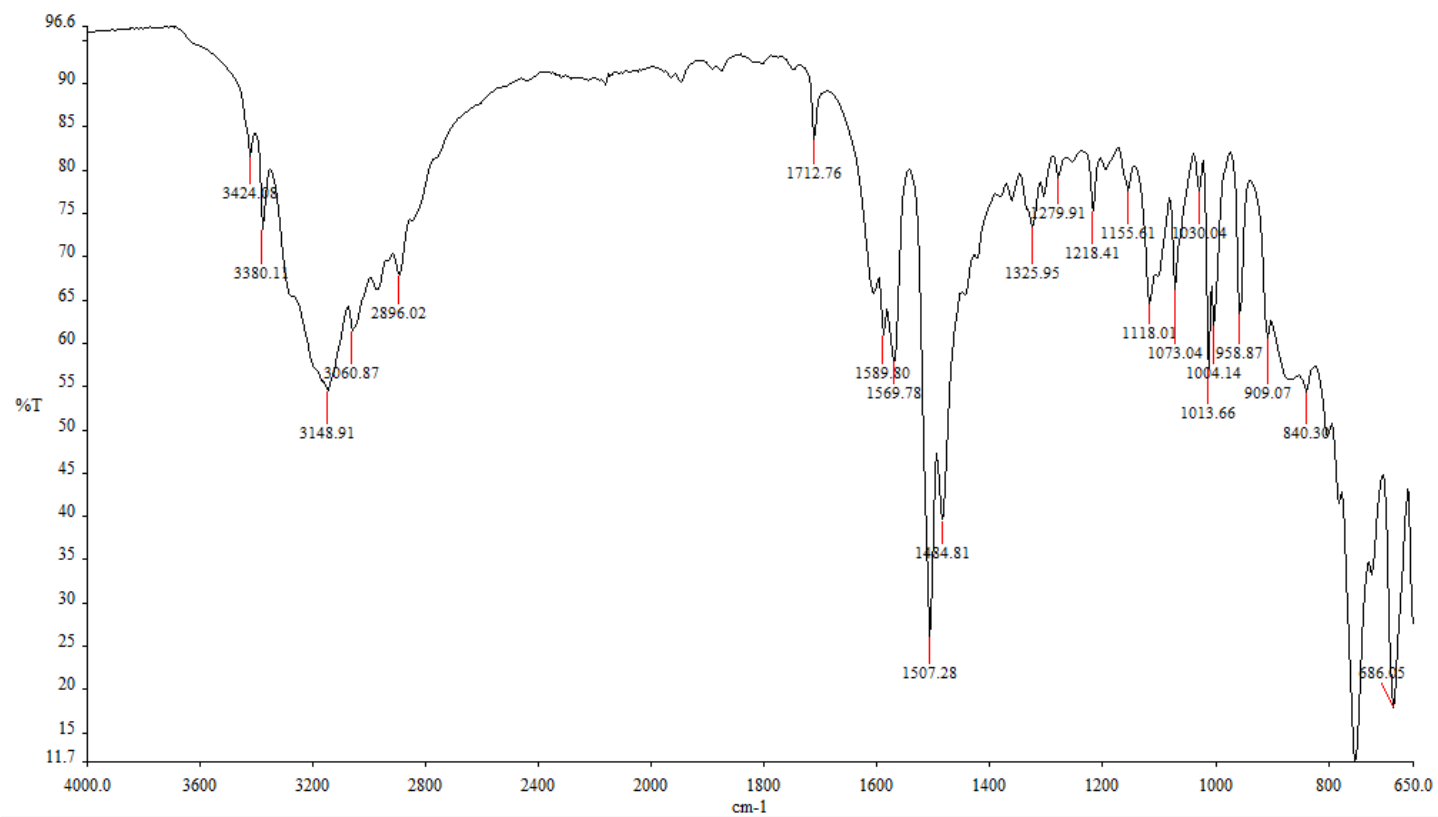
### 1.1.1.1 $^1\text{H}$ NMR Spectrum



### 1.1.1.2 LC-MS Spectrum



### 1.1.1.3 FTIR Spectrum



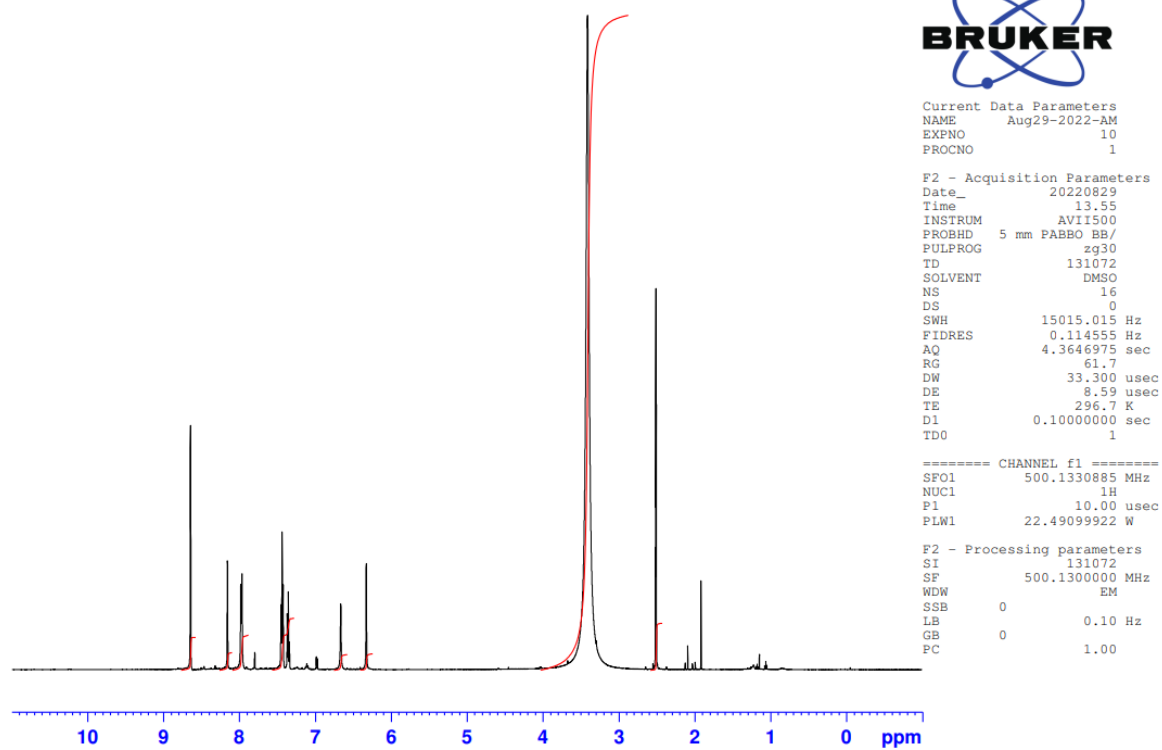
#tum-2a-001 intermediate.sp



## 1.1.2 TUM-2A-001

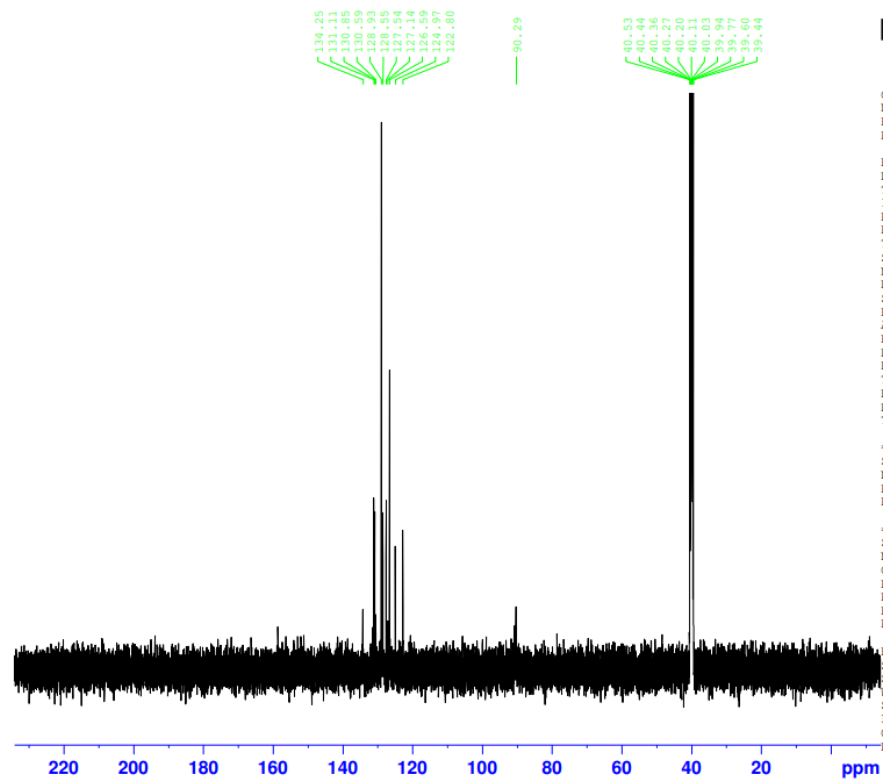
### 1.1.2.1 $^1\text{H}$ NMR Spectrum

tum-2a-001 H



### 1.1.2.2 $^{13}\text{C}$ NMR Spectrum

tum-2a-001 C



Current Data Parameters  
NAME Aug29-2022-AM  
EXPNO 11  
PROCNO 1

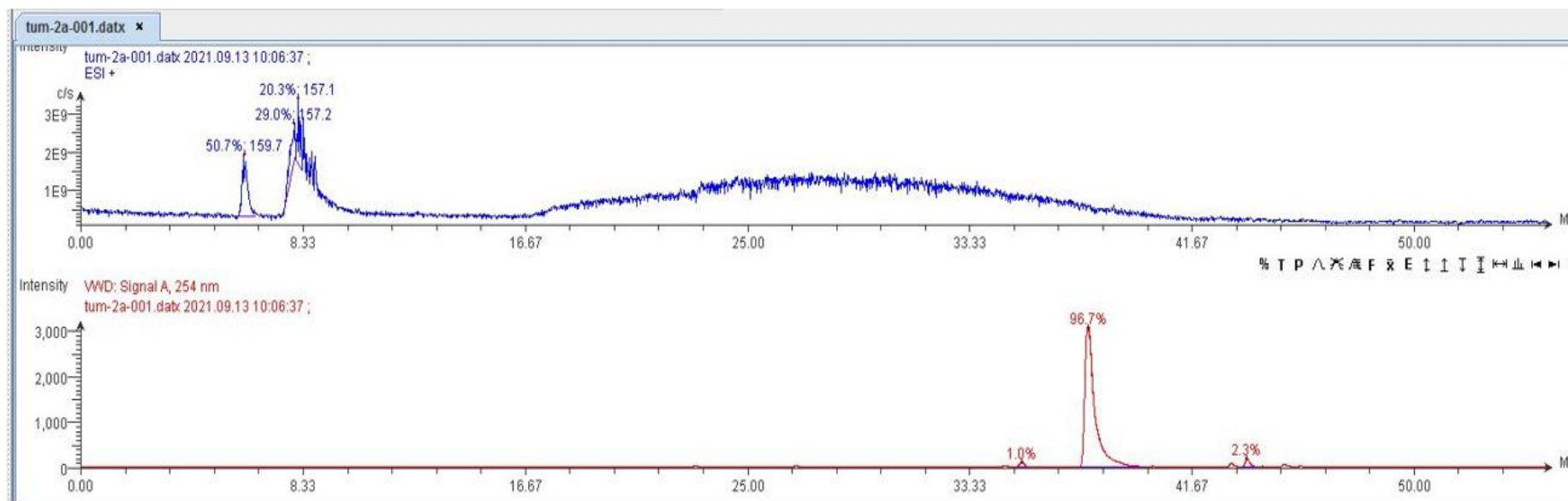
F2 - Acquisition Parameters  
Date\_ 20220830  
Time 2.43  
INSTRUM AVII500  
PROBHD 5 mm PABBO BB/  
PULPROG zgpg30  
TD 119044  
SOLVENT DMSO  
NS 512  
DS 4  
SWH 31250.000 Hz  
FIDRES 0.262508 Hz  
AQ 1.9047040 sec  
RG 2050  
DW 16.000 usec  
DE 8.87 usec  
TE 297.4 K  
D1 1.00000000 sec  
D11 0.03000000 sec  
TD0 1

===== CHANNEL f1 =====  
SFO1 125.7716202 MHz  
NUC1 13C  
P1 10.00 usec  
PLW1 83.75299835 W

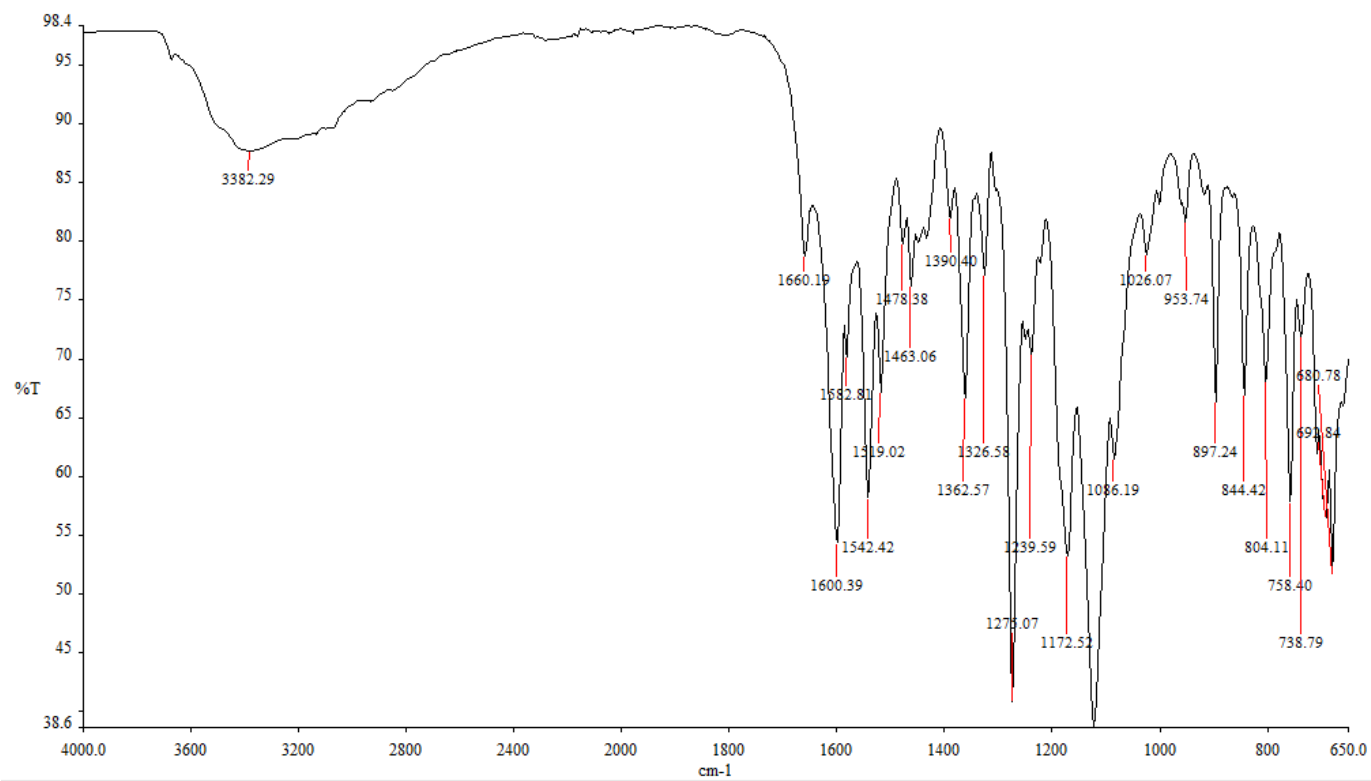
===== CHANNEL f2 =====  
SFO2 500.1320005 MHz  
NUC2 1H  
CPDPRG2 waltz64  
PCPD2 80.00 usec  
PLW2 22.49099922 W  
PLW12 0.35141999 W  
PLW13 0.17676000 W

F2 - Processing parameters  
SI 131072  
SF 125.7577885 MHz  
WDW EM  
SSB 0  
LB 1.00 Hz  
GB 0  
PC 1.40

### 1.1.2.3 LC-MS Spectrum



#### 1.1.2.4 FTIR Spectrum

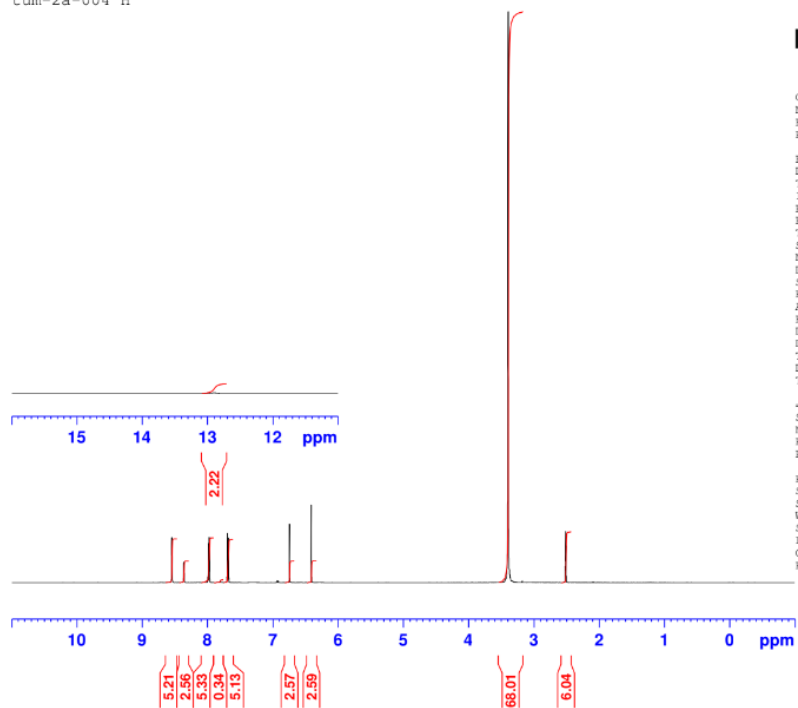


tum-2a-001 kb.sp

## 1.1.3 TUM-2A-004

### 1.1.3.1 $^1\text{H}$ NMR Spectrum

tum-2a-004 H



**BRUKER**

Current Data Parameters  
NAME Aug29-2022-AM  
EXPNO 20  
PROCNO 1

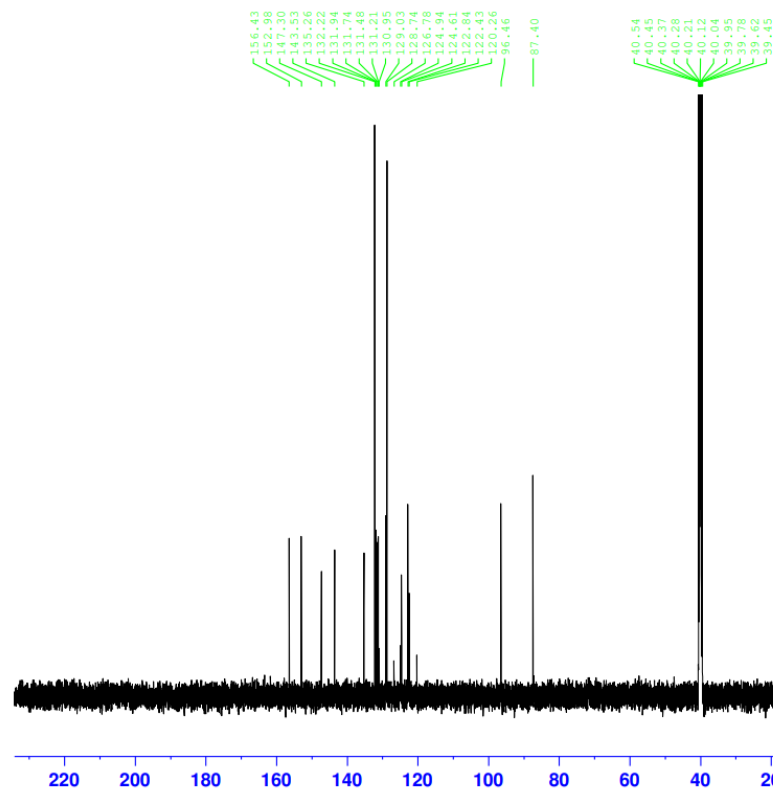
F2 - Acquisition Parameters  
Date\_ 20220830  
Time 3.36  
INSTRUM AVI1500  
PROBHD 5 mm PASBO BB/  
PULPROG zg30  
TD 131072  
SOLVENT DMSO  
NS 16  
DS 0  
SWH 15015.015 Hz  
FIDRES 0.114555 Hz  
AQ 4.3646975 sec  
RG 69.13  
DW 33.300 usec  
DE 8.59 usec  
TE 296.2 K  
D1 0.10000000 sec  
TD0 1

----- CHANNEL f1 -----  
SFO1 500.1330885 MHz  
NUC1 1H  
P1 10.00 usec  
PLW1 22.49099922 W

F2 - Processing parameters  
SI 131072  
SF 500.1300000 MHz  
WDW EM  
SSB 0  
LB 0.10 Hz  
GB 0  
PC 1.00

### 1.1.3.2 $^{13}\text{C}$ NMR Spectrum

tum-2a-004 C



Current Data Parameters  
NAME Aug29-2022-AM  
EXPNO 21  
PROCNO 1

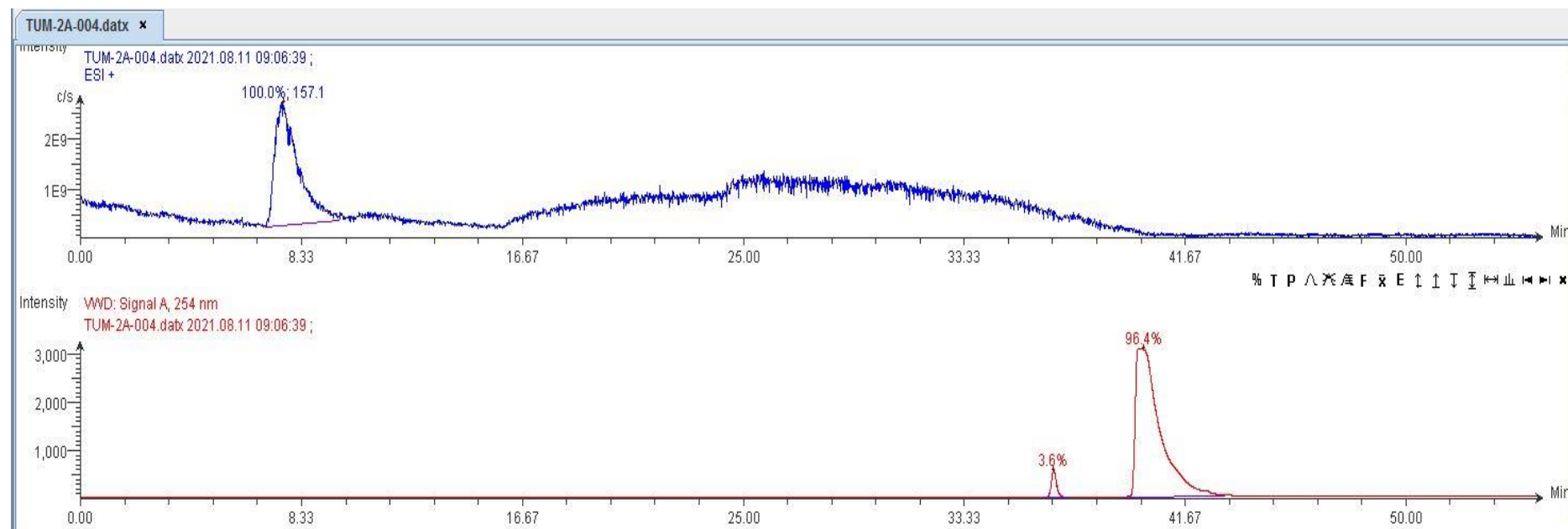
F2 - Acquisition Parameters  
Date\_ 20220830  
Time 4.02  
INSTRUM AVII500  
PROBHD 5 mm PABBO BB/  
PULPROG zgpg30  
TD 119044  
SOLVENT DMSO  
NS 512  
DS 4  
SWH 31250.000 Hz  
FIDRES 0.262508 Hz  
AQ 1.9047040 sec  
RG 2050  
DW 16.000 usec  
DE 8.87 usec  
TE 297.3 K  
D1 1.00000000 sec  
D11 0.03000000 sec  
TD0 1

===== CHANNEL f1 =====  
SF01 125.7716202 MHz  
NUC1  $^{13}\text{C}$   
P1 10.00 usec  
PLW1 83.75299835 W

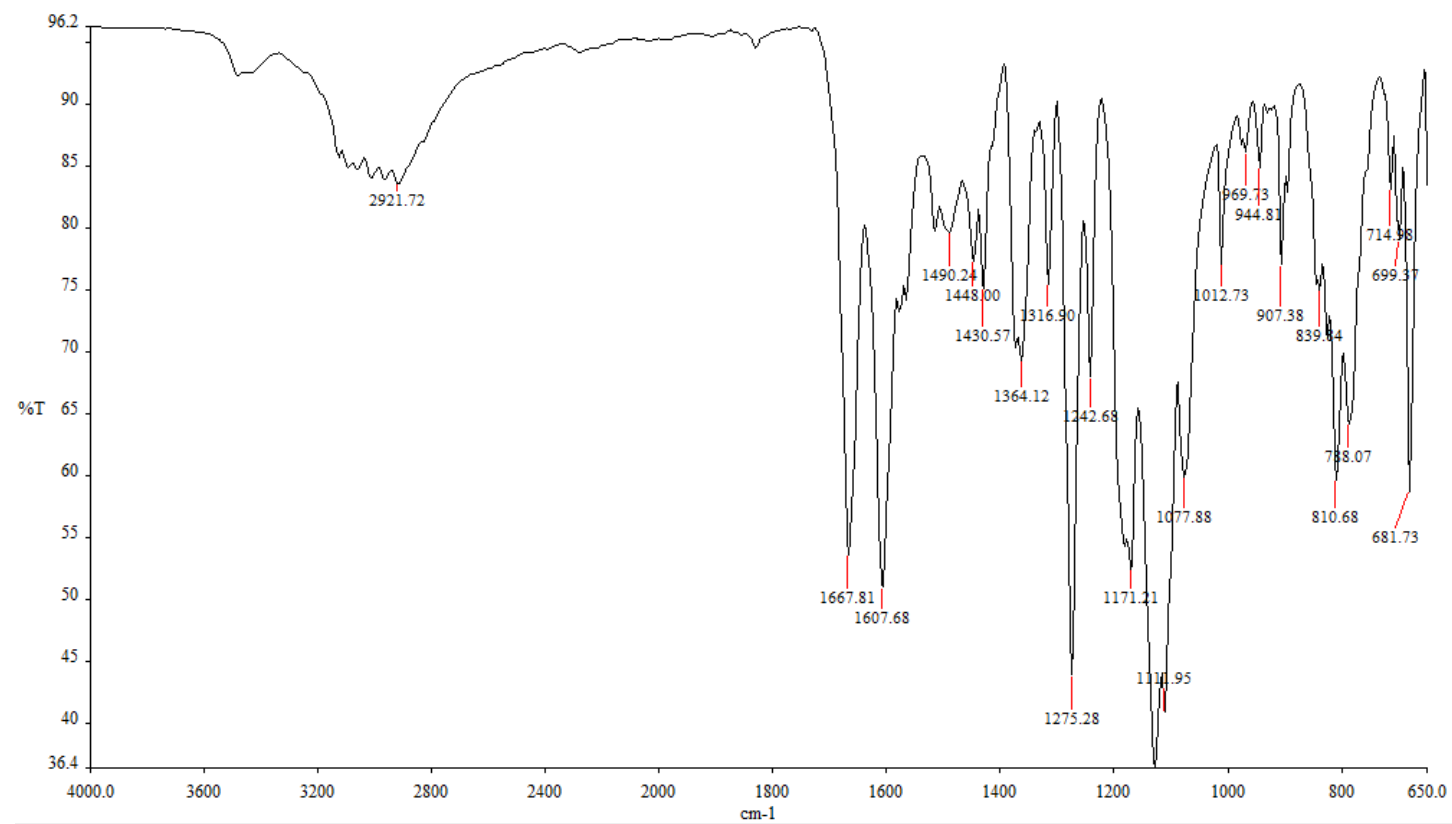
===== CHANNEL f2 =====  
SF02 500.1320005 MHz  
NUC2  $^1\text{H}$   
PCPDPRG[2] waltz64  
PCPD2 80.00 usec  
PLW2 22.49099922 W  
PLW12 0.35141999 W  
PLW13 0.17676000 W

F2 - Processing parameters  
SI 131072  
SF 125.7577885 MHz  
WDW EM  
SSB 0  
LB 1.00 Hz  
GB 0  
PC 1.40

### 1.1.3.3 LC-MS Spectrum



#### 1.1.3.4 FTIR Spectrum

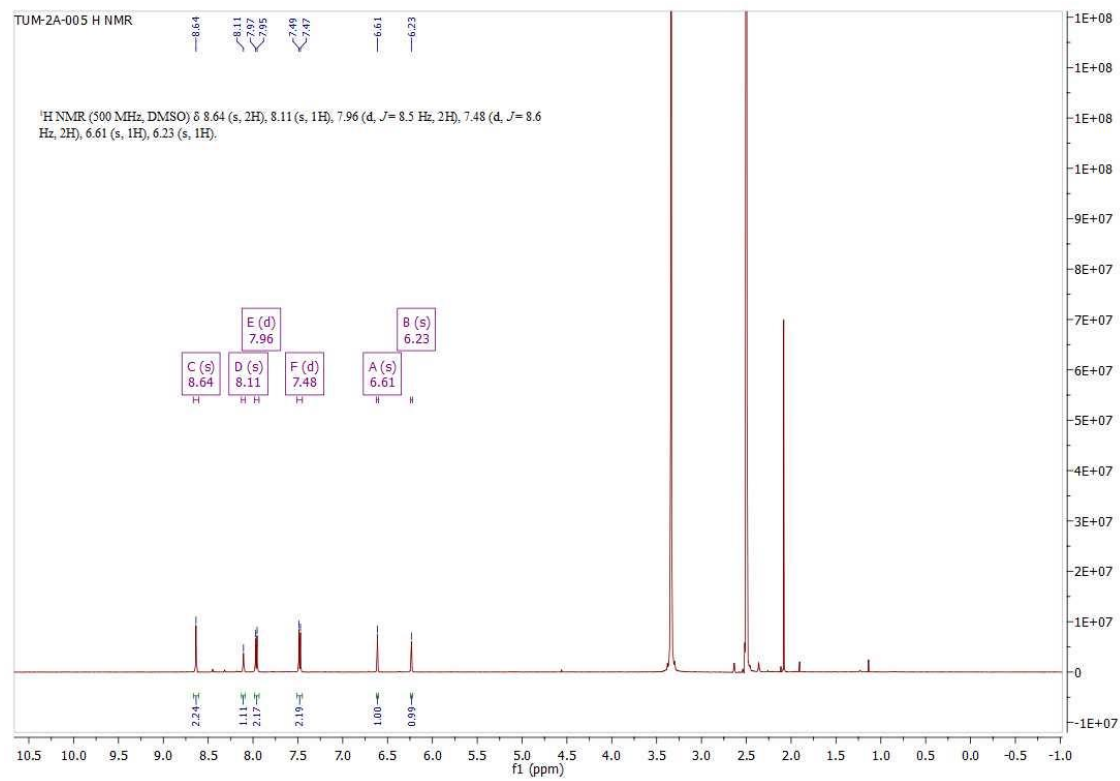


kb tum-2a-004 16 aug.sp

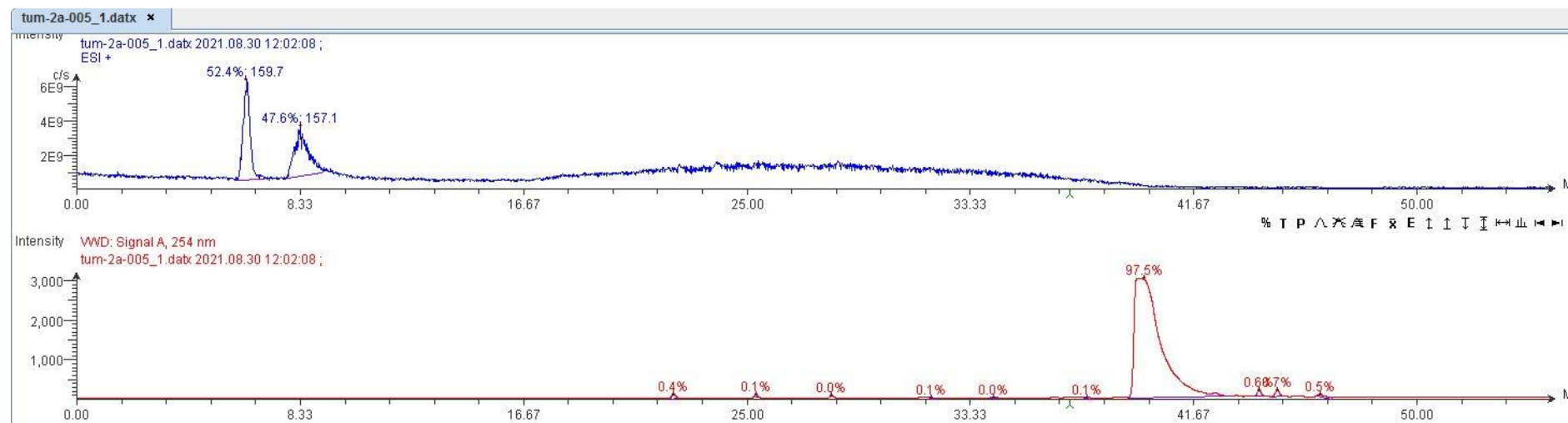


## 1.1.4 TUM-2A-005

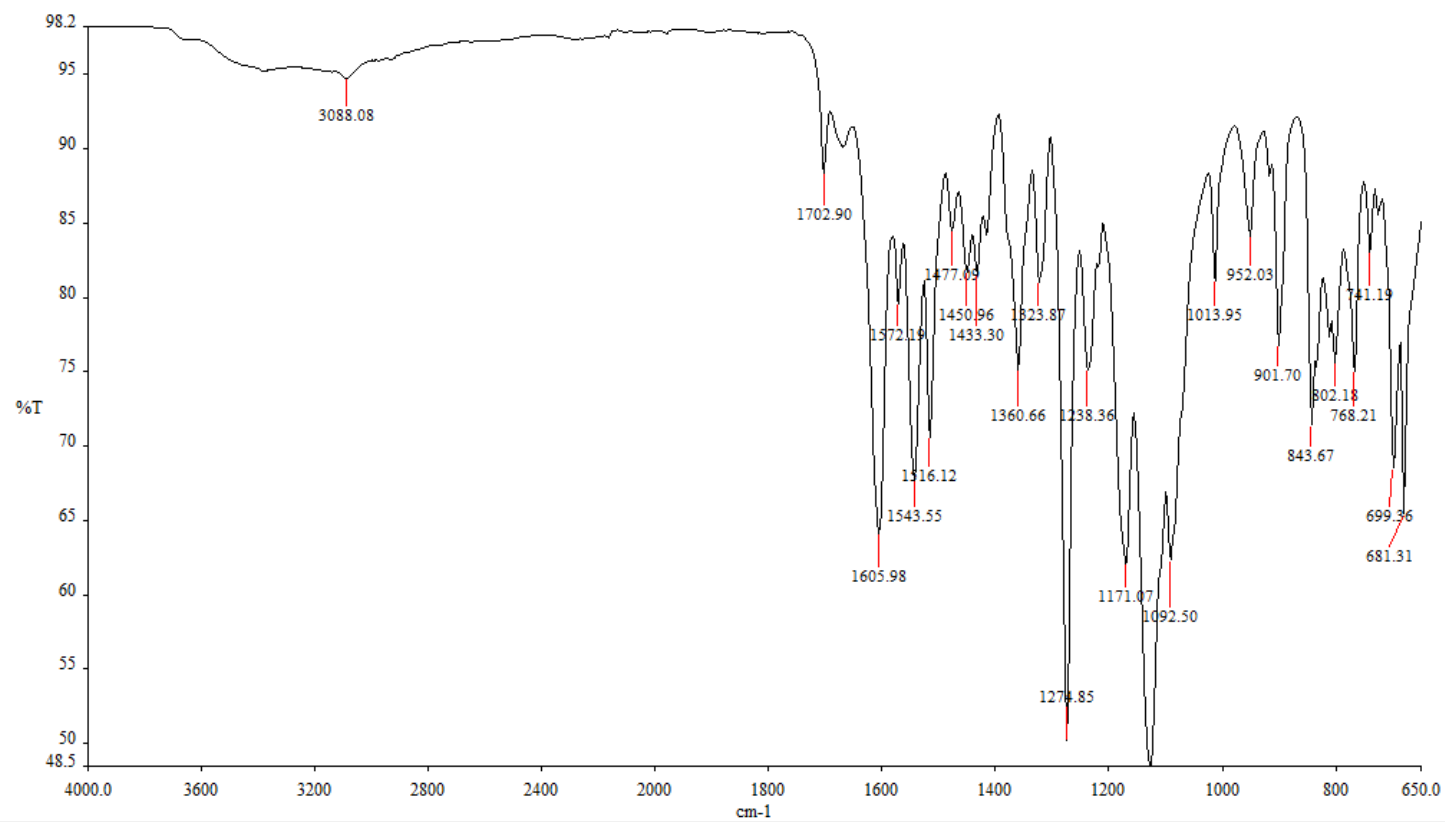
### 1.1.4.1 $^1\text{H}$ NMR Spectrum



### 1.1.4.2 LC-MS Spectrum



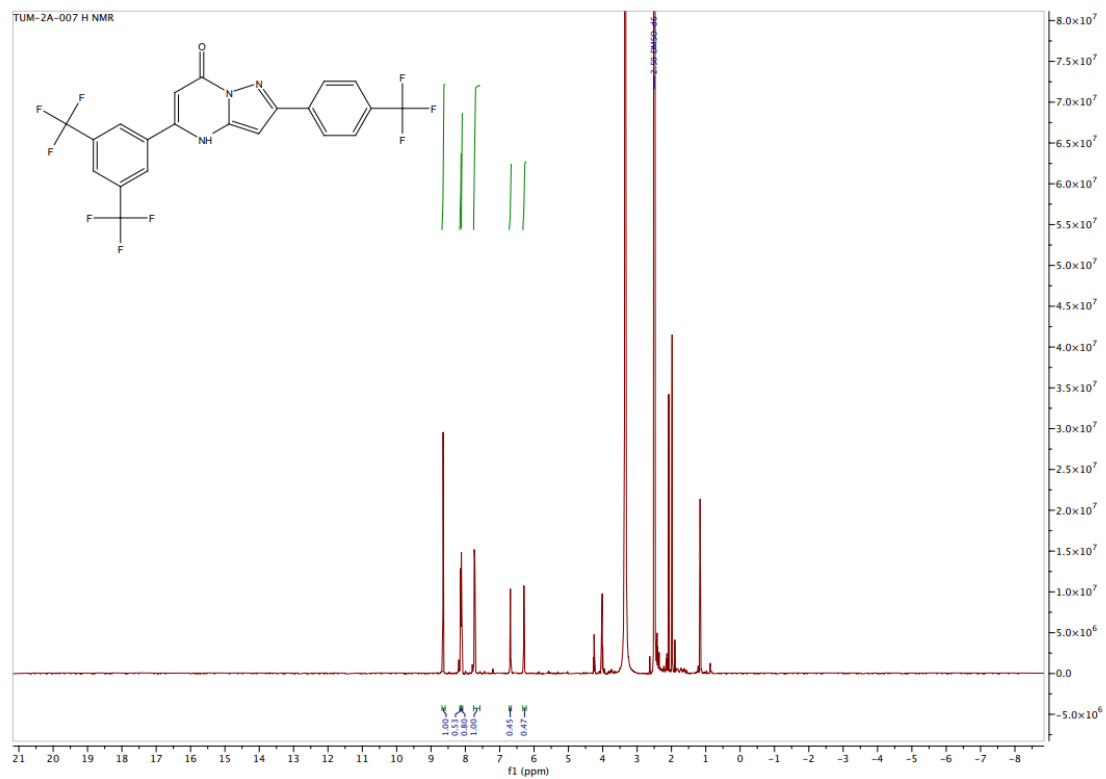
### 1.1.4.3 FTIR Spectrum



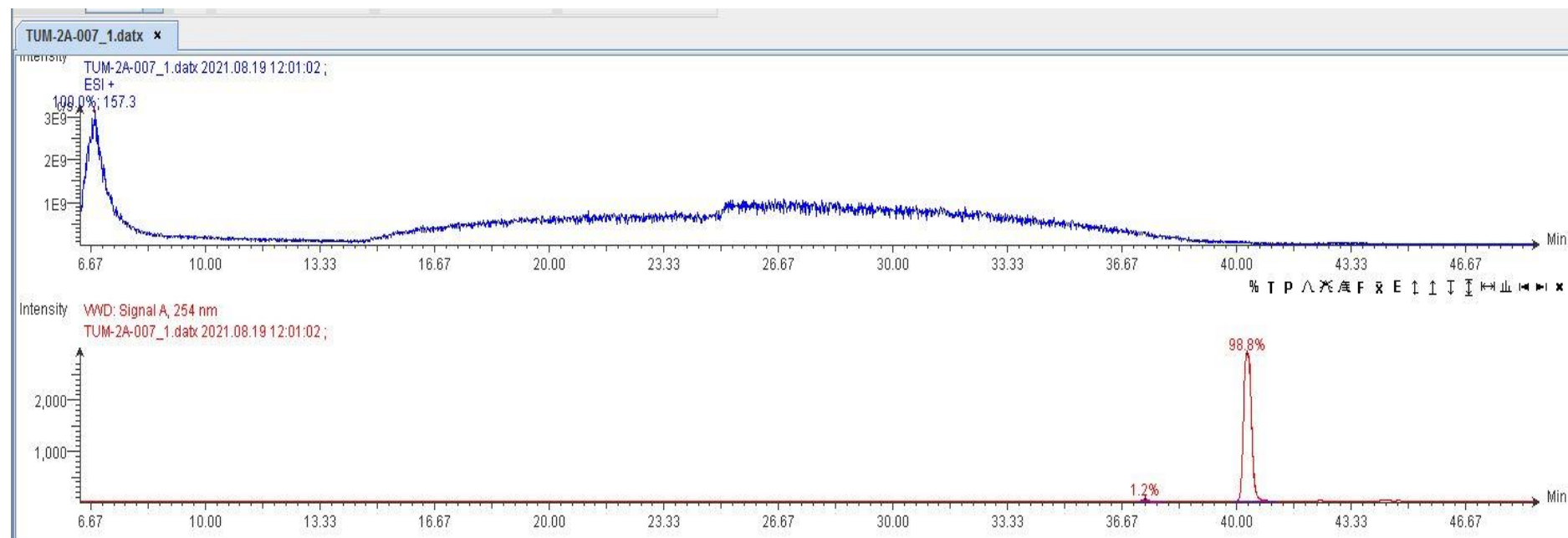
tum-2a-005 30 aug.sp

### 1.1.5 TUM-2A-007

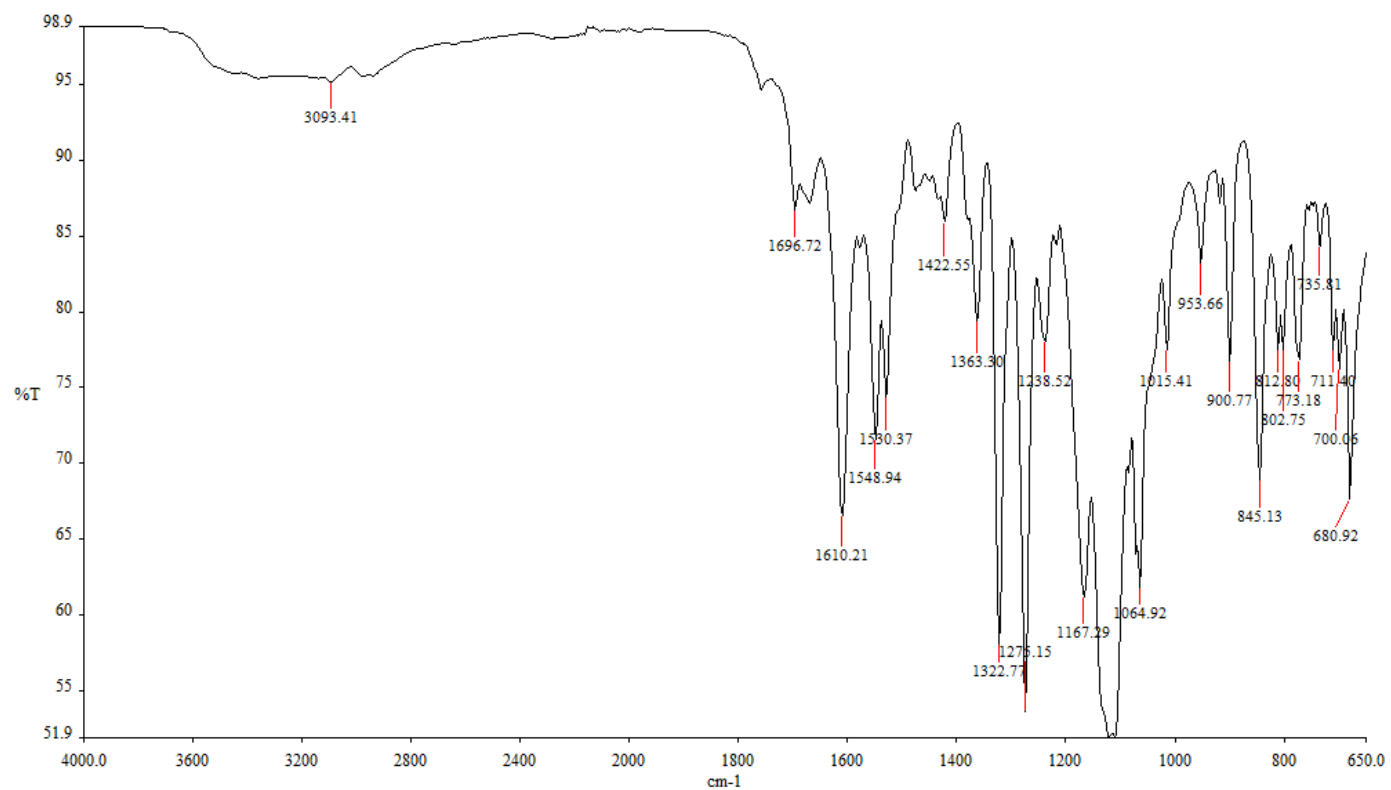
#### 1.1.5.1 $^1\text{H}$ NMR Spectrum



### 1.1.5.2 LC-MS Spectrum



### 1.1.5.3 FTIR Spectrum

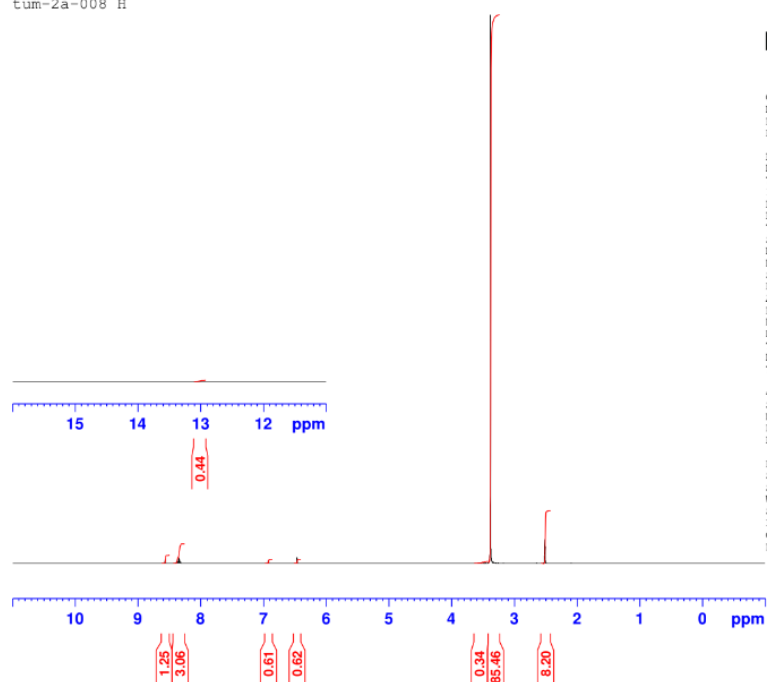


tum-2a-007 kb 19 aug.sp

## 1.1.6 TUM-2A-008

### 1.1.6.1 $^1\text{H}$ NMR Spectrum

tum-2a-008 H



Current Data Parameters  
NAME Aug29-2022-AM  
EXPNO 40  
PROCNO 1

F2 - Acquisition Parameters  
Date\_ 20220829  
Time 14.04  
INSTRUM AVII300  
PROBHD 5 mm PABBO BB/  
PULPROG zg30  
TD 131072  
SOLVENT DMSO  
NS 16  
DS 0  
SWH 15015.015 Hz  
FIDRES 0.114555 Hz  
AQ 4.3646975 sec  
RG 78.78  
DW 33.300 usec  
DE 8.59 usec  
TE 296.7 K  
D1 0.10000000 sec  
TD0 1

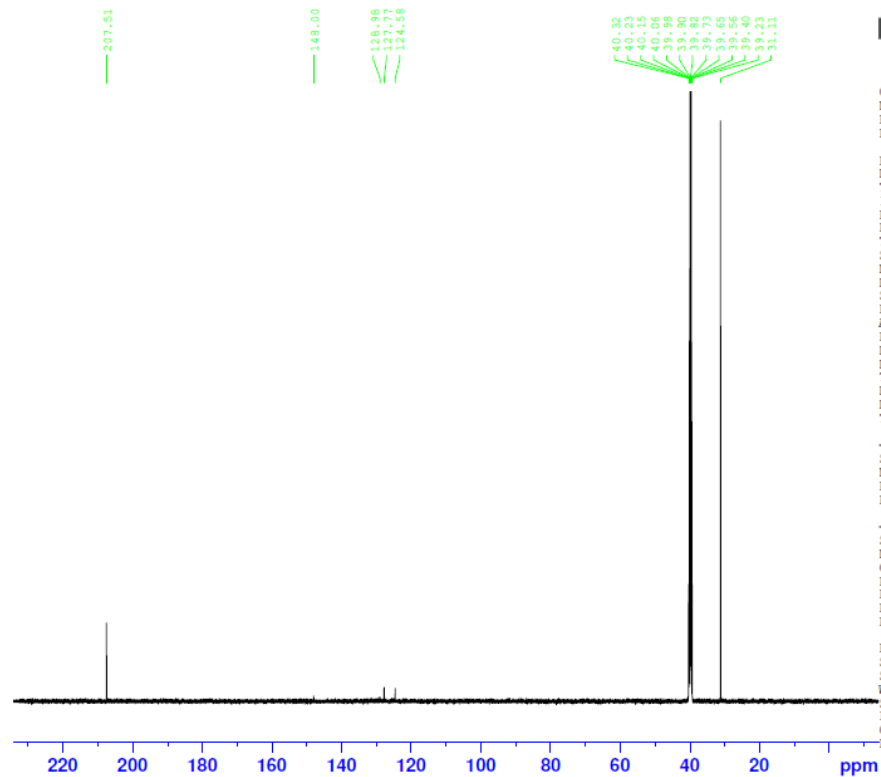
----- CHANNEL f1 -----  
SFO1 500.1330885 MHz  
NUC1 1H  
P1 10.00 usec  
PLW1 22.49099922 W

F2 - Processing parameters  
SI 131072  
SF 500.1300000 MHz  
WDW EM  
SSB 0  
LB 0.10 Hz  
GB 0  
PC 1.00

XX

### 1.1.6.2 $^{13}\text{C}$ NMR Spectrum

TUM-2A-008



Current Data Parameters  
 NAME Nov19-2021-KB  
 EXPNO 21  
 PROCNO 1

F2 - Acquisition Parameters  
 Date\_ 20211119  
 Time 11.47  
 INSTRUM AVII500  
 PROBHD 5 mm PABBO BB/  
 PULPROG zgpg30  
 TD 119044  
 SOLVENT DMSO  
 NS 512  
 DS 4  
 SWH 31250.000 Hz  
 FIDRES 0.262508 Hz  
 AQ 1.9047040 sec  
 RG 2050  
 DW 16.000 usec  
 DE 8.87 usec  
 TE 298.0 K  
 D1 1.00000000 sec  
 D11 0.03000000 sec  
 TD0 1

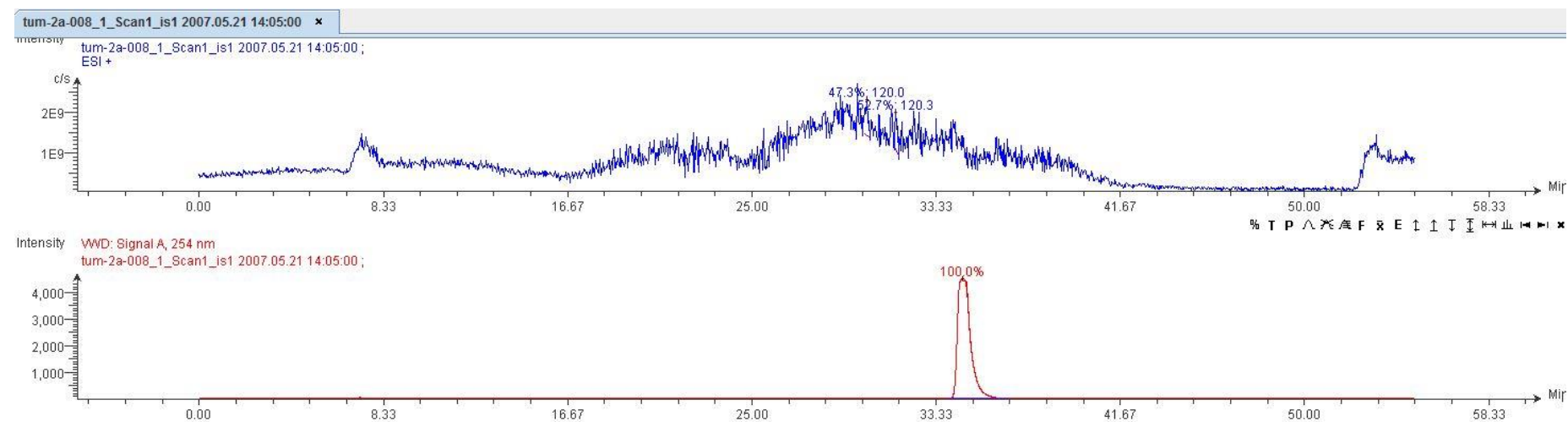
----- CHANNEL f1 -----  
 SF01 125.7716202 MHz  
 NUC1 13C  
 P1 10.00 usec  
 PLW1 83.75299835 W

----- CHANNEL f2 -----  
 SF02 500.1320005 MHz  
 NUC2 1H  
 CPDPRG[2] waltz64  
 PCPD2 80.00 usec  
 PLW2 22.49099922 W  
 PLW12 0.35141999 W  
 PLW13 0.22491001 W

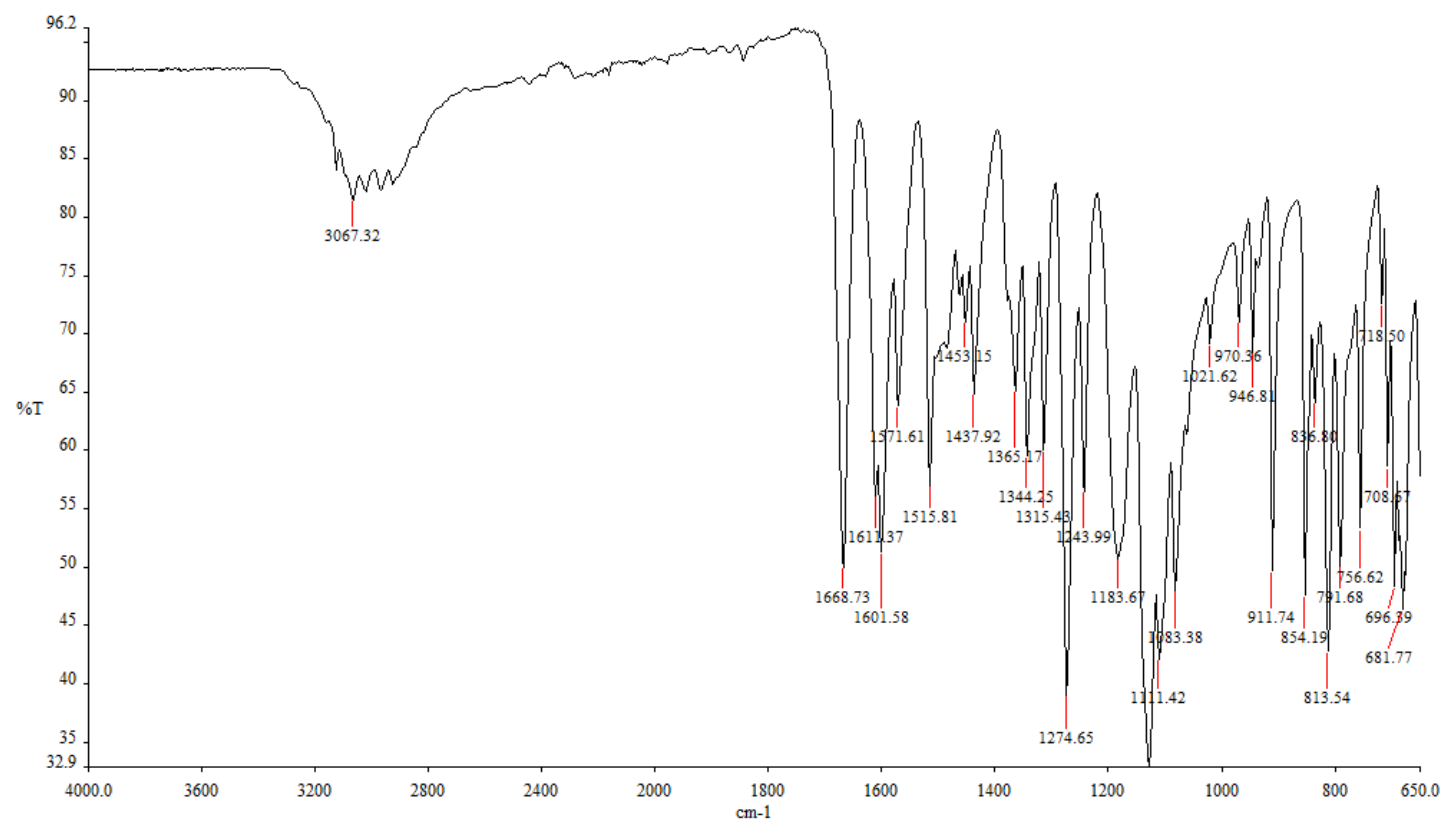
F2 - Processing parameters  
 SI 131072  
 SF 125.7577885 MHz  
 WDW EM  
 SSB 0  
 LB 1.00 Hz  
 GB 0  
 PC 1.40



### 1.1.6.3 LC-MS Spectrum



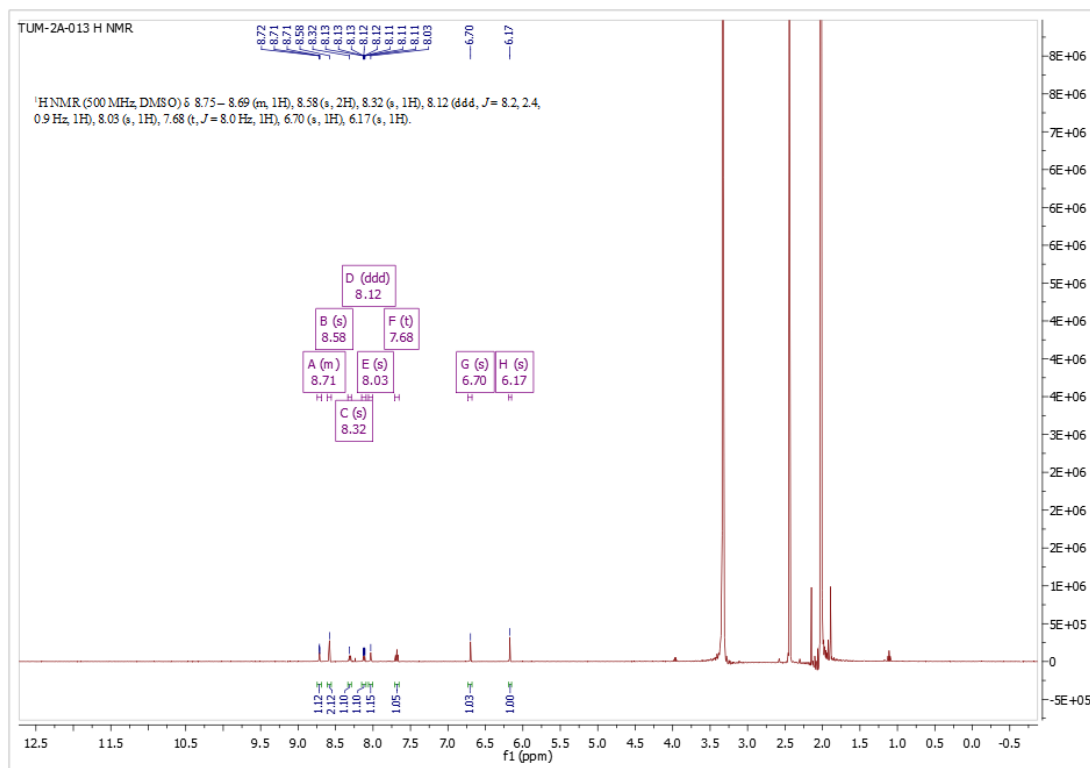
#### 1.1.6.4 FTIR Spectrum



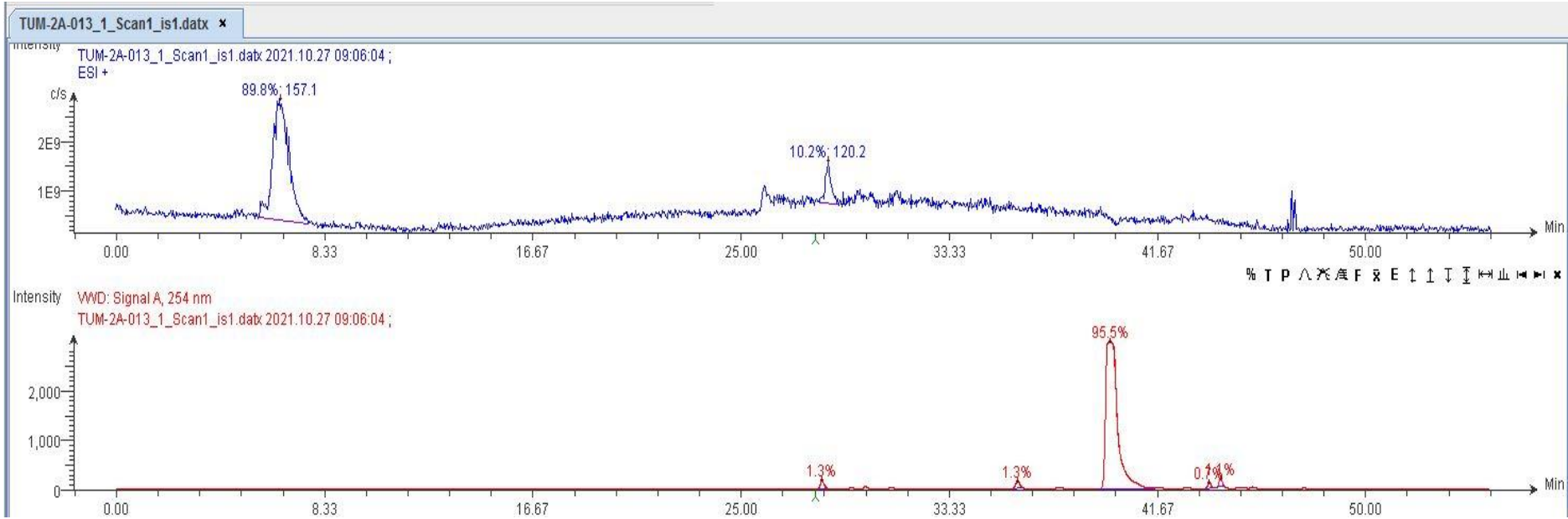
tum-2a-008.sp

## 1.1.7 TUM-2A-013

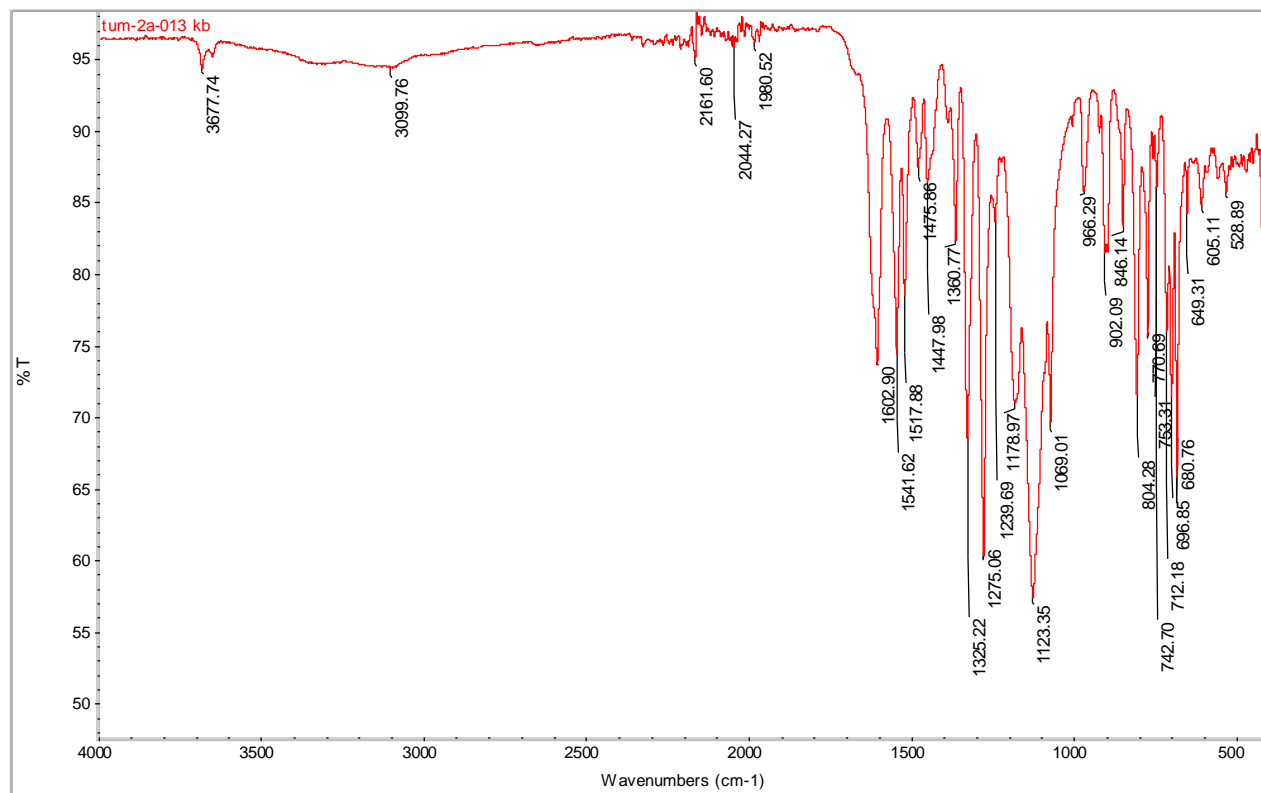
### 1.1.7.1 $^1\text{H}$ NMR Spectrum



1.1.7.2 LC-MS Spectrum

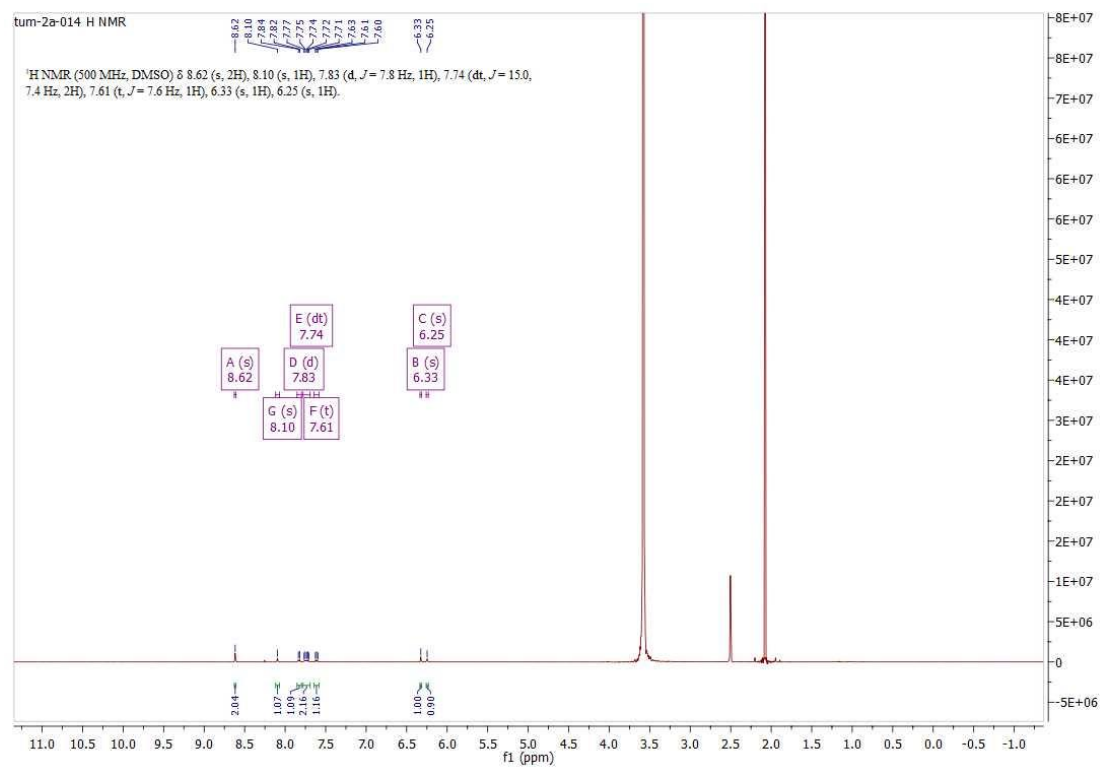


### 1.1.7.3 FTIR Spectrum

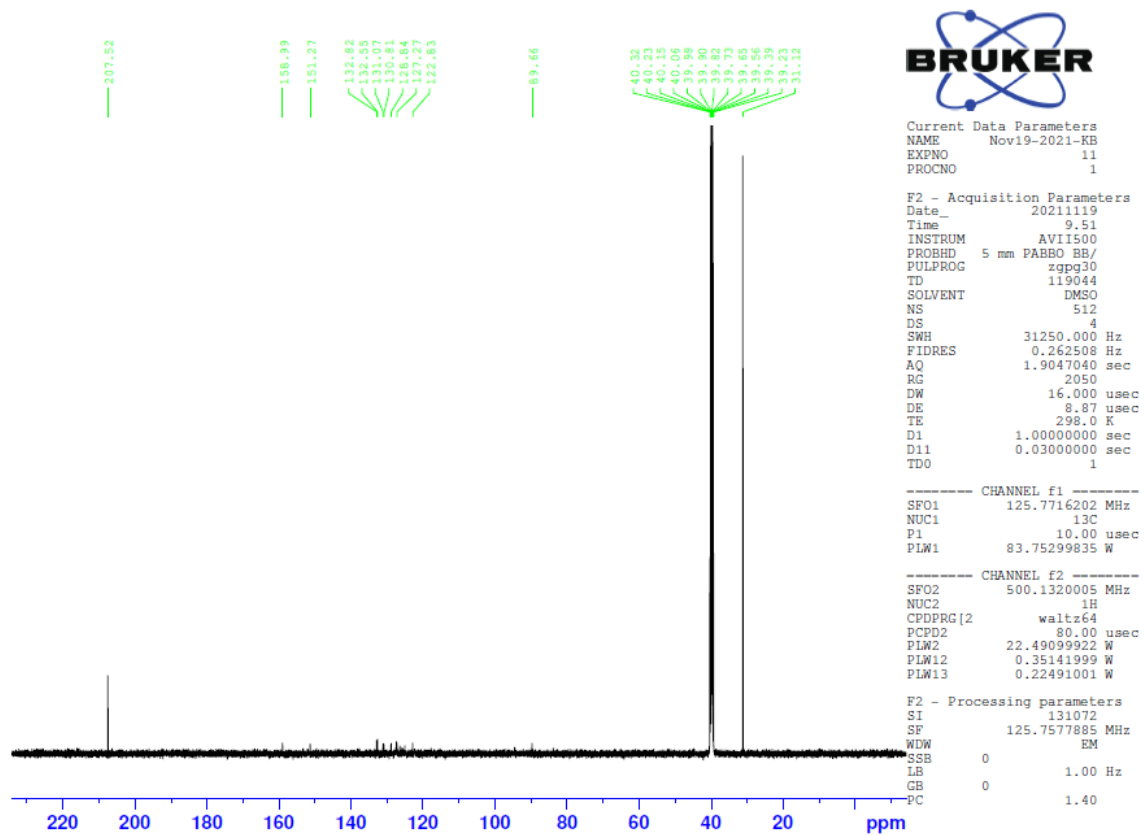


## 1.1.8 TUM-2A-014

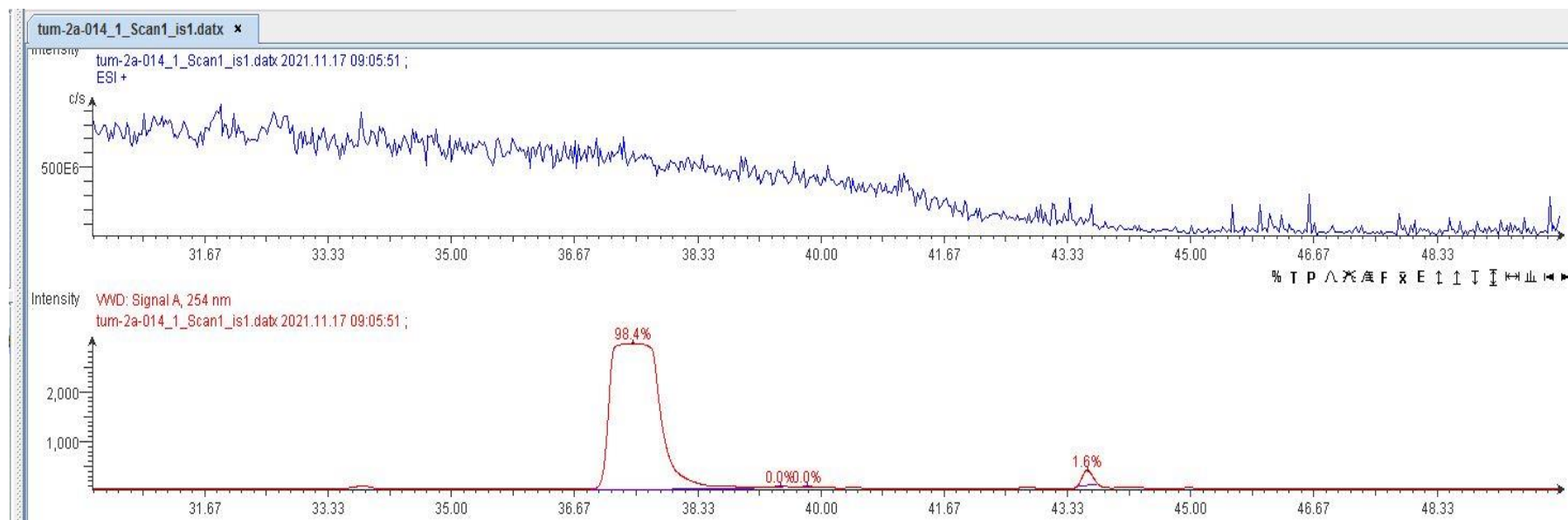
### 1.1.8.1 $^1\text{H}$ NMR Spectrum



### 1.1.8.2 $^{13}\text{C}$ NMR Spectrum

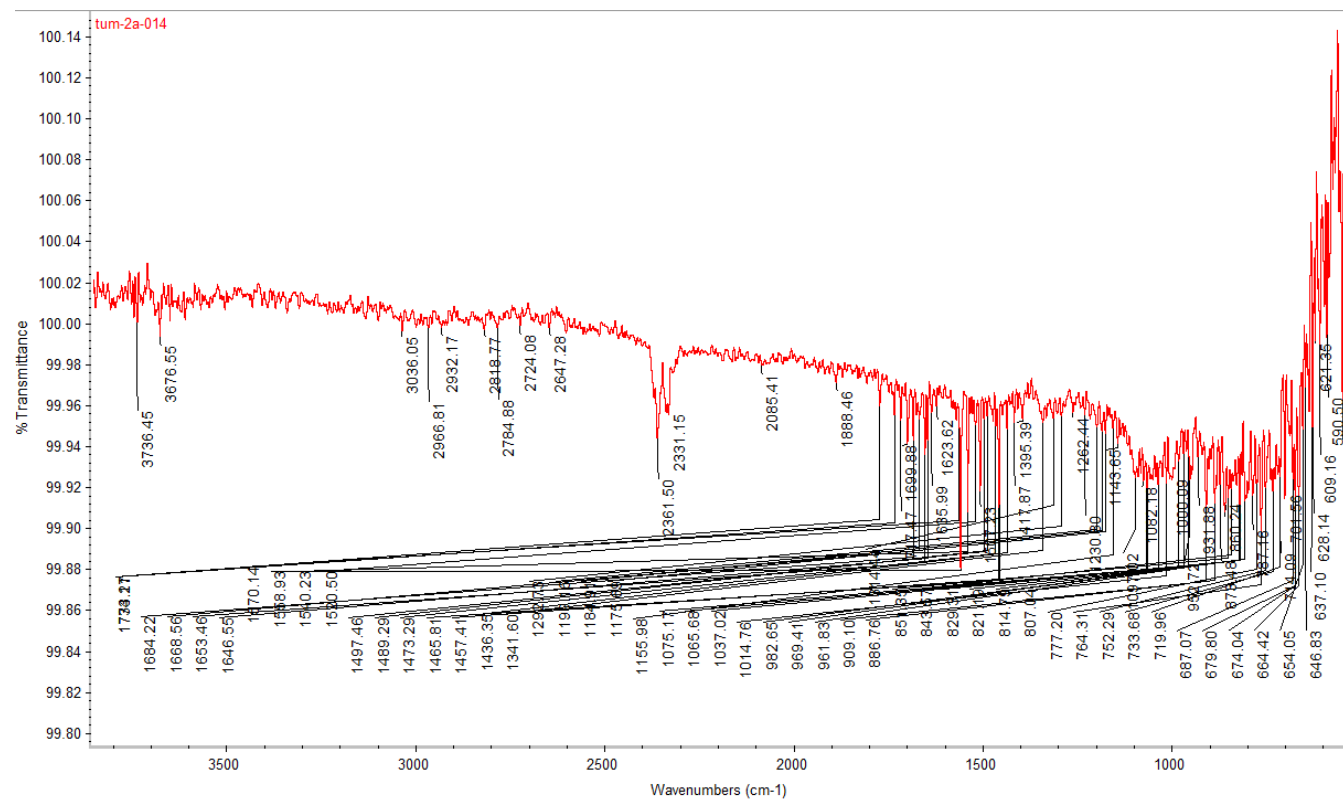


### 1.1.8.3 LC-MS Spectrum





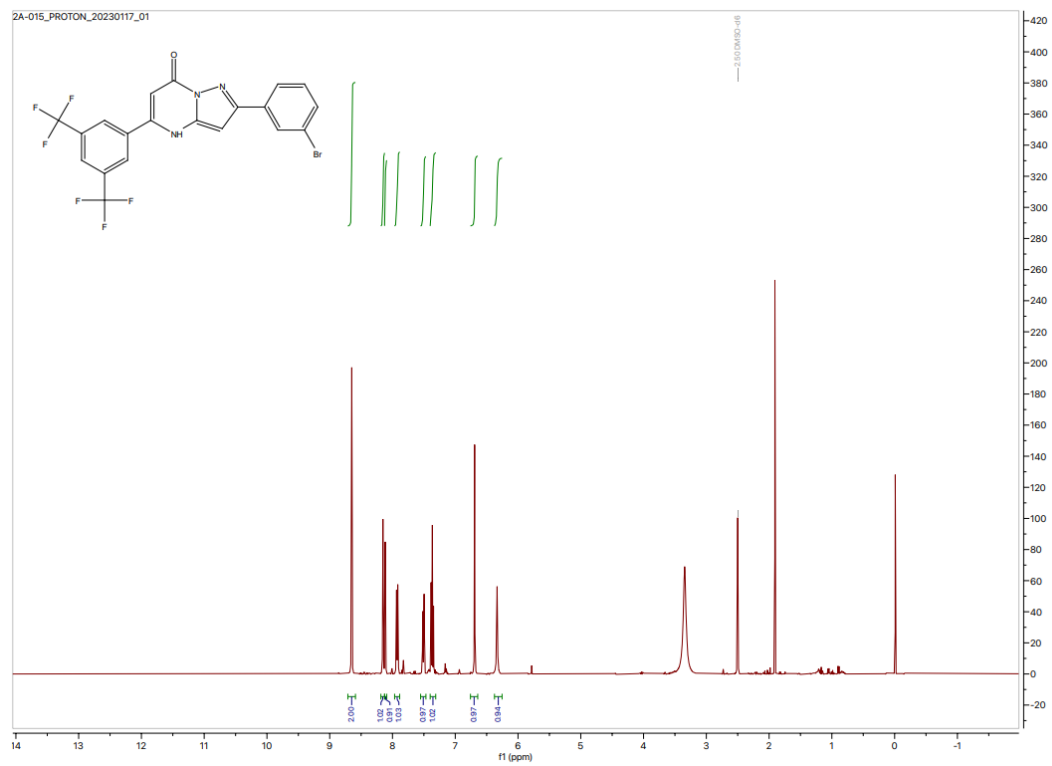
### 1.1.8.4 FTIR Spectrum



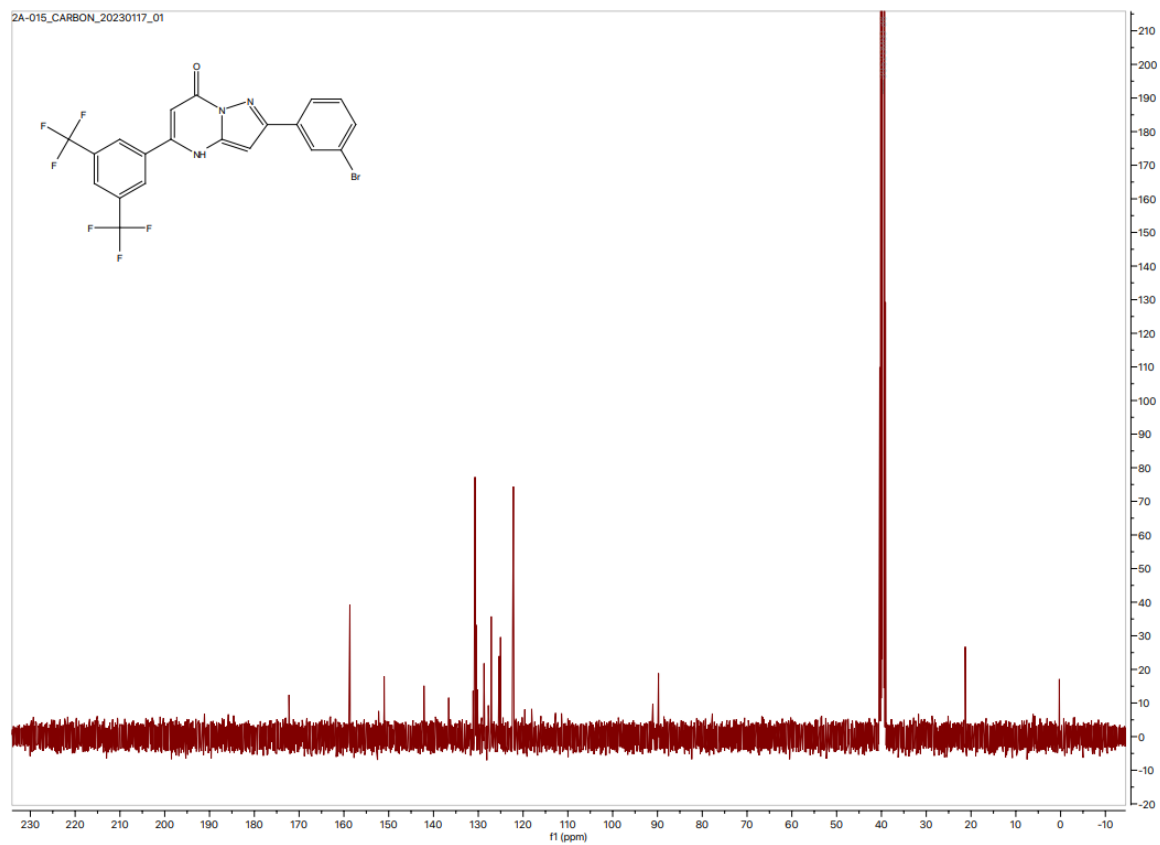
XXX

## 1.1.9 TUM-2A-015

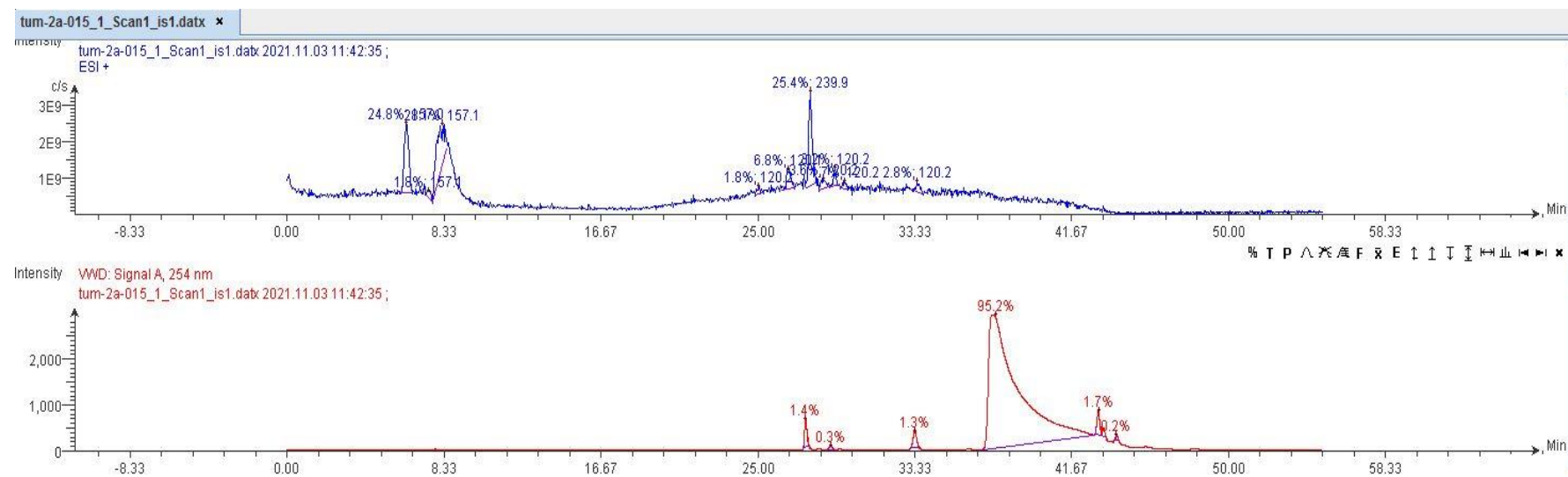
### 1.1.9.1 $^1\text{H}$ NMR Spectrum



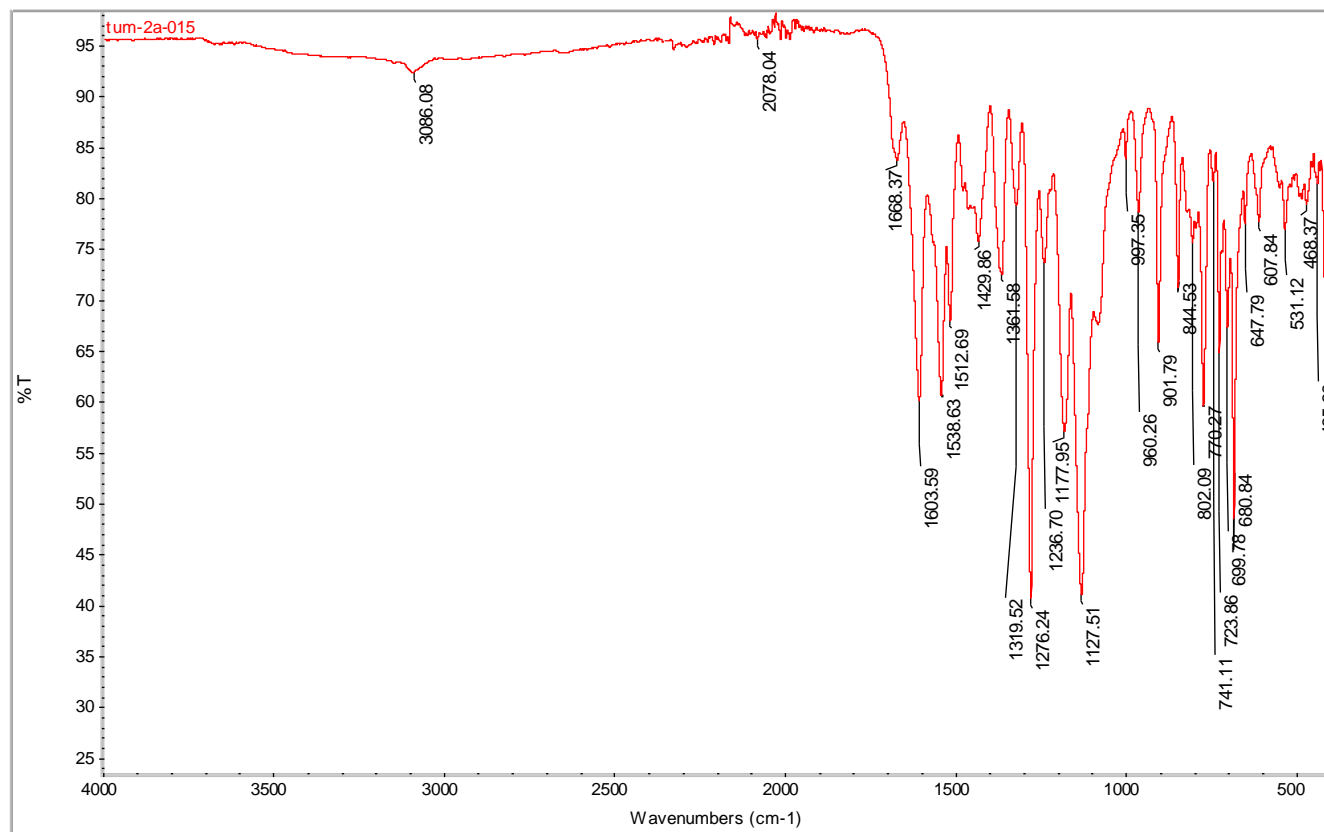
### 1.1.9.2 $^{13}\text{C}$ NMR Spectrum



### 1.1.9.3 LC-MS Spectrum

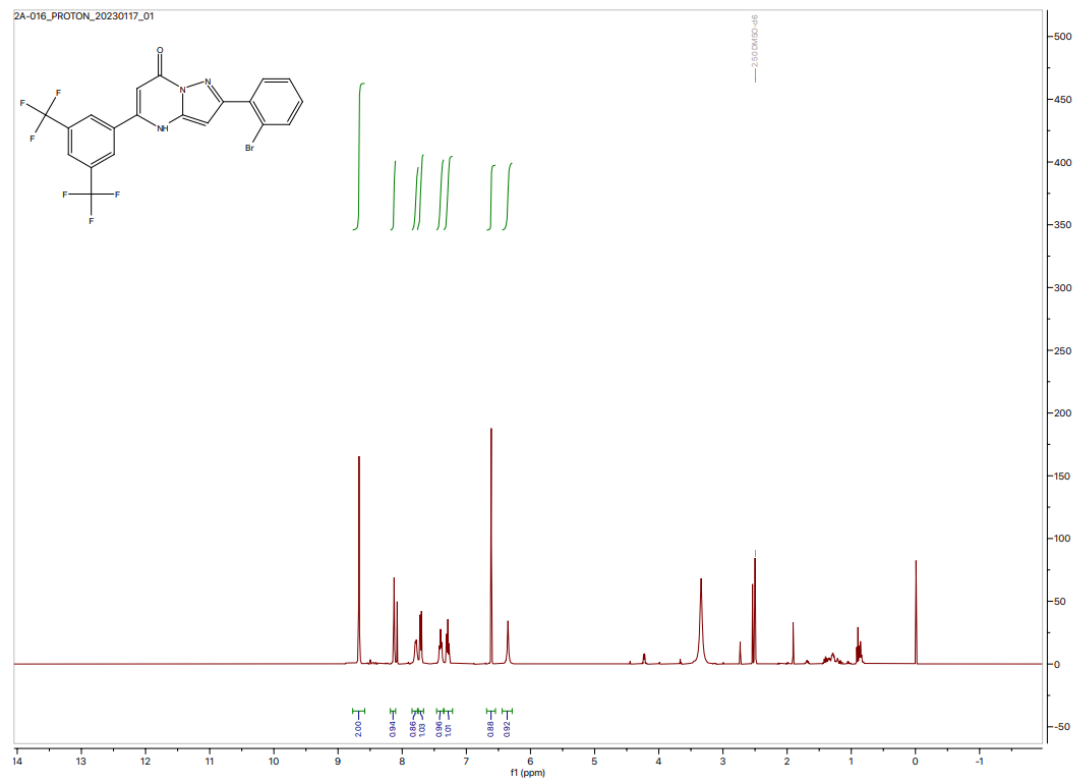


#### 1.1.9.4 FTIR Spectrum



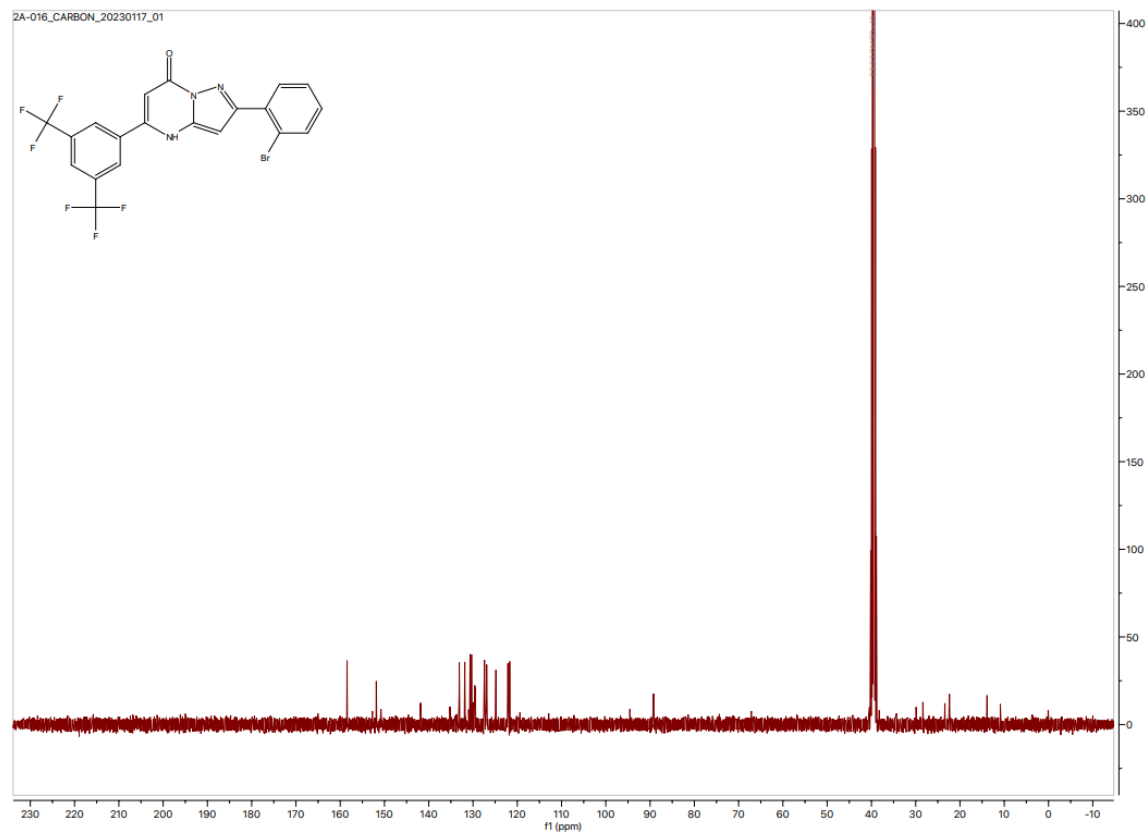
## 1.1.10 TUM-2A-016

### 1.1.10.1 $^1\text{H}$ NMR Spectrum

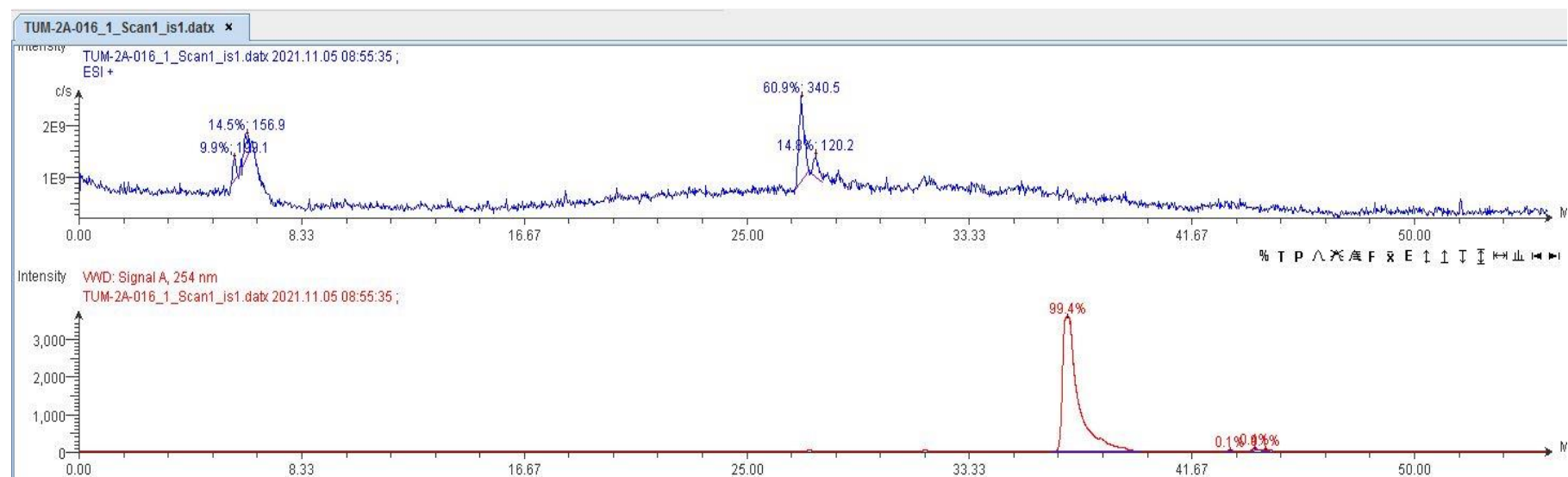


XXXV

**1.1.10.2** *<sup>13</sup>C NMR Spectrum*

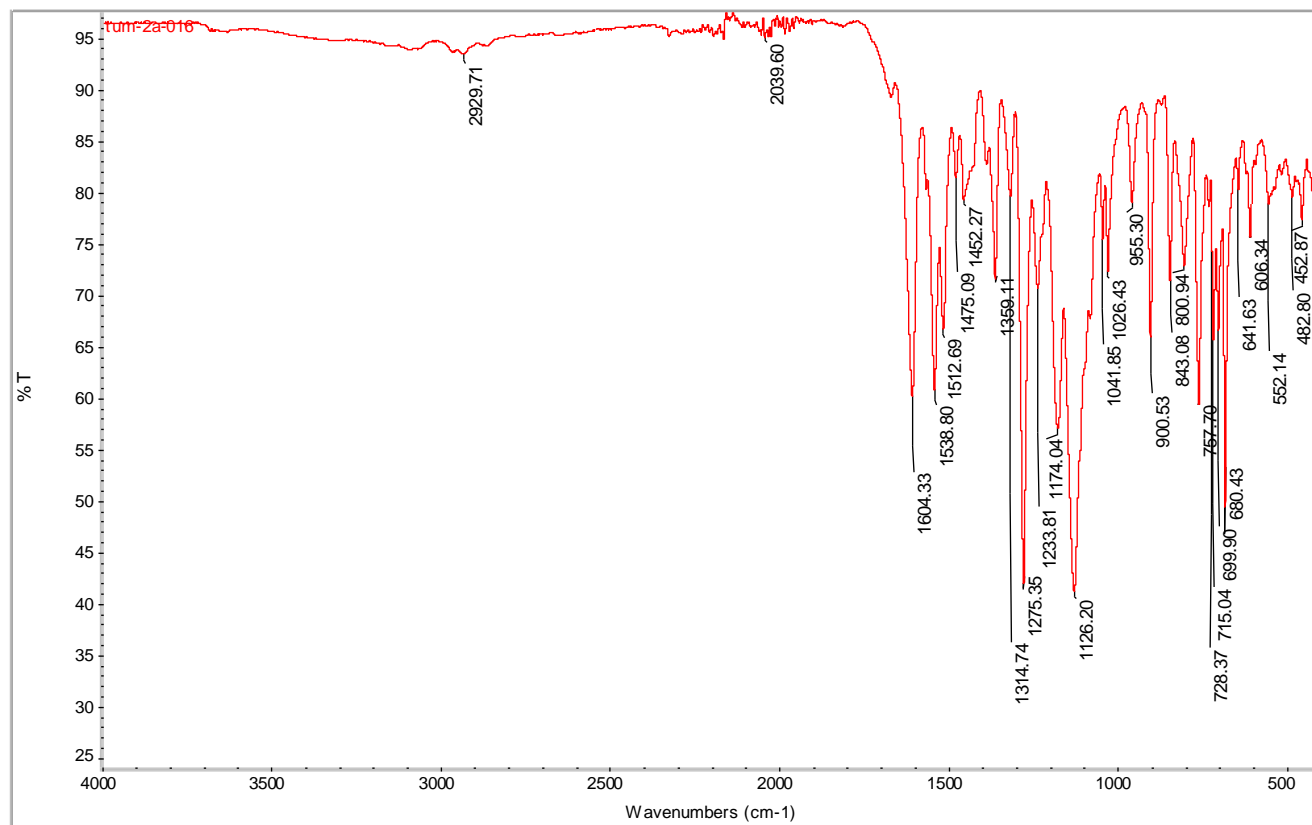


### 1.1.10.3 LC-MS Spectrum



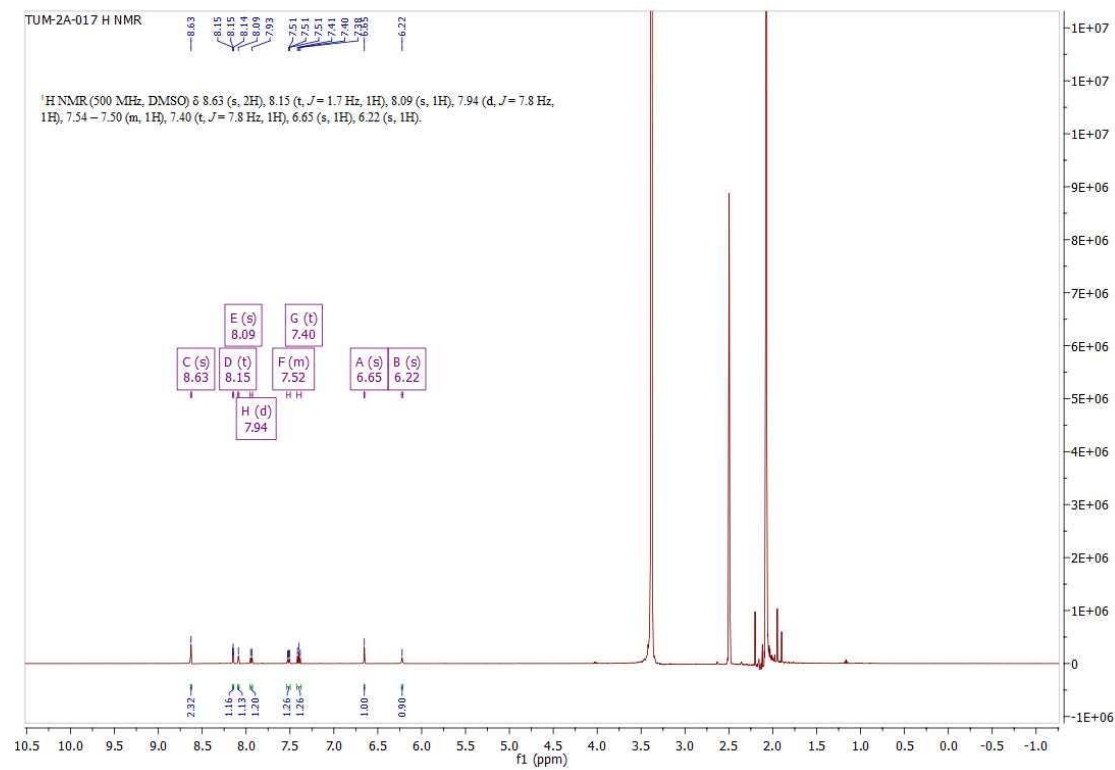


#### 1.1.10.4 FTIR Spectrum

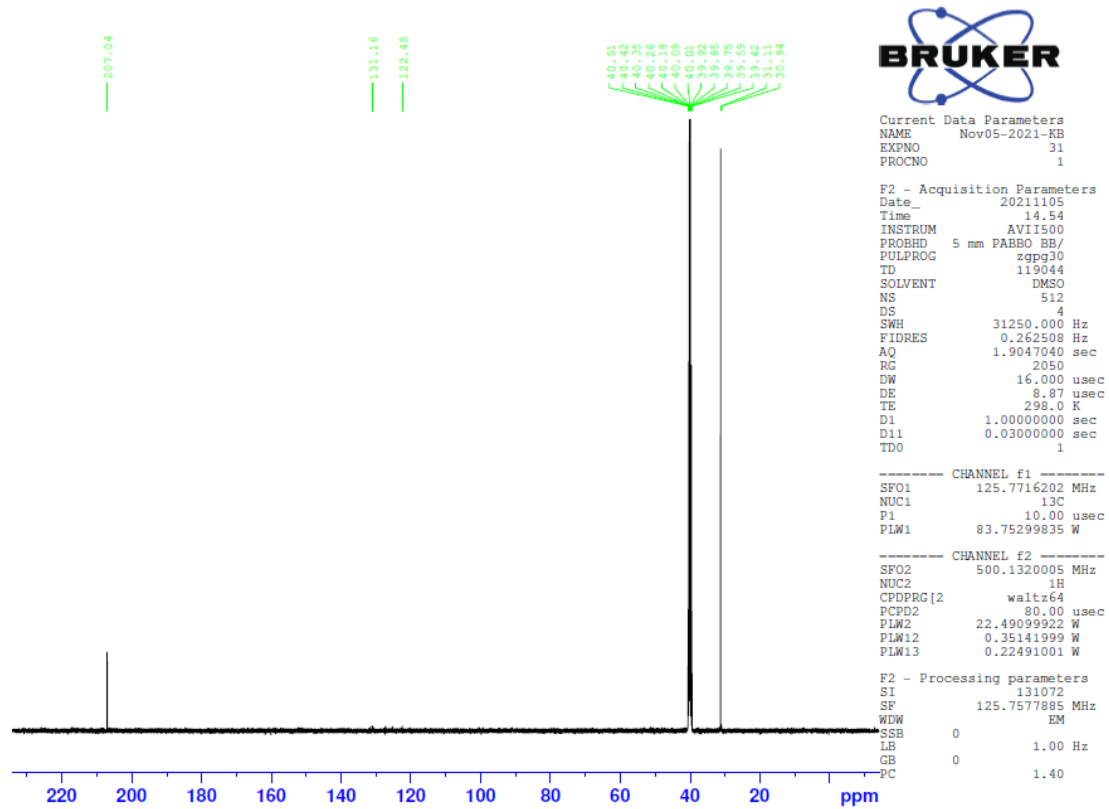


## 1.1.11 TUM-2A-017

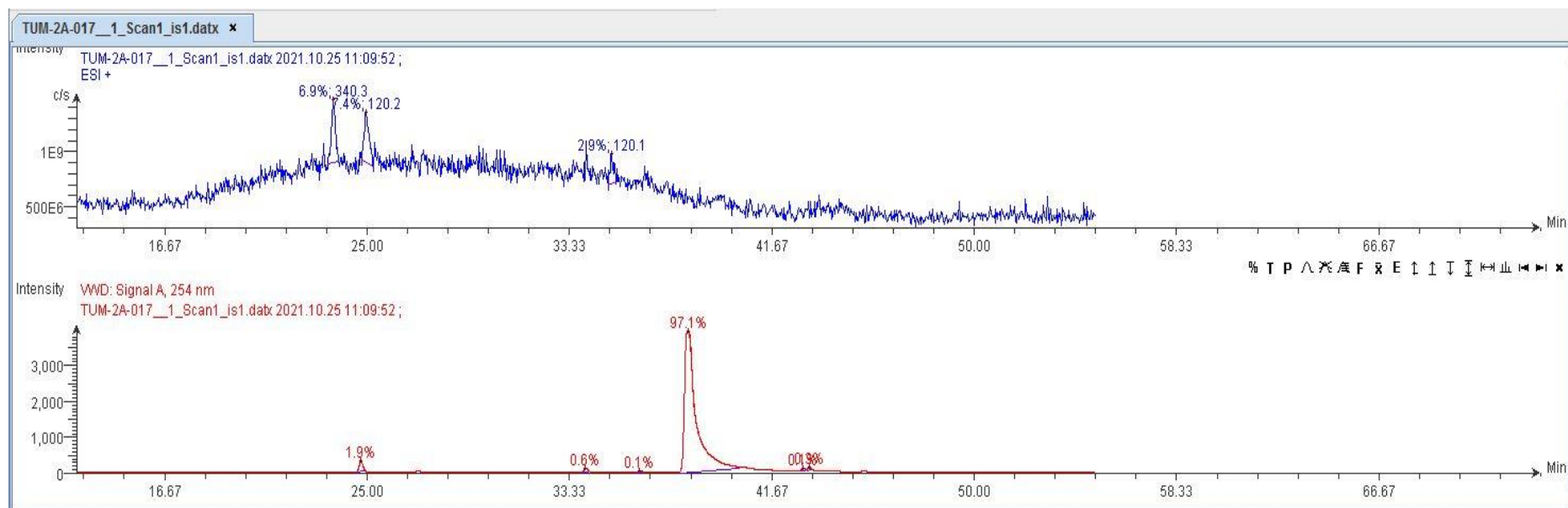
### 1.1.11.1 $^1\text{H}$ NMR Spectrum



### 1.1.11.2 <sup>13</sup>C NMR Spectrum



### 1.1.11.3 LC-MS Spectrum



#### 1.1.11.4 FTIR Spectrum

